The Development and Characterisation of Enhanced Hybrid Solar Photovoltaic Thermal Systems

A thesis submitted in partial fulfilment for the degree of Doctor of Engineering

James Allan

School of Engineering and Design, Brunel University

May 2015

I. Authors Declaration

I declare that this thesis is my own unaided work. It is being submitted for the degree of Doctor of Engineering (EngD) at Brunel University, Uxbridge, Middlesex UK. It has not been previously submitted for any other degree or examination in any other university.

James Allan

Gyeongsang, May 2015

II. Acknowledgements

I would first like to thanks my parents, Janet and Peter Allan for their continued support and encouragement throughout my studies. I would like to thank the EPSRC and ChapmanBDSP for their financial support, particularly Sinisa Stankovic who organised the EngD and was a source of invaluable information throughout. I would also like to thank Dr Alan Harries for his guidance and CFD expertise; and Dr Neil Campbell who managed me and provided me with great insight into the industry. From Brunel University I would like to thank the lab technicians, Abdul Ghani, Peter Warren, Clive Barret, Costas Xanthos and Eamon Wyse, who all went out of their way to make the experimental work possible. I would like thank my academic supervisor Dr Zahir Dehouche who organised the EngD and gave encouragement and advice from day one. I would like to thank my second supervisor Dr George Fern for his support and advice during tough times. I would like to thank my good friend Seong Ha for being patient and giving me the motivation and tools to get over the last hurdle. I would also like to thank Harry Pinder, Anuj Dabeesingh and Lascelle Mauricette who were all a massive help during the experimental stages. It is impossible to list everyone but I am grateful to all my family, friends and co workers who have helped me through the last 5 years.

III. Abstract

A photovoltaic thermal solar collector (PVT) produces both heat and electricity from a single panel. PVT collectors produce more energy, for a given area, than conventional electricity and heat producing panels, which means they are a promising technology for applications with limited space, such as building integration. This work has been broken down into 3 subprojects focusing on the development of PVT technology.

In the first subproject an experimental testing facility was constructed to characterise the performance of PVT collectors. The collectors under investigation were assembled by combining bespoke thermal absorbers and PV laminates. Of the two designs tested, the serpentine design had the highest combined efficiency of 61% with an 8% electrical fraction. The header riser design had a combined efficiency of 59% with an electrical fraction of 8%. This was in agreement with other results published in literature and highlights the potential for manufacturers of bespoke thermal absorbers and PV devices to combine their products into a single PVT device that could achieve improved efficiency over a given roof area.

In the second project a numerical approach using computational fluid dynamics was developed to simulate the performance of a solar thermal collector. Thermal efficiency curves were simulated and the heat removal factor and heat loss coefficient differed from the experimental measurements by a maximum of 12.1% and 2.9% respectively. The discrepancies in the findings is attributed to uncertainty in the degree of thermal contact between the absorber and the piping. Despite not perfectly matching the experimental results, the CFD approach also served as a useful tool to carry out performance comparisons of different collector designs and flow conditions. The effect of 5 different flow configurations for a header collector was investigated. It was found that the most efficient design had uniform flow through the pipe work which was in agreement with other studies. The temperature induced voltage mismatch, that occurs in the PV cells of PVT collector was also investigated. It was concluded that the temperature variation was not limiting and the way in which PV cells are wired together on the surface of a PVT collector did not influence the combined electrical power output.

IV. Reader's Guide to the Portfolio

Section	Title	Content
I	Abstract and guide to portfolio	A guide to the layout and structure of the portfolio
1.0	Executive summary	An introductory chapter giving an overview of the work completed
2.0	Literature review	Literature review of solar technologies and their applications
3.0	Design and construction of experimental validation equipment	The design and construction of the experimental work used to characterise the performance of solar collectors
4.0	Thermal analysis of a PVT collector	Validation of empirical models and development of a CFD approach to simulate the performance of a solar collector
5.0	Enhancing the conductivity of EVA	Investigation into the use of thermally enhanced PV laminate materials to enhance thermal performance of PVT collectors
6.0	General conclusions	Final conclusions drawn from each section of the project

V. Table of Contents

I. Authors Declaration 2

II. Acknowledgements 3

III. Abstract 4

IV. Reader's Guide to the Portfolio 5

V. Table of Contents 6

VI. Nomenclature 9

VII. List of Figures 11

VIII. List of Figures 15

1. Executive Summary 17

1.1 Background 17

1.2 Introduction 17

1.3 Project 1: Construction of Experimental Facility 18

1.4 Project 2: CFD Simulation of a Solar Collector 22

1.5 Project 3: Thermal Enhancement of Photovoltaic Laminates 28

1.6 Events and Presentations 31

1.7 Publications 31

2. Literature Review 32

2.1 Introduction 32

2.2 The Solar Resource 33

2.3 Photovoltaics 33

2.4 Solar Thermal 43

2.5 PVT Collectors 47

2.6 Formation of a PVT collector 58

2.7 Discussion 60

3. Experimental Characterisation of Solar Collectors 61

3.1 Introduction 61

3.2 Experimental Design and Construction 62

3.3 Thermal Performance 66

3.4 Solar Simulation 68

3.5 Control of Inlet Temperature 69

3.6 Flow Control 70

3.7 Temperature Measurements 73
3.8 Error and Reliability 74
3.9 Solar Simulator 77
3.10 Repeatability 84
3.11 Results 87
3.12 Conclusions 108
3.13 Recommendations for Further Work 108
4. Thermal Analysis of a PVT Collector 111
4.1 Introduction 111
4.2 Thermal Analysis of a Flat Plate Solar Thermal Collector 112
4.3 Header-and-Riser Collectors 113
4.4 Serpentine Collectors 116
4.5 Thermal Analysis of a PVT Collector 121
4.6 Transient Models 124
4.7 Empirical Analysis of Experimental Collectors 127
4.8 Empirical Analysis of Serpentine Collector 130
4.9 Empirical Analysis of Header Riser Collector 131
4.10 Discussion of Results from Empirical Analysis 132
4.11 Computational Fluid Dynamics 133
4.12 CFD Modelling of Solar Collectors 136
4.13 Simulation Results 147
4.14 Analysis of Results 157
4.15 Discussion of discrepancies 168
4.16 Summary of CFD Approach 169
4.17 PV Cell Mismatch 170
4.18 Analysing Mismatch using CFD Models 180
4.19 Results from Temperature Mismatch Study 181
4.20 Conclusions 182
4.21 Recommendations for Future Work 183
5. Enhancing the Thermal Conductivity of EVA 184
5.1 Introduction 184
5.2 Influence of Temperature on Photovoltaic Efficiency 184
5.3 Layers of a Photovoltaic Laminate 184

5.4 Enhancing the Thermal Conductivity of EVA 185
5.5 Measuring Thermal Conductivity 186
5.6 Project Summary 189
5.7 Methodology 189
5.8 Heat Transfer Numerical Models 193
5.9 Results 197
5.10 Conclusions 203
5.11 Recommendations for future work 203
6. General Conclusions 204
7. References 207

VI. Nomenclature

A	Area	[m^2]	α	Thermal diffusivity	[m^2/s]
A_c	Collector area	[m^2]	α	Absorbtance	
C_b	Bond conductance	[W/m·K]	δ	Thickness	[m]
c_{ef}	Specific heat of front EVA layer	[J/K·kg]	α_g	Thermal diffusivity of PV layer	[m^2/s]
c_g	Specific heat of glass	[J/K·kg]	α_{pv}	Thermal diffusivity of glass layer	[m^2/s]
c_p or c	Specific heat	[J/K·kg]	η	Efficiency	
c_{pv}	Specific heat of PV layer	[J/K·kg]	δ	Thickness	[m]
D	Tube Diameter	[m]	τ	Transmittance	
D_e	External pipe diameter	[m]	β	Temperature coefficient of PV cell efficiency	[%/K]
D_i	Internal pipe diameter	[m]	ζ_x	Exergetic efficiency	
FF	Fill Factor				
F'	Collector efficiency factor		ρ	Density	[kg/m^3]
F_R	Heat removal factor		σ	Stefan-Boltzmann constant [5.67 x 10^{-8}]	[Wm^{-2}K^{-4}]
G	Irradiance	[W/m^2]			
g	Volumetric heat generation	[W/m^3]	λ	Thermal Conductivity	[W/m·K]
H	Heat of fusion		ρ_g	Density of glass	[kg/m^3]
h	Convective heat transfer coefficient	W/m^2·K	φ	Volume fraction	
h_b	Convective heat transfer coefficient of back surface	W/m^2·K			
h_{fi}	Internal heat transfer coefficient	[W/m^{2}K]			
HR	Header Riser Collector				
HWB	Hottel Whillier Bliss				
k	Thermal conductivity	[W/m·K]			
K_{eb}	Thermal conductivity of back EVA layer	[W/m·K]			
K_{ef}	Thermal conductivity of front EVA layer	[W/m·K]			
K_g	Thermal conductivity of glass	[W/m·K]			
K_{pv}	Thermal conductivity of PV cell	[W/m·K]			
K_t	Thermal conductivity of tedlar	[W/m·K]			

m	Mass flow rate	[kg/s]
M	Gradient of slope	
MPP	Maximum Power Point	[MPP]
Q or Q_u	Useful energy per unit time	[W]
S	Absorbed Solar Energy	[W]
T	Temperature	[°C]
t	Time	[s]
T	Temperature	[K]
t	Time	[s]
T_a	Ambient temperature	[°C]
T_b	Fixed temperature of plate in contact with laminate	[°C]
T_c	Cover temperature	[°C]
T_i	Inlet temperature	[°C]
T_o	Outlet temperature	[°C]
T_p	Local plate temperature	[°C]
T_{pm}	Average plate temperature	[°C]
U_L	Overall heat loss coefficient	[W/m^{2}K]
v	Kinematic Viscosity	[m^2/s]
V	Volume	[m^3]
W	Distance between tubes or weight	[m] [kg]
w/w	Mass fraction	
x	Layer width	[m]
X_e	Exergy per unit time	[W]
x_{eb}	Thickness of back EVA layer	[m]
x_{ef}	Thickness of front EVA layer	[m]
x_g	Thickness of glass layer	[m]
x_{pv}	Thickness of PV layer	[m]
X_t	Exergy per unit time	[W]
x_t	Thickness of tedlar layer	[m]

VII. List of Figures

Figure 1-1: Testing equipment used to characterise the performance of solar collectors 18
Figure 1-2: Comparison of a serpentine and header riser collector 19
Figure 1-3: Readings from thermocouples mounted on the rear surface of a serpentine 20
Figure 1-4: Combined power output of a serpentine PVT collector 21
Figure 1-5: Comparison of experimental and simulated thermal efficiency. 23
Figure 1-6: Comparison of simulated (left) and measured temperature distribution (right) 23
Figure 1-7: Flow configurations investigated during the study 24
Figure 1-8: The results from the CFD study into different single flow configurations 25
Figure 1-9: The results from the CFD study into different dual flow configurations 26
Figure 1-10: Wiring Configurations 27
Figure 1-11: Layers of a PV Laminate 28
Figure 1-12: Cross section of PV laminate investigated in this study 29
Figure 1-13: Thermal conductivity vs. concentration of boron nitride filler 29
Figure 1-14: Temperature profile across PV laminate 30
Figure 2-1: Average hourly radiation data for each month for Gatwick, London. Source [84] 33
Figure 2-2: Types of PV Technology 34
Figure 2-3: Operation of multijunction devices. Source [3]. 36
Figure 2-4: Efficiency-cost trade-off for the three generations of solar cell technology 37
Figure 2-5: Operation of crystalline PV cell. Source [3] 39
Figure 2-6: IV relationship between solar cell performance characteristics. Source [3]. 40
Figure 2-7: Effect of series and parallel resistance on IV curve. Adapted from [100] 41
Figure 2-8: Effect of irradiance on PV cell performance 41
Figure 2-9: Effect of temperature on PV cell performance 42
Figure 2-10: Technology tree of main solar thermal technologies 44
Figure 2-11: Angular Fractherm panels for building integration. Source Hermann 2011 [67] 45
Figure 2-12: Thermal efficiency curves of solar thermal collector technologies. 46
Figure 2-13: Hybrid PVT Panel. Source Solimpeks 48
Figure 2-14: Solimpeks PowerTherm PVT panel Source: Solimpeks 49
Figure 2-15: PVT Solar Duct left and PVT Solar Wall Right. Source Conserval Engineering 49
Figure 2-16: BIPVT water system. Source Englert [46] 50
Figure 2-17: TRNSYS flow diagram 56
Figure 3-1: System used to test the thermal performance of solar collectors 62
Figure 3-2: Dimensions in mm of the collectors analysed in this study 63
Figure 3-3: Layers of the PVT Collector 65
Figure 3-4: Schematic of the system used to characterise thermal performance 66
Figure 3-5: Supporting frame for performance characterisation of a solar collector 67
Figure 3-6: Dimensions used to calculate focal length 68
Figure 3-7: Positioning of lamps 68
Figure 3-8: Extractor fans used to cool lamps 69

Figure 3-9: 5 stage temperature profile, programmed using Presto A40 70
Figure 3-10: Mass flow controller and gear pump..... 71
Figure 3-11: System and pump curves 73
Figure 3-12: Location of thermocouples organised on grid A1 – D8 73
Figure 3-13: Calibration of thermocouples and data logger..... 75
Figure 3-14: Calibration curve for thermocouples..... 76
Figure 3-15: ASTM 1.5 reference spectra..... 78
Figure 3-16: Calibrated reference cell and grid for testing irradiance..... 78
Figure 3-17: Graph to determine absorbed solar energy using uncovered 81
Figure 3-18: Plot to determine absorbed solar energy with ±20% absorbtance uncertainty 82
Figure 3-19: Spectral distribution of the lamp output, ... 83
Figure 3-20: Irradiance measurements as a function of time 84
Figure 3-21: Repeatability testing with no cover 85
Figure 3-22: Repeatability testing with cover 86
Figure 3-23: Comparison of uncovered header riser and serpentine collector..... 87
Figure 3-24: Comparison of average plate temperature for uncovered 89
Figure 3-25: Temperature distribution for header riser and serpentine designs. 90
Figure 3-26: Comparison of thermal efficiency curves for uncovered and covered collectors ... 92
Figure 3-27: Mean plate temperature for covered and uncovered collector..... 93
Figure 3-28: Comparison of the absorber temperature for covered (left) and uncovered (right) 94
Figure 3-29: PV laminates connected in series and clamped to the surface of the absorber 95
Figure 3-30: IV curve from series connected PV laminates at varying inlet temperature..... 96
Figure 3-31: Power voltage plot at different inlet temperatures 96
Figure 3-32: Resistance vs. power plot for different inlet temperatures 97
Figure 3-33: Measuring the current output of the PVT collector 97
Figure 3-34: Power calculated using fixed resistance 98
Figure 3-35: Thermal efficiency curve for PVT collector with and without electricity 99
Figure 3-36: Breakdown of power output from the PVT collector 100
Figure 3-37: Average plate temperature for the cases with and without electricity 102
Figure 3-38: Temperature profiles for cases without (left) and with electricity generation 103
Figure 3-39: Thermal efficiency curve for the cases of glass and Tedlar backing materials 105
Figure 3-40: Average plate temperature for the cases of different backing materials 106
Figure 3-41: Comparing the surface temperature distribution for PVT collectors..... 107
Figure 4-1: Header and Riser Collector 113
Figure 4-2: Energy balance on fin section (adapted from Duffie and Beckman, 1991) 114
Figure 4-3: Influence of fin width on fin efficiency (adapted from Duffie and Beckman 1991) . 115
Figure 4-4: Serpentine Collector 116
Figure 4-5: Serpentine Collector as analysed by Abdel Khalik. 117
Figure 4-6: Illustration of the Finite Difference Method 119
Figure 4-7: Influence of Number of Turns and Tube Spacing on Heat Removal Factor 119
Figure 4-8: Effect of number of turns and mass flow rate on heat removal factor.[33]..... 120
Figure 4-9: Designs of water based PVT systems. Source [27]. 121

Figure 4-10: Exergy Dependence on UL and Collector Width. Source Xiowu 2005. 124
Figure 4-11: Development of internal laminar flow 128
Figure 4-12: Successful diagnostic topology. 139
Figure 4-13: Global prism settings 140
Figure 4-14: Surface meshing controls applied to the geometry 141
Figure 4-15: Comparison of Histogram before (left) and after (right) 141
Figure 4-16: Segment of cut plane through the mesh 142
Figure 4-17: Velocity contour across inlet assigned with develop flow profile 144
Figure 4-18: Solution residuals for serpentine collector with 50°C inlet temperature 145
Figure 4-19: Solution residuals for parallel collector with 50°C inlet temperature 146
Figure 4-20: Comparison of experimental and CFD thermal efficiency curves serpentine 148
Figure 4-21: Comparison of experimental and CFD thermal efficiency header riser 148
Figure 4-22: Plot of energy useful energy per m^2 of collector surface serpentine 150
Figure 4-23: Plot of energy useful energy per m^2 of collector surface header riser 150
Figure 4-24: Serpentine experimental and CFD results for average absorber temp. 151
Figure 4-25: Header Riser experimental and CFD results for average absorber temp. 152
Figure 4-26: Heat transfer process and surface temperature across an absorber 154
Figure 4-27: Separation of laser welded pipes on similar absorber. Source [133] 155
Figure 4-28: Thermal image of serpentine collector during dark testing 156
Figure 4-29: Comparison of temperature distribution for serpentine collector 156
Figure 4-30: Comparison of temperature distribution for header riser collector 157
Figure 4-31: Thermal contact :simulation and the actual 158
Figure 4-32: Temperature distribution for different contact situations. 159
Figure 4-33: Velocity profile along the header and risers 160
Figure 4-34: Velocity profile in one of the U bends of the serpentine collector 160
Figure 4-35: Streamlines in the U bend of the serpentine collector to show fluid mixing 161
Figure 4-36: Pressure drop comparison in the header-riser and serpentine collector 162
Figure 4-37: The control surfaces of the parallel collector 163
Figure 4-38: Comparison of temperature distribution for non-uniform irradiance 164
Figure 4-39: Flow patterns for header riser collector 165
Figure 4-40: Comparison of single flow conditions for a parallel collector 166
Figure 4-41: Comparison of dual flow systems 167
Figure 4-42: Effect of absorber thickness on heat transfer in the simulation 168
Figure 4-43: Effect of voltage mismatch on a bad and good cell connected in parallel. 171
Figure 4-44: Calculation of operating voltage of two mismatched cells 172
Figure 4-45: Graph used to calculate temperature coefficient 173
Figure 4-46: Experimental testing of output voltage for two cells connected in parallel. 173
Figure 4-47: Effect of temperature difference on total voltage 174
Figure 4-48: Experimental testing of output voltage for four cells connected in parallel. 174
Figure 4-49: Effect of temperature difference on total voltage for five cells 175
Figure 4-50: Comparison of the impact of a low voltage cell on the overall voltage 176
Figure 4-51: Comparison of the impact of a low voltage cell on the overall voltage 176

Figure 4-52: Calculation of V_{mp} coefficient using data from the IV curve. 177
Figure 4-53: Calculation of V_{oc} temperature coefficient using data from the IV curve. 178
Figure 4-54: Calculation of maximum power point (P_{mp}) temperature coefficient 178
Figure 4-55: Calculation of V_{mp} temperature coefficient using datasheet values 179
Figure 4-56: The wiring configurations of PV cells applied to each flow configuration. 180
Figure 4-57: Extracting average cell temperature using sample planes in CFX Post. 181
Figure 5-1: The layers of a PV laminate and their respective thicknesses 185
Figure 5-2: Twin screw extrusion of the composite material..... 190
Figure 5-3: Illustration of the DSC melting standard method. Source [38]. 191
Figure 5-4: Interface of the results analysis program and the resulting graph 192
Figure 5-5: Laminated photovoltaic cells. 193
Figure 5-6: Experimental measurement of the temperature at the interface of each layer 193
Figure 5-7: Illustration of the finite difference model 194
Figure 5-8: Thermal conductivity vs. BN concentration of the composite..... 197
Figure 5-9: Average temperature at each interface vs time for standard EVA backed PV cell 199
Figure 5-10: Average temperature at each interface vs. time..... 199
Figure 5-11: A comparison of the average laminate temperature 200
Figure 5-12: Temperature profile for Case 1..... 201
Figure 5-13: Temperature profile for Case 2..... 202

VIII. List of Figures

Table 1-1: Parameters extracted from the thermal efficiency curve 19
Table 1-2: Results from mismatch study..... 27
Table 2-1: Confirmed efficiencies for solar cells and commercially available modules [63]..... 37
Table 2-2: Temperature coefficients for PV technologies. Source [143] 42
Table 2-3: Default values of collector specific performance parameters. Adapted from [15]..... 46
Table 2-4: Experimental findings for the zero loss efficiency..... 53
Table 2-5: Case studies of PVT Systems 55
Table 2-6: Methods of bonding PV cells to a thermal absorber..... 59
Table 3-1: Technical data of Lazerplate fins. Source (S-Solar, Sweden)..... 63
Table 3-2: Electrical characteristics of individual PV cells 64
Table 3-3: Temperature coefficients of PV cells 64
Table 3-4: Operating conditions for inline heat exchanger as calculated by the manufacturer.. 70
Table 3-5: Flow controller calibration certificate as supplied by manufacturer 71
Table 3-6: Fittings for system plus serpentine and HR collector 71
Table 3-7: Summary of the uncertainties used in the calculations in this report 74
Table 3-8: Calibration data for 0.2mm thermocouples..... 76
Table 3-9: Calibration data for 0.125mm thermocouples..... 77
Table 3-10: Solar simulator requirements for the performance testing of solar collectors. 77
Table 3-11: Solar simulator requirements for the performance testing of PV collectors 77
Table 3-12: Distribution of irradiance measured using a calibrated reference cell 79
Table 3-13: Distribution of irradiance when using diffuser..... 79
Table 3-14: Summary of measurements from each irradiance method 82
Table 3-15: Effect of the uncertainty associated with the variable absorbtance..... 82
Table 3-16: Determination of spectral distribution using the spectral intervals 83
Table 3-17: Results of repeatability testing without cover 85
Table 3-18: Results of repeatability testing with cover 86
Table 3-19: Parameters extracted from the thermal efficiency curve 88
Table 3-20: Comparison of parameter for the covered and uncovered collector 92
Table 3-21: Measured current values at different inlet set points. 98
Table 3-22: Parameters extracted from thermal efficiency curves 100
Table 3-23: Combined output of the PVT system..... 100
Table 3-24: Comparison of 3 cases with a polycarbonate sheet 101
Table 3-25: Comparison of the thermal performance of using different backing materials 105
Table 3-26: Comparison of electrical output from glass and tedlar backed PV laminates 106
Table 4-1: Exergetic comparison of PVT electrical and thermal output..... 124
Table 4-2: Determining the internal heat transfer coefficient inside the pipes 127
Table 4-3: Calculation of heat transfer coefficient for the header riser collector 129
Table 4-4: Calculation of heat transfer coefficient for the serpentine collector 130
Table 4-5: Example calculation of F_R using the Zang and Lavan approach 130

Table 4-6: Comparison of calculated vs experimental values for the serpentine collector 131
Table 4-7: Example calculation of F_R for the header riser collector using the HWB 131
Table 4-8: Comparison of calculated vs experimental values for the header riser collector 132
Table 4-9: Velocity parameters for each inlet temperature 143
Table 4-10: Results of mesh sensitivity study for the serpentine collector 147
Table 4-11: Comparison of values of F_R and U_L measured experimentally and CFD 149
Table 4-12: Distribution of absorber temperature for serpentine collector 152
Table 4-13: Distribution of absorber temperature for header riser collector 153
Table 4-14: Effect of increasing the thermal contact resistance 157
Table 4-15: Effect of increasing the contact length between the fluid and the absorber 158
Table 4-16: Calculation of internal heat transfer coefficient from CFD 159
Table 4-17: Calculation of thermal output to pumping power for serpentine collector 161
Table 4-18: Calculation of thermal output to pumping power for header riser collector 162
Table 4-19: Coefficients used to adjust the average value of irradiance 163
Table 4-20: Comparison of temperature coefficient values obtained from different methods. 179
Table 4-21: The electrical power output of each flow configuration 182
Table 5-1: Summary of methods used to test the thermal conductivity of polymers] 187
Table 5-2: The general properties of CrodaTherm 25 192
Table 5-3: Calculation of volume fraction..... 198

1. Executive Summary

1.1 Background

This project was sponsored by ChapmanBDSP, an engineering consultancy specialising in building services. The focus of the research was understanding the fundamentals that underpin the performance of solar technologies so that they can be incorporated into commercial projects.

1.2 Introduction

Over the past decade solar energy has been one of the fastest growing renewable energy technologies. Financial support has pushed it from being a niche technology into a major player in the energy industry.

A review of literature showed that there is limited suitable space in the built environment for the integration of solar technologies due to shading and inadequate orientation; therefore any space that is available, must be used as efficiently as possible. Another problem for solar is its low efficiency compared with other forms of energy generation.

There are two main types of solar energy technology available; photovoltaic (PV) which generates electricity and solar thermal which generates heat. There are also photovoltaic-thermal collectors where PV and solar thermal are combined to create a hybrid panel that produces both heat and electricity. Results published in literature show that PV-T collectors can produce a greater energy output than individual technologies installed side by side.

In the first project two PVT collectors, a serpentine and header riser design, were created using bespoke PV laminates and a solar thermal absorber. To test their performance, new facilities were constructed comprised of the following components; an artificial source of irradiance, temperature control, mass flow control, structural support for the collector and data logging. The testing facility was constructed so that it could be adapted and adjusted easily to accommodate for future research projects.

The second project developed a numerical method using CFD to visualise the performance of solar thermal collectors. These models were validated against experimental measurements and used to determine the electrical efficiency of PV cells if they were mounted onto the surface.

The final project enhanced the conductivity of PV cell encapsulation materials. By mixing EVA polymer with ceramic powders a composite was created that had increased thermal conductivity but maintained electrical resistivity. A method was developing using differential scanning calorimetery to test the thermal conductivity of polymers with a low melting point (<200°C). A numerical model based on the finite difference approach was created to simulate the temperature profile through the cross section of a PV laminate and validated against experimental measurements.

1.3 Project 1: Construction of Experimental Facility

1.3.1 Aim

To build an adaptable testing facility to characterise the performance of solar technologies and validate numerical models

1.3.2 Method

The purpose of the experiment was to measure the thermal efficiency curve and pressure drop of different designs of solar thermal collector. It can also be used to determine the electrical output of PV and PVT systems when combined with an IV tracer. The rig is made up of two frames - one to mount the collector and the other to mount the solar simulator. The simulator consists of 4 x 1000W metal halide lamps and is used for indoor testing. Collectors measuring 1m x 0.7m can be tested using the simulator. As well as providing mounting for the collector, the collector frame also contains the dynamic temperature control system, the mass flow controller, gear pump and a manometer for differential pressure measurements across the collector. The collector frame can be detached from the solar simulator and can be used for outdoor testing. Larger collectors can be tested outdoors provided that mounting brackets and weather monitoring equipment is supplied. Both frames are adaptable and can be modified in future if it is required. The testing station is shown in Figure 1-1.

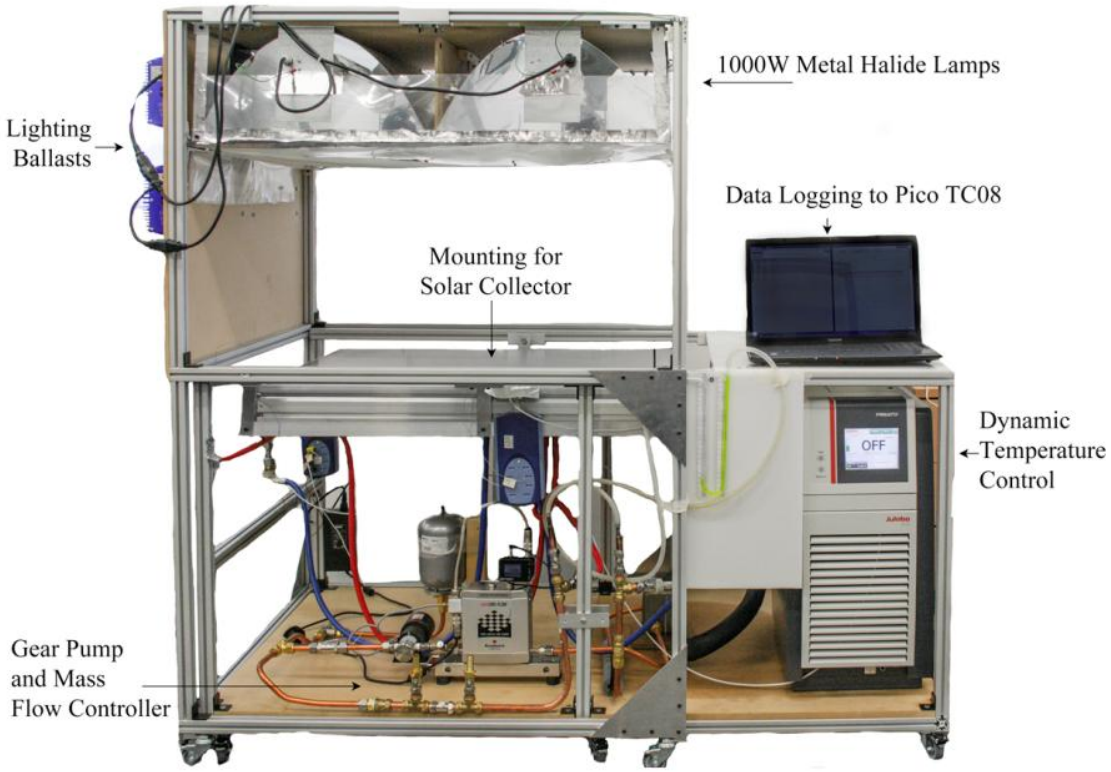

Figure 1-1: Testing equipment used to characterise the performance of solar collectors

1.3.3 Results

To show the capability of the equipment several cases were compared. In the first case a serpentine collector was compared against a header riser collector using the same mass flow rate, see Figure 1-2. It was found that the header riser was less efficient, with a 34% increase in the overall loss coefficient.

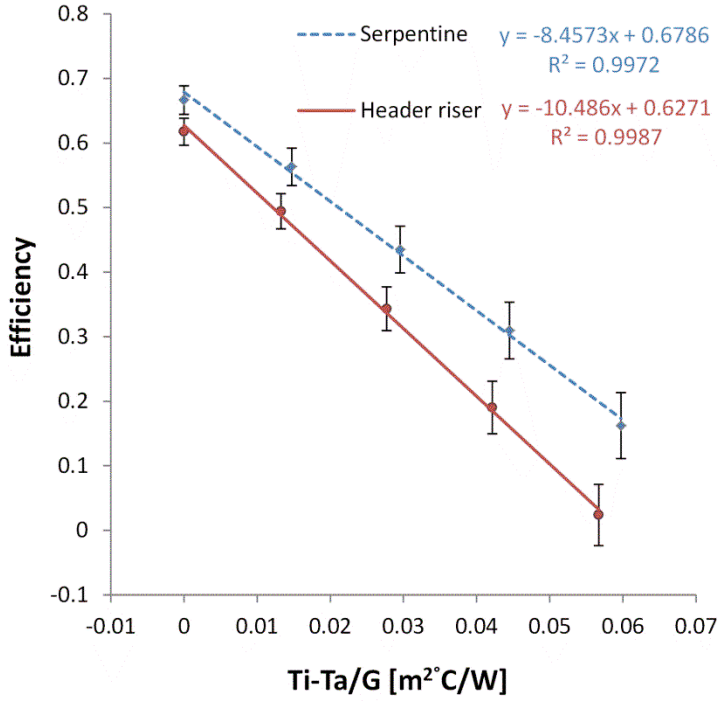

Figure 1-2: Comparison of a serpentine and header riser collector

The curves were used to determine performance characteristics of the solar collector and these are shown in Table 1-1. The experimental results were compared with commonly used empirical models and showed close agreement.

Table 1-1: Parameters extracted from the thermal efficiency curve

Parameter	Serpentine (abs)	Header Riser (abs)
Zero Loss Efficiency ($FR\alpha\tau$)	67.86 (± 2.19)%	62.71 (± 2.08)%
$U_L F_R$ [W/m^2°C]	8.4573 ± 0.071	10.486 ± 0.08
F_R	0.71 ± 0.037	0.66 ± 0.035
U_L [W/m^2°C]	11.84 ± 0.60	15.89 ± 0.84

Thermocouples attached to the back surface of the absorber were used to record its temperature. A comparison of the temperature distribution for a serpentine and header riser design is shown in Figure 1-3. It can be seen that in the serpentine design, the temperature gradient occurs from left to right; whereas in the header riser collector, it occurs from top to bottom.

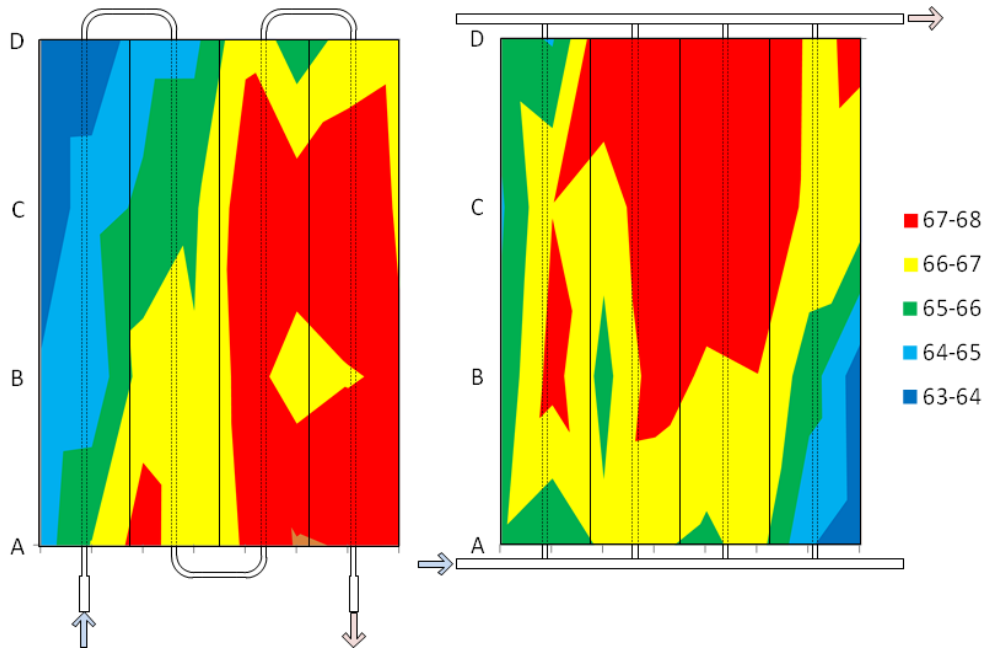

Figure 1-3: Readings from thermocouples mounted on the rear surface of a serpentine (left) and header riser absorber (right)

In the second case, the impact on performance of using a polycarbonate cover is presented. The results show that the optical efficiency of the collector is reduced by 12% when using a cover; however because the loss coefficient is reduced by 53%, the covered collector has a higher efficiency when there is a large temperature difference between the absorber and the ambient.

The third case investigates the combined performance of a photovoltaic thermal collector that can produce both heat and electricity from a single device. It was found that by placing PV laminates on top of the serpentine absorber, the thermal efficiency is reduced by 15%. When electricity is generated by laminates the thermal efficiency is reduced by a further 3.5%. This drop in thermal efficiency is a result of the incident radiation producing electricity before reaching the absorber.

The combined efficiency of the PV-T collectors were compared at controlled inlet temperatures. The serpentine design had the highest combined efficiency of 61% with 8% electricity at the lowest inlet temperature (21°C), see Figure 1-4. The dominant form of loss in the PV-T system is temperature driven; as the thermal efficiency decreases, electricity generation makes up a larger percentage of the combined output.

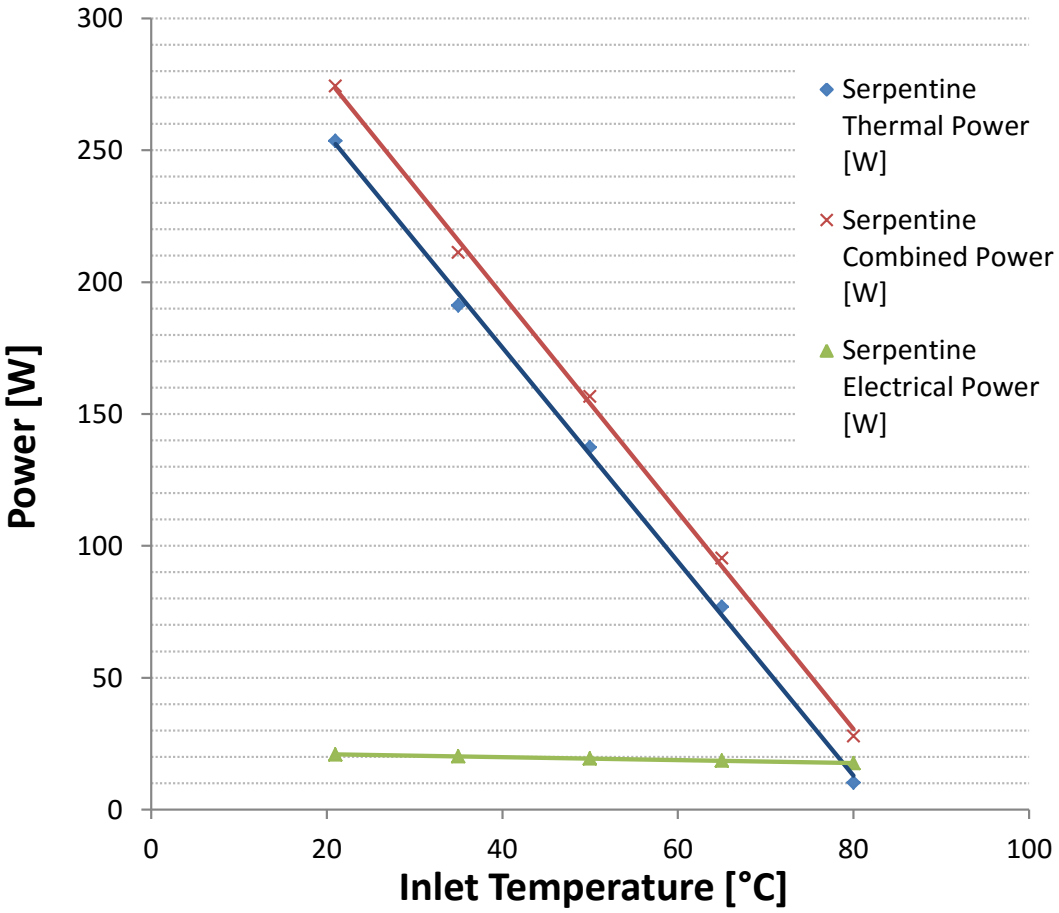

Figure 1-4: Combined power output of a serpentine PVT collector

1.3.4 Contribution to knowledge

- Design and construction of unique testing facility that benefit both researchers and students
- Developed an automated solar testing station for fundamental parameters (U_L, F_R and FF and MPP states) identification and measurement that determine the solar PVT performance and design integration
- Addresses a gap in the current literature of a comprehensive methodology to compare the performance of solar collectors.
- The combination of PV and solar thermal into a single device highlights the opportunity for collaboration between manufacturers of bespoke systems to create devices that will produce a greater energy yield over a given area.

1.4 Project 2: CFD Simulation of a Solar Collector

1.4.1 Aim

To model the performance of different designs of solar collector using CFD. The surface heat distribution will be measured and the implications this has on the performance of PV cells mounted on the surface will be determined.

1.4.2 Method

A CFD methodology was developed and applied to the header riser and serpentine collectors that were characterised experimentally. The measured values of heat loss coefficient, irradiance and ambient temperature were all specified as boundary conditions in the simulation.

Industry standards require solar collectors to have their performance tested using thermal efficiency curves. These are obtained by measuring the energy gain of a solar collector across a range of different inlet temperatures, from ambient to 100°C. By recording the energy gain at each inlet temperature, an efficiency curve can be created. From this, the overall heat loss coefficient and the heat removal factor of the collector can be determined. These are important design parameters of a solar collector in the performance simulation of a solar thermal collector.

1.4.3 Results

The value of heat loss coefficient was obtained experimentally and then specified as a fixed parameter in the CFD simulation. The simulation was run at varying inlet temperatures and a thermal efficiency curve was created, see Figure 1-5. Using this thermal efficiency curve, a check was made to see if the heat loss coefficient matched the specified input value. This resulted in a difference of +2.9% and -0.70% between the experimental and simulated results for the header riser and serpentine collector respectively.

The heat removal factor was calculated from the simulated thermal efficiency curve and compared with the experimental value. For the serpentine collector it was 4.2% higher and for the header riser it was 12.1% less than the experimental value. After investigating this disagreement, it was concluded that the problem is due to uncertainty regarding the thermal of contact between the plate and the pipes. Future work should be focused around the creation of simple geometries with controlled contact between the plate and the pipes to validate the simulations.

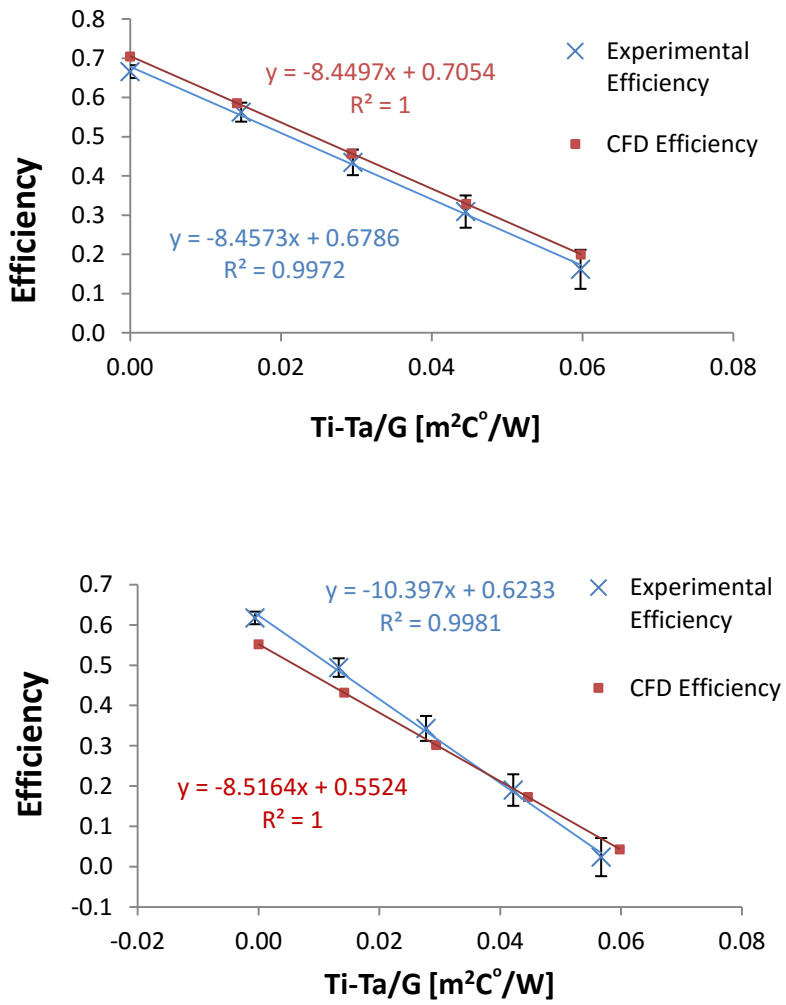

Figure 1-5: Comparison of experimental and simulated thermal efficiency curve for a serpentine collector (top) and header riser collector (bottom).

The CFD approach was also used to compare the performance of different collector designs and flow conditions. In this study it was found that the reduced pressure drop in the header riser collector gave a higher thermal yield to pumping power of 1022 $W_{th}/W_{electricity}$ compared to 71 $W_{th}/ W_{electricity}$ for the serpentine, at $T_i = T_a$.

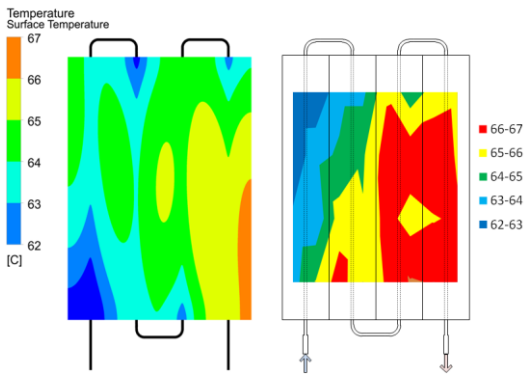

Figure 1-6: Comparison of simulated (left) and measured temperature distribution (right)

A comparison between simulated and measured temperature distribution is shown in Figure 1-6.

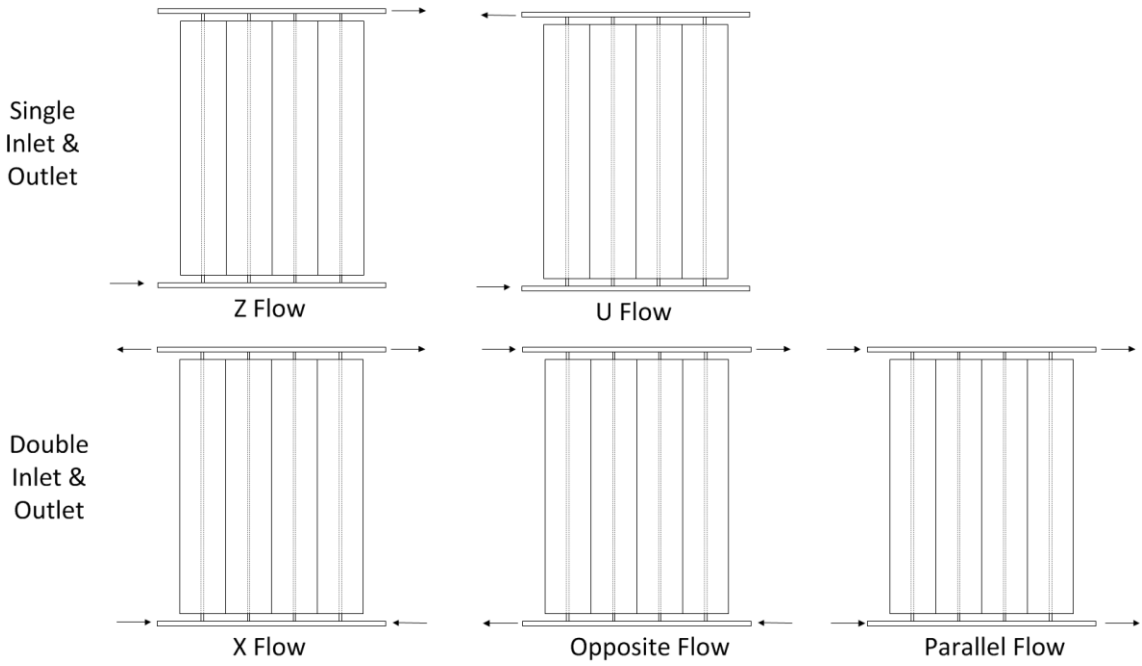

Figure 1-7: Flow configurations investigated during the study

The effect of different flow configurations for a parallel collector was also investigated. The designs investigated in this study are shown in Figure 1-7 and the results are shown in Figure 1-8 and Figure 1-9.

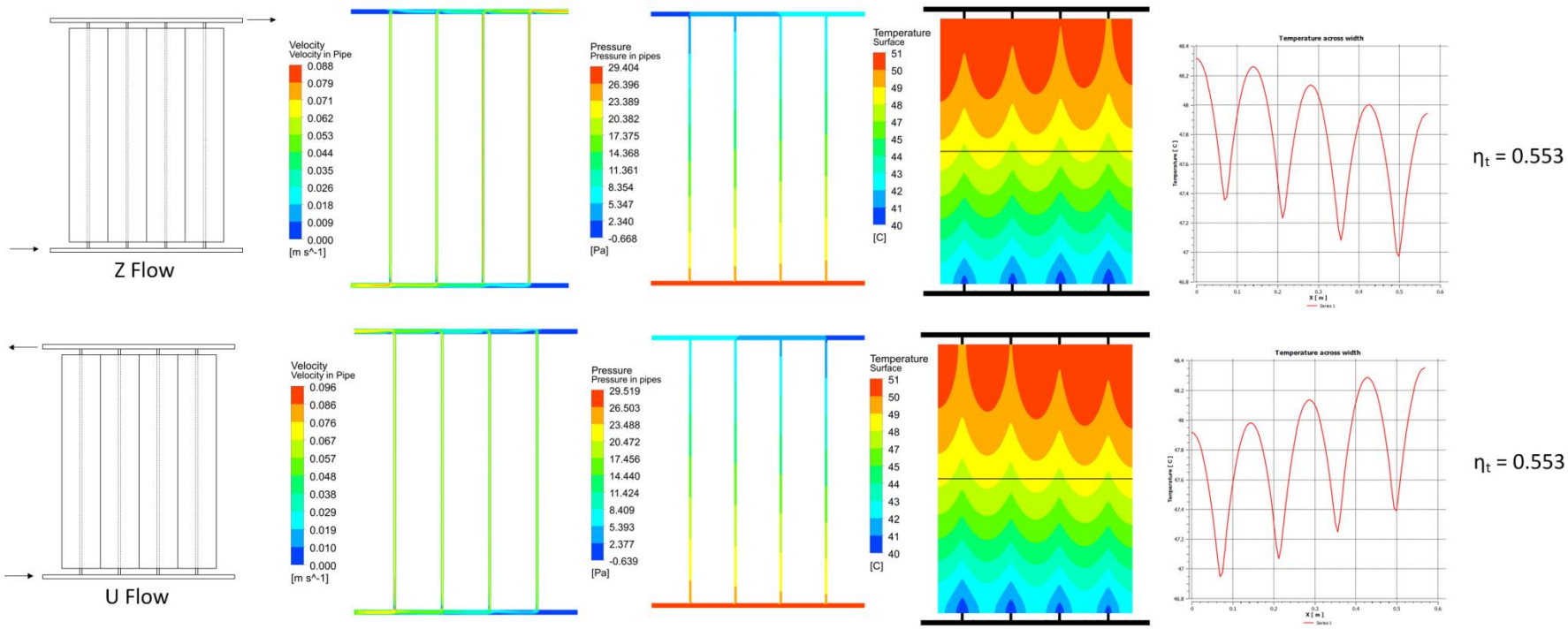

Figure 1-8: The results from the CFD study into different single flow configurations for a header riser collector

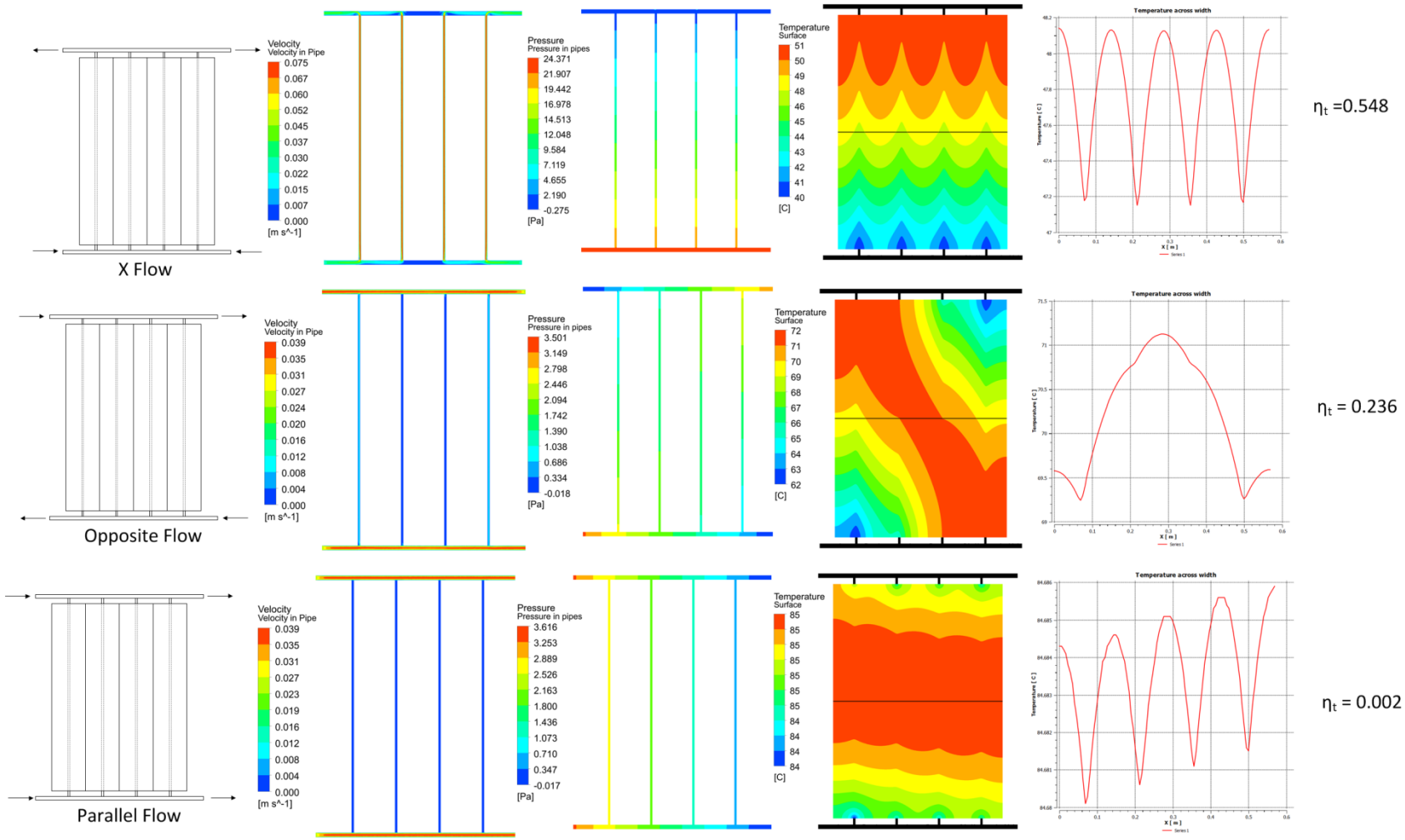

Figure 1-9: The results from the CFD study into different dual flow configurations for a header riser collector

It was found that the most efficient designs of collector had uniform flow through the risers. The opposite and parallel flow systems had low flow rate in the risers that led to high surface temperatures and poor thermal efficiency. This finding was in agreement with other studies that have investigated the flow in large arrays of parallel collectors.

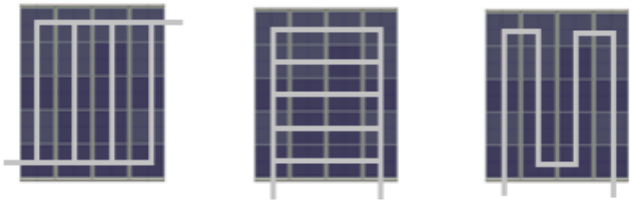

Figure 1-10: Wiring Configurations

The surface temperature distribution across the collector surface was used to estimate the temperature of PV cells in perfect thermal contact with the surface of the absorber. Voltage mismatch occurs when two connected cells are operating at different temperatures. The effect of mismatch was investigated in the wiring configurations shown in Figure 1-10. In this study the voltage was assumed to be the average of the two cells, which is a reasonable assumption if the cells are identical. This meant that the temperature variation was not limiting and the way in which PV cells are wired together on the surface of a PVT collector did not influence the combined electrical power output, see Table 1-2.

Table 1-2: Results from mismatch study

	Average Temperature [°C]	**Electrical Power [W]**		
		Vertical Strings	**Horizontal Strings**	**All in Series**
Z Flow	45.8	52.36	52.36	52.36
U Flow	47.1	51.52	51.52	51.52
X Flow	47.1	51.52	51.52	51.52
Opposite Flow	69.4	37.59	37.59	37.59
Parallel Flow	84.6	28.05	28.05	28.05

1.4.4 Contribution to knowledge

- Presented a poster on the CFD approach at EU PVSEC in 2011
- This is a novel approach to the modelling of solar thermal collectors using CFD
- First ever thermal efficiency curves for a solar collector using CFD
- The first time CFD has been used in conjunction with PV modules to determine the electrical output of a PV-T collector
- All geometries and simulations have been provided to the university so that they can be further developed

1.5 Project 3: Thermal Enhancement of Photovoltaic Laminates

1.5.1 Aim

Manufacture composites containing EVA and boron nitride to enhance the thermal conductivity of photovoltaic encapsulate material and assess the impact this has on the performance of a PV and PVT device.

1.5.2 Method

EVA is used to encapsulate PV cells to protect their electrical connections from the environment; however this material is a thermal insulator that prevents heat flow. Figure 1-11 shows the materials used in a typical PV laminate. To overcome this problem, EVA was doped with ceramic boron nitride particles (BN) to increase its thermal conductivity. Ceramics can increase thermal conductivity while still providing adequate electrical resistivity to protect the PV cell. In this study, EVA:BN composites were prepared and the thermal conductivity measured using a novel differential scanning calorimeter (DSC) technique. The technique involves placing a 'melting standard' on top of the sample; the thermal conductivity is proportional to the melting rate of this standard and can be quantified by comparison with a known reference material.

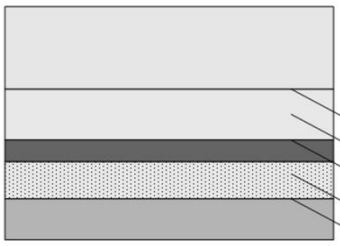

Layer	Layer Thickness (m)	Thermal Conductivity (W/m•K)
Glass	0.003	0.98
EVA	0.0004	0.23
Solar Cell	0.00018	148
EVA	0.0004	0.23
Tedlar	0.0005	0.36

Figure 1-11: Layers of a PV Laminate

To determine the value of using the enhanced encapsulate material, a numerical model based on the finite difference approach was developed to simulate the temperature distribution across the cross section of the PV laminate. The laminate cross section and locations of the temperature nodes are shown in Figure 1-12.

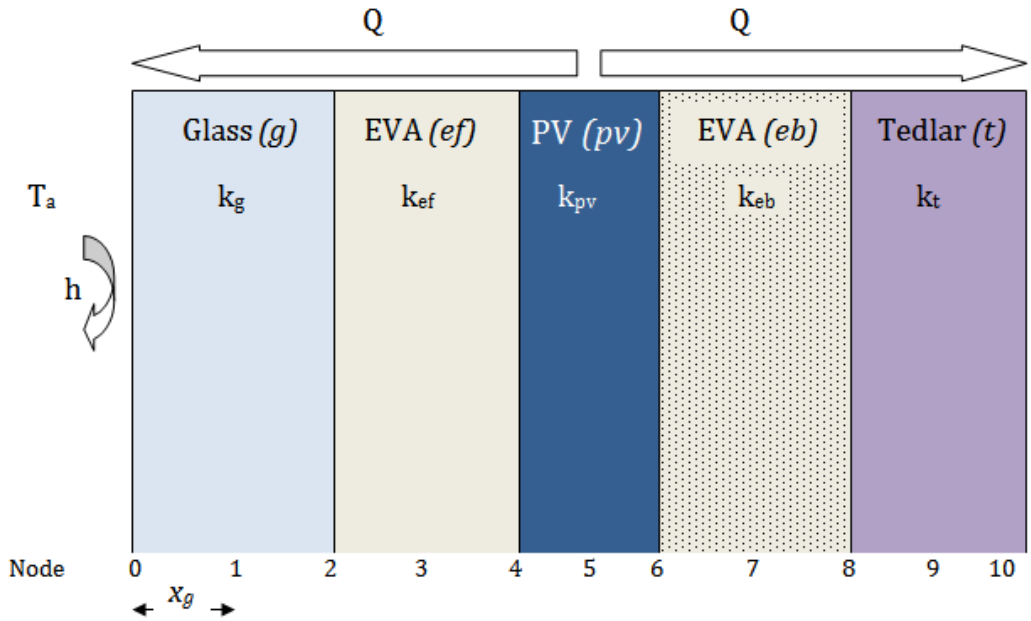

Figure 1-12: Cross section of PV laminate investigated in this study

1.5.3 Results

Composite material was prepared with varying concentration of BN filler (10,20,30 and 60%). The thermal conductivity was measured for each sample and the results are shown in Figure 1-13.

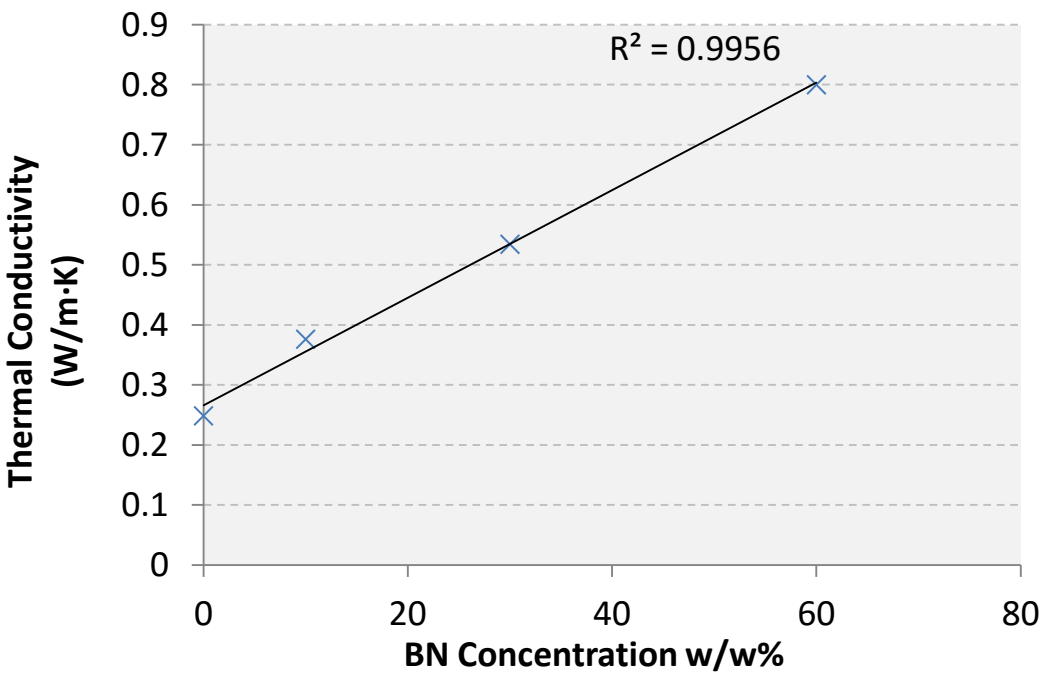

Figure 1-13: Thermal conductivity vs. concentration of boron nitride filler

By increasing the BN concentration from 0% to 60% w/w, thermal conductivity increases from 0.23 W/m·K to 0.83 W/m·K. This finding was in agreement with that of other studies.

The steady state numerical model was applied to two cases; one that resembled a PV laminate in contact with a cooled surface, i.e. a PVT collector, and the other, a PV module ventilated on both the front and rear surfaces. For each case different conductivities of the EVA-backing were investigated. The study found that the use of 60% BN achieved a 0.7°C difference in PV cell temperature compared to standard EVA. This improved PV performance by 0.3%. For the ventilated PV laminate, an improvement of 0.04% was achieved. The cost of the filler material was 240€/kg; it was concluded that this mediocre improvement would not justify the additional material and manufacturing costs. A PV cell temperature difference of 23°C, between the PVT and ventilated module, resulted in a 10% increase in electrical performance. This finding shows that actively cooled PVT systems increase PV efficiency. Although this is only true if the fluid temperature is less than the cell operating temperature.

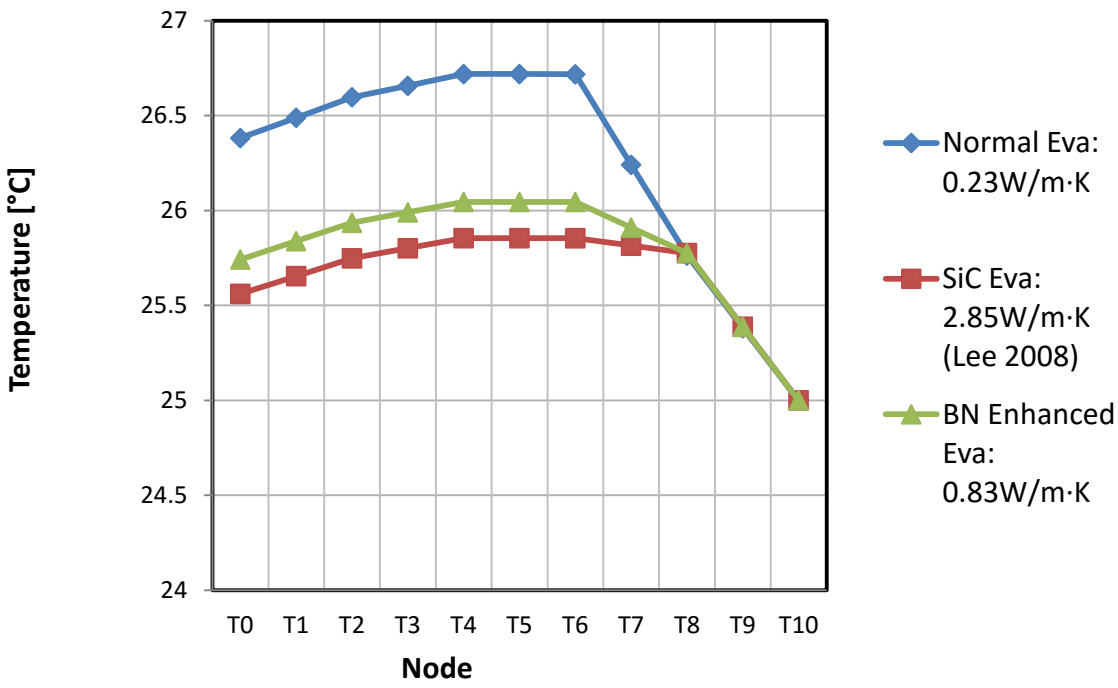

Figure 1-14: Temperature profile across PV laminate in perfect contact with cooled back surface

1.5.4 Contribution to knowledge

- Extending the use of filler materials to PV-T collectors
- Used a novel method to determine the thermal conductivity of the samples
- Unique mathematical model to simulate temperature across a PV laminate

1.6 Events and Presentations

- **Brunel Research Conference 2011:** Presented an oral presentation titled "The Potential of Hybrid PVT Systems Throughout Europe" and a poster titled 'Advanced PV Integration for the Decentralised Power Supply of Buildings'
- **Young Generation Conference 2011:** Presented an oral presentation titled 'Is Solar PV Good value for Money?'
- **EU PVSEC 2011 - Hamburg, Germany**: Presented a poster titled ' Maximising Energy Yields from Solar Rooftops Using Building Integrated Photovoltaic Thermal Systems (BIPVT)'
- **Brunel Research Conference 2012:** Oral presentation titled 'Integrated Energy Demand Matching with Multi-Functional Solar Panels'
- **Brunel Research Conference 2013:** Oral presentation titled **'**CFD Design Optimisation of Photovoltaic Thermal Collectors to Reduce Cell Temperature and Increase Energy Yield**'**
- **Brunel Research Conference 2014:** Oral presentation titled 'Enhancing the Thermal Conductivity of Photovoltaic Encapsulates'
- **Life after PhD conference:** Oral presentation and poster entitled 'Enhancing the Thermal Conductivity of Photovoltaic Encapsulates'

1.7 Publications

Energy Science and Engineering: Performance Testing of Thermal and Photovoltaic Thermal Solar Collectors to Determine the Combined Efficiency of a Co-generation Device .
Accepted 18/05/2014

2. Literature Review

2.1 Introduction

The finite reserves of fossil fuels are in decline and many will be exhausted within the next 100 years if consumption remains at its current rate [1]. The burning of fossil fuels also creates atmospheric pollution that was attributable to around 3 million premature deaths in 2002 [2]. Fossil fuel emissions are a key contributor to climate change, which has been described as the biggest threat to humanity over the next century [3]. In addition to this, around 50% of the energy used in the UK is from imports [4] making it vulnerable to international disputes and price fluctuations. As a result many nations, such as the UK, are focused on relieving their reliance on fossil fuels in favour of cleaner and more sustainable energy resources.

There are a number of natural driving forces that can be harnessed to supply renewable energy. These can be summarised as sunlight, wind, rain, tides, and geothermal heat. Solar energy is unique as it is the only resource that is available to the majority of the entire global population regardless of location. As a result it is an ideal renewable energy technology for distributed rural electrification in parts of developing countries that do not have access to an electricity grid.

In the interest of sustainable development it is also important to minimise our impact on the natural environment. We already take considerable amounts of land for urban development and it is important that we use this land as efficiently as possible. The simplicity of solar technology allows it to be easily integrated into construction materials making it an ideal candidate distributed energy production.

2.2 The Solar Resource

Solar irradiance is the power available from the sun and is the source of energy used by a solar energy system. Solar irradiance is commonly measured by weather stations and historical data can be obtained. A comprehensive global database of weather files is available on the EnergyPlus website [5]. These include hourly irradiance values that can be used in the performance simulation of solar technologies.

	Jan	Feb	Mar	Apr	May	Jun	Jul	Aug	Sep	Oct	Nov	Dec	hour	Avg year
0:01- 1:00	0	0	0	0	0	0	0	0	0	0	0	0	1	0
1:01- 2:00	0	0	0	0	0	0	0	0	0	0	0	0	2	0
2:01- 3:00	0	0	0	0	0	0	0	0	0	0	0	0	3	0
3:01- 4:00	0	0	0	0	0	0	0	0	0	0	0	0	4	0
4:01- 5:00	0	0	0	0	8	13	9	1	0	0	0	0	5	3
5:01- 6:00	0	0	0	13	60	64	56	20	2	0	0	0	6	18
6:01- 7:00	0	0	9	72	155	153	148	99	38	7	0	0	7	57
7:01- 8:00	0	6	60	167	276	253	249	198	128	57	9	0	8	117
8:01- 9:00	17	53	135	279	381	352	366	317	221	137	57	13	9	194
9:01-10:0(	65	121	225	349	460	462	440	405	312	212	119	54	10	269
10:01-11:0	108	164	263	411	516	539	523	479	383	272	167	89	11	326
11:01-12:0	140	195	289	453	564	594	580	518	412	290	173	116	12	360
12:01-13:0	142	204	331	464	565	560	596	518	400	269	180	124	13	363
13:01-14:0	128	187	296	467	537	510	567	549	365	218	148	94	14	339
14:01-15:0	78	151	229	381	480	471	503	469	318	165	87	48	15	282
15:01-16:0	31	87	167	296	379	378	400	373	234	93	28	11	16	206
16:01-17:0	2	25	89	189	286	282	290	251	125	26	1	0	17	131
17:01-18:0	0	1	22	84	176	180	192	120	34	1	0	0	18	68
18:01-19:0	0	0	1	14	62	80	84	31	2	0	0	0	19	23
19:01-20:0	0	0	0	0	7	17	15	2	0	0	0	0	20	3
20:01-21:0	0	0	0	0	0	0	0	0	0	0	0	0	21	0
21:01-22:0	0	0	0	0	0	0	0	0	0	0	0	0	22	0
22:01-23:0	0	0	0	0	0	0	0	0	0	0	0	0	23	0
23:01-24:0	0	0	0	0	0	0	0	0	0	0	0	0	24	0

Figure 2-1: Average hourly radiation data for each month for Gatwick, London. Source [6]

In the absence of recorded data, it is possible to estimate radiation with knowledge of the local climate for that location. The methods vary in complexity and summaries of the methods used to estimate radiation data is given by Duffie and Noorian [7] [8].

2.3 Photovoltaics

Photovoltaic's (PV) are the most rapidly growing renewable energy technology. Growth from 2006 to 2011 averaged at 58%/year [9] . At the end of 2014 there was 139GW of PV capacity globally, making it the third largest renewable electricity generator by capacity after wind and hydro [10] .

All PV devices convert irradiation directly into electricity using the photovoltaic effect that was first observed in 1839 by William Becquerel [11]. Since then the photovoltaic effect has been harnessed and is supplying a considerable portion of the global energy demand. This section gives a summary of PV technologies, their applications, theory of operation, their performance and an overview of the current industry.

2.3.1 Types of PV Technology

The history of the PV can be split into three distinct generations:

1. First Generation – Crystalline silicon wafer, single junction devices
2. Second Generation – Thin film technologies, a-Si, CdTe, CIGS
3. Third Generation – High efficiency low cost thin films and multi-junction devices

Figure 2-2 shows a technology tree for commercially available PV technologies.

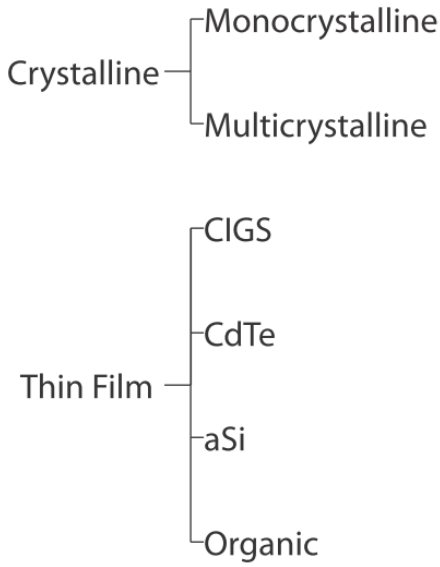

Figure 2-2: Types of PV Technology

2.3.1.1 First Generation - Crystalline Silicon

Crystalline PV cells are made from silicon semiconductors that have an inbuilt electric field. The first crystalline PV cell was fabricated by Bell Labs in 1954. This device had an efficiency of around 6% [12]. There are two types of silicon wafer; monocrystalline and multicrystalline. It is cheaper and less material intensive to produce multicrystalline silicon but it has a lower efficiency [13]. The record efficiencies for monocrystalline and multicrystalline PV cells are currently 25.6% and 20.4% respectively [14].

PV cells made using crystalline silicon wafer still dominates the market with around 90% share of the market [15]. Multi-crystalline technology with its lower cost and modest efficiency is the makes up the largest share with around 55% of total production.

2.3.1.2 Second Generation - Thin Films

Using thin films, which have better light absorption properties, it is possible to reduce the material requirement compared with crystalline methods by 100 times [16]. The aim of second generation photovoltaics is to reduce the material costs of the first generation by using 'thin-films' instead of bulk crystalline silicon. The first thin film PV cell was made from amorphous silicon and was constructed in 1976 [17]. The problem with amorphous silicon is that, even though it is cheap to produce, it is inefficient and prone to light degradation through the Staebler Wronski effect [18]. Despite this, the ability to print amorphous silicon onto flexible substrates

captured the imagination of Stanford Ovshinsky who patented methods for the production of large scale amorphous silicon [19]. However the company who owned the patent, Energy Conversion Devices went bankrupt in 2012, never reaching the scale envisaged by Ovshinsky. A similar story has unfolded for many companies backing amorphous silicon technology and nowadays amorphous silicon makes up a insignificant fraction of the global PV market.

There are also thin film PV cells constructed using polycrystalline chalcogenides; cadmium telluride (CdTe) and cadmium indium gallium (di)selenide (CIGS). Although crystalline, these materials have much better absorption properties than silicon and can be used in much thinner layers [20]. They also have much higher efficiency than amorphous silicon with record efficiencies of 19.6% and 20.5% for CdTe and CIGS respectively. CdTe is the most successful thin film solar technology and is used in the modules produced by First Solar, one of the top 10 global manufacturers by quantity [10]. CIGS solar is less successful, it was the chosen technology of Solyndra and Odersun, both received large volumes of funding but went bankrupt. There are other CIGS manufacturers that have suffered a similar fate. The largest CIGS manufacturers in operation today is Solar Frontier and Solibro [21]. One of the main advantages of thin film technologies over crystalline technologies is that they can be deposited onto flexible substrates; however the most widespread thin film products available today are those incorporated into rigid panels. This is the product of First Solar, one of largest PV cell manufacturers in the world.

2.3.1.3 Third Generation Multi-junction

Single junction solar cells are limited by the theoretical Shockley-Quisser limit which is the maximum efficiency of a silicon PV cell [22]. This is because there is a threshold energy, known as the band gap, that needs to be overcome in order to induce the photovoltaic effect. The limiting efficiency, calculated for a silicon PV cell, with a band gap energy of 1.12eV is 29.8% for a solar spectrum of AM1.5 [23]. As mentioned earlier, the record efficiency achieved for a crystalline silicon cell is 25% which is approaching this limit. Multijunction cells are able to overcome the restrictive Shockley limit by incorporating numerous p-n junctions into the same device, each with different band gap energies. Through doing this they are able to absorb a greater proportion of the solar spectrum and thus produce more power per unit of irradiance see Figure 2-3.

Multijunction cells are currently the most efficient PV cells with a record efficiency of 37.9% under standard testing conditions [14]. The problem with multijunction cells is that they are extremely expensive and are only suited to applications where high efficiency is required, such as a power source for satellites [24].

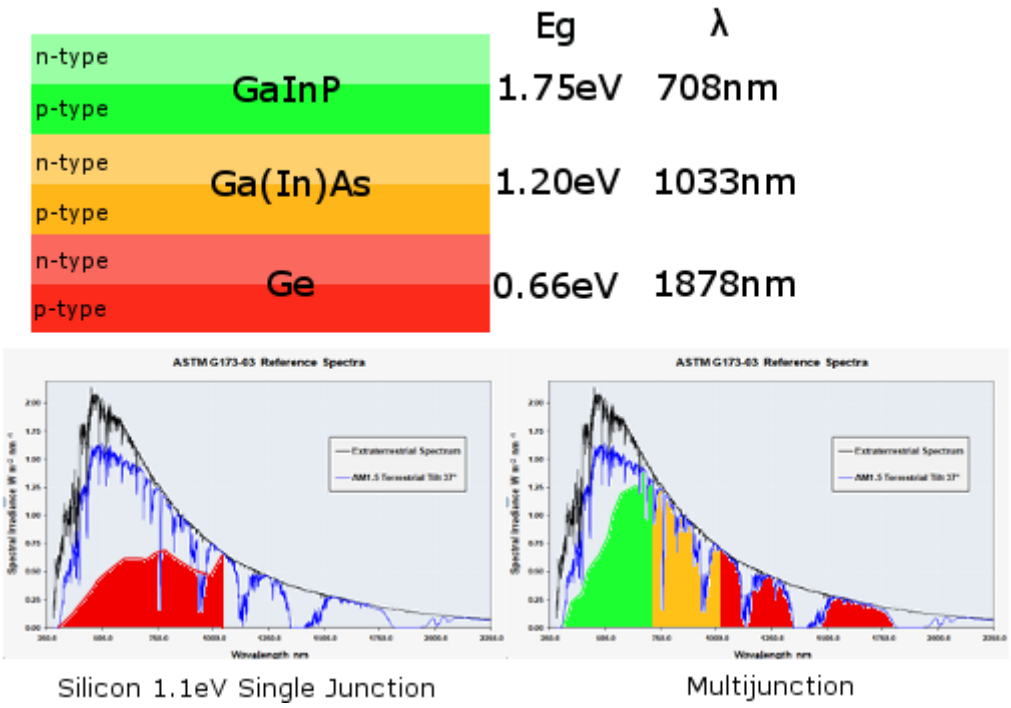

Figure 2-3: Operation of multijunction devices. Source [25].

2.3.1.4 Horizon Technologies

Horizon technologies are those that are beginning to emerge but are yet to be produced on a large scale. The main two horizon technologies are dye-sensitised and organic solar cells. The promise of these horizon technologies are much the same as thin film; production at low cost and on flexible substrates; however both have suffered from severe technical hurdles. Ongoing research to address these problems may see them play a role in the PV industry in the near future.

There are a small handful of companies that produce dye sensitised and organic cells. The most well known was Konarka who raised a large amount of funding since its inception but ultimately went bankrupt in 2012. Of the remaining companies the largest is Dyesol in Australia.

2.3.1.5 Third Generation Distant Technologies

The most ambitious third generation technologies aim to exceed the single band gap limit while at the same time achieving the low cost associated with thin films. A relationship of the efficiency-cost trade-off for the three generations is shown in Figure 2-4.

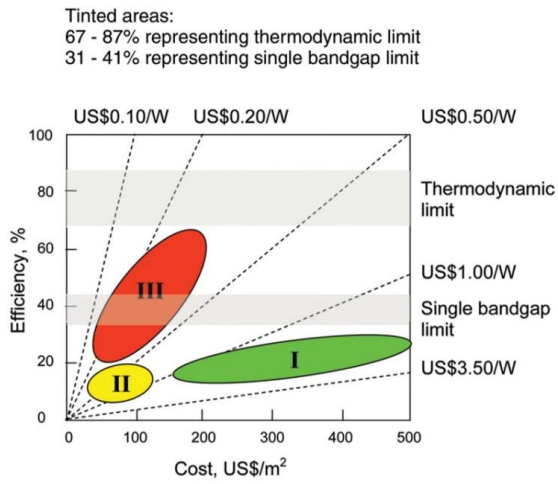

Figure 2-4: Efficiency-cost trade-off for the three generations of solar cell technology; wafers, thin-films and advanced thin-films. [26]

Example of third generation technologies include hot carrier, quantum dot and intermediate band PV technologies. A detailed explanation of third generation technologies is provided by Green [27]. These technologies aim to increase the efficiency of PV technologies to between 40-60%.

2.3.2 PV Performance

The most important performance measurement of a PV device is its efficiency at converting sunlight into electricity. As the efficiency of a PV device is dependent on temperature and irradiance, Standard Testing Conditions (STC) have been created to compare the performance of different PV devices. Standard testing conditions are carried out at a controlled module temperature of 25°C, with an irradiance of 1000W/m^2 and a spectrum equivalent to solar radiation received on the surface of the earth after passing through an atmospheric thickness of 1.5 (AM1.5). The methodology for testing the performance of a photovoltaic module is detailed in the international standard IEC 60904. Table 2-1 shows the confirmed cell and module efficiencies for the range of photovoltaic devices currently available.

Table 2-1: Confirmed efficiencies for solar cells and commercially available modules [14]

Generation	Technology	Cell Efficiency (%)	Module Efficiency (%)
1st	Monocrystalline Silicon	25.6	22.9
	Multicrystalline Silicon	20.4	18.5
2nd	CIGS	20.5	15.7
	CdTe	19.6	17.5
	Amorphous Silicon	10.1	11.6
	Thin film polycrystalline silicon	11.0	8.2
3rd	Multijunction	37.9	NA
	Organic	10.7	NA
	Dye Sensitised	11.9	NA

2.3.3 PV Applications

2.3.3.1 Modules

A standard solar module consists of a glazed panel that is encased within a metallic frame. The PV cells are encapsulated in EVA and sandwiched between the glazing and a protective polyvinyl fluoride sheet; also known as Tedlar. Both crystalline silicon and thin film technologies can be installed inside a standard collector. The efficiency of the collector depends on the photovoltaic technology used, for example a crystalline PV panel will be more efficient than one with a thin film technology.

2.3.3.2 Building Integration

Solar radiation is available everywhere and one of the main advantages of PV is that it is maintenance free, has no moving parts and can be integrated into a range of different building materials. It would be logical to use the land area that is already urbanised to generate electricity before using up valuable agricultural space. Photovoltaic's are the only renewable technology that could transform buildings from energy users into energy generators using the building fabric. A review of the research carried out into building integration has been carried out by Norton [28]. Here is an example of some of the building materials that have integrated PV:

- Glazing and Facades
- Shading Devices
- Roofing Materials
- Walls
- Flexible Modules
- Luminescent concentrators

PV is not just confined to buildings and can be integrated into a range of different applications, examples include:

1. Canopies over car parking spaces [29]

2. Sound breakers on the side of roads [30]

2.3.4 PV Theory

2.3.4.1 Description of operation

The PV cell is formed using electrically charged p- and n- materials. In p-type material, silicon (4 valence electrons) is doped with boron (3 valence electrons) and there is an electron deficiency, making it net positive. In n-type material silicon (4 valence electrons) is doped with phosphorous (5 valence electrons) and there is an excess of electrons, making it net negative.

A crystalline PV cell is formed when the n-type and p-type semiconductor material are brought together to form a PN junction. When these materials are brought together the majority carriers diffuse from each side of the junction into the other. This ionises each side; the n-type becomes positively charged, as the electrons migrate, and the p-type becomes negatively charged as the holes migrate. This creates an electric field. Once established the majority carriers diffuse and minority carriers drift from one side to the other but there is no net current.

When a photon strikes a PV cell it can be reflected, absorbed or transmitted. The energy of the photon and the band gap of the material determine what happens. A semiconductor only requires the band gap energy to promote an electron into the conduction band. If the energy of a photon is less than the band gap, the photon is not absorbed and passes through the PV cell. If the photon has greater energy than the band gap, a carrier is created but the excess in energy is wasted.

In order for a net current to be created, a voltage which opposes the direction of the electric field across the PN junction must be connected to the terminals of the PV cell. This is known as forward biasing. The result is a net increase in current due to the barrier of diffusion being removed; drift current on the other hand remains the same. When majority carriers diffuse across the junction, a minority carrier is created in its place, this diffuses into the bulk material where it recombines with a majority carrier that has flown through the external circuit. It is this process that allows PV cells to continually produce electricity.

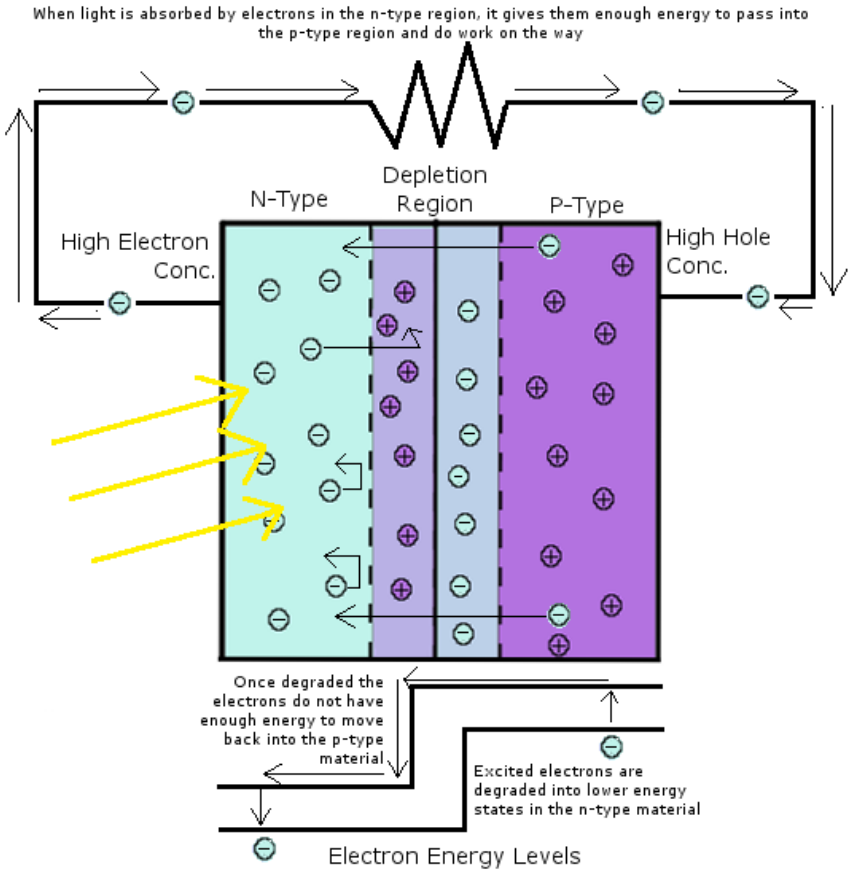

Figure 2-5: Operation of crystalline PV cell. Source [25]

2.3.4.2 Performance characteristics

In addition to efficiency there are several other parameters that are used to measure the performance of a PV cell. These are:

V_{oc}: The voltage when there is infinite resistance between the terminals [V]

I_{sc}: The maximum current when there is no resistance between the terminals [A]

P_{max}: Maximum power point [W]

V_{mp}: The voltage at maximum power point [V]

I_{mp}: The current at maximum power point [A]

Using these values it is possible to determine the fill factor of the cell using (2.1).

$$FF = \frac{I_{mp}V_{mp}}{I_{sc}V_{oc}} = \frac{P_{max}}{I_{sc}V_{oc}} \tag{2.1}$$

The fill factor is an indication of the quality of a solar cell and can be used to identify parasitic resistances. Typically, crystalline silicon cells have a fill factor between 0.7 and 0.8 and amorphous cell a value of between 0.5 and 0.7 [31].

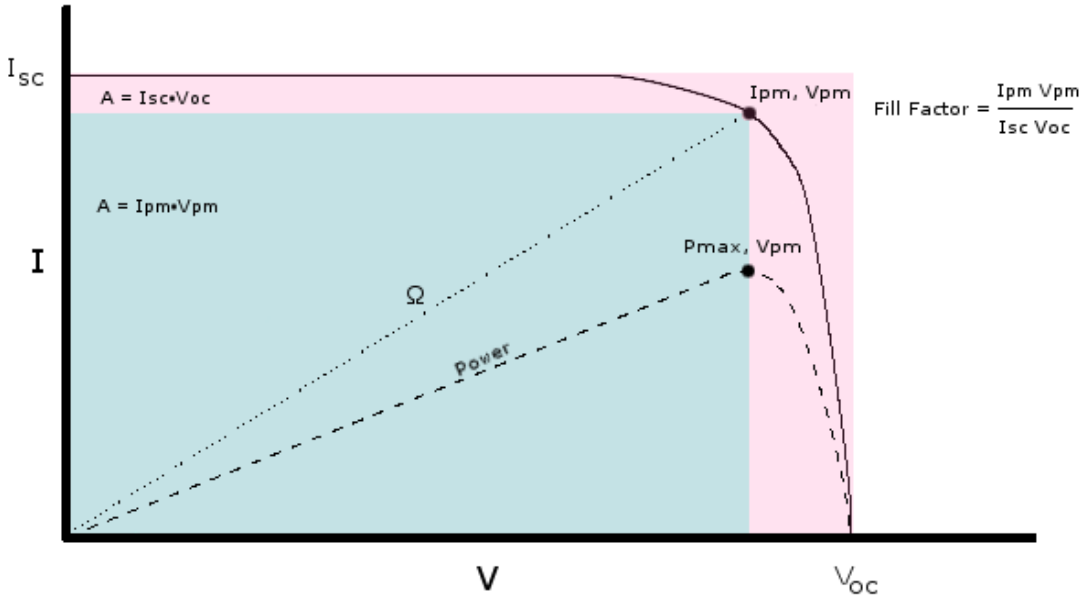

Figure 2-6: IV relationship between solar cell performance characteristics. Source [25].

An ideal solar cell would have a FF of 1. In Figure 2-6 the red area shows the area occupied by an ideal solar and the green area is that of a typical cell. The effect of series and parallel resistances on an IV curve are shown in Figure 2-7.

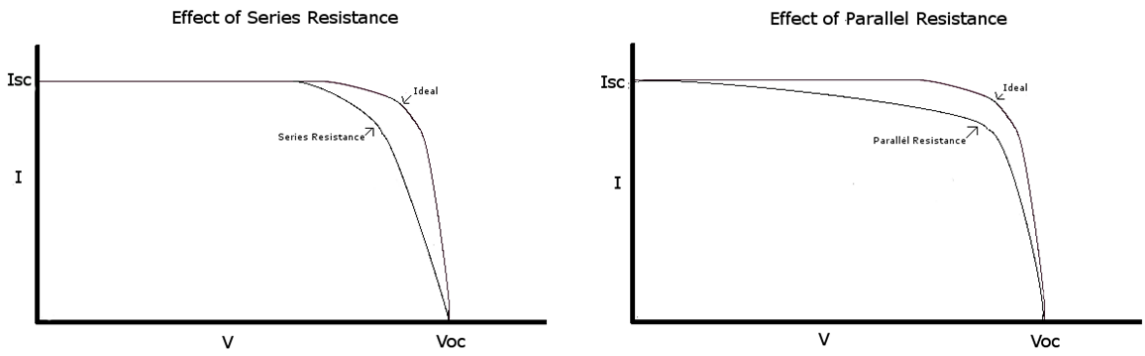

Figure 2-7: Effect of series and parallel resistance on IV curve. Adapted from [32]

2.3.4.3 Effect of temperature and irradiance on performance

The current produced by a PV cell is directly proportional to the irradiance. Increasing irradiance increases efficiency. The effect of irradiance on the IV curve of a PV cell is shown in Figure 2-8. The reduction in efficiency can be estimated using (2.2) [33].

$$\Delta\eta \approx -0.04\eta \ln\left(\frac{S}{S_\eta}\right) \tag{2.2}$$

Where S is the solar irradiance, η is the nominal efficiency and S_η is the irradiance used to measure the nominal efficiency.

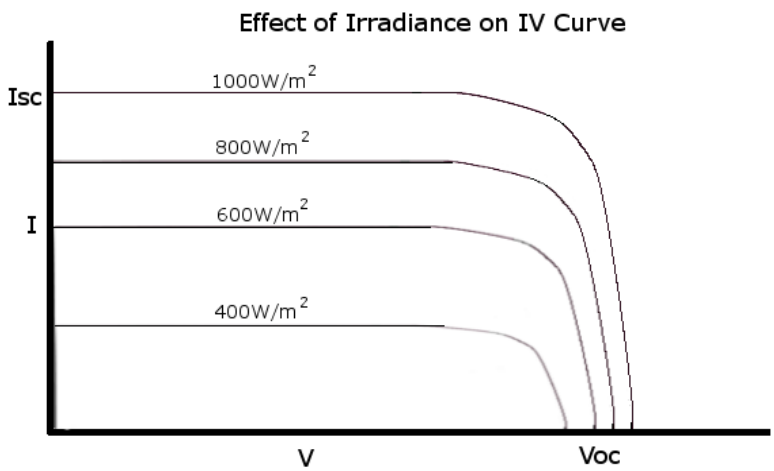

Figure 2-8: Effect of irradiance on PV cell performance

Increasing temperature reduces the band gap of the semiconductor. This means that electrons in the material have a higher thermal energy and less energy is required from the photons to release them. This improvement is offset by a drop in open circuit voltage at higher PV cell temperatures; thus reducing efficiency. The effect of temperature on the IV curve of a PV cell is shown in Figure 2-9.

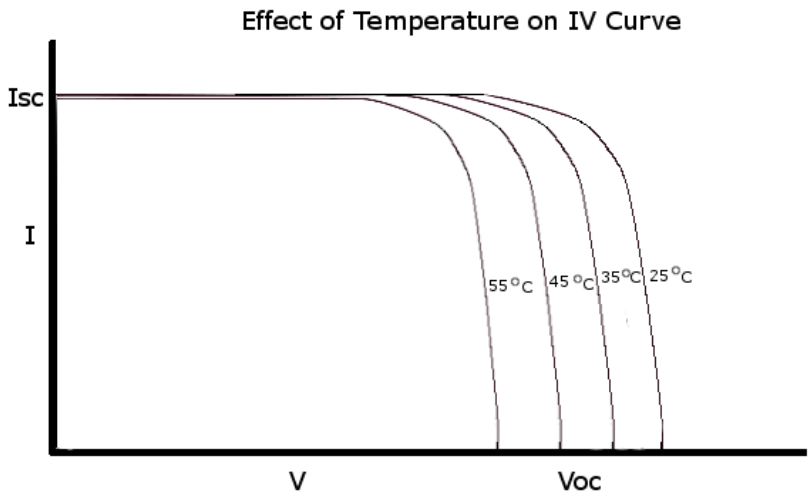

Figure 2-9: Effect of temperature on PV cell performance

The efficiency of a PV cell decreases linearly with temperature, (2.3) is used to determine the PV electrical efficiency for a given PV cell operating temperature, T_c [34].

$$\eta = \eta_r \left(1 - \beta\left(T_c - T_r\right)\right) \tag{2.3}$$

Where η is the PV efficiency; η_r is the reference efficiency at reference temperature T_r and β is the efficiency temperature coefficient of the PV cell.

The temperature coefficient is dependent on the type of PV technology; the coefficients for different PV technologies are given in Table 2-2.

Table 2-2: Temperature coefficients for PV technologies. Source [35]

PV Technology	Temperature Coefficient β(°C)
Amorphous Silicon	0.0013
Cadmium Telluride	0.0021
CIGS	0.0036
Crystalline Silicon	0.0045

2.3.5 The PV Industry

The PV market is volatile and ever changing, the reason for this is due to the strong reliance on Government Incentives. The European Photovoltaic Industry Association (EPIA) monitor the global industry and their most recent report was published in June 2014 [36]. At the end of 2013 the global installed capacity was 138.9GW. PV now produces 3% of the electricity demand in Europe and approximately 6% of the peak demand . Since 2003 Europe has dominated the industry in terms of new installations; however in 2013 Asia overtook Europe as the market leader, in particular in China where 11.8GW was installed.

One study has shown that in 2013 the cost of electricity from PV was below the retail electricity prices in several countries [10]; however the industry is still reliant on incentives and the strongest markets are those with the generous fiscal support. The sudden drop in demand from the European market has reduced module prices as the large quantities being manufactured are not being used, resulting in an industry bottle neck. There is concern that the withdrawal of support could lead to irreversible damage to the PV industry, in countries such as Germany, due to breakdown of the infrastructure that currently supports it [37]. Despite the bleak outlook, the PV industry has outperformed projections in the past. In 2012 projections were made using 2010 data and the installed capacity of photovoltaics at the end of 2013 exceeded the projected 110 GW by nearly 30GW [36] [38]

In the UK, PV has been supported under Feed in Tariff since April 2010 where owners of a PV system receive payments for each kWh of electricity generated by the system. Since being introduced the rate is periodically reduced to take into account falling manufacturing and installation costs. In January 2015 there was 2.8GW of PV installed in the UK making in the largest renewable energy technology supported under the FiT Scheme [39]. The average installation cost for the average domestic PV system (<4kW) was £2080/kW in 2013/14 [40].

2.4 Solar Thermal

Unlike PV, solar thermal collectors do not generate electricity. Instead they absorb sunlight and produce heat. There are three main types of solar thermal technology; non-concentrating concentrating and evacuated tube. A technology tree of solar thermal technologies is shown in Figure 2-10.

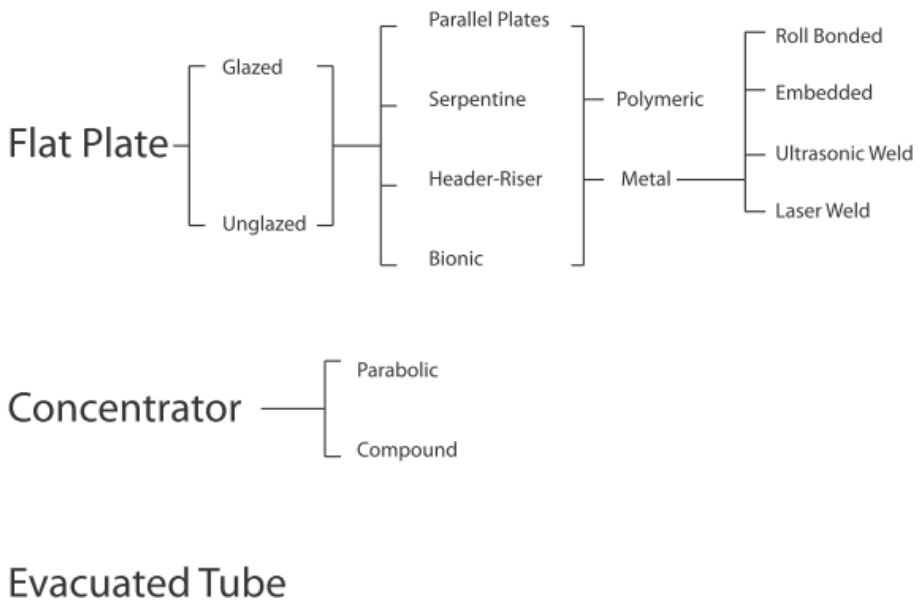

Figure 2-10: Technology tree of main solar thermal technologies

2.4.1 Solar Thermal Technologies

Solar thermal collectors use a fluid to absorb and transport heat. Non-concentrating systems typically use water or air as the heat transfer fluid. In concentrating systems, oil and molten salts are used due to the high operational temperatures experienced.

2.4.1.1 Flat Plate

These are the most common solar thermal collector. They consist of a thin flat-plate that can be selectively coated to absorb as much sunlight as possible. Flat plate collectors can be used with both air and water as the heat removal fluid. In water systems, the fluid is pumped through pipework that is directly attached to the back of the collector. There are several configurations of piping that can be used in a flat plate collector. These include, parallel plates, serpentine, header-riser and bionical. The absorber can either be metallic or polymeric. Polymer absorbers are particularly desirable for climates with extremely low temperatures as polymers are flexible and freeze tolerant.

2.4.1.2 Evacuated Tube

To reduce temperature driven heat losses that occur in flat plate collectors, evacuated tubes have a evacuated space between the absorber and the ambient air. Evacuated tube collectors can either be a direct or heat pipe system. In a direct system water flows through a copper pipe in the centre of the evacuated tube. In a heat pipe system, heat travels up a heat pipe in the centre of the tube and is transferred to the fluid of the system it is serving. Evacuated tubes are particular suited to climates where there is a large temperature difference between the absorber and the ambient.

2.4.1.3 Concentrator

Concentrated solar power (CSP) systems focus the suns energy onto a small area allowing higher temperatures to be achieved. This concentration is achieved through the use of mirrors or lenses. Some CSP systems produce steam that then drives a turbine to produce electricity while others produce high temperatures for use in commercial applications such as drying.

2.4.1.4 Building Integration

Building integration of water solar thermal collectors is difficult due to the piping. However advances in the roll-bonded collector plates have allowed for pipe structures to be constructed in a way that mimics natural structures and makes angular thermal collectors a possibility, the conceptual design is shown in Figure 2-11.

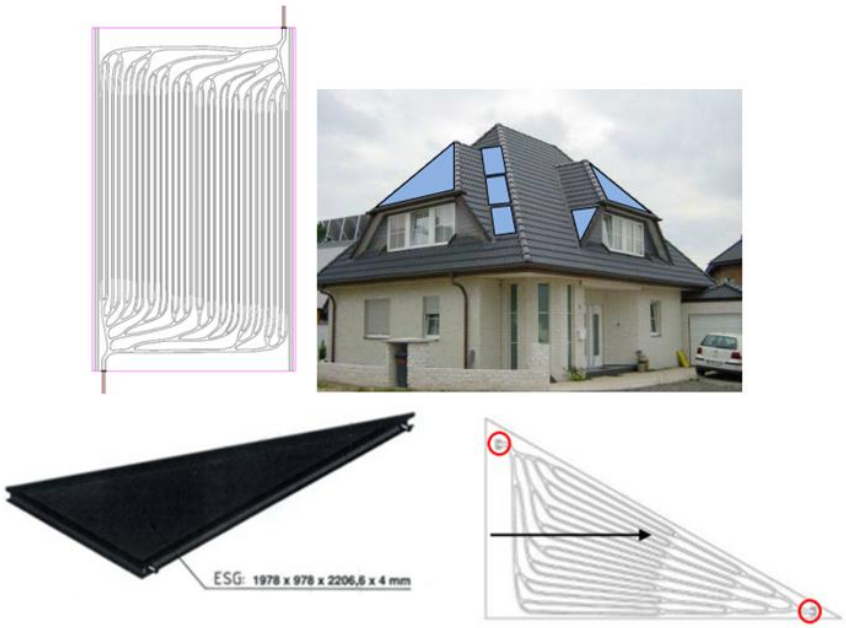

Figure 2-11: Angular Fractherm panels for building integration. Source Hermann 2011 [41]

It is important to achieve good thermal contact between the absorber and the pipework. The most effective way of achieving this is through the use of a metallic bond. The price of copper has resulted in manufacturers making a transition from using copper plates to using aluminium plates. The difficultly in joined dissimilar material has prompted the use of sophisticated welding methods. Historically the pipes were embedded into the plate and this has since been succeeded by ultrasonic welding and now laser welding has become the preferred method for attaching a copper tube to the back of the absorber plate [42] Roll bond absorbers eliminate the need to attach pipes but there has been a lot of doubt cast in its suitability in the solar thermal market due to problems with corrosion [41].

2.4.2 Performance of Solar Thermal Technologies

The performance of a solar thermal collector can be modelled using the Hotel Whiller Bliss (HWB) model [7]. This approach is based on the one dimensional energy transfer across the fin of a solar collector. The HWB model is detailed in a Section 4.3.1.

Solar thermal technologies are included under the Renewable Heat Incentive introduced by the UK government to increase the installed capacity of renewable heating systems. The amount of money that can be claimed through the scheme is dependent on how much energy the system will produce. The calculation can be found in Appenix H of the Governments Standard Assessment Procedure for Energy Rating of Dwellings (SAP) [43].

The default values of zero loss efficiency and heat loss coefficient for each of the different technologies considered under SAP are shown in Table 2-3. It can be seen from this table that the unglazed collector has the highest zero loss efficiency but at the same time it has the greatest heat loss coefficient. This makes unglazed panels suited to climates with warm ambient temperatures and lots of sunlight. Evacuated tubes on the other hand have a low zero loss efficiency and a low heat loss coefficient. This makes these collectors suited to cold regions with low ambient temperatures.

Table 2-3: Default values of collector specific performance parameters. Adapted from [43]

Collector Type	Zero Loss Efficiency	Heat Loss Coefficient	Ratio of aperture area to gross area
Evacuated tube	0.6	3	0.72
Flat plate, glazed	0.75	6	0.9
Unglazed	0.9	20	1.0

The performance of different solar thermal collectors can be compared using their thermal efficiency curves, see Figure 2-12.

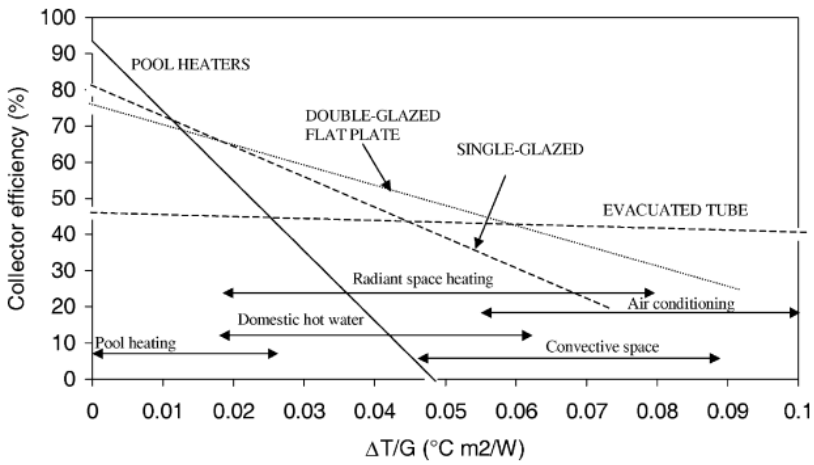

Figure 2-12: Thermal efficiency curves of solar thermal collector technologies. On the x-axis is the temperature difference between the collector and the ambient divided by the irradiance. It can be seen that for a constant irradiance, as the temperature gradient increases, the efficiency of all collectors decreases. The gradient of the line represents the overall heat loss coefficient and it can be seen that the most insulated, the evacuated tube, maintains the highest efficiency at the greatest temperature difference. Also marked on the graph are applications most commonly used at each temperature range. Source Kalogirou 2004.

2.4.3 The Solar Thermal Industry

The global cumulative capacity of solar thermal was 269.3GW_{th} at the end of 2012 [44]. This number is comprised of 26.4% glazed-flat plate collectors, 64.6% evacuated tube collectors, 8.4% unglazed water heaters and 0.6% glazed and unglazed air collectors. The majority of solar heating technologies are installed in China where they are cost effective in comparison to gas and electric heaters [45]. Evacuated tubes are the favoured technology in China which explains why they make up such a large portion of the cumulative capacity.

2.5 PVT Collectors

PVT collectors are a type of cogeneration device that produces both electricity and heat from a single collector. In a PVT device the PV cells act as the solar absorber and a heat removal fluid is used to recover the excess thermal energy. Many believe that the purpose of a PVT collector is to actively cool PV cells so that they operate at a lower temperature and thus more efficiently; however for non-concentrator systems this is not always true, as the hot water in the system may be higher than the temperature reached by the PV cells under normal conditions [46]. The most desirable aspect of PVT technology is to be able to use available roof space as efficiently as possible [47], as research has shown that more energy can be produced from a PVT system than conventional PV and thermal collectors installed side by side [48].

The are several types of PVT system that have been introduced in literature, the design depends on the heat removal fluid that is used:

1. Water (PVT/w) [49] [50] [51]
2. Air (PVT/a) [49] [50] [51]
3. Refrigerant [49] [51]
4. Heat Pipe [49]
5. Dual Fluid (PVT/wa) [51] [52] [53]
6. PVT Concentrator [54] [55] [56]

A PVT Technology Roadmap was published as part of PV Catapult of the 6th Framework Programme [57]. To reduce system costs associated with conventional solar technologies, the roadmap suggested that the development of PVT systems should be focused on residential systems in an attempt to reduce system costs . As a result, commercially available PVT technologies closely resemble standard solar collectors. A number of priority areas were identified including technical issues, marketing issues and building integration issues. One aspect was building integration with an emphasis on the development of plug-and-play systems that could be integrated with existing building practices. The PVT forum was a coordination action from the 2003 PVT Catapult Programme which aimed to prepare the Europe for the expansion of the PV market [58].

Since April 2014, households in the UK have been able to receive payments as part of the Renewable Heat Incentive (RHI) which pays participants of the scheme for the thermal energy produced from renewables [59]. This is the heating equivalent of the electricity Feed in Tariff

(FIT) for solar PV panels that was introduced in April 2010. As of January 2015, PVT panels are not eligible to receive both FIT and RHI.

2.5.1 PVT Collector Designs

The design of a PVT collector is dependent on both the heat removal fluid and the application that it will be used for. A comprehensive review of the different flow designs for water and air PVT systems is provided by Chow [50]. Despite much research being carried out into different designs, there are a very limited number of PVT systems that are commercially available.

2.5.1.1 Standard Modules

Solimpeks is an established manufacturer of solar thermal collectors and they manufacture PVT panels alongside their range of conventional thermal collectors. They produce two designs of PVT panel; one is optimised for electricity generation (PowerVolt), the other is optimised for heat generation (PowerTherm). The difference is that the PowerTherm collector has an extra layer of glazing to reduce the overall loss coefficient; whereas the PowerVolt is unglazed and can achieve greater electrical efficiency without transmission losses. The panels look identical to standard PV modules, see Figure 2-13, but the layers inside the module are very different with the main difference being the presence of a copper absorber and thermal insulation, see Figure 2-14.

The PVT panels have the same 10 year warranty as their conventional counterparts and electrical output is guaranteed at 80% after 20 years. As a result, the collectors offered by Solimpeks are the only PVT devices accredited under the MCS scheme of the UK government. This means that they are eligible for payments through the electricity Feed in Tariff; however PVT collectors are currently not eligible for the Reneable Heat Incentive.

Figure 2-13: Hybrid PVT Panel. Source Solimpeks

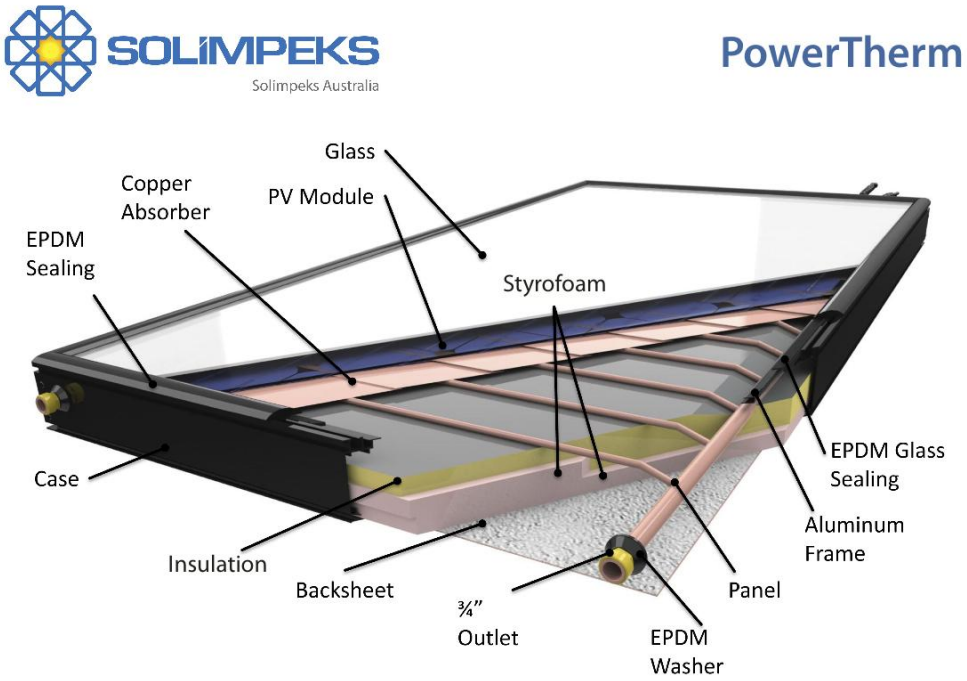

Figure 2-14: Solimpeks PowerTherm PVT panel Source: Solimpeks

2.5.1.2 Building Integrated PVT

PVT systems integrated into the building fabric have shown promise since the mid 1990's. A study of a prototype semi transparent solar facade with heat recovery showed that the total efficiency of the system in the UK climate was 33.2%, 44.1% and 56.9% for Winter, Spring and Summer respectively [60].

Nowadays, commercially available building integrated PVT (BIPVT) is limited to air based systems and these can provide space heating for the building. The PVT Solar Wall by Conserval is a modified version of the standard transpired solar collector. They have also developed a PVT Solar Duct that operates using the same principle.

Figure 2-15: PVT Solar Duct left and PVT Solar Wall Right. Source Conserval Engineering

A liquid based PVT system was developed by Anderson by modifying a metallic trough roof [61]. He showed that a zero loss efficiency of around 0.6 could be achieved for the glazed

BIPVT collector. This result is comparable to that achieved in other studies of standard PVT systems [62]. The study however was mainly focused on the parameters that influence the performance of such a collector and there was no comment on commercial viability.

An example of a water based commercial BIPVT system was installed by Englert Inc. The 'Roofing Solar Sandwich' was comprised of several layers, see Figure 2-16. The bottom layer, a standard roofing undergarment with a radiant reflective membrane. This was followed by thermal purlins with embedded cross linked poly ethylene tubing, through which the heat removal fluid for the solar energy system is circulated. A metal seam roof is then placed onto the purlins and flexible thin film solar laminates were laid across the roofing channels [63]. As of 2014, the 'Solar Sandwich' is no longer a standard product offered by Englert. There is also no information on how the system performs.

Figure 2-16: BIPVT water system. Source Englert [63]

2.5.2 Performance of PVT Collectors

There is currently no standard method for the assessment of performance of a PVT collector; however a draft was proposed as part of the PV Catapult Programme [64]. This however was a combination of existing standards used to determine the performance of conventional solar thermal and PV collectors, EN 12975 and IEC 61215 respectively.

There are number of methods used to measure the performance of a PVT device. The first is using overall energy efficiency. This is a measure of the useful energy produced from incident solar radiation but no distinction is made between the grade of the energy. In a PVT device the thermal efficiency is much greater than the electrical efficiency. A second law exergy analysis takes into account the grade of energy produced. The energy and exergy analysis of a solar collector is explained in more detail in Section 4.5.2.

2.5.3 Numerical analysis of PVT collectors

There are several numerical methods that have been used to simulate performance of a solar collector; these vary in complexity and can be modified depending on the objective.

Florchuetz modified the HWB model so it can be applied to PVT collectors [65]. This included a modification of the terms for absorbed solar radiation and energy losses that occur due to electricity production from the PV cells mounted on the surface of the collector. The Florchuetz model is detailed in Section 4.5.

Zondag developed several methods based on the finite difference approach [62]. The models varied in complexity, the most complex being a transient 3 dimensional model and the simplest was a one dimensional model based on the HWB. It was concluded that for the determination of performance for a solar collector, a steady state model is satisfactory as the inclusion of dynamical effects varied the results by 0.2%. They also found that there was little variation between the 1D model and the 3D model (~3%) so it was concluded that the 1D model is satisfactory for performance modelling of a solar collector. This is convenient as the computation of the 1D model is 180000 faster than the dynamical 3D model. Zondag later applied the numerical method to 9 different designs of PVT collector [48]. They showed that the models followed experiments with 5% accuracy. [66]

Sandes and Rekstad used a modified Hottel Whillier model [67] and applied it to a photovoltaic thermal collector with a polymer absorber plate [68]. In agreement with the work of Florchuetz, they found that the PVT collector had a reduced thermal efficiency compared to a conventional standard solar thermal collector. These losses were attributed to:

- The available energy for thermal conversion was reduce due to the additional electricity generation from PV cells
- A lower optical absorbtion in the photovoltaic cells compared to the black absorber plate
- Increased heat resistance in the cell/absorber interface

They found that the presence of solar cells reduce heat absorption by 10%.

Rockendorf used a 1 dimensional thermal analysis to compare the performance of a PVT collector with the performance of a thermoelectric generator [69]. The latter generates electricity from a temperature gradient across dissimilar materials. The numerical method took into account the different conductivities of the layers that make up the PVT collector and thermoelectric device. Rokendorf found that, due to the high temperatures required by themoelectric devices, the performance of PVT is superior and produces 9 times more electricity for the same collector area.

De Vries also used a modified HWB model to investigate the long term performance of several PVT designs in the Netherlands [70]. He found that the single covered design was the best compromise between thermal and electrical efficiency compared to the uncovered and double covered designs.

Hegazy used a 1 dimensional, quasi-steady state numerical model to investigate the thermal performance of four different designs of air PVT collectors [71]. The heat transfer mechanisms were identified and an energy balance through the cross section of each design was detailed. Each of the collectors considered in the study had similar performance with an overall efficiency ranging from around 30-55% depending on the mass flow rate of air. It was found that for each design there was a critical mass flow rate, beyond which the collector overall performance decreases.

Tonui and Tripanagnostopoulos created a quasi steady-state numerical model and used it to determine the performance benefits of a thin metal sheet and fins, suspended in the channel of a PVT air system as low cost modifications to improve performance [72]. The study concludes that the modification of the air channel increases the thermal efficiency of the collector and the additional pumping requirements due to increased pressure drop are compensated by the increased energy output of the collector.

Joshi collected irradiation data for a region in India and created a quasi-steady state numerical model based on the energy balance across the cross section of a parallel plate PVT air collector. The study found the instantaneous energy and exergy efficiency to be between 55-65 and 12-15% respectively [73].

Steady state models cannot be used to determine working temperatures of the PV module and heat-removal fluid during intermittent operating conditions. To overcome this Chow developed an explicit dynamic model to analyse the perform of a PVT collector [74] . The approach used a control-volume finite difference approach. Parametric studies using the model highlighted the importance of good thermal contact throughout the PVT collector. For a collector with perfect thermal contact (10000W/mK) the maximum combined efficiency exceeds 70% however for poor thermal contact (25W/mk) the efficiency drops to less than 60%. Using the model Chow was also able to show the temperature distribution across different panel segments as well as how the temperature, heat gain and electrical gain change with a sudden change in mass flow rate.

Dubey developed a quasi-steady state numerical model that incorporated both the PVT collector and the heat storage tank [75]. The aim of the study was to derive a "characteristic equation" that could be applied to different climates and designs to understand how the PVT collector will perform. The study used MATLAB to carry out the simulation and showed good agreement with experimental results.

Ibrahim used the HWB model to analyse various designs of PVT collector and concluded that a counter current spiral design was the most thermally efficient design [76].

2.5.4 Laboratory testing of PVT collectors

Laboratory testing involves the characterisation of the performance under controlled laboratory testing. This type of test is short term, has well defined parameters and the experimental variables are monitored. It is standard practice to validate the numerical models using experimental methods.

Zondag carried out experimental validation of the numerical models detailed in the previous section. The results from Zondag's study are summarised in Table 2-4. The thermal efficiency of the PVT collector was found to be 33% compared to 54% for the conventional solar thermal collector. The electrical efficiency of the PVT collector was 6.7% compared to 7.2% for the conventional PV laminate under the same conditions.

Table 2-4: Experimental findings for the zero loss efficiency of a PVT and thermal collector. Source [62]

Panel	Zero Loss Efficiency
Thermal collector	0.84 ± 0.011
PVT without electricity	0.59 ± 0.015
PVT with electricity	0.54 ± 0.015

Zakharchecko carried out an experimental test that investigated the use of different types of PV panels and methods of thermal contact in a PVT system. The study found that a metal substrate gave a 10% increase in thermal power due to improved thermal contact. They also found that PV cells must be placed on the cooler section, near the inlet, to optimise electrical efficiency. They concluded that a PVT system requires a special type of modified PV panel for efficient heat extraction and commercial panels were not suitable for use in a PVT collector [77].

Tonui and Tripanagnostopoulos validated their steady state numerical model using temperature readings taken from thermocouples placed in the PVT air collector. The collector was tested outdoors and a pyranometer and anenometer were used to record irradiation and wind speed respectively [72].

2.5.5 Real life case studies

It is useful to understand how a PVT system will perform in practice compared to standard technologies. The annual performance data from installed PVT systems can then be compared with the performance data from standard PV and thermal collectors. An extensive database of performance for PV installations can be found on the Sunny Portal website [78].

Information on the performance of solar thermal systems is less accessible due to the difficulty in monitoring heat output To monitor the performance of a thermal system, knowledge of the temperature difference across the collector as well as the mass flow rate is needed. The installation of such sensors is beyond the scope of domestic installations. Independent monitoring studies have been carried out and there is a great variation in performance in published results. One monitoring study of domestic solar thermal hot water (STHW) systems found that none of the solar collectors achieved their design specification [79].

In January 2005 a three year research project, SHC Task 35, was launched by the International Energy Agency into the development of PVT systems. The work included the testing of commercially available water and air PVT collectors.

The tested PVT air system was a transpired solar collector with PV cells mounted on top. The transpired solar collector is a well proven technology that operates by heating air in the boundary layer above a solar absorber [80]. The air in the boundary layer is then drawn through small perforations in the absorber and can be used to supply hot air for space heating. In the study, the performance of the PVT air system was compared with the performance of a PV module and a transpired solar collector [81]. Thermal efficiency and PV temperature was compared in the study. Surprisingly it was found that the temperature of PV modules in the PVT system was higher than the naturally ventilated PV base case. This was attributed to poor heat

transfer from the PVT modules to the air. It was concluded that air PVT systems should not be used on the basis of cooling PV cells. The combined thermal efficiency was reduced for the PVT system by around 30% due to the blockage of sunlight to the surface of the collector; however it was found that the combined efficiency of PV and thermal energy conversion is higher than conventional side by side configuration. The performance of a commercially available PVT water collector was also carried out. In this study no base case measurements are presented but the zero-loss efficiency of the PVT collector was measured at 0.60. When the PV cells mounted on the surface were disconnected the thermal efficiency increased to 0.67 [81]. A survey was also carried out as part of the study and there was significant interest in PVT technologies by both architects and solar companies. The most desirables aspects of PVT technology was that it can be used when roof top space is limited, reduce installation costs, scope for building integration and is more aesthetically pleasing than side by side systems [47]. The aesthetic issues associated with PV and thermal collectors installed side by side has been addressed by Viridian Solar who have developed the Clearline range of PV and thermal panels that look identical to each other.

A monitoring study was conducted on the first ever BIPVT air system installed in the UK. The active system forces air through several ventilated PV modules and the heat is either used directly for space heating or stored in the central heat store. Results from the first few months of monitoring exceeded those predicted in simulation [82].

There is no published data in peer review regarding the real life performance of PVT water systems; however some manufacturers and installers have published the results of case studies, see Table 2-5.

Table 2-5: Case studies of PVT Systems

Organisation / Project Name	Size	Site	Annual Electricity	Annual Thermal	Electricity Thermal Ratio	Reference
Encraft	NA	UK	2100kWh	8900kWh	20:80	[83]
Solimpeks/ Crossway	2.95kW	UK	3408kWh	12064kWh	22:78	[84]
Solimpeks/ Kumluca	3.55kW	Turkey	3808kWh	14064kWh	21:79	[84]
Solimpeks/ Sunnybank	3.41kW	UK	3715kWh	13289kWh	22:78	[84]
Solimpeks/ Chetwode	3.30kW	UK	3988kWh	9992kWh	29:71	[84]

The case studies are in agreement with the research carried out by Huang that showed a PVT collector reaches around 76% of the efficiency of a conventional solar hot water heater [46].

A long term experimental analysis was carried out by Fujisawa to investigate the exergy produced by a PVT system for an entire year [85]. The testing monitored the performance of a PVT collector against a PV and thermal collector. This experiment is more indicative of how a system will perform in a real life setting compared to an instantaneous laboratory test. The exergy of the PVT collector was the total value of the electrical and thermal exergies produced. . The best performing technology in terms of overall energy was achieved by a single covered PVT collector which produced 614kWh/ year followed by the standard thermal collector at 575kWh/ year and then the uncovered PVT which produced 480kWh/year and finally the worst performer was the PV module which produced 72.6kWh/year. An exergy analysis on the other hand showed that the uncovered PVT collector was the best performer at 80.8kWh/year and the worst was the standard thermal collector at just 6.0 kWh/year. This finding shows how little value is placed on the thermal energy in an exergy analysis.

2.5.6 PVT Applications

PVT collectors can be incorporated into a range of applications:

- Domestic hot water
- Space heating
- Space cooling and dehumidification

PVT collectors can also be combined with other storage and renewable technologies such as

- Heat pumps
- Energy storage such as phase change materials

2.5.6.1 Domestic hot water PVT Systems

A comprehensive review of PVT technology and its applications has been carried out by Zhang [49]. They highlighted that in the future more work needs to be carried out in understanding the dynamic performance of PVT systems. They also suggested that feasibility studies into how PVT will perform in real buildings need to be carried out.

Kalogirou solved a quasi-steady state model, based on the HWB, using the TRNSYS simulation program. In TRNSYS the system is built using components that represent subroutines that require a number of inputs. The components can be connected in anyway provided that the output of one component feeds the input for the next, see Figure 2-17. When the simulation is performed the system is converted into differential equations and solved over the specified time period.

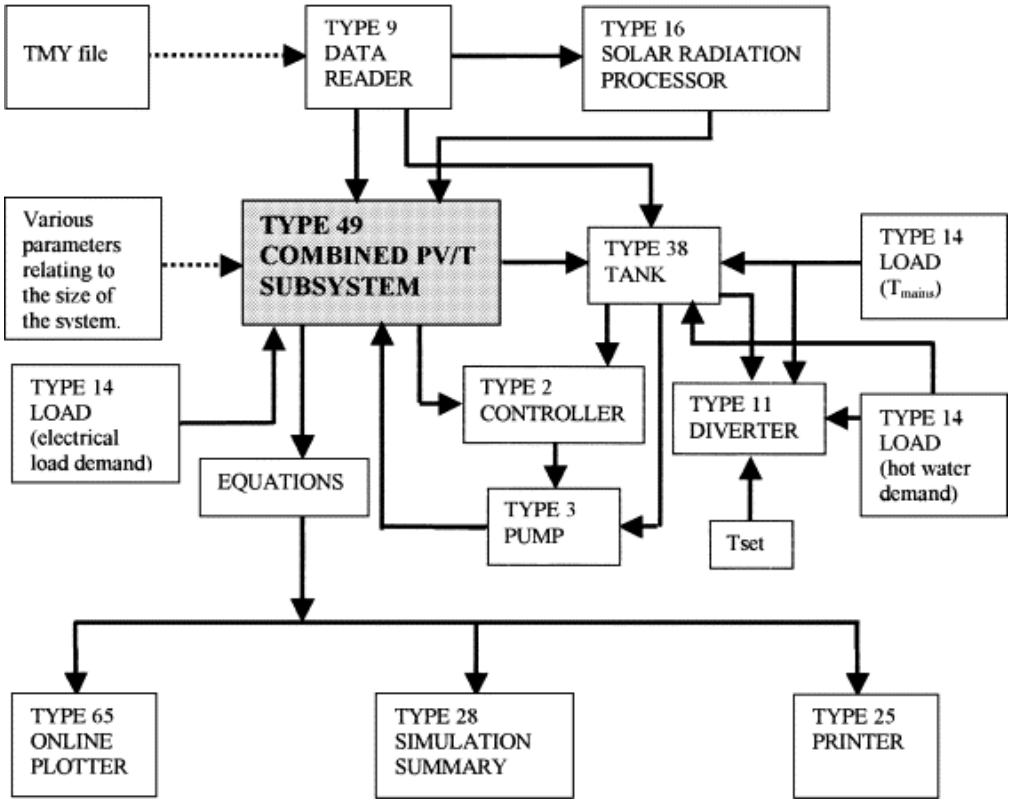

Figure 2-17: TRNSYS flow diagram showing the components used to simulate the operation of a PVT system. Source [86]

Kalogirou used TRNSYS to model a pump operated [86] and thermo syphon domestic PVT/w systems [87]. The simulations investigate the use of both crystalline and amorphous silicon modules. They conclude that a considerable amount of energy is produced by the PVT system and that it is most suitable for applications where both electricity and hot water are required.

2.5.6.2 Space heating

As previously explained, the modified transpired solar collectors are used to supply the heating demand of buildings. There are some examples of solar hot water systems that can be used to power underfloor heating [88].

2.5.6.3 Space cooling and dehumidification

Generally speaking, sunny regions require more cooling. There are two main ways that solar technology can be used to provide space cooling to a building. The first is to supply electricity to air conditioning units and the second is to supply heat to an absorption chiller. A comprehensive review of solar cooling methods has been carried out by Chidambaram [89].

Dehumidification works in a similar way to cooling; the surface temperature of a condensing unit has to be lowered to below the dew point temperature of the room. A theoretical solar trigeneration system was proposed and simulated by Calise [90]. If realised, this system will be able to provide heat, cooling (via absorption chiller) and electricity.

2.5.6.4 PVT heat pump systems

A PVT system can be combined with a heat pump directly or indirectly. In a direct system the solar collector forms the evaporator of the heat pump system to increase the coefficient of performance. This concept has been applied to both conventional solar collectors [91] and PVT collectors [92]. In the latter a coefficient of performance of 6 could be achieved during winter and the presence of PV cells did not have a significant adverse effect on the system compared to the conventional solar collector.

PVT collectors can also be combined with a heat pump to cool PV cells. Daghigh reviewed available technologies and concluded that direct expansion solar-assisted heat pump system achieved better cooling effect of the PV/T collector than the standard piping configuration[51].

A study of a indirect PVT system coupled with a ground source heat pump was simulated using TRNSYS. The results show that the system was able to cover 100% of the total heat demand for an energy efficient Dutch one family dwelling [93]. The principle of this system was to primarily store heat from the PVT collector in a water cylinder. During the summer excess heat was stored in the ground and then recovered during the winter. This heat could either be used for space heating or hot water. The electricity produced by the PV cells was able to cover the electricity requirements of the heat pump.

2.5.6.5 PVT and phase change materials

Although work has not been done specifically with PVT collectors, phase change materials have been previously used in conjunction with conventional solar thermal collectors. An extensive review of thermal collectors with PCM has been carried out by Shukla [94]

2.5.7 PVT Industry

A survey of the market revealed that there are more than 130 PVT collectors from over 80 companies for the production of domestic water and space heating [10]. Although there is no mention or published material on the size of the industry compared with conventional solar thermal and PV technologies.

2.6 Formation of a PVT collector

In most research studies, the method of combining a PV laminate and solar thermal absorber together is to use a thermal adhesive. In some cases this has been reported as adequate [48] but others claim that better thermal contact between the PV module and the thermal absorber must be achieved [95] [77]. Solimpeks, a major manufacturer of PVT collectors, previously used a thermal paste and copper strips to bond the thermal and PV elements together but have recently adopted a vacuum lamination approach to improve thermal contact [Personal communication with David Browne of MinimiseGeneration 2015]. A review of different manufacturer and the bonding methods used in their products is given in Table 2-6.

2.6.1 Achieving good thermal contact

Chow used a dynamic simulation to investigate the importance of good thermal contact between the layers of a PVT device [74]. Zakharchenko carried out an experimental test that investigated the use of different types of PV panels and methods of thermal contact in a PVT system [77]. To ensure optimum contact, an aluminium substrate was coated with silicon oxide coating. This 2 μm think electrically insulating layer protects the electrical contacts of the PV cell. The use of this layer reduced the aluminium coating by 5%. The result was that the PV collector was cooled by around 10°C with a conversion efficiency increase of 10%. This led to the conclusion that a special type of collector is required for use in a PVT system, and simply combining a PV module and thermal absorber together would not provide a sufficient contact for energy extraction. Rebollo investigated the feasibility of constructing a PVT collector using standard PVT and a heat exchanger [95]. A semiconductor thermal paste was used to improve thermal contact; however it was noted that it was not possible to get an even coating and there were air gaps present in the paste. They found that simply placing the panels on top of each other was not sufficient; however no useful results or comparisons were presented by the study. On the other hand a more comprehensive report was produced by Zondag which showed that using adhesive to connect PV laminate was sufficient. The study reported that the combined efficiency of a glazed PVT was 0.67 compared to the thermal collector which was 0.83 [48]. The majority other studies into combining PV and thermal absorbers has followed the approach of Zondag with promising results. In another study He et al. created a hybrid PVT collector where layers of TPT, silicone gel and EVA separated the absorber and the PV cells [96]. They found that the daily efficiency was around 80% of a conventional solar thermal collector.

Joshi 2009 showed that a glass-glass PVT air collector performed better than the tedlar backed module in terms of overall efficiency [97]. The same research group carried out a parametric study into various configurations of PVT collector Tiwari 2007 [98]. The parametric study investigated the heat transfer in a PVT air collector with and without a tedlar backing layer but the EVA encapsulation was always present. The study found that there was only a marginal increase in temperature of the air at the outlet.

Table 2-6: Methods of bonding PV cells to a thermal absorber by manufacturers of PVT devices. * Either no information was available or the manufacturer saw this as commercially sensitive information

PVT Manufacturer	**Description of Product**	**Method of Bonding**
Solar Zentrum	Header riser PVT collector	PV-EVA-Tedlar-Heat Exchanger
Solimpeks	Header riser pipe with copper absorber. One design optimises heat and the other electricity	Vacuum lamination is used to bond the PV laminate to the absorber
Minellium Electric	Standard PVT panels	No information*
TESZEUS	Thermosyphon PVT System	No infomation*
Wiosun	Header riser PVT collector	PV-EVA-Tedlar-Heat Exchanger
Solar Angel	Header riser design with aluminium absorber	Standard PV laminate to thermal absorber
Dual Sun	Innovative refrigeration style stainless steel heat exchanger	The absorber is vacuum laminated in a single step [99]
Silia	Header riser with copper absorber	No information *
Fototherm	Serpentine PVT	No information*
H-NRG	Refrigeration style heat exchanger	No information*

The high temperatures experienced in a concentrator system means than heat removal is more important than non concentrator systems. To remove contact thermal resistance, Zhu immersed the PV cells of a 250x concentrator system and was able to cool the cells to 45°C at an irradiance of 940W/m^2 [100]. The convective heat transfer coefficient of the fluid was around 6000W/m^{2}K.

Although there is no doubt about the importance of good thermal contact, it has been shown in literature that it is possible to combine a PV laminate and thermal absorber to form a PVT device with little modification. One consistency in all designs is the use of encapsulation for the PV cells to protect against degradation and short circuiting. This is achieved by encapsulating the PV cells with EVA polymer. This protective layer is followed by a Tedlar backing sheet for additional protection. The problem is that these materials are thermally insulating which means heat flow is hindered. The thermal conductivity enhancement of this material using ceramic powders has been investigated for the microelectronics industry [101] and its use has been investigated for standard PV panels [102]. This work will investigates its use in a PVT collector to enhance the amount of heat that can be recovered.

2.7 Discussion

There is no shortage of simulation studies and often details of the testing methods used to validate the models are vague or non-existent. The first area of work will be focused on the design and development of a PVT testing facility that can extract fundamental performance characteristics from a PVT collector. The construction of the PVT module will incorporate crystalline PV technology as this is the most widespread PV technology. The second project will be focused on developing a numerical model, using CFD, that can visualise the surface temperature of the PVT collector. The results of such a study will be useful to optimise the design and use of PVT technologies in buildings. The third study will involve improving the heat transfer properties of the collector; as this was identified as a pertinent area in previous work [77] [74]. The conductivity of the EVA encapsulant will be increased using boron nitride powder. A steady steady heat transfer model, due to its proven reliability [48], will be used to simulate the performance of the enhanced EVA and compared with the base case.

3. Experimental Characterisation of Solar Collectors

3.1 Introduction

This chapter details the experimental methodology used to characterise the combined electrical and thermal performance of photovoltaic thermal (PVT) collectors. The experimental construction of the measurement system is detailed in Section 3.2-3.7 and the error analysis is detailed in Section 3.8-3.10.

This study compared several cases, the results of which are presented and discussed in Section 3.11. A summary of the comparisons covered in this report include:

- **Header riser vs. serpentine configuration**: The serpentine collector outperformed the header riser design due to reduced heat losses at higher temperature differences between the inlet and ambient.
- **Covered vs. uncovered**: In this case the performance of the serpentine collector was characterised with and without the use of a polycarbonate cover. The uncovered collector had better performance when the temperature difference between the inlet and ambient was lowest, due to more light reaching the surface of the absorber. The covered collector on the other hand, reduced temperature driven convective losses, and the thermal efficiency was greater at higher temperature differences between the inlet and the ambient.
- **Electricity generation vs. no electricity generation**: In both cases photovoltaic laminates were secured to the top of the serpentine thermal absorber. In the no-electricity generation case, the thermal efficiency of the absorber was determined. In the electricity generating case, both the thermal performance and electrical output was measured. In both cases the thermal efficiency was reduced by placing the laminates onto of the absorber. In the electricity generation case, the thermal efficiency was further reduced due to some of the light being used to generate electricity before reaching the absorber.
- **Glass backed PV laminates vs. Tedlar backed PV laminates**: In this study two different backing materials were used for PV laminates placed onto the parallel absorber. The results were not significantly different from each other and therefore indicate that there was a bottleneck in heat transfer occurring between laminate and the absorber.

Conclusions are made in Section 3.12 and the improvements and future recommendations are provided in Section 3.13.

3.2 Experimental Design and Construction

This project involved the design and construction of a testing system that can characterise the performance of solar thermal collectors. The system is made up of four components; thermal management, flow control, temperature logging and solar simulation. The completed system is illustrated in Figure 3-1. This section describes the design and construction of the system.

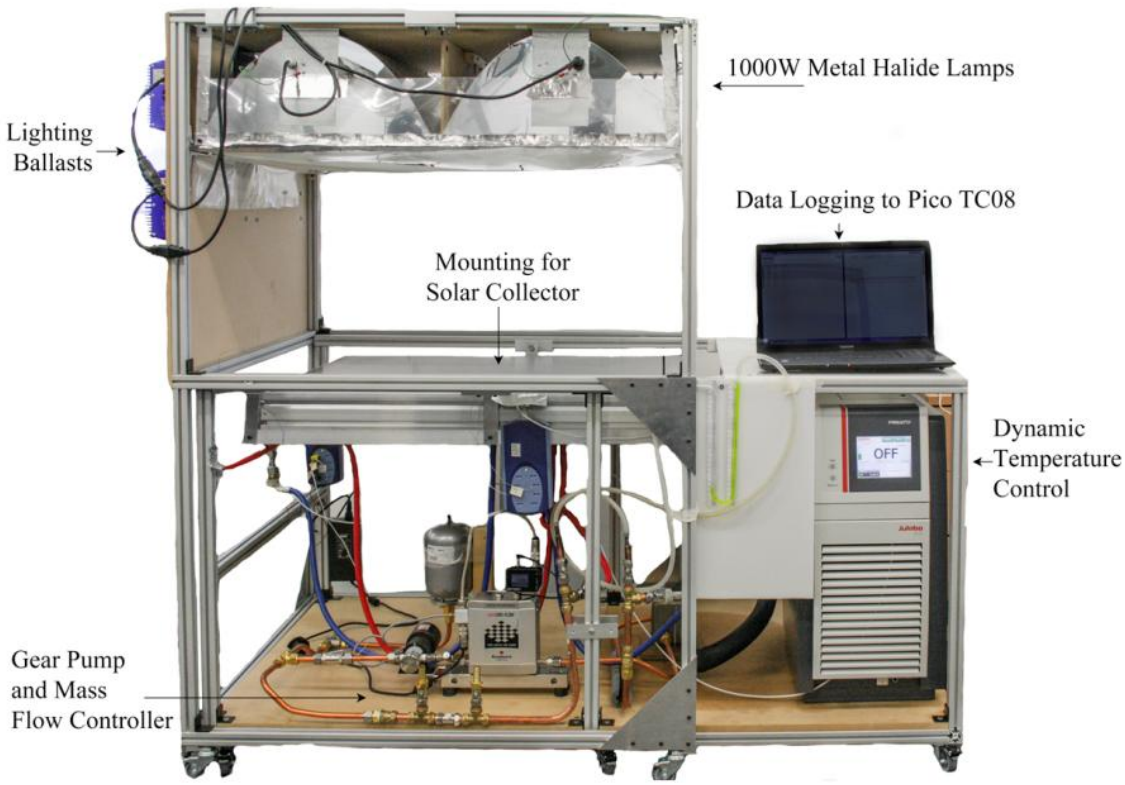

Figure 3-1: System used to test the thermal performance of solar collectors

3.2.1 Solar Thermal Collectors

The collectors in this study were constructed using Sunstrip Lazerplate fins (S-Solar, Sweden). These consist of copper pipes laser welded to an aluminium sheet. Each strip consists of one pipe with two fins, one on either side of the pipe. The upper surface of the fin is treated with a selective coating to maximise absorbance and minimise emittance. The technical data of the Lazerplate fins is shown in Table 3-1.

Table 3-1: Technical data of Lazerplate fins. Source (S-Solar, Sweden).

Parameter	Value
Fin efficiency 20L/h	0.938
Fin efficiency 60L/h	0.975
Emissivity	0.05 ± 2%
Absorptivity	0.95 ± 2%
Thickness	0.5mm

In this study the fins were used to create the two designs of solar collector shown in Figure 3-2

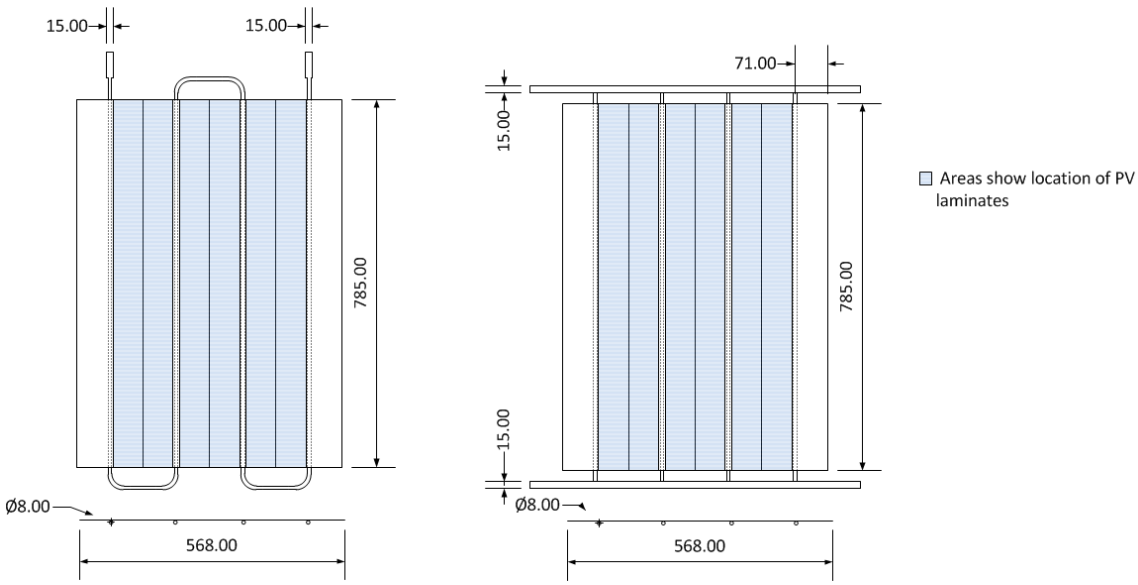

Figure 3-2: Dimensions in mm of the collectors analysed in this study

The copper pipes attached to the back of the collector have an external diameter of 8mm and a wall thickness of 0.5mm. The connection pipes and header pipe of the header/riser absorber have an external diameter of 15mm with 1mm wall thickness. The fins were assembled into absorbers by AES Solar, UK.

3.2.2 PV Laminates

Bespoke PV laminates were constructed by GB-Sol, UK. The laminates were designed as strips, measuring 785mm x 129mm. Each strip contained a row of 6, series connected monocrystalline PV cells, 125 mm x 125 mm. The technical information, as supplied by the manufacturer is displayed in Table 3-2 and Table 3-3.

Table 3-2: Electrical characteristics of individual PV cells at STC conditions 1000W/m^2 AM1.5

Efficiency (%)	P_{mpp}[W]	V_{mp} [V]	Imp [A]	Voc	Isc	FF
17.70	2.72	0.524	5.204	0.631	5.666	76.21

Table 3-3: Temperature coefficients of PV cells

Voc Temp. Coef.%/K	-0.329
Isc Temp. Coef. %/K	+0.043
Pm Temp. Coes %/K	-0.42

The PV cells were encapsulated with EVA. 3 strips were produced with the encapsulated PV cells sandwiched between two layers of glass and 3 were produced with a layer of glass on the front side and a sheet of polyvinyl fluoride (Tedlar) on the back. This was to investigate whether the use of different material had an influence on the performance of the resulting PVT collector.

3.2.3 PVT Collectors

The PVT collectors were assembled by placing the PV laminates directly onto the absorber. To improve the contact, clips were used to secure the laminates. An exploded diagram of the layers of the PVT collector is shown in Figure 3-3.

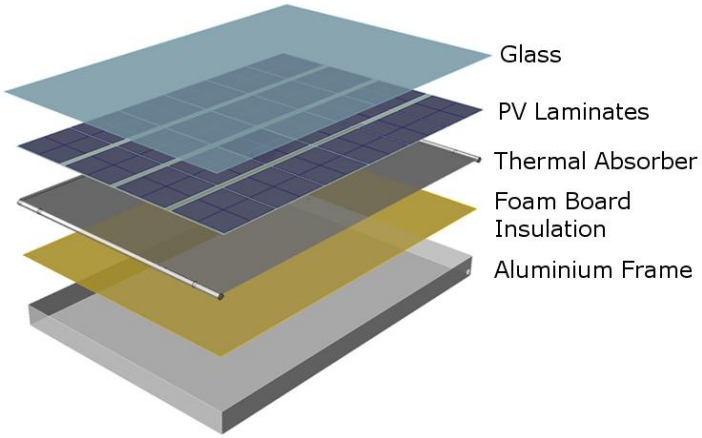

Figure 3-3: Layers of the PVT Collector

Despite using the clamps, the surface of the absorber was not completely flat. This meant that air gaps were present in-between the laminate and the absorber. This is not ideal as intimate contact is required to ensure the best possible heat transfer between the laminate and the absorber.

3.3 Thermal Performance

To characterise the performance of a solar thermal system a controlled testing environment is required. Figure 3-4 shows the schematic of the system, used to test the performance of solar collectors. The system was built following the guidance of the relevant BSI standard [103] The components that make up the schematic are discussed in the following subsections.

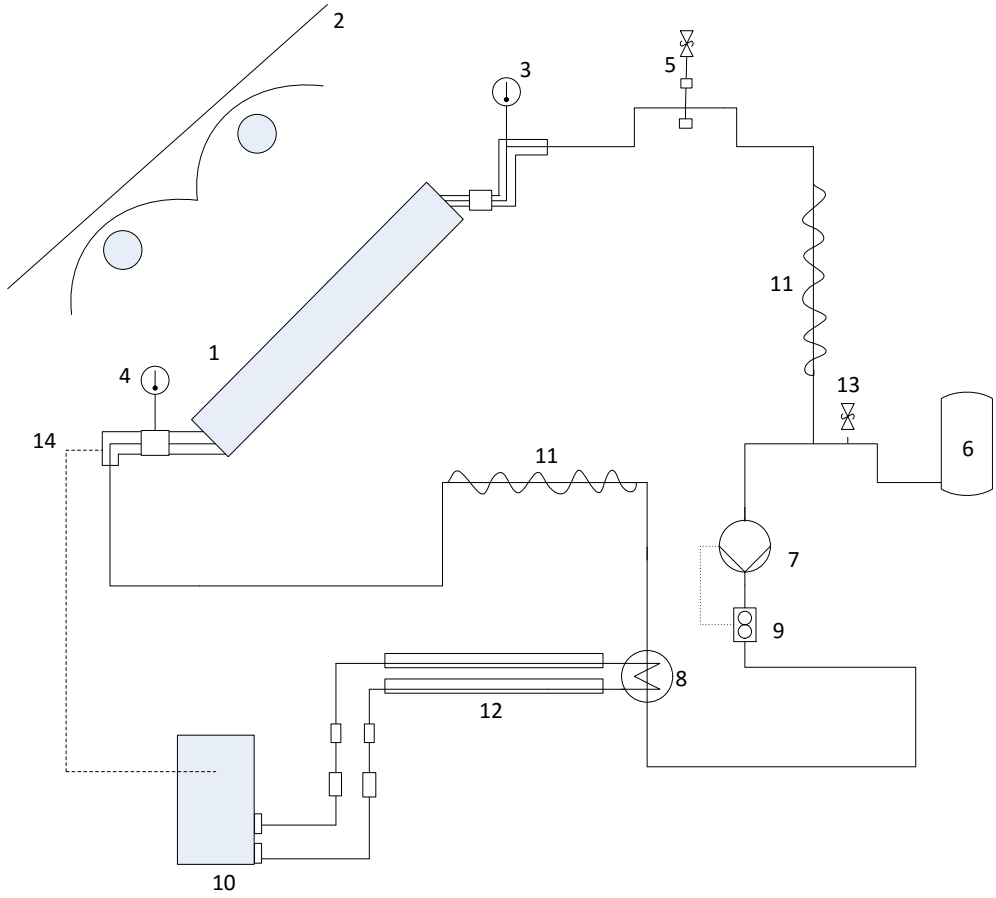

Figure 3-4: Schematic of the system used to characterise thermal performance

Key:

1: Solar Collector

2: Light Source

3: Outlet Temperature T-Type Thermocouple

4. Inlet T-Type Thermocouple

5. Bleed Valve

6. 2 Litre Expansion Vessel

7. Gear Pump

8. Inline Heat Exchanger

9. Mass Flow Control – controls pump speed

10. Julabo Presto A40 Dynamic Temperature Control – controls inlet temperature

11. Flexible 15mm Piping

12. Triple Insulated Hosing

13. Pressure Relief Valve

14. Pt100 Sensor

3.3.1 Supporting Frame

The supporting frame was designed to securely hold the collector and its auxiliary testing system to enable the performance characterisation of photovoltaic and solar thermal technologies. The requirements of the frame was:

- To support the filled weight of the collector and the auxiliary system shown in the Figure 3-4.
- To allow performance measurements to be taken at various angles on inclination
- To be lightweight, mobile and collapsible so that it can be transported easily for
- To be adaptable so that different designs of collector can be easily tested

With this criteria in mind, the frame shown in Figure 3-5 was designed.

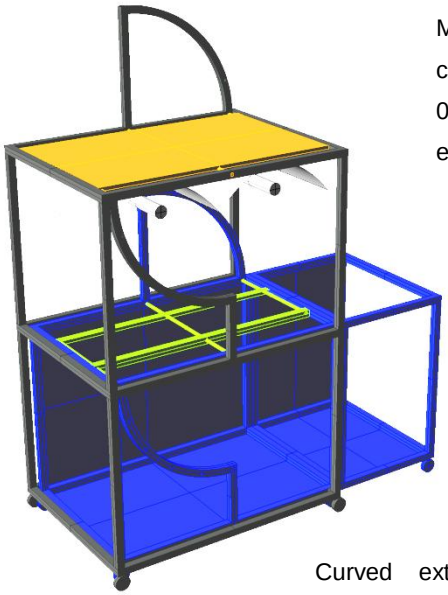

Mounting rails to support collectors with an area up to 0.63m^2. The collectors can be easily removed and replaced.

The test station is mobile and can be used with or without the light source so it can be used outdoors during

The support for the mounting collector is independent of the light support allowing the orientation to be adjusted

Curved extrusions allow the inclination angles (0-90°) of the mounting rails and light source to be

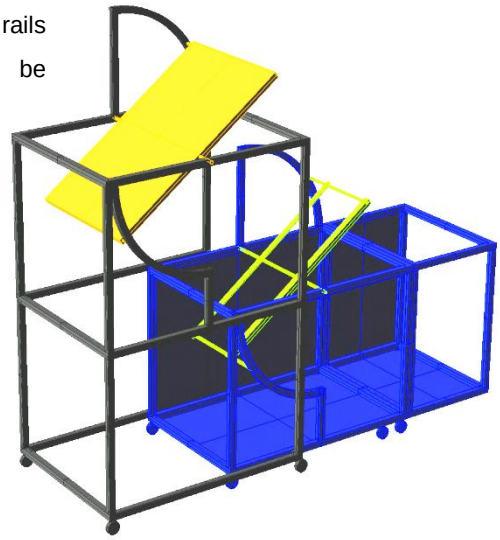

Holes in the curved extrusions can be matched up with the collector and light mounting panels and screwed into place.

Auxiliary equipment and pipe work is kept below the collector.

Figure 3-5: Supporting frame for performance characterisation of a solar collector

3.4 Solar Simulation

The lighting source consists of four 1000W metal halide lamps, which were chosen because they have a spectrum closely matches that of natural sunlight.

To direct the light onto the surface of the collector, the lamps are positioned at the focal point of a Miro-Sun reflective 90 reflector (Alanod Solar, Germany). The focal length of a parabolic reflector is calculated using (3.1):

$$F = \frac{D^2}{16d} \tag{3.1}$$

Where

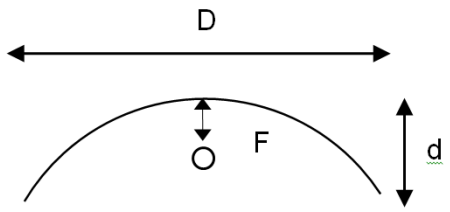

Figure 3-6: Dimensions used to calculate focal length

There are two lamps places in each reflector as shown in Figure 3-7.

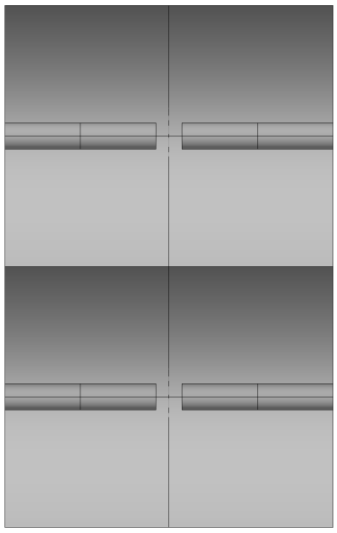

Figure 3-7: Positioning of lamps

The lamps get extremely hot during operation so two 150m^3/h high temperature extractor fans were installed to remove the heat (MMotors JSC, UK), see Figure 3-8. The flow of air was isolated to the lighting chamber to prevent the disruption to the airflow across the surface of the collector.

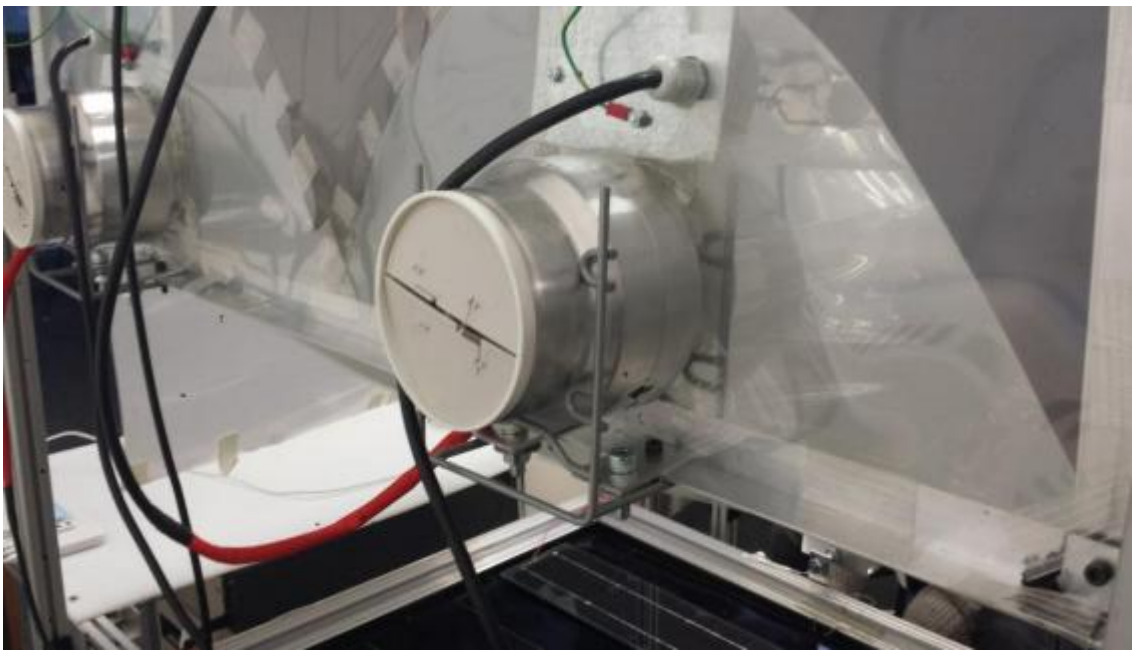

Figure 3-8: Extractor fans used to cool lamps

3.5 Control of Inlet Temperature

To characterise the thermal performance of a solar collector, measurements must be taken during steady state conditions at controlled, constant inlet temperature. Steady state is required to determine the overall loss coefficient, which is an important component in the characterisation of a thermal collector, see Section 4.2.1.

The purpose of the temperature control system is to remove the heat gained by the fluid inside the collector and reset it back to the set inlet temperature.

The inlet temperature range for thermal performance measurements to taken has been specified by EN 12975-2, as from 20-100°C.

The dynamic temperature control unit has a cooling capacity of 1.2kW from 20-200°C (Presto A40, Julabo, Germany). An external pt100 connected to the unit allows for external control of the inlet temperature. Figure 3-9 shows the temperature profile achieved by the controller for a 5 steady state measurements (21°C, 35°C, 50°C, 65°C and 80°C).

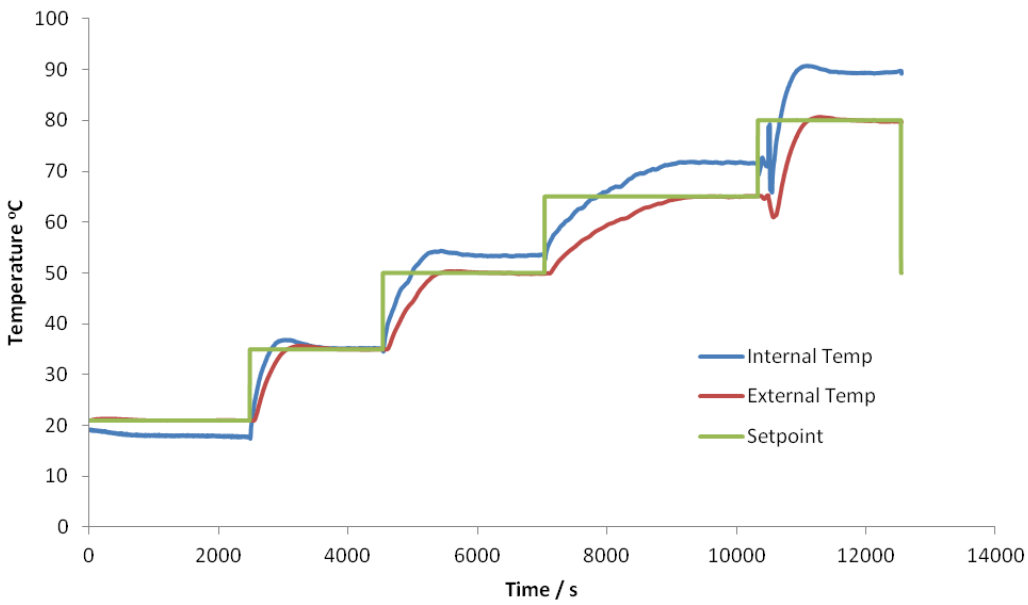

Figure 3-9: 5 stage temperature profile, programmed using Presto A40

The temperature controller delivers a flow rate of 16l/min at a pressure of 1.7bar. This cooling circuit is connected to an inline heat exchanger to remove the heat from the collector circuit (Bowman, UK). The operating conditions of the heat exchanger are shown in Table 3-4.

Table 3-4: Operating conditions for inline heat exchanger as calculated by the manufacturer.

Part No.	Hot side: water				Cold Side: water				
	Flow rate	Temp (°C)		P Drop	Flow rate	Temp (°C)		P Drop	Heat
	l/min	In	Out	kPa	l/min	In	Out	kPa	kW
10-9	0.36	44	20	0.03	16	18.2	18.7	25.5	0.6
10-9	0.36	88	80	0.02	16	79.8	79.9	21.1	0.2
10-9	1.08	28	20	0.19	16	17.8	18.3	25.6	0.6
10-9	1.08	83	80	0.15	16	79.6	79.8	21.1	0.22

3.6 Flow Control

EN 12975 requires the flow rate through the collector to be controlled to within 1% despite temperature fluctuations.

This is achieved using a Bronkhorst Cori-Flow M15 mass flow controller (Bronkhorst Cori-Tech B.V., The Netherlands) which controls the speed of a Tuthill, DGS series, gear pump (Tuthill, USA) see Figure 3-10. The accuracy of flow control increases with decreased flow rate, as is shown in the results from the factory calibration in Table 3-5.

Table 3-5: Flow controller calibration certificate as supplied by manufacturer

Calibrated flow H_2O	Flow indicated by instrument (DUT)	Flow indicated by reference	Flow deviation
300.0 kg/h	300.0 kg/h	300.0 kg/h	0.01% Rd
150.0 kg/h	150.0 kg/h	150.0 kg/h	-0.01% Rd
75.00 kg/h	74.97 kg/h	74.99 kg/h	-0.03% Rd
30.00 kg/h	29.98 kg/h	30.00 kg/h	-0.05% Rd
15.00 kg/h	14.99 kg/h	15.00 kg/h	-0.07% Rd
5.010 kg/h	5.002 kg/h	5.002 kg/h	0.00% Rd
0.000 kg/h	0.000 kg/h	0.000 kg/h	-

The lowest mass flow rate that will be used in this experiment is 32.4kg/h, using Table 3-5 the flow deviation is -0.05% at 23°C.

To calculate the pressure drop in the system, the fittings are listed in Table 3-6 for the system plus connection with the serpentine or header riser collector.

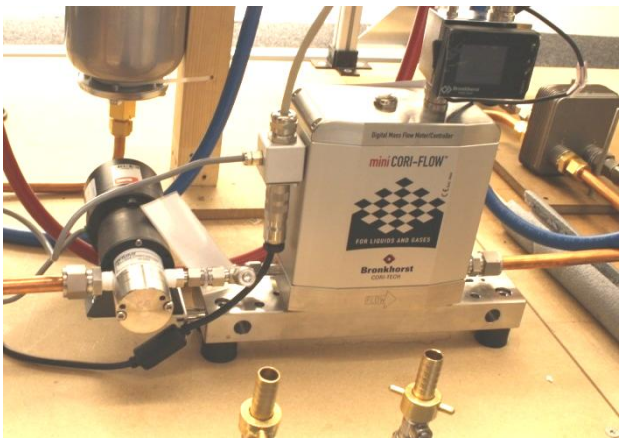

Figure 3-10: Mass flow controller and gear pump

Table 3-6: Fittings for system plus serpentine and HR collector

Fitting Type	Quantity	
	Serpentine	HR
Gate Valve	3	3
90° Elbow, threaded	2	2
90° Elbow, welded	13	7
Tee, threaded, straight through	2	2
Tee, threaded, through branch	4	6

The pressure drop in the system can be calculated using the Darcy Weisbach method. The Darcy- Weisbach formula is given by (3.2):

$$h_L = \left(\frac{fL}{D_i}\right)\frac{\left(v^2\right)}{2g} \tag{3.2}$$

Where:

h_L = height of fluid needed to pump (m)

f = Moody friction factor, which is dependent on the flow regime

L = straight pipe length

D_i = inside diameter in length

v = average fluid velocity

g = gravitational acceleration

To compensate for the pressure losses due to fittings present in the system, the equation needs to be modified. There are several methods that can be used to modify the Darcy-Weisbach formula to account for minor pressure losses in pipe. These include:

1. The equivalent length method
2. The resistance coefficient (K) method
3. The valve coefficient method

This work will employ the resistance coefficient method. In this case the fittings are represented by a dimensionless number, which is used to characterise the roughness of the pipe. The Weisbach formula is modified to:

$$h_L = \left(\frac{fL}{D_i}\right)\frac{\left(v^2\right)}{2g} \tag{3.3}$$

$$h_L = \left(\frac{fL}{D_i} + \sum K\right)\left(\frac{v^2}{2g}\right) \tag{3.4}$$

Where:

$$K = \frac{k_m}{Re} + K_i\left(1 + \frac{K_d}{D_i^{0.3}}\right) \tag{3.5}$$

The pressure drop in the system has been calculated for the range of flow rates that will be used in the system (0.36-0.18L/min).

To determine the operating point of the pump with no flow control, the system pressure is plotted against the pump curve, see Figure 3-11. From this it can be seen that the pump will operate at around 4L/min without any flow control. To be brought down to the operating flow

rates of 0.36L/min, which is specified by the EN12975-2, we need to incorporate a flow control device into the system. The Cori-Flow M15 is capable of achieving this.

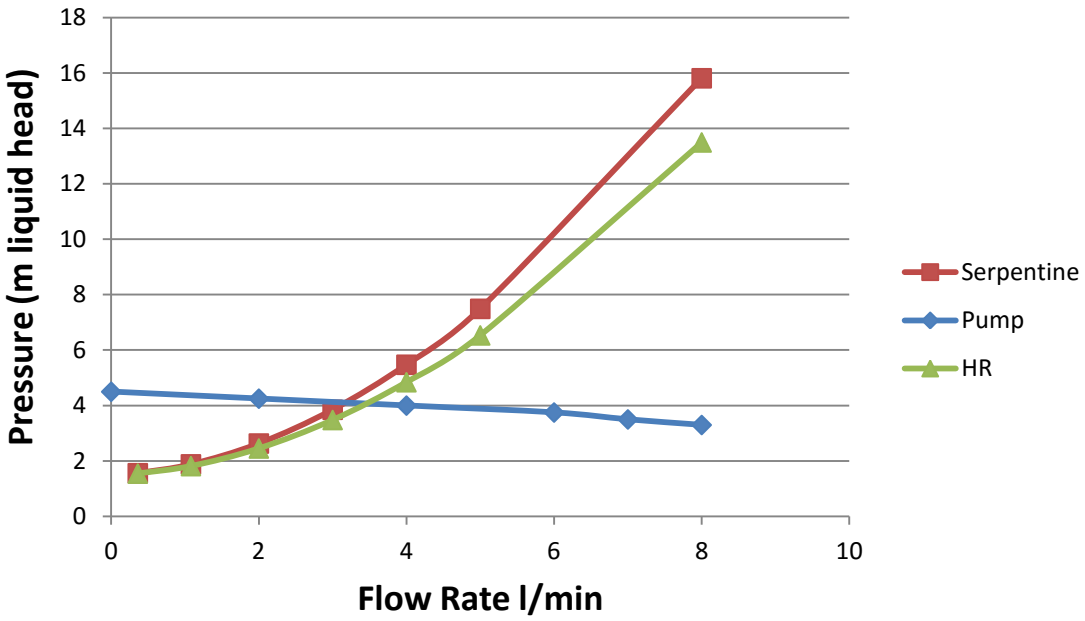

Figure 3-11: System and pump curves for when scenarios when the serpentine and HR collector is connected to the system

3.7 Temperature Measurements

The EN 12975-2 states that three temperatures are required to determine the thermal efficiency of a solar thermal collector; outlet, inlet and ambient air. To ensure mixing of fluid, the inlet and outlet sensors have been placed downstream of fixings. The ambient air sensor is sheltered from radiation and positioned underneath the wooden base of the testing system.

To measure the temperature distribution across the surface of the collector, thermocouples were also attached to the back of the absorber using copper tape. 32 thermocouples were used in total and the location of these thermocouples is shown in Figure 3-12.

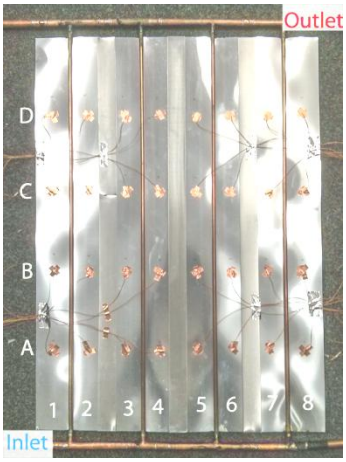

Figure 3-12: Location of thermocouples organised on grid A1 – D8

The measurements from the thermocouples were logged using Picologger TC-08 (Picotech, UK).

3.8 Error and Reliability

This section identifies the main sources of uncertainty and discusses the assumptions and limitations of the experimental methodology.

3.8.1 Calculation of Uncertainty

Table 3-7 summarises the values of uncertainties that have been used in this report. Justifications for the uncertainty of the measured values are given in the following subsections.

Table 3-7: Summary of the uncertainties used in the calculations in this report

Parameter	Value	Uncertainty	Origin
Mass Flow	0.009 kg/s	- 0.05%	Manufacturer
Temperature (Inlet, outlet, ambient, mean plate temperature)	Variable	± 0.5%	Manufacturer and confirmed through measurement
Collector Area	0.45m^2	± 0.31%	Measured
Absorbtivity	0.95	± 2%	Manufacturer
Transmittance*	0.85	± 2.5%	Manufacturer
Emissivity	0.05	± 2%	Manufacturer
Specific Heat of Water	Variable	NA	No information available - interpolated from fluid property tables [ThermExcel]
Incident Angle Modifier	1	NA	No information available - assumed value
Irradiance	Variable	±0.729%	Measured

*This is only used when for calculations when the poly carbonate cover is used. In cases when the absorbed is uncovered, the value of transmittance is unity and uncertainty is no longer needed.

The values listed Table 3-7 have been used in a multivariate analysis of the results to calculate the total combined uncertainty, ω_T , see (3.6).

$$y = f(x_1, x_2, ...x_n)$$

$$\omega_T = \left[\sum_{i=1}^{n} \left(\frac{\delta y}{\delta x_i} \omega_{xi} \right)^2 \right]^{1/2} \tag{3.6}$$

Where y is the output, x is the independent variable, and ω_x is the variable uncertainty of x.

In absence of information claiming otherwise, the datasheet values of uncertainty reported by the manufacturers has been taken as the standard uncertainty. These values were used to determine the combined uncertainty which was then multiplied by a coverage factor of 2 to give a confidence interval of 95%.

The standard deviation, σ, is used in instances where the uncertainty is associated with the measurement of a known value, such as thermocouple calibration, see (3.7).

$$\sigma = \sqrt{\frac{\sum\left(x-\bar{x}\right)^2}{n-1}} \tag{3.7}$$

The standard error, *SE*, is used when uncertainty is associated with the mean, $\bar{x}$, of a sample of measurements, for example measurement of irradiance across the collector surface see (3.8)

$$SE = \frac{\sigma}{\sqrt{N}} \tag{3.8}$$

3.8.2 Thermocouple Calibration

The thermocouples used in this experiment were Type-T (Copper vs. Copper-Nickel). These have an operating range of -200 to 350°C.

Two thickness of thermocouple were acquired for this experimental work 0.2mm (TCDirect, UK) and 0.125mm (Omega, UK). The thermocouple junctions were created using a capacitive discharge welder.

The limits of error stated on the manufacturers' data sheet for type T thermocouples is the greatest of either 0.5°C or 0.4% (Omega, UK).

To establish the error for the thermocouples and data logging equipment used in this study, the thermocouples were placed into a water bath and calibrated against a high precision thermometer, see Figure 3-13.

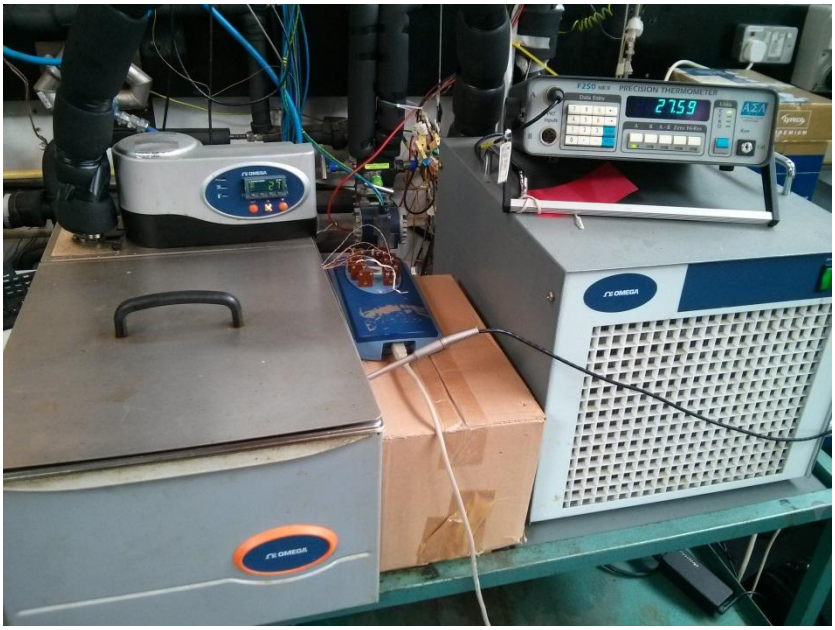

Figure 3-13: Calibration of thermocouples and data logger

A 5-point calibration curve was created across the temperature range that will be experienced in this study (10-70°C). The calibration curve for the two thicknesses of thermocouples used is shown in Figure 3-14.

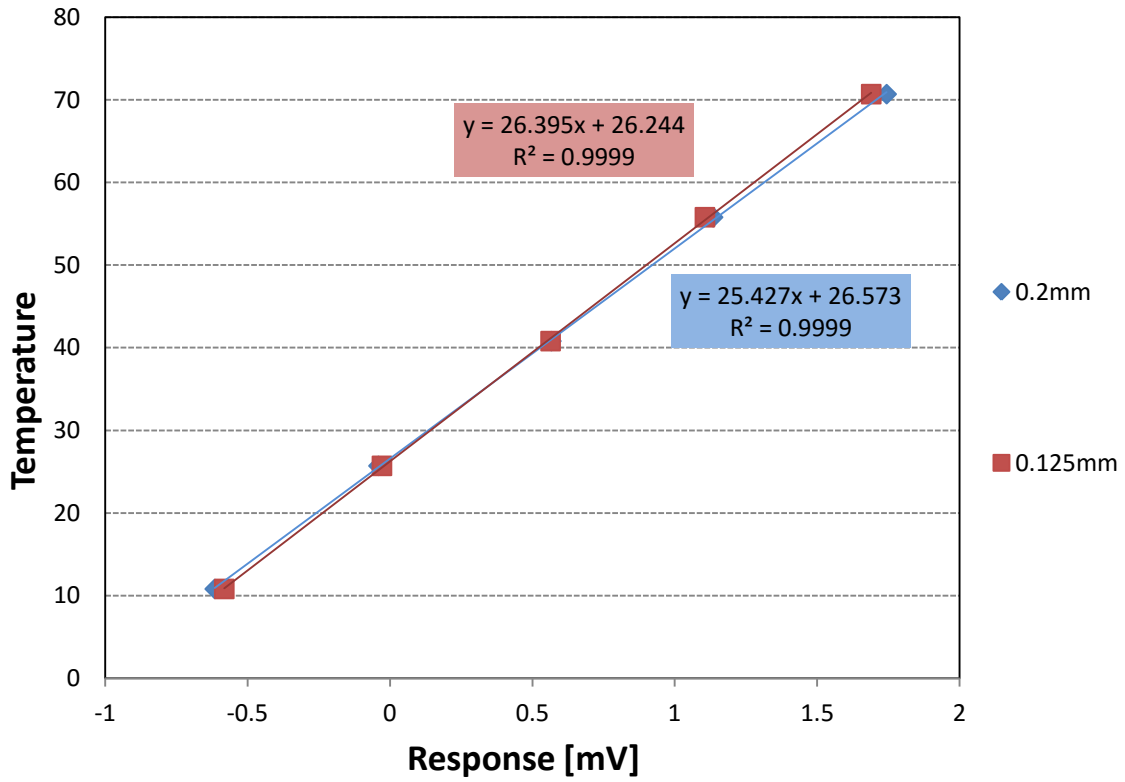

Figure 3-14: Calibration curve for thermocouples

Each point on the calibration curve is the average result from 4 thermocouples. The standard deviation was taken for each set of readings and the °C error at each temperature was calculated using the gradient of the calibration curve, as displayed in Figure 3-14. The error was calculated as a percentage of the reference temperature recorded by the high precision thermometer. The calibration for two thicknesses of thermocouples used in the experiment is shown in Table 3-8 and Table 3-9.

Table 3-8: Calibration data for 0.2mm thermocouples

Ref Temp	Tc1 [mV]	Tc2 [mV]	Tc3 [mV]	Tc4 [mV]	Average 0.2mm	Standard Deviation [mV]	Standard Deviation [°C]	Uncertainty
10.8	0.612	0.615	0.618	0.617	-0.6155	0.0026	0.070	0.65%
25.7	0.035	0.039	0.043	0.045	-0.0405	0.0044	0.117	0.46%
40.8	0.572	0.568	0.565	0.562	0.56675	0.0043	0.113	0.28%
55.8	1.146	1.137	1.132	1.124	1.13475	0.0092	0.243	0.44%
70.7	1.759	1.748	1.741	1.729	1.74425	0.0126	0.332	0.47%

Table 3-9: Calibration data for 0.125mm thermocouples

Ref Temp	Tc1	Tc2	Tc3	Tc4	Average 0.125mm	Standard Deviation [mV]	Standard Deviation [°C]	Uncertainty
10.8	0.593	-0.58	0.575	-0.58	-0.5820	0.0077	0.2033	1.88%
25.7	-0.04	0.028	0.022	0.023	-0.0283	0.0083	0.2181	0.85%
40.8	0.555	0.563	0.57	0.568	0.5640	0.0067	0.1764	0.43%
55.8	1.096	1.099	1.107	1.122	1.1060	0.0116	0.3071	0.55%
70.7	1.677	1.678	1.69	1.715	1.6900	0.0177	0.4667	0.66%

3.9 Solar Simulator

The purpose of the solar simulator is to provide an energy source so that the performance of a solar collector can be assessed.

If a commercial solar thermal product is certified using the EN 12975 standard, there is a criteria for determining the suitability of the solar simulator.

Table 3-10: Solar simulator requirements for the performance testing of solar thermal collectors. Source: EN 12975-2.

Requirement	Value
Mean Irradiance	>700W/m^2
Non-uniformity	±15%
Spectral Match	Approx. AM 1.5*
Thermal Irradiance	<5% of global irradiance
Collimation	Incidence angle modifier should not vary by more than 2% for 80% of the simulated radiation

*AM 1.5 is the spectrum of solar radiation that passes through the Earth's atmosphere when the air mass coefficient is 1.5.

Because PV devices are more sensitive to discrepancies in solar irradiance, such as cell mismatch, the requirements for the solar simulator are stricter. The EN 60904-9 covers the use of solar simulators in the performance of photovoltaic devices and the criteria of this standard is shown in Table 3-11.

Table 3-11: Solar simulator requirements for the performance testing of photovoltaic collectors. Source EN 60904-9.

Classification	Spectral Match	Non-uniformity of irradiance	Temporal Instability	
			Short term	Long term
A	0.75 - 1.25	2%	0.5%	2%
B	0.6 - 1.4	5%	2%	5%
C	0.4 - 2.0	10%	10%	10%

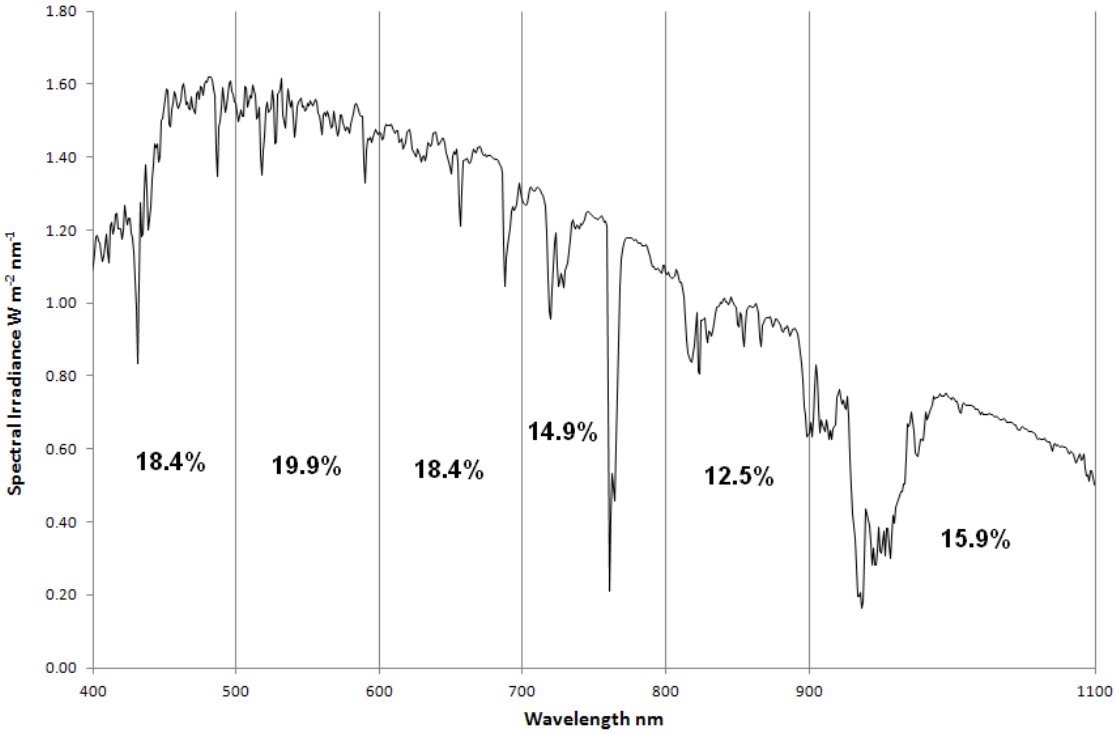

Figure 3-15: ASTM 1.5 reference spectra with percentage contributions each wavelength band. Spectrum data obtained from American Society for Testing and Materials.

3.9.1 Mean Irradiance and Non-Uniformity

A 5x4 grid measuring 85.5 x 68 cm was created as a guide to measure the irradiance from the lamps. Measurements were taken using a silicon reference cell (GBsol, UK) and a Class I pyranometer (Kipp and Zonen, The Netherlands).

Figure 3-16: Calibrated reference cell and grid for testing irradiance

Non-uniformity is calculated using (3.9) as per EN 60904-9.

$$Non-uniformity(\%) = \left[\frac{\max irradiance - \min irradiance}{\max irradiance + \min irradiance}\right] \quad (3.9)$$

Table 3-12: Distribution of irradiance measured using a calibrated silicon reference cell and a thermopile pyranometer

Silicon Reference Cell	Irradiance Reading [W/m^2]			
Pyranometer	A	B	C	D
1	1096.83	1133.61	1085.97	979.17
	1140.00	1165.00	1114.00	1156.00
2	1371.37	1495.68	1536.01	1442.94
	1489.00	1585.00	1542.00	1523.00
3	596.06	632.39	631.51	586.97
	652.00	689.00	634.00	625.00
4	1207.40	1247.51	1173.50	1015.29
	1305.00	1325.00	1275.00	1103.00
5	1182.58	1230.44	1188.79	1081.76
	1274.00	1298.00	1201.00	1135.00

	Reference Cell	Pyranometer
Mean Irradiance	1095.7	1161.5
StDev (StError)	263.4 (58.9)	300.0 (61.3)
Max Difference	40.17%	36.46%
Min Difference	46.43%	46.19%
Non-uniformity	44.70%	43.44%

Table 3-13: Distribution of irradiance when using diffuser

Silicon Reference Cell	Irradiance Reading [W/m^2]			
Pyranometer	A	B	C	D
1	716.38	803.62	811.07	726.33
	765.00	835.00	831.00	746.00
2	792.09	908.02	921.81	843.84
	860.00	970.00	982.00	890.00
3	763.16	861.69	873.90	797.29
	805.00	891.00	900.00	825.00
4	787.57	888.36	889.04	809.04
	880.00	942.00	920.00	816.00
5	737.40	819.89	820.79	741.92
	820.00	880.00	872.00	805.00

	Reference Cell	Pyranometer
Mean Irradiance	815.66	861.75
StDev (StError)	61.0 (13.7)	63.2 (12.91)
Max Difference	13.01%	13.95%
Min Difference	12.17%	13.43%
Non-uniformity	12.54%	13.66%

3.9.2 Collimation

To determine collimation, the requirement of EN 12975 states that the angles of incidence for at least 80% of the radiation from simulator must lie in the range in which the Incident Angle Modifier (IAM) of the collector varies, by no more that ±2% from its value at normal incidence.

The IAM takes into account the reduction in absorbance and transmission that occurs due to the incident radiation not being directly overhead. The IAM, $K_{\alpha\tau}$, is calculated using (3.10).

$$K_{\alpha\tau} = 1 - b_0\left(\frac{1}{\cos(\theta)} - 1\right) \tag{3.10}$$

Where b_0 is the incidence angle modifier coefficient and θ is the angle of incidence. Using the IAM, the calculation of absorbed solar radiation becomes (3.11).

$$S = G_T K_{\alpha\tau}(\alpha\tau) \tag{3.11}$$

As mentioned in the previous subsection, a diffuser was required to evenly distribute the irradiation from the lamp. The function of the diffuser is to scatter the beam radiation to create a more even distribution. In doing so, the diffuser creates multiple angles of incidence from a single source and the diffuse fraction of the total irradiance is increased.

The reported value of absorbance from the manufacturer is measured under beam radiation directly overhead. The use of the IAM is to modify the absorbance-transmission product in cases when this is not true, but this modification only applies to beam radiation at different angles of incidence. It is for this reason that the use of this simulator cannot be used to make comparisons with solar collectors tested under beam radiation. This was considered acceptable for this study as the objective is to compare the performance and distribution of temperature in different collector designs. As the conditions will be kept constant, the study will provide a relative comparison between the collectors. In future more work is required to determine the amount of diffuse in the total radiation from the simulator. The simulator could also serve a study into the effects of diffuse radiation on collector performance.

With these considerations in mind, the value of the IAM used in this study is 1 and the values of absorbtance and transmittance shown in Table 3-7 are used.

3.9.3 Thermal Irradiance

Despite the cooling from the extractor fans, the temperature of the reflectors and the diffusers increase rapidly when the lamps are switched on. This creates radiative/infrared heat exchange (thermal irradiance) between the hot surfaces and the collector. To quantify the amount of exchange that was occurring; the collector itself was used to measure incident radiation. The reason for this is because the spectral sensitivity of the calibrated silicon cell (300-1100nm) and the pyranometer (285-2800nm) are outside of the range of infrared emissions (>3000nm). By measuring the average plate temperature, it is possible to quantify the absorbed radiation, irrespective of wavelength. With knowledge of the absorbtance of the collector as well as the

transmittance of any covers, if they are used, it is possible to determine the incident global radiation.

The steady state energy gain, Q_u, of a solar collector can be calculated using (3.12).

$$Q_u = A_c\left[S - U_L\left(T_{pm} - T_a\right)\right] \tag{3.12}$$

Where A_c is the collector area, S is the absorbed solar energy, U_L is the overall heat loss coefficient, T_{pm} is the average plate temperature and T_a is the ambient temperature.

If the average reading taken from the thermocouples placed on the back of the plate is assumed to equal to the mean plate temperature (3.12) can be plotted onto a graph to determine the absorbed solar radiation, see Figure 3-17 .

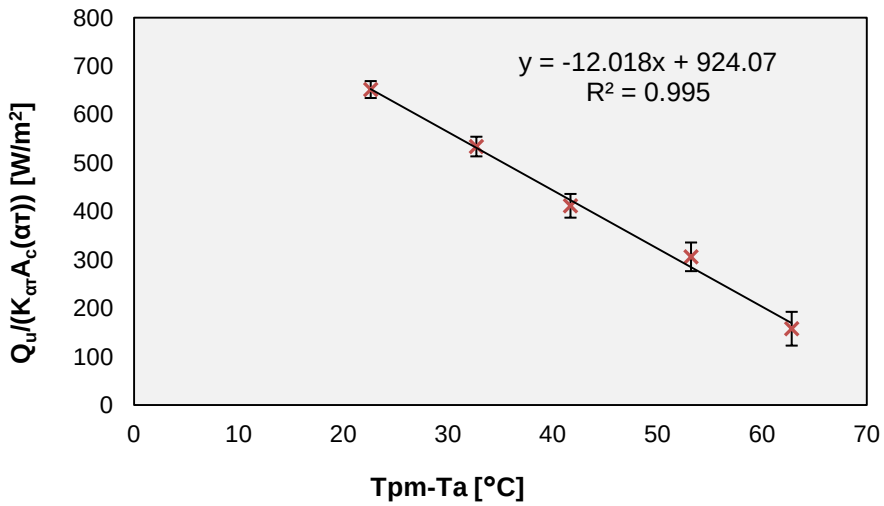

Figure 3-17: Graph to determine absorbed solar energy using uncovered

The y-intercept of Figure 3-17 occurs when the losses are zero, i.e. the plate temperature is equal to ambient temperature and no losses occur. Substituting (3.11) into (3.12) and solving for total irradiance when $(T_{pm}-T_a) = 0$ gives (3.13).

$$G_T = \frac{Q}{A_c K_{\alpha\tau}\left(\alpha\tau\right)} \tag{3.13}$$

This is the intercept of the graph and can be read from the equation of the line displayed in Figure 3-17 . In this case the value of $K_{\alpha\tau}$ is assumed to be 1 and the absorbance, α, is equal to 0.95 ± 2% as specified on the technical datasheet. In this case the irradiance has been calculated at 924W/m^2.

We are able to break down the measurements of irradiance obtained from each method based on the sensitivity of the instrument used to measure it. This is shown in Table 3-14.

Table 3-14: Summary of measurements from each irradiance method

Method	Sensitivity	Reading
Silicon Reference Cell	300-1100nm	815 ± 13.7 W/m^2
Pyranometer	285-2800nm	861 ± 12.9 W/m^2
Collector Absorbance	All absorption wavelengths	924 ± 6.74 W/m^2

EN 12975-2 states that the thermal irradiance on the collector plane should not exceed 5% of the global irradiance.

This calculation of irradiance is however susceptible to the value of absorbance that is used. For example if the collector absorbs the diffuse light less effectively than the direct light used to determine the value of absorbtance, then the value of irradiance will be underestimated. By increasing the error associated with absorbtance from ±2% as used in Figure 3-17, to ±20% the effect on the error interval is shown in Figure 3-18.

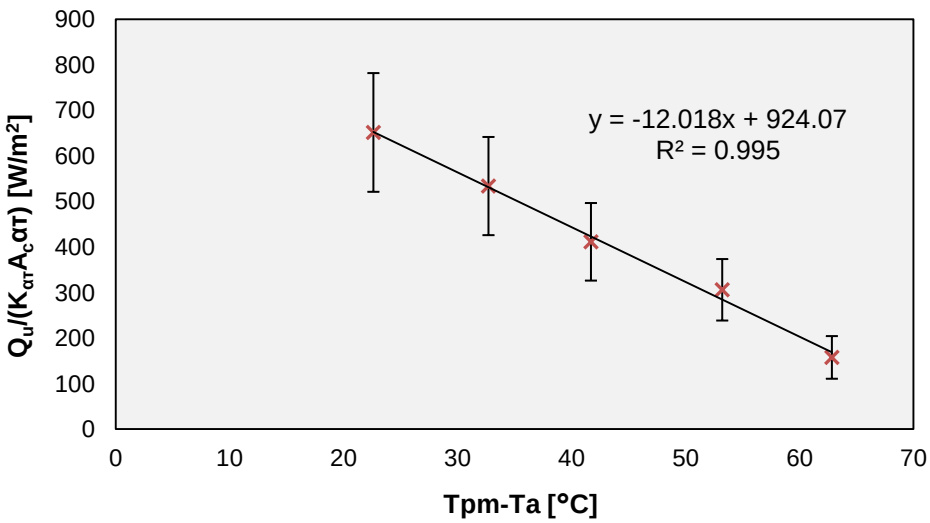

Figure 3-18: Plot to determine absorbed solar energy with ±20% absorbtance uncertainty

When Figure 3-18 is compared against Figure 3-17 it can be seen that the margin of error increases disproportionately, with higher values of error seen at lower values of T_{pm}-T_a. The reason for this is because at lower values of T_{pm}-T_a, a greater portion of the useful energy, Q_u, is dependent on the absorbed energy. At higher values of T_{pm}-T_a these losses become more dominant and the uncertainty of absorbtance becomes less influential on the overall uncertainty. The impact of uncertainty of absorbance on the final calculation of irradiance is shown in Table 3-15.

Table 3-15: Effect of the uncertainty associated with the variable absorbtance on the absolute uncertainty of G_T

Absorbtance Uncertainty (%)	2	5	10	15	20
G_T Uncertainty 924W (abs)	±6.74	±32.6	±79.0	±127	±175

3.9.4 Spectral Match

The spectral distribution of the lamps were obtained from the manufacturer; however they could only provide the spectrum from 380-800nm, see Figure 3-19.

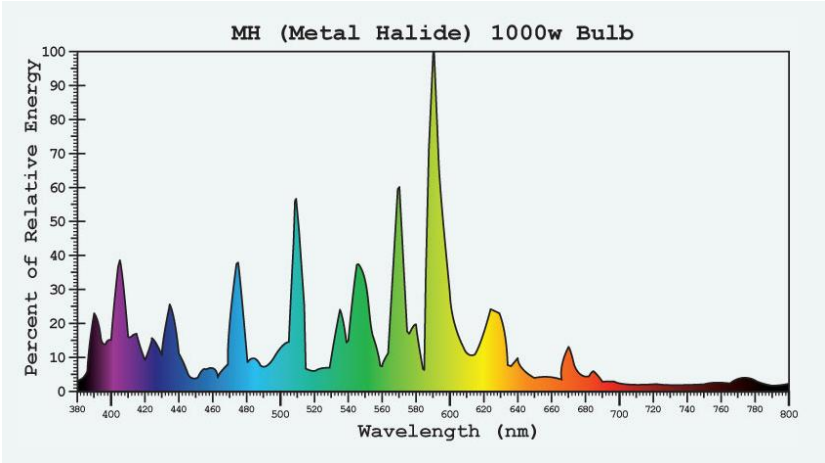

Figure 3-19: Spectral distribution of the lamp output, across the range 380-800nm as supplied by the manufacturer

By using the values in Table 3-14, it is possible to estimate the amount of irradiance in each wavelength interval using knowledge of the spectral sensitivity of each of the measurement techniques. The result is shown in Table 3-16.

Table 3-16: Determination of spectral distribution using the spectral intervals of the measurement techniques

Wavelength Band	Value
300-1100nm	815 ± 13.7 W/m^2
1100-2800nm	46 ± 26.6 W/m^2
>2800nm	64 ± 33.3 W/m^2

This indicates that there is agreement with the lamp manufacturer data shown in Figure 3-19, and it appears that the diffuser does not greatly influence the spectral output.

This result also shows that the thermal irradiance (>2800) is calculated at approximately 7% of the global irradiance.

3.9.5 Temporal Instability

Temporal instability is a measure of variation in irradiance over time. To determine this, measurements were taken using the silicon reference cell, once every 5 min, for 60 min. The results are shown in Figure 3-20.

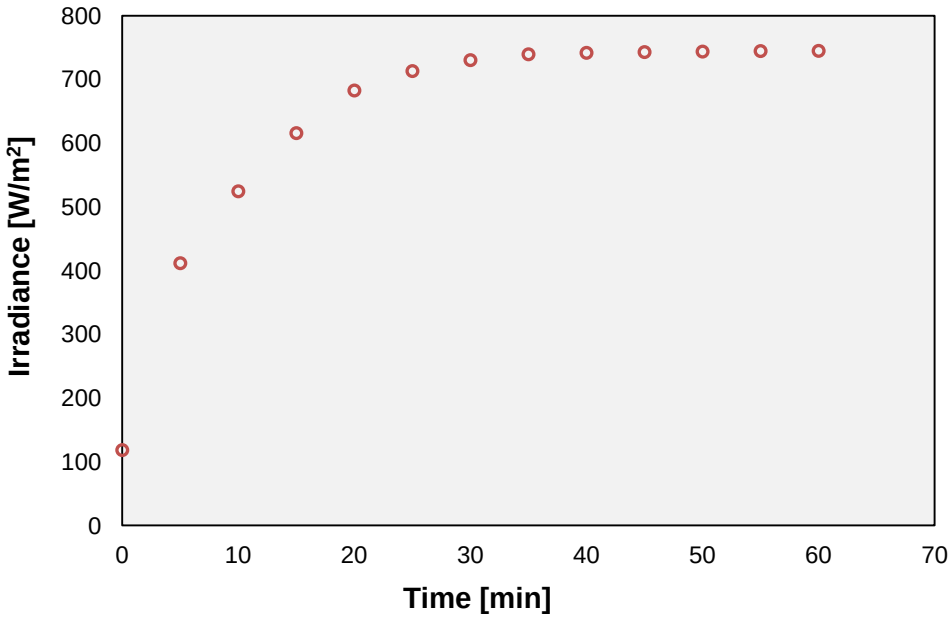

Figure 3-20: Irradiance measurements as a function of time

Metal halides have a warm up period before they reach full output. This process can be seen in Figure 3-20 from 0-30min, after which the irradiance begins to level out. The temporal instability between 30 and 60 min was calculated as per the requirements of EN 60904-9 see (3.14).

$$Temporal\ instability(\%) = \left[\frac{\max irradiance - \min irradiance}{\max irradiance + \min irradiance}\right] \tag{3.14}$$

Using this methodology the temporal instability after 30 min was measured at 0.37%. For this reason, all experiments were conducted after the lamps were preheated for 30min.

3.10 Repeatability

Thermal efficiency curves were obtained for the same collector, under the same conditions to determine the repeatability of the method. To investigate whether repeatability was influenced by the presence of a cover, tests were performed with and without it. The results of the repeatability testing are presented in Figure 3-21/Table 3-17 and Figure 3-22/Table 3-18 for uncovered and covered respectively.

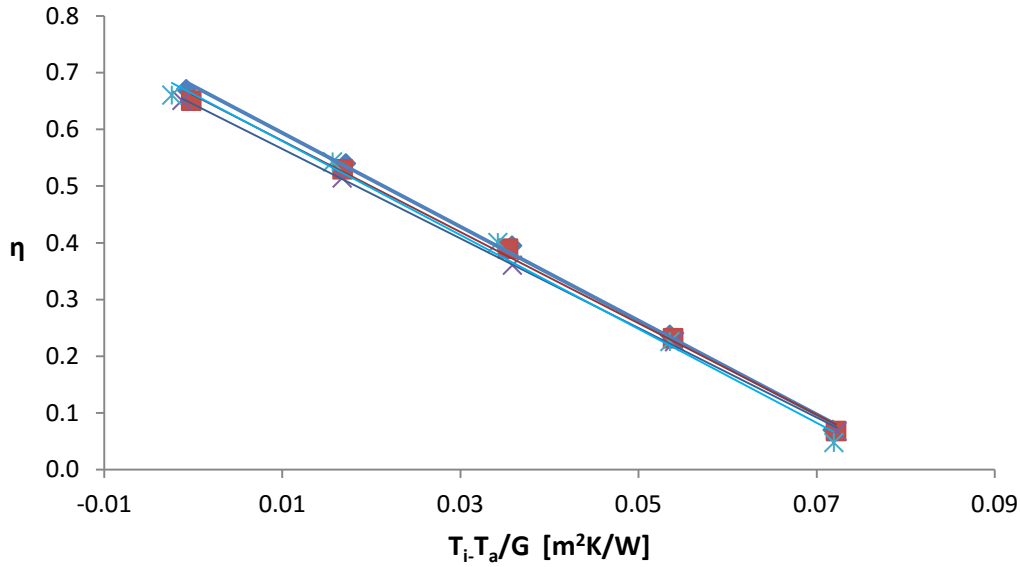

Figure 3-21: Repeatability testing with no cover

Table 3-17: Results of repeatability testing without cover with calculation of experimental uncertainty

Repeat		Without	
		F_RU_L	$F_R(\alpha\tau)$
	1	8.0482	0.6606
	2	8.2766	0.6619
	3	8.2802	0.6768
	4	7.8937	0.6445
Mean		8.150	0.661
StDev		0.132	0.0090
% Uncertainty (±)		0.84	0.70

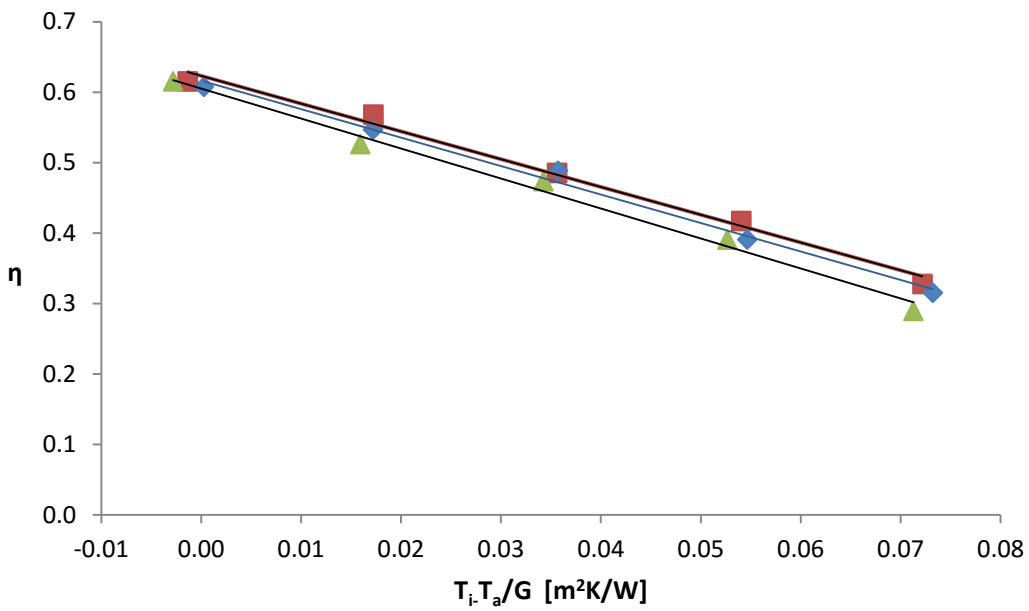

Figure 3-22: Repeatability testing with cover

Table 3-18: Results of repeatability testing with cover with calculation of experimental uncertainty

Repeat	With Cover	
	F_RU_L[W/m^{2}C]	$F_R(\alpha\tau)$
1	3.9468	0.6232
2	4.26	0.6052
3	4.0448	0.6164
Mean	4.083	0.615
StDev	0.1602	0.00909
% Uncertainty (±)	1.96	0.74

The average calculated experimental uncertainty shown in Table 3-17 and Table 3-18 is taken into account on any results that include calculations from thermal efficiency measurements (in addition to the equipment error calculated in the previous section).

3.11 Results

In this section two types of results are compared, the thermal performance and the temperature distribution across the surface. In all cases the parameters listed in Table 3-7 were used.

3.11.1 Header Riser vs. Serpentine

3.11.1.1 Thermal Efficiency Curve

Figure 3-23 compares the thermal efficiency curve obtained for the header riser and the serpentine collector.

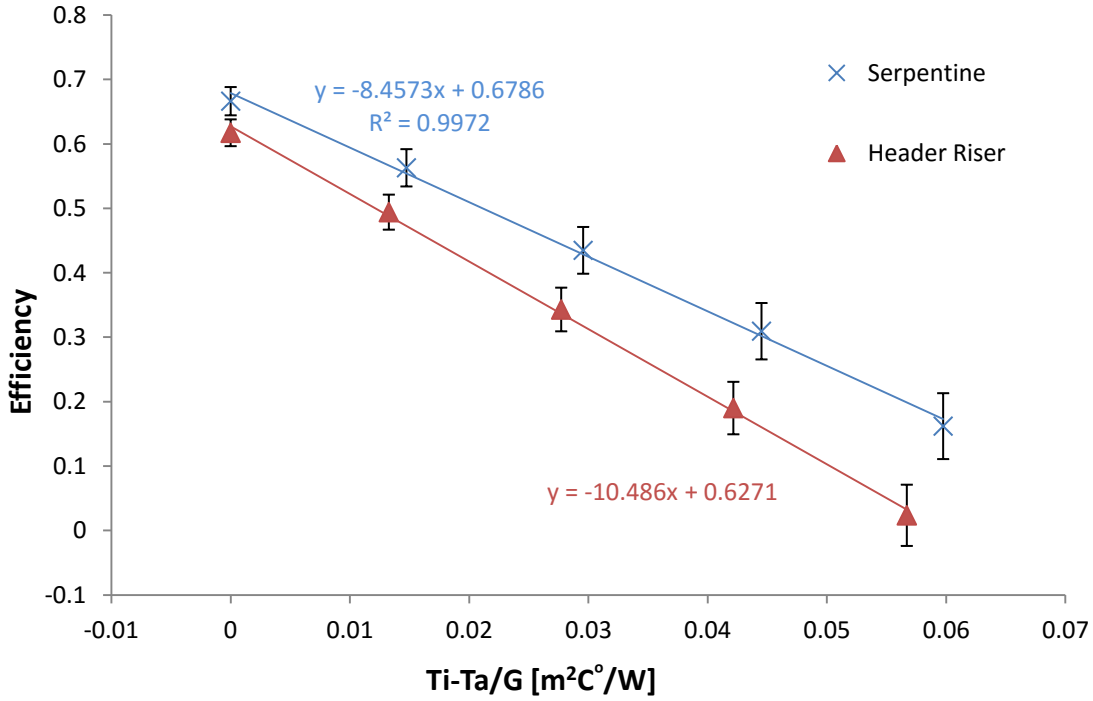

Figure 3-23: Comparison of thermal efficiency curves for the uncovered header riser and serpentine collector

The lines in Figure 3-23 represents the equation shown in (3.15).

$$\eta_i = F_R(\alpha\tau) - \frac{F_R U_L (T_i - T_a)}{G} \tag{3.15}$$

Where U_L is the overall loss coefficient, F_R is the dimensionless ratio of actual energy gain to the theoretical maximum gain if the entire collector was at inlet temperature, G is irradiance, T_i is inlet temperature, T_a is ambient, $\alpha\tau$ is absorbtance and transmittance of the collector respectively. U_L and F_R can be extracted from the equation of the lines shown in Figure 3-23 and the values are shown in Table 3-19.

Table 3-19: Parameters extracted from the thermal efficiency curve

Parameter	Serpentine (abs)	Header Riser (abs)
Zero Loss Efficiency ($FR\alpha\tau$)	67.86 (± 2.19)%	62.71 (± 2.08)%
$U_L F_R$ [W/m^2°C]	8.4573 ± 0.071	10.486 ± 0.08
F_R	0.71 ± 0.037	0.66 ± 0.035
U_L [W/m^2°C]	11.84 ± 0.60	15.89 ± 0.84

An observation common to both designs was the low value of zero loss efficiency compared with other studies. In this study the zero loss efficiency for an unglazed collector was <0.70 however in previous studies it is reported to be >0.80 [62] and sometimes even greater than >0.90 [43]. To identify the causes of the discrepancy it is necessary to examine the equation for collector efficiency and heat removal factor that are detailed in Section 4.3. These equations show that the collector efficiency is inversely proportional to heat transfer resistances in the tube-plate bond and in the fluid flowing through the tubes. In terms of riser-plate resistances confidence must be had in the integrity of the metal bond that connects the pipes to the back of the collector. In this study the fins were comprised of copper pipes laser welded to the back of an aluminium collector. A known issue with these collectors is that separation can occur at the interface, leading to poor thermal contact [104]. This would contribute to the low values of zero loss efficiency. Internal heat transfer resistances in the riser pipes can also have the same effect. In this study care was taken to ensure the system was purged of air bubbles before experimental measurements were taken; however the collector was tested horizontally and it is possible that there were still air bubbles present in the system during the experiment. These air bubbles are thermally insulating and would create resistance to heat transfer inside the tubes. In the horizontal position, these bubbles would form at the top of the pipe which is in contact with the plate, so the effect on zero loss efficiency could be dramatic. Future tests should fully purge the collectors at a tilted angle to ensure that no air remains in the system. It may be more difficult to clear the serpentine collector of air bubbles due to the 180 degree bends and absence of header pipes. Another factor that could lead to poor values of zero loss efficiency is flow rate. The mass flow rate in this collector was calculated using the recommendation of EN12975 (0.04kg/s/m^2) however these fins are often incorporated into much larger collectors >2m^2, which are several times larger than the collectors used in this study. At a higher mass flow rate, the increased internal heat transfer would increase the zero loss efficiency.

The comparison of each design shows the rate of heat loss from the header riser design is greater than that from the serpentine collector. They start with quite similar values for zero loss efficiency, but as the temperature difference between the inlet and the outlet increases, the performance between the two collectors begins to diverge. The reason for this is because the flow is split between multiple pipes in the header riser collector. As a consequence, the header riser design is a better at cooling the fluid than the serpentine collector; if the operation of the solar panel was to be reversed then it would provide a more efficient means of dissipating heat into the environment. It can also be seen from Figure 3-23 that the efficiency of the header riser design would exceed that of the serpentine collector at a point below T_i-T_a/G = 0. In these

conditions the heat transfer would be occurring from the ambient into the collector and, again as a result of the increased surface area, the header riser collector would perform better in this situation.

3.11.1.2 Average Plate Temperature

Figure 3-24 shows a plot of the mean plate temperature against inlet temperature. Despite having different U_L this indicates that the majority of the heat loss from the fluid is not occurring from the plate, but from the pipes. This is in agreement with the results from the thermal efficiency curve.

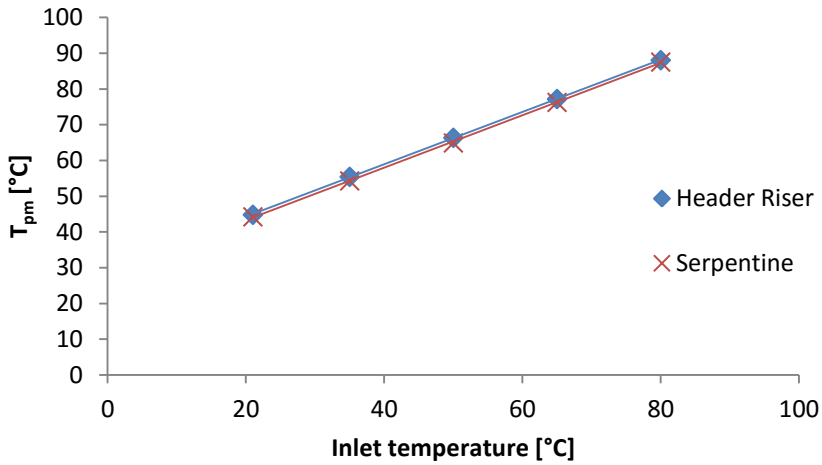

Figure 3-24: Comparison of average plate temperature for uncovered header riser and serpentine collector

3.11.1.3 Surface Temperature Distribution

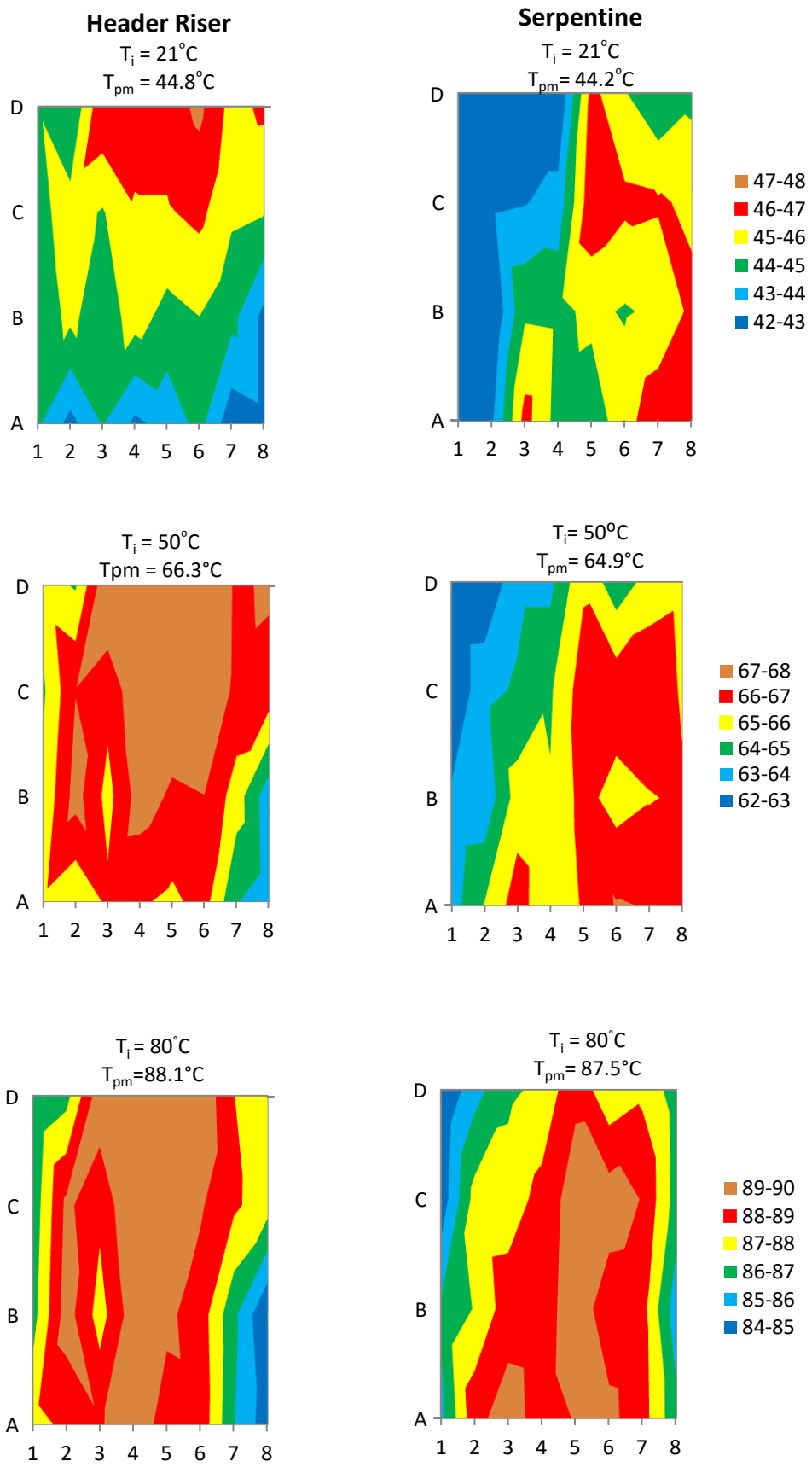

Figure 3-25: Temperature distribution for header riser (left) and serpentine designs (right). Inlet for all designs is located between A1 and A2 and the outlet is between D7 and D8 at 987W/m^2

The temperature distribution across the plate of the header riser and serpentine collector (as recorded by the thermocouples shown in Figure 3-12) at different inlet temperatures is shown in Figure 3-25.

For the header riser design the coldest area on the plate is always located at the bottom right (A7-A8); this is the location of the parallel pipe, furthest from the inlet and closest to the outlet. The pressure drop on this pipe will be greatest and therefore the flow through this pipe will also be the greatest, explaining why this area is colder. On the other side of the header riser, column A1-D1, there is also a cold area on the edge of the collector. This is unexpected as the flow is likely to be lowest in this pipe. This could be explained by the irradiance distribution shown in Table 3-13. From this it can be seen that there is a drop in irradiance at the edges of around 10-13%. Considering that the variation of temperature across the plate only varies by around 6% this could be caused by this deficit in irradiance. The general pattern of temperature seen in the header riser design is a temperature profile that increases along the length of the collector, from A to D.

In the serpentine collector, a temperature profile is seen across the width of the collector, increasing from 1 to 8. The temperature profile follows the pattern of the pipes, with the pipe joining just after the inlet between A1 and A2, leaving for the first bend at D1 and D2 and then rejoining the collector between D3 and D4. At the inlet temperature of 80°C a cold strip is seen along fin 8. The reason for this could be a result of lower irradiance at the edges. This is less of a problem at lower temperatures, but as the temperature increases, more thermal energy is lost, resulting in a larger difference in temperature in these regions.

3.11.2 Covered and Uncovered

This section details the comparison of the serpentine absorber with and without the use of a poly carbonate covering.

3.11.2.1 Thermal Efficiency Curve

No information was supplied by the manufacturer regarding the transmittance of the polycarbonate covering. The value of transmittance was instead determined by recording the output of the pyranometer with and without the covering. An area was chosen in the middle of the testing area to carry out this test. A reading of 913W/m^2 and 776W/m^2 was recorded with and without the cover respectively giving a transmittance value of 0.85 ± 2.5%; where the error is that quoted by the manufacturer of the pyranometer. The thermal efficiency curves are shown in Figure 3-26.

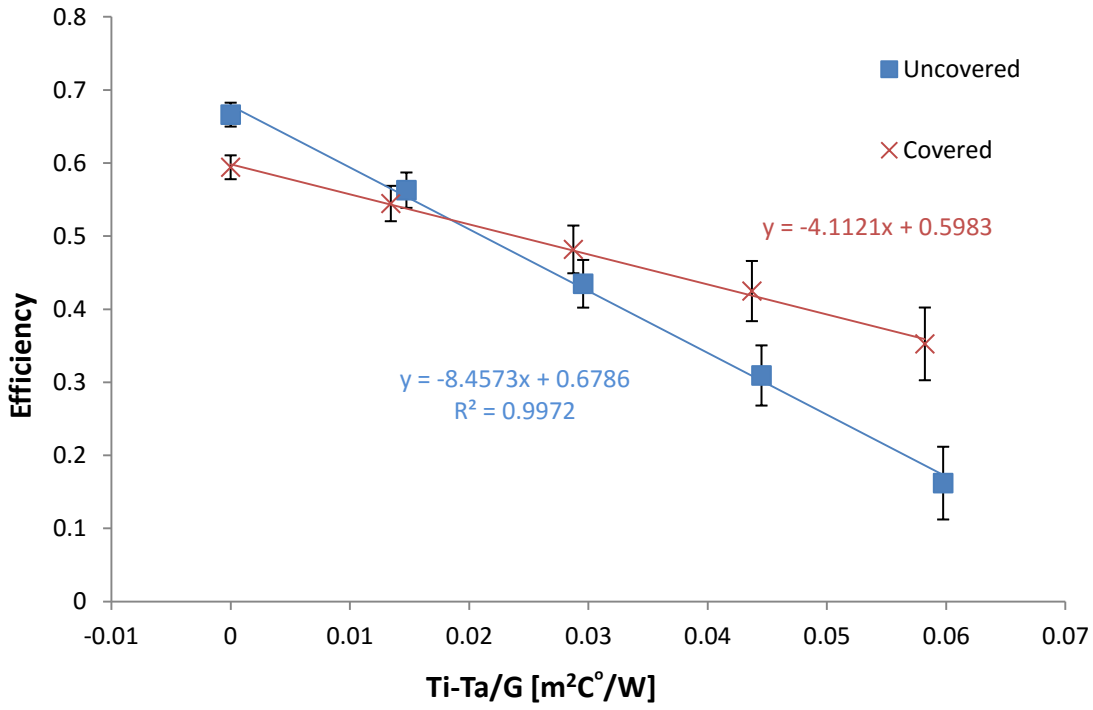

Figure 3-26: Comparison of thermal efficiency curves for uncovered and covered collectors

Figure 3-23 shows that the uncovered collector has a higher zero loss efficiency (T_i-T_a/G = 0) than the covered collector before being overtaken by the covered collector at around T_i-T_a/G = 0.02. The reduced zero loss efficiency of the uncovered collector is a result of reflection and transmission losses (optical losses) that occur as light passes through the cover. The use of a cover insulates the collector and as a result the top loss coefficient is reduced. This effect can be seen in the reduction of U_L in Table 3-20.

Table 3-20: Comparison of parameter for the covered and uncovered collector

Parameter	Uncovered (abs)	Covered (abs)
Zero Loss Efficiency ($FR\alpha\tau$)	67.86 (± 2.19)%	59.83 (±1.16)%
$U_L F_R$ [W/m^2°C]	8.4573 ± 0.071	4.1112 ± 0.08
F_R	0.71 ± 0.037	0.74 ± 0.06
U_L [W/m^2°C]	11.84 ± 0.60	5.55 ± 0.32

3.11.2.2 Average Plate Temperature

The case of covered and uncovered is compared in Figure 3-27. The graph shows that the mean plate temperature follows the same trend shown in the plot of thermal efficiency. The temperature inside the collector begins to rise more rapidly due to the insulating effect of the cover.

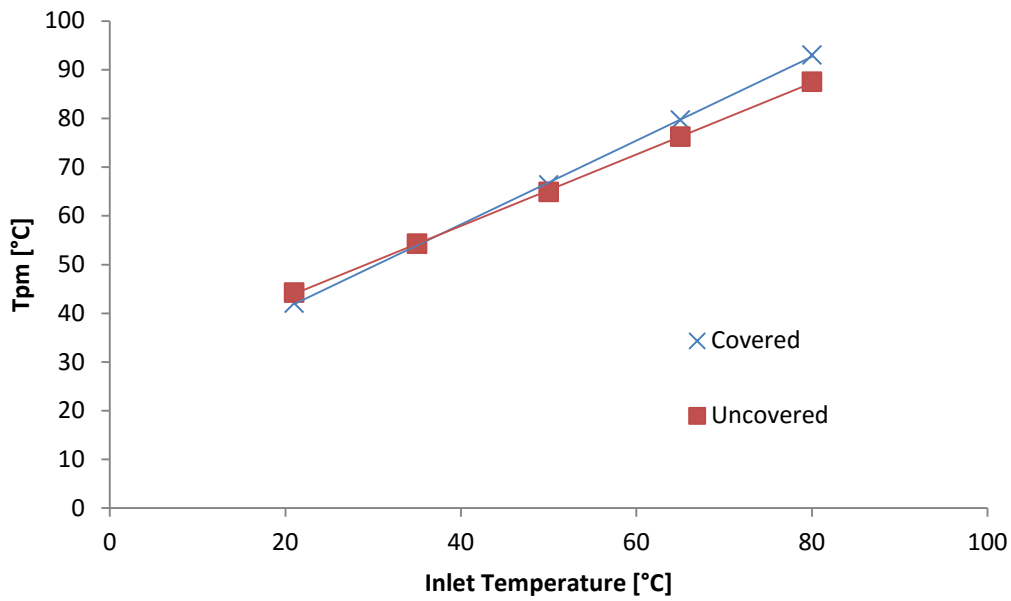

Figure 3-27: Mean plate temperature against inlet temperature for covered and uncovered collector. Irradiance 987W/m^2

3.11.2.3 Temperature Distribution

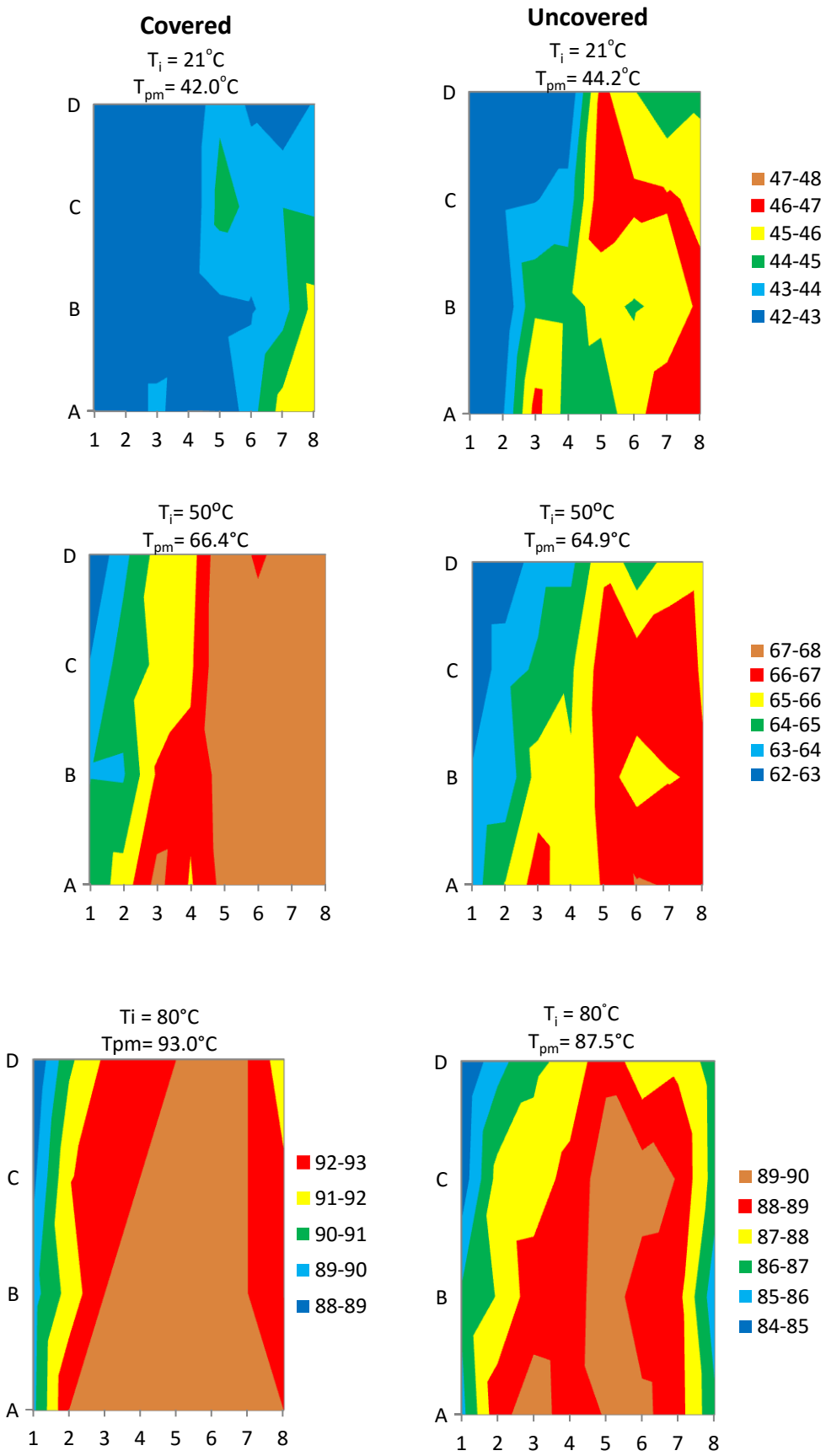

Figure 3-28: Comparison of the absorber temperature for covered (left) and uncovered (right)

Figure 3-28 shows the comparison in the average surface temperature for the covered and uncovered case of a serpentine collector. The results are in agreement with the thermal efficiency curve. At the 21°C inlet temperature the covered plate is cooler than the uncovered plate; this is because transmission and reflection are reducing the amount of irradiation incident to the collector. At an inlet temperature of around 35 °C, the temperature inside the covered collector becomes saturated and as a result the temperature distribution across the absorber plate becomes more uniform and localised hot and cold spots present in the uncovered collector disappear. This results in considerably higher average plate temperatures in the covered collector.

3.11.3 Electricity Generation

In this section, the first case involves determination of the thermal efficiency under open circuit conditions; and the second case involves connecting the PV laminates in series with a resistive load. The IV response of the PV laminates was measured using a Keithley 2601B Sourcemeter (Keithley, US) to identify the maximum power point conditions at varying inlet temperatures. Once this was determined a suitable resistor was chosen and the current through the circuit was measured at each steady state condition. Combined with the results from the thermal efficiency curve, it was possible to calculate the combined electrical and thermal output from the system.

3.11.3.1 Current Voltage Curve at Varying Inlet Temperature

Figure 3-29 shows the layout of the laminates on the surface of the absorber. The thermal contact was achieved solely by clamps placed at either end of each laminate; because the fins of the absorber are not flat, this meant that good contact was not achieved along the length of each laminate.

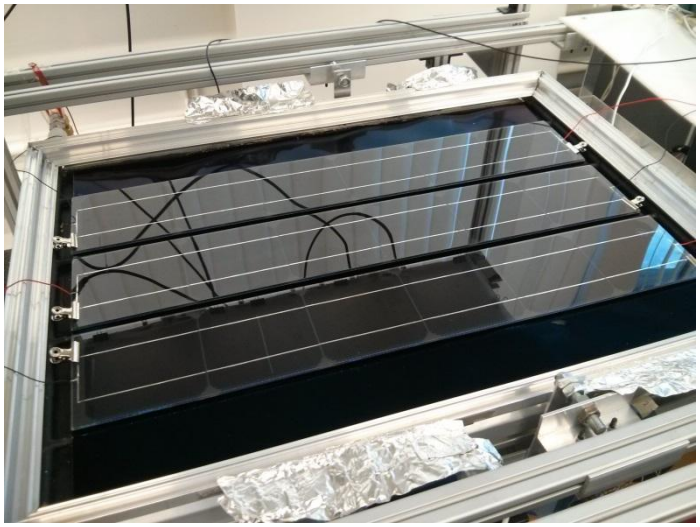

Figure 3-29: PV laminates connected in series and clamped to the surface of the absorber

The IV response of one of the laminate strips, shown in Figure 3-29, was measured using the Keithley source meter. Assuming that the IV characteristics are identical for all three laminates,

the total power output for the series connected system was obtained by multiplying each voltage reading by 3. The resulting IV curve at different inlet temperatures is shown in Figure 3-30.

The IV plot shows that as inlet temperature increases the voltage begins to reduce. This reduction in voltage reduces the maximum power that is possible from the PV system. This is more easily seen when power, the product of I and V, is plotted against voltage, see Figure 3-31. From this it is easy to see that the maximum possible power is highest when the inlet temperature is at 21°C and lowest when the inlet temperature is 80°C. To achieve a given power, a resistance must be connected to the circuit. The optimum resistance is dependent on the current and voltage output. Figure 3-32 shows the plot of resistance vs. power and using this graph it is possible to identify the optimum resistance for each inlet temperature. The optimum resistance for each inlet temperature varies from 1.86Ω at 21°C inlet to 2.26Ω at 80°C inlet. Based on these values the system was connected to a 2Ω resistor for all inlet temperatures.

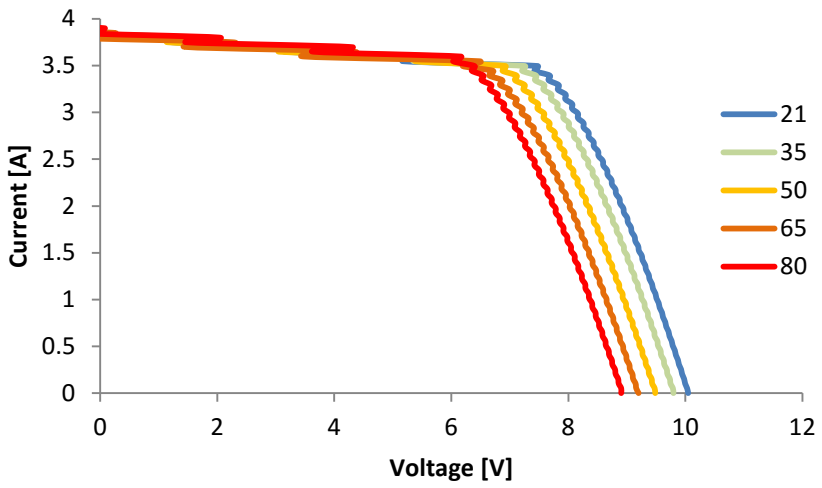

Figure 3-30: IV curve from series connected PV laminates at varying inlet temperature

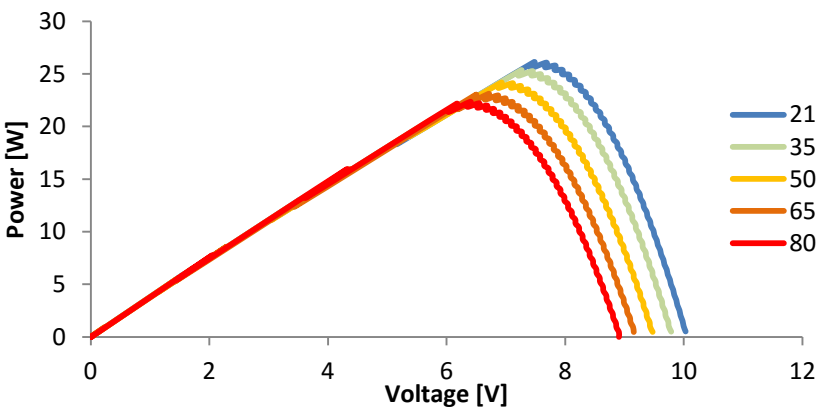

Figure 3-31: Power voltage plot at different inlet temperatures

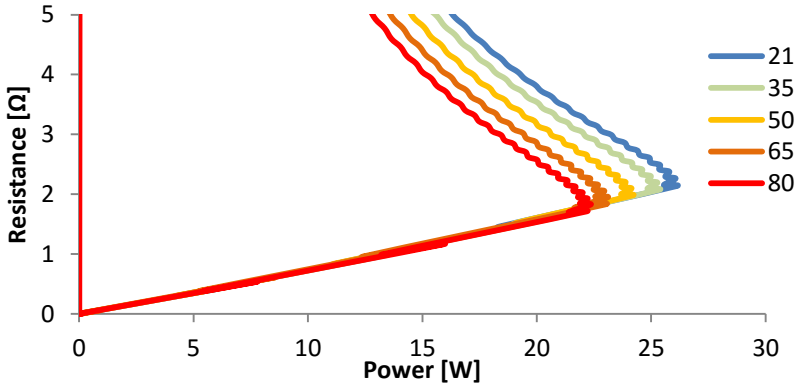

Figure 3-32: Resistance vs. power plot for different inlet temperatures

3.11.3.2 Electricity Generation

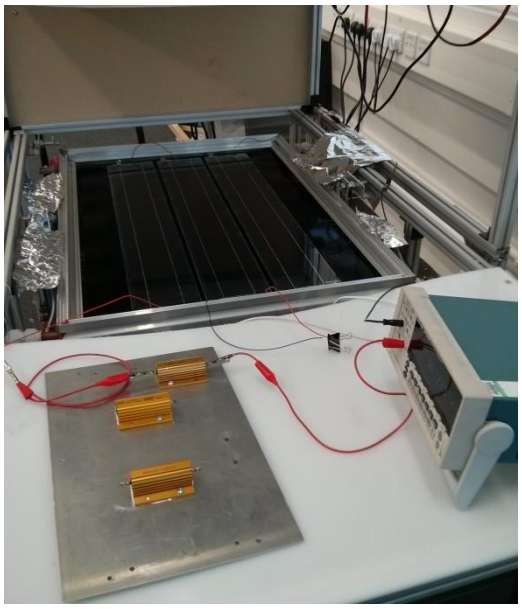

Figure 3-33: Measuring the current output of the PVT collector

During operation, the temperature of the resistor began to rise. The temperature of the resistor was measured using a handheld infrared temperature sensor. The temperature was found to increase from 40°C at the first inlet temperature to 80°C at the final inlet temperature. The temperature of the resistor is not influenced by inlet temperature but by the electrical output of the PV system. This is important as resistance is dependent on temperature; with temperature, resistance increases. Based on a reference temperature and resistance the effect of temperature on resistance can be calculated using(3.16).

$$R = R_0[1+\alpha(T-T_0)] \tag{3.16}$$

Where, R_0 is the reference resistance at the reference temperature T_0. The temperature coefficient of resistance, α, is dependent on the material of the resistor. For copper this value is $3.9\text{x}10^{-3}$Ω/°C [105].

This is important because when using a fixed value resistor, its resistance will change with its temperature. This means that a less than optimal value of resistance could be connected to the system, resulting in reduced power output.

This poses an additional problem of inaccurate readings when the value of resistance is used to calculate the output of the system. In this case the electrical power output was calculated using:

$$P = I^2 R \tag{3.17}$$

Where *P* is power, *I* is current and *R* is resistance.

The influence of using the fixed resistance value vs. the temperature adjusted value is shown in Figure 3-34.

Table 3-21: Measured current values at different inlet set points. The power is adjusted to reflect the temperature dependence of resistance.

Inlet [°C]	Current [A] (measured)	Resistor Temperature [°C] (approx.)	Adjusted Resistance [Ω]	Power [W]	Adjusted Power [W]
21	3.2274	40	2.152	20.8	22.4
35	3.172	50	2.228	20.1	22.4
50	3.1106	60	2.304	19.4	22.3
65	3.0435	80	2.456	18.5	22.7
80	2.9637	80	2.456	17.6	21.6

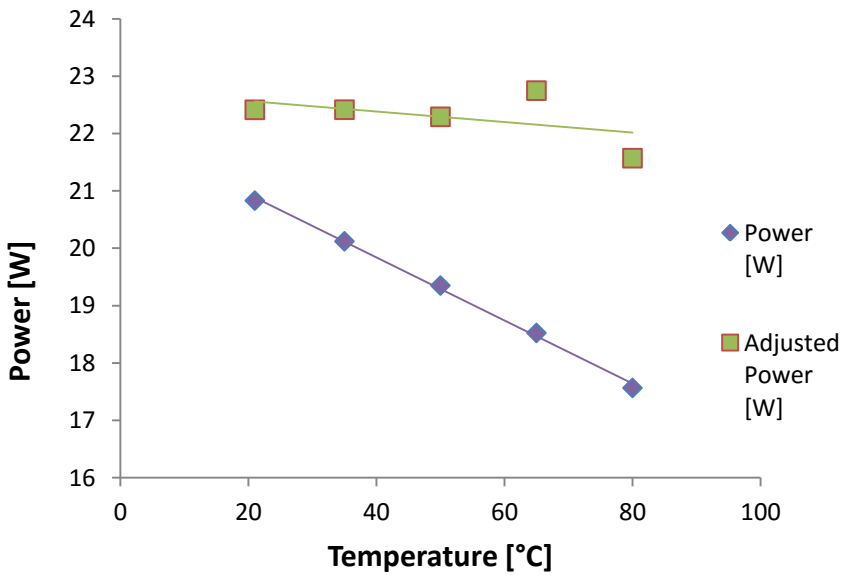

Figure 3-34: Power calculated using fixed resistance and adjusted power using temperature dependent value of resistance

Unless the precise value of resistance is known, there will be inaccuracies in the calculated power output. An alternative approach would be to measure voltage and current simultaneously to determine the power output of the system. Better still, a maximum power point tracking

system could be developed that automatically adjusts the connected resistance to match the maximum operating point of the collector. By using this approach the collector would always be operating at the optimum conditions.

3.11.3.3 Thermal Efficiency Curve

Figure 3-35 shows the thermal efficiency curves obtained for the case of electricity and no electricity generation for a PVT collector. The backing of the laminates used in this study was Tedlar and the absorber was the serpentine design.

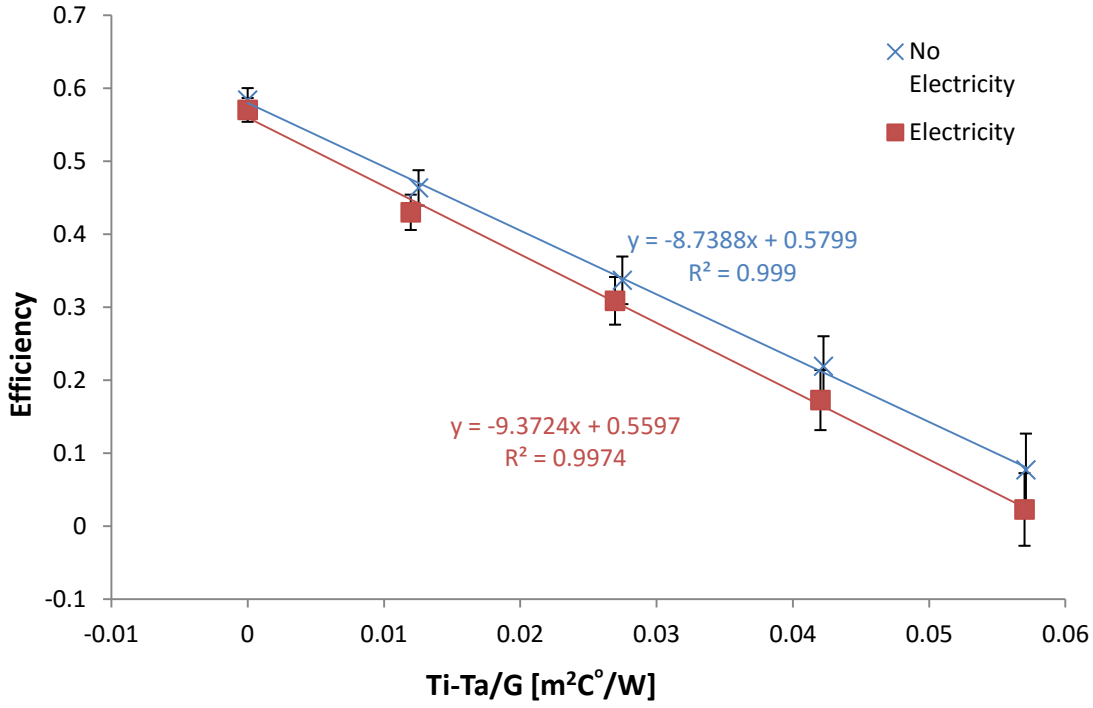

Figure 3-35: Thermal efficiency curve for PVT collector with and without electricity generation with the serpentine collector

The graph shows that the placing of the laminates onto the surface of the absorber reduces the zero loss efficiency from 67.82% (see Table 3-20) to 57.97%, a 14.5% reduction. This occurs because a large portion is obstructed from the light source.

The graph also shows that when electricity is being generated by the panels, the thermal efficiency is reduced. This is because the incident radiation is being used to generate electricity before reaching the absorber. However it is unexpected that the curves diverge as *Ti-Ta/G* increases. A more rational result would be convergent curves because as the efficiency of the PV modules reduces with increasing temperature, more energy would be available for thermal collection.

The uncertainty associated with the resistance could explain this finding. As shown in the previous section, resistance is dependent on temperature. If a suboptimal value of resistance is used, the power output of the system will be compromised. If a change in temperature brought the resistance closer to the maximum power point then there would be an increase in electrical performance resulting in the divergent curves shown in Figure 3-35.

Table 3-22: Parameters extracted from thermal efficiency curves for cases of electricity and no electricity

Parameter	No Electricity (abs)	Electricity (abs)
Zero Loss Efficiency ($FR\alpha\tau$)	57.97 (± 1.94)%	55.97 (±2.05)%
$U_L F_R$ [W/m^2°C]	8.7388 ± 0.090	9.3724 ± 0.079
F_R	0.61 ± 0.038	0.59 ± 0.033
U_L [W/m^2°C]	14.31 ± 1.02	15.91 ± 1.034

3.11.3.4 Combined Output

The combined output of the PVT system can be determined by taking the results from the thermal efficiency curve and the current readings from the ammeter. The irradiance of the test was measured at 993W/m^2 and the electrical, thermal and overall performance is summarised in Table 3-23.

Table 3-23: Combined output of the PVT system

Inlet [°C]	Thermal Power [W]	Thermal Efficiency [%]	Electrical Power [W]	Combined Power [W]	Electrical Efficiency [%]	Electrical Ratio	Combined Efficiency
21	253.5	57.1	22.4	275.9	8.026	0.09	0.621
35	191.2	43.0	22.4	213.6	8.027	0.12	0.481
50	137.3	30.9	22.3	159.6	7.982	0.16	0.359
65	76.8	17.3	22.7	99.6	8.146	0.30	0.224
80	10.2	2.3	21.6	31.8	7.724	2.11	0.072

The results show that the combined efficiency is severely affected by the inlet temperature to the collector. The electrical efficiency only makes up 9% of the overall efficiency at the steady state inlet temperature of 21°C.

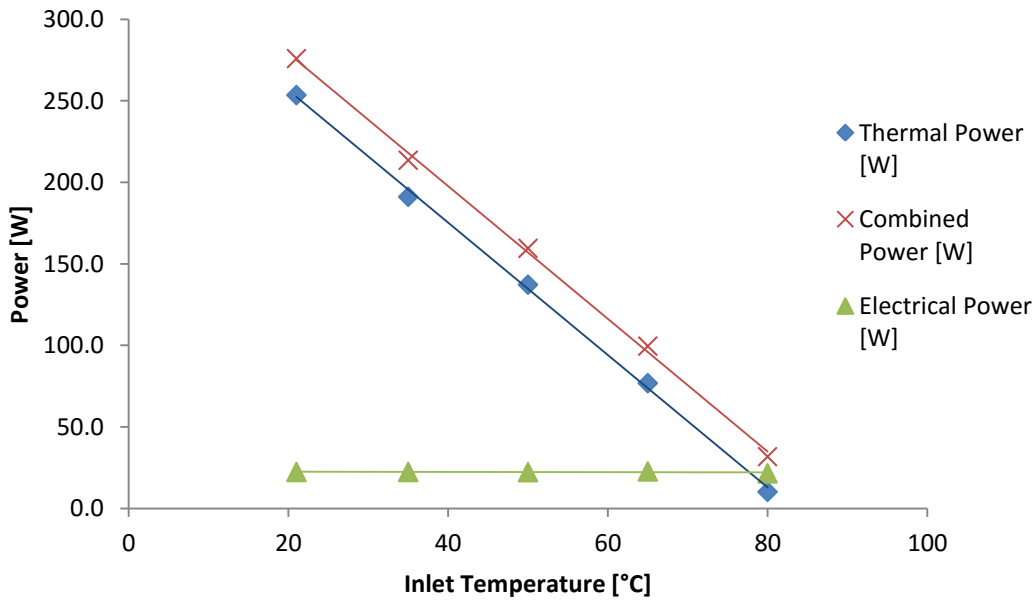

Figure 3-36: Breakdown of power output from the PVT collector

Figure 3-36 shows that the electrical generation is more consistent than thermal generation and becomes the dominant form of generation just before the steady state inlet temperature of 80°C. The low thermal efficiency of the parallel collector is in close agreement with the results shown in Figure 3-23.

The comparison of having the absorber completely uncovered, covered with the polycarbonate sheet and uncovered with PV laminates clamped to the surface is shown in Table 3-24. From this comparison it can be seen that the use of PV laminates does not reduce the zero loss efficiency much more than using the cover; however there is a drop in heat removal factor and a rise in overall heat loss coefficient. The increased heat loss coefficient could be a result of disruption to the low emissivity coating of the absorber.

It can also be seen that the performance of an uncovered serpentine collector with PV laminates on the surface has an overall heat loss coefficient (-14.31W/m^2°C) similar to that of the uncovered header riser collector (-15.89W/m^2°C).

Table 3-24: Comparison of 3 cases for serpentine collector; uncovered, covered with a polycarbonate sheet uncovered with PV laminates clamped onto the surface

Parameter	Uncovered (abs)	Covered (abs)	Laminate (abs)
Zero Loss Efficiency ($FR\alpha\tau$)	67.86 (± 2.19)%	59.83 (±1.16)%	57.97 (± 1.94)%
$U_L F_R$ [W/m^2°C]	8.4573 ± 0.071	4.1112 ± 0.08	8.7388 ± 0.090
F_R	0.71 ± 0.037	0.74 ± 0.06	0.61 ± 0.038
U_L [W/m^2°C]	11.84 ± 0.60	5.55 ± 0.32	14.31 ± 1.02

3.11.3.5 Average Plate Temperature

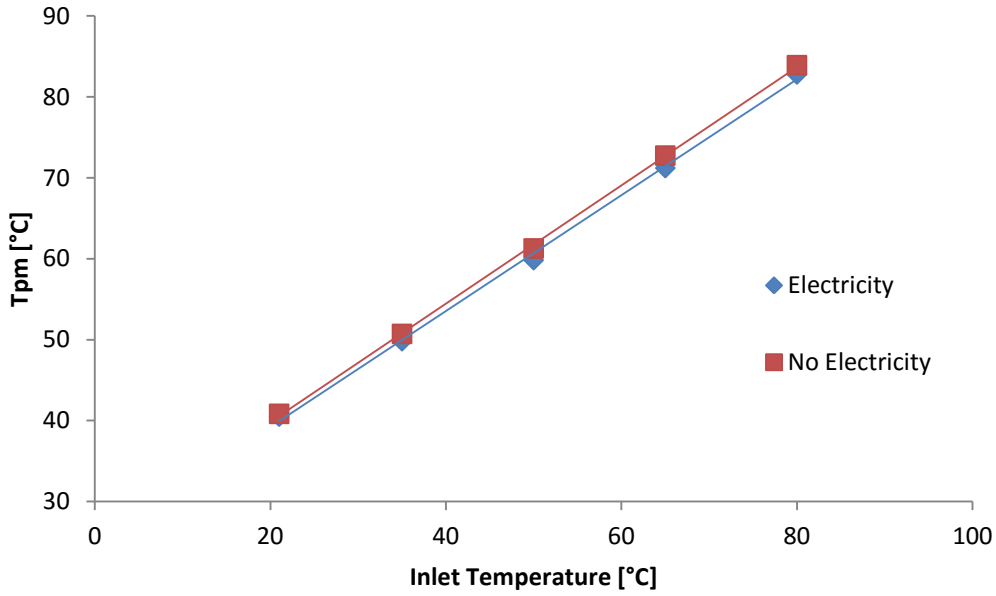

Figure 3-37: Average plate temperature for the cases with and without electricity generation for header riser

In agreement with the thermal efficiency curve, Figure 3-37 shows that the average plate temperature for the case with electricity has a lower average temperature. Again this is a result of incident radiation being converted into electricity instead of heat.

3.11.3.6 Temperature Distribution

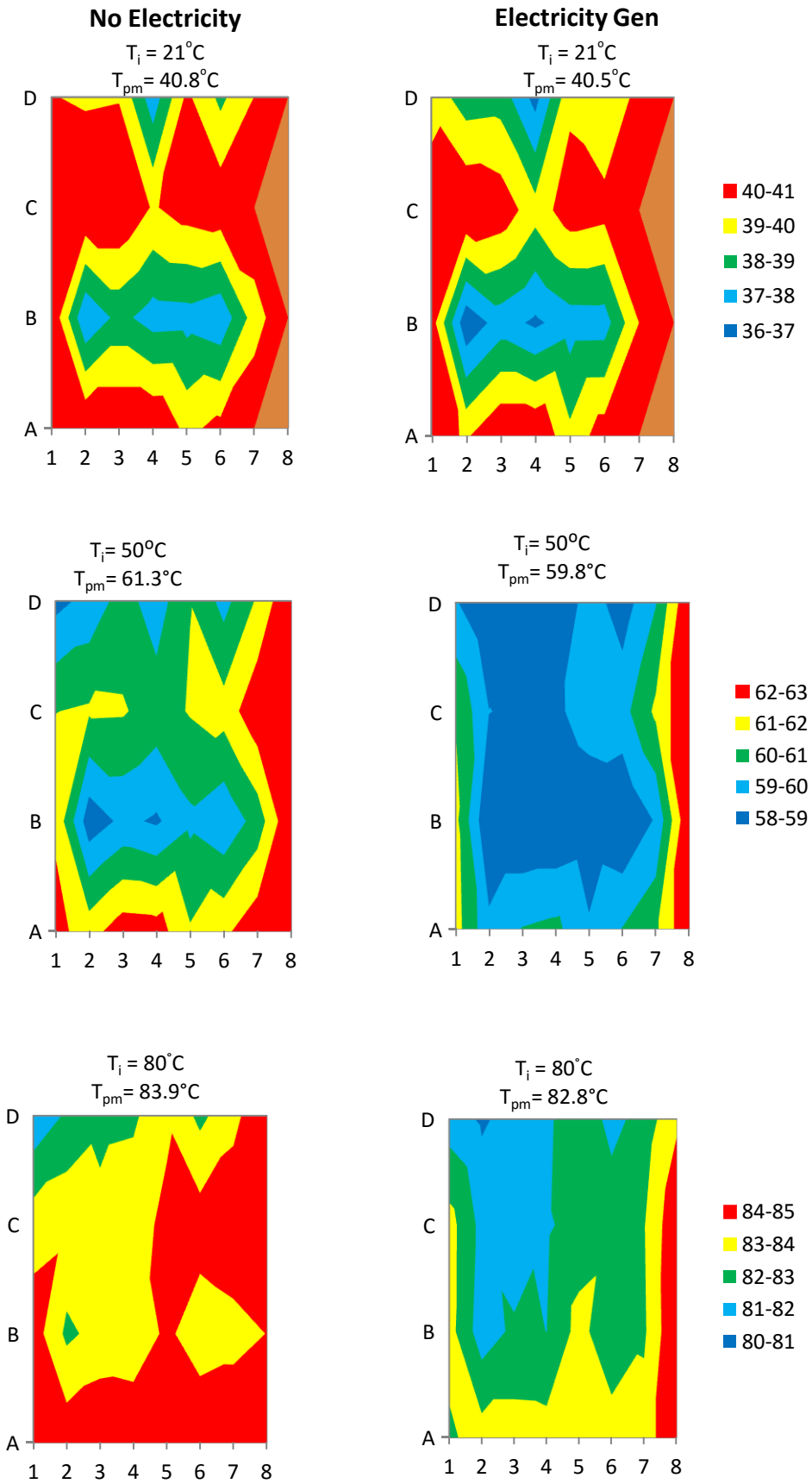

Figure 3-38: Temperature profiles for cases without (left) and with electricity generation (right). The inlet is located between A1 and A2 and outlet between D7 and D8 for all designs.

Figure 3-38 shows that there is some disruption caused to the surface temperature when PV laminates are place onto the surface, see Figure 3-28 for the uncovered case. In both cases laminates were present on each absorber from columns 2 – 7. The fins represented by nodes 1 and 8 were not covered by the PV laminate.

The cold spot in row B, that is present in both cases, indicates poor thermal contact between the laminate and the absorber. This is expected as consistent contact could not be achieved along the entire length of the laminate. It is thought that this could be improved if a flat absorber was used. The hot areas at the edges of the collector are consistent with the fact that no laminates were covering these areas. This means that they were exposed to irradiance and were able to heat up. The other hot areas such as those in C3 and C6 indicate that there was good thermal contact between the laminate and the absorber in these areas.

When comparing the cases together it is evident that the average temperature of the electricity generation case is less than that of the non-electricity case. It is also possible to see that the reduction in temperature in these cases occurs in the area that is covered by the PV laminate; thus adding support to the explanation that the PV cells are converting radiation, that would otherwise be used to generate heat, into electricity.

3.11.4 Tedlar vs. Glass as Backing Materials

To investigate the use of different backing materials used by the PV laminates, two different cases are compared; glass backed PV laminates and Tedlar backed PV laminates. Apart from a difference in the thermal conductivities in the material, the glass laminates are transparent in areas not containing the PV cell; thus allowing for irradiance to pass through to the absorber surface.

3.11.4.1 Thermal Efficiency Curve

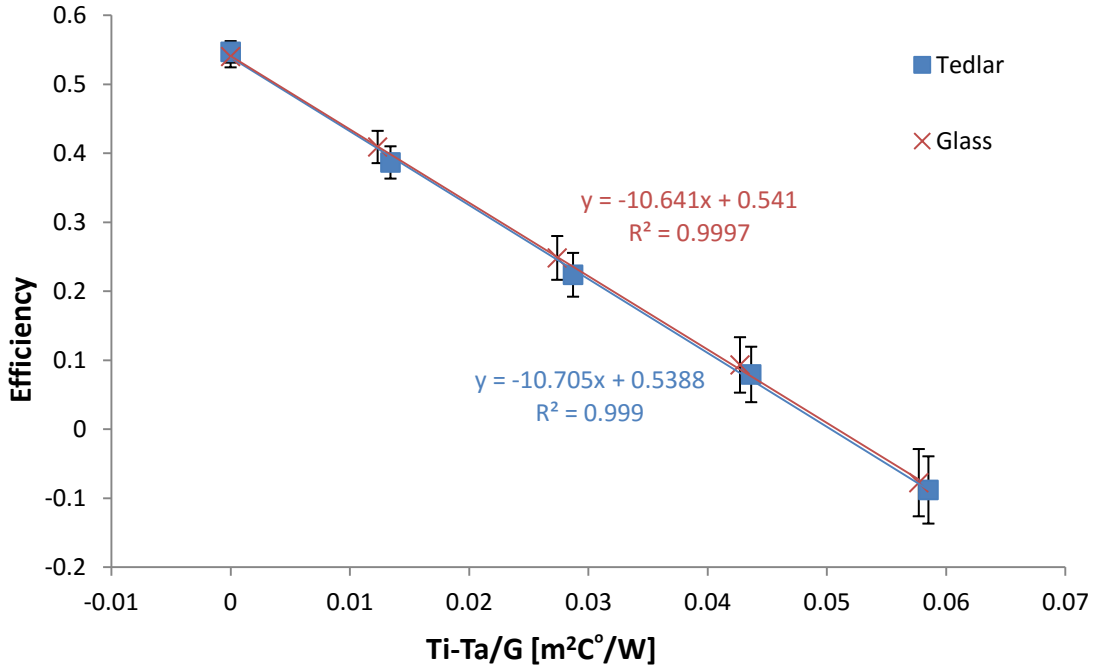

Figure 3-39: Thermal efficiency curve for the cases of glass and Tedlar backing materials

The thermal efficiency of the header and riser design was obtained for the cases using Tedlar and glass laminates on the surface of the absorber. The results are consistent with the high value of heat loss coefficient seen in Figure 3-23 for the header riser collector.

The performance of the glass case has a slightly improved thermal efficiency over the Tedlar case (0.4%) this is expected due to the increased light transmittance but is not significant due to the degree of uncertainty of the results.

Both the Tedlar and the glass case have similar thermal performance characteristics as shown in Table 3-25.

Table 3-25: Comparison of the thermal performance parameters of using different backing materials

Parameter	Tedlar (abs)	Glass (abs)
Zero Loss Efficiency ($FR\alpha\tau$)	53.88 (± 1.94)%	54.1 (±1.94)%
$U_L F_R$ [W/m^2°C]	10.705 ± 0.090	10.641 ± 0.09
F_R	0.57 ± 0.036	0.57± 0.032
U_L [W/m^2°C]	18.87 ± 1.35	18.69 ± 1.2

3.11.4.2 Electricity Generation

The electrical output of the Tedlar and glass cases is compared in Table 3-26. It appears that the glass module is performing slightly better but the effect is marginal and inside the margin of error.

Table 3-26: Comparison of electrical output from glass and tedlar backed PV laminates

Glass Current [A]	Tedlar Current [A]	Glass Power [W]	Tedlar Power [W]
3.2596	3.1641	22.865	21.545
3.2037	3.1098	22.868	21.547
3.1417	3.0496	22.741	21.427
3.0739	2.9838	23.206	21.866
2.9933	2.9055	22.005	20.733

3.11.4.3 Average Plate Temperature

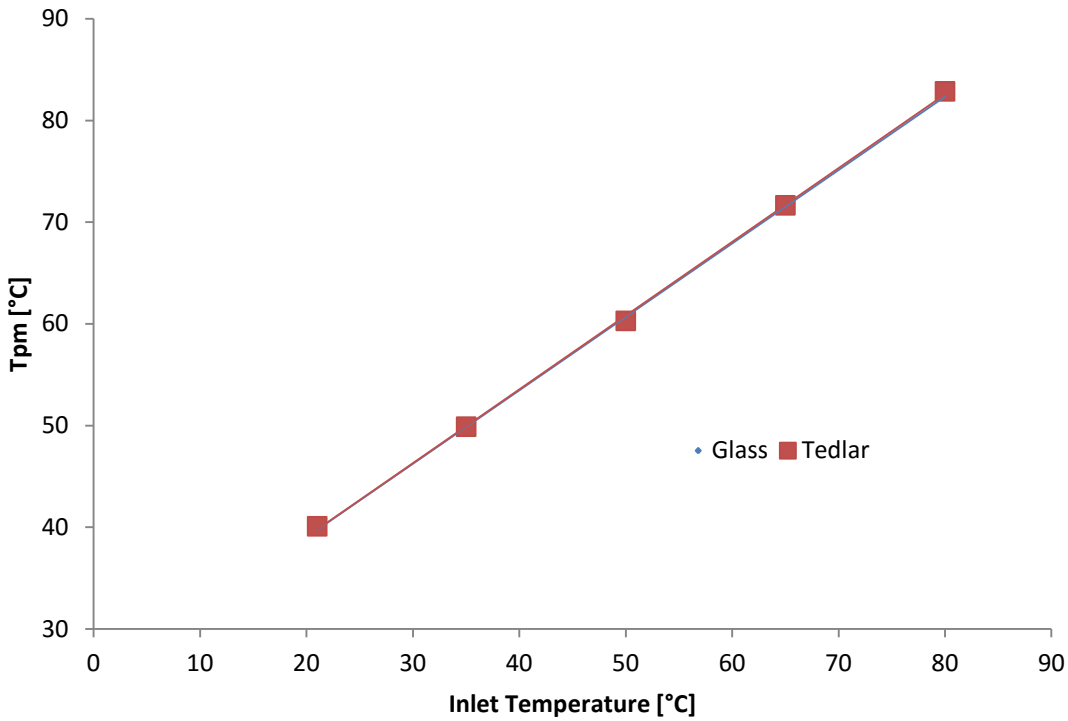

Figure 3-40: Average plate temperature for the cases of different backing materials

The average temperature for both cases across the inlet temperature range is shown in Figure 3-40. The average temperature for both the glass and the Tedlar case is very similar across the range.

3.11.4.4 Temperature Distribution

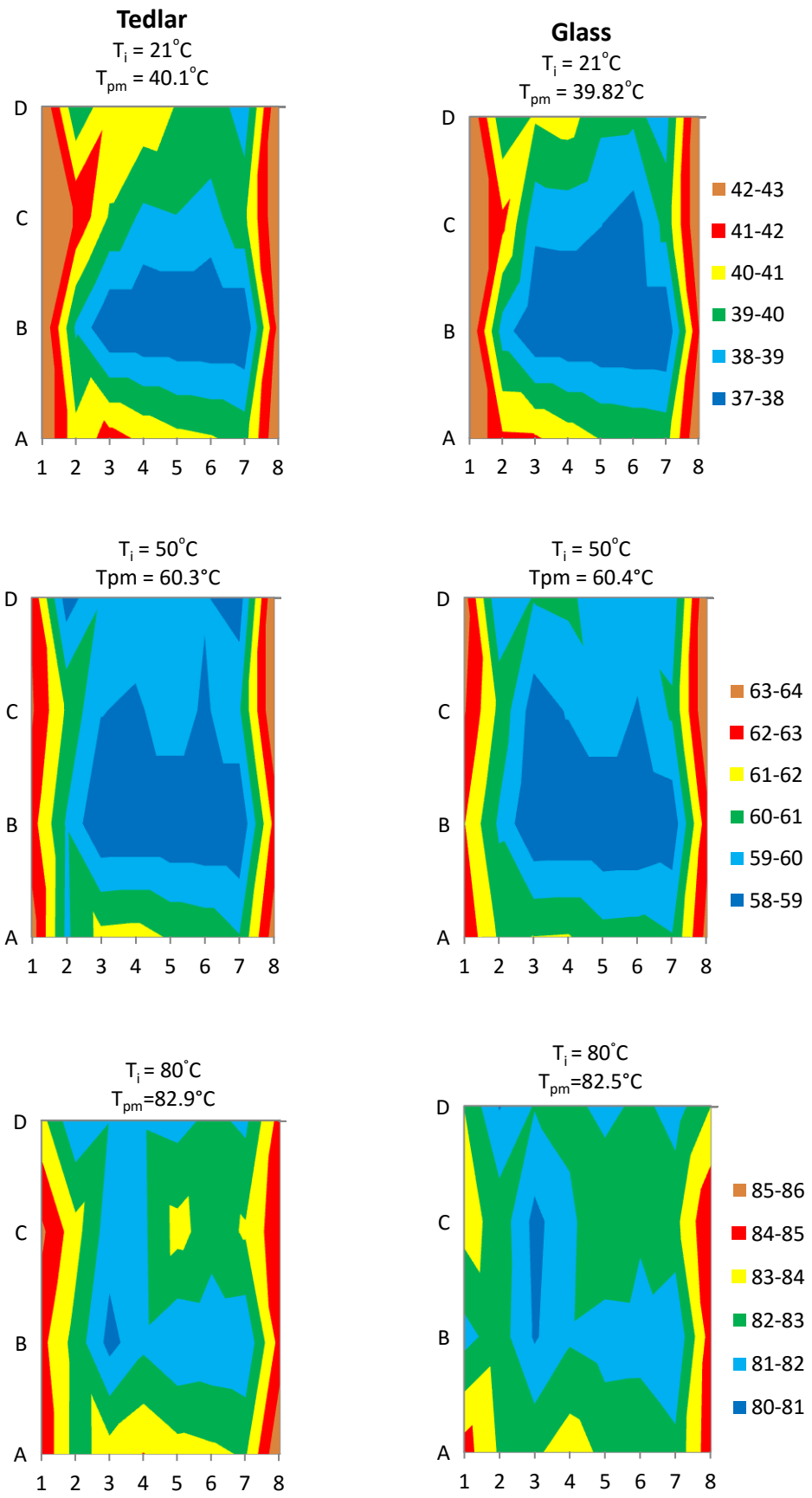

Figure 3-41: Comparing the surface temperature distribution for PVT collectors with glass and Tedlar backing

The temperature distribution for the Tedlar and glass cases is illustrated in Figure 3-41. The results are similar to the results obtained for the Tedlar PV laminate covering the serpentine absorber (see Figure 3-37) in that there is a large cold spot in the area covered by the laminate materials. This is indicative of poor thermal contact between the laminate and the absorber surface.

3.12 Conclusions

This study has developed an experimental system and methodology to characterise the thermal performance of a solar collector. The results have shown that it is possible to obtain the thermal efficiency of different designs of collector. The study showed that the serpentine collector outperformed the header riser collector under the same conditions and a polycarbonate cover is more efficient when there is a large different between inlet temperature and ambient temperature.

When incorporating PV laminates into the system to form a PVT collector it is possible to obtain both the thermal and electrical output of the system. The generation of electricity from laminates placed on the surface of the absorber reduces the amount of irradiation that is converted to thermal energy because a portion is used to generate electricity in the device. The use of different backing materials in the laminate was also investigated and it showed that regardless of the material the performance was the same. This indicates that there is a limiting factor that is influencing the rate of heat transfer into the fluid.

In closing, this study has developed an approach that can be used to determine the fundamental parameters that influence the performance of solar thermal and PVT systems. Further work is required to improve the methodology but it will continue to serve as a useful tool to understand the factors that influence performance of such systems.

3.13 Recommendations for Further Work

Improvements to methodology:

- **Removal of thermal irradiance**. The presence of thermal irradiance >3000nm was higher than the recommendations set out in the testing standard. To address this, the heat needs to be removed. Other solar simulators used in the characterisation of solar thermal systems have addressed this problem with the use of a cooled medium such as a pane of glass in-between the light source and the collector. The important aspect of these systems is that the glass is cooled using air to represent a set sky temperature.
- **The impacts of diffuse radiation vs beam radiation on collector performance**. In this study it was not possible to quantify the proportions of direct and diffuse irradiance from the light source; as a diffuser was required it is expected that the diffuse component would have been quite high. This report highlighted the error that is presented as a result of uncertainty in the absorbance of irradiance; therefore this is an area that should be investigated.

- **Uniformity of irradiance**. The uniformity of irradiance in this testing was adequate for the testing of thermal collectors however when testing photovoltaics it is essential that this be improved upon due to the effects of irradiance mismatch in PV cells. This non-uniformity in the light source could be a contributing factor as the efficiency of the PV cells was found to be around 50% of that stated by the manufacturer.
- **Current and voltage logging**. To accurately determine the PV output of the system, it is necessary to measure both the voltage and current produced. This should also be logged alongside the temperature readings used to determine thermal performance.
- **New light source.** The problems of non-uniformity could be addressed with the use of an entirely different light source. One of the main issues was that the large metal halide lamps used in this study were not straight when fixed into the reflectors. This resulted in the source of light being offset from the focal point. As a result this created bands of high and low irradiance on the testing surface. The reflector is also 2 dimensional whereas an ideal parabolic reflector is 3 dimensional. An appropriate light source in this case would be strip lighting; however these normally consist of fluorescent tubes that do not have adequate power output for this application. The light from fluorescent tubes is also predominantly diffuse. Another alternative would be to use smaller metal halide spot lights (~150W each) that are each positioned it its own paraboloidal reflector. The spectral output should be measured and if necessary supplemented with LEDs that emit a specific wavelength of light.

Future research studies:

- **Different designs of collector**. In this study only several cases have been considered but there are a vast number of different configurations that could be compared. Standardised testing should be followed and a record of all testing should be maintained.
- **Selective coatings.** Investigate the necessity of having a selective coating on an absorber that is to be used as part of a PVT system. As the absorber in these devices will not be exposed to irradiance it is thought the use of this coating is irrelevant and more work should be done to improve the conductive heat transfer between the laminate and the absorber.
- **Thermal contact.** It is difficult to get good thermal contact by simply placing the laminate onto the surface and the use of a conductive paste/grease could greatly improve this. Such pastes contain ceramic or metal particles to improve thermal contact.
- **Geometric factors**. Investigate parameters such as fin width, plate thickness on the thermal performance
- **Operational factors**. To investigate the implications of different operating conditions on performance. All the studies in this report have been conducted under the same flow rate, irradiance and ambient temperature. It would be interesting to isolate these parameters and measure their influence of collector performance.

- **Reducing heat loss coefficient.** Improve airtightness of covered designs to ensure that there is no air movement inside the collector. One step further would be to evacuate airspace in the collector or to fill with a low conductivity gas such as argon.
- **Outdoor testing.** The performance measured using the indoor simulator should be compared with outdoor performance. The testing system is portable and outdoor testing should be carried out following the requirements outlined in EN 12975-2.
- **Different heat removal fluid.** In this study the heat removal fluid used in the testing was confined to water. It would be interesting to understand how the use of different collector fluids would influence performance. Suggestions include glycol and more exotic fluids containing nano or phase change materials.
- **Maximum power point tracking of PVT.** This study had a high degree of uncertainty associated with the value of resistance used in the calculation of PV output. This could be addressed by developing a method that automatically tracks the maximum power point of the PV array and selects the optimum resistance for the system.

4. Thermal Analysis of a PVT Collector

4.1 Introduction

This chapter describes the development of a computational methodology to simulate the performance of a hybrid solar thermal collector.

In sections 4.2-4.10 , the factors that govern the performance of a solar collector are detailed. This begins with an examination of the thermal losses that occur in all collectors. The different empirical models applied to header-riser and serpentine are then detailed. The section is concluded by comparing the results of the empirical models with measured experimental data.

In sections 4.11-4.15 a technique using computational fluid dynamics is used to simulate the performance of a solar thermal collector. The methodology behind the approach is detailed and then validated using experimental data. The limitations of the simulation are then investigated to understand the differences between the simulated and experimental results. The CFD approach is then used to compare the influence of different flow patterns in a header riser collector and the impact this has on thermal performance.

Sections 4.17-4.19 looks at the thermal loss coefficients of connected, but unevenly heated PV cells. The aim of this section is to investigate the impact of temperature distribution and determine the best cell configuration for PVT performance. The temperature of localised PV cells were extracted from the results of the CFD simulation. 3 wiring patterns were assessed for different flow patterns of a header riser collector.

4.2 Thermal Analysis of a Flat Plate Solar Thermal Collector

The useful energy output of a flat plate solar collector can be described using an energy balance equation (4.1) [106]:

$$Q_u = A_c\left[S - U_L\left(T_{pm} - T_a\right)\right] \tag{4.1}$$

Where A_c is the collector area, S is the absorbed solar energy, U_L is the overall heat loss coefficient, T_{pm} is the average plate temperature and T_a is the ambient temperature.

As discussed in Section 2.4, there are several piping configurations that can be used in a solar collector. This section describes the thermal analysis of two common designs of flat plate collector; serpentine and header-riser.

4.2.1 Temperature driven losses

The overall temperature driven loss coefficient of a solar collector U_L is made up of several different losses; those that occur from the top of the collector, U_t , those that occur through the back of the collector, U_b, and those that occur from the edge of the collector, U_e. The sum of these losses is equal to U_L as shown in (4.2).

$$U_L = U_t + U_b + U_e \tag{4.2}$$

As the back of the collector is often insulated and the edges only makeup a small portion of the exposed area, U_t is the most significant term in (4.2). U_t is made up of convective and radiative losses driven by a temperature gradient; an empirical method to estimate its value was developed by Klein and is shown in (4.3) [107].

$$U_t = \left\{\frac{N}{\frac{C}{T_{pm}}\left[\frac{T_{pm} - T_a}{N + f}\right]^e} + \frac{1}{h_w}\right\}^{-1} + \frac{\sigma\left(T_{pm} + T_a\right)\left(T_{pm}^2 + T_a^2\right)}{\left(\varepsilon_p + 0.00591Nh_w\right)^{-1} + \frac{2N + f - 1 + 0.133\varepsilon_p}{\varepsilon_g} - N} \tag{4.3}$$

Where,

N = number of glass covers

$F = (1+0.089h_w - 0.1166h_w\varepsilon_p)(1 + 0.07866N)$

$e = 0.431(1-100/t_{pm})$

B = collector tilt

σ = Boltzmann constant

ε_g = emittance of glass

ε_p = emittance of plate

h_w = wind heat transfer coefficient

4.3 Header-and-Riser Collectors

In a header-riser (HR) collector, flow is delivered to a network of parallel riser pipes using two header pipes (inlet and outlet) that run perpendicular to the network. A HR collector is illustrated in Figure 4-1.

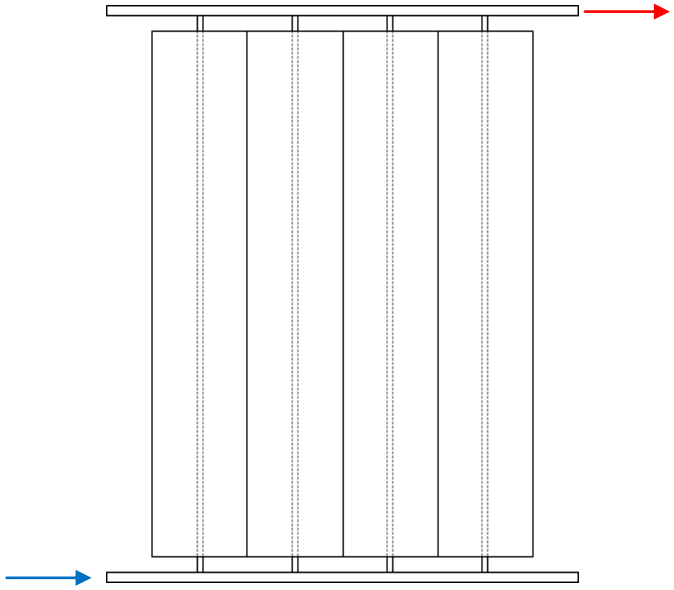

Figure 4-1: Header and Riser Collector

An numerical method to analyse the thermal performance of a flat plate HR collector was first developed by Hottel and Whiller Bliss [108]. They developed a steady- state approach which remains a widely used approach in the performance analysis of solar thermal collectors.

4.3.1 Steady State - Hottel Whillier Bliss Model

The Hottel Whillier Bliss (HWB) model divides the solar collector down into individual fins. A fin is defined as the section of absorber that is half the width of the spacing between the parallel pipes. So each pipe has two fins, one on either side.

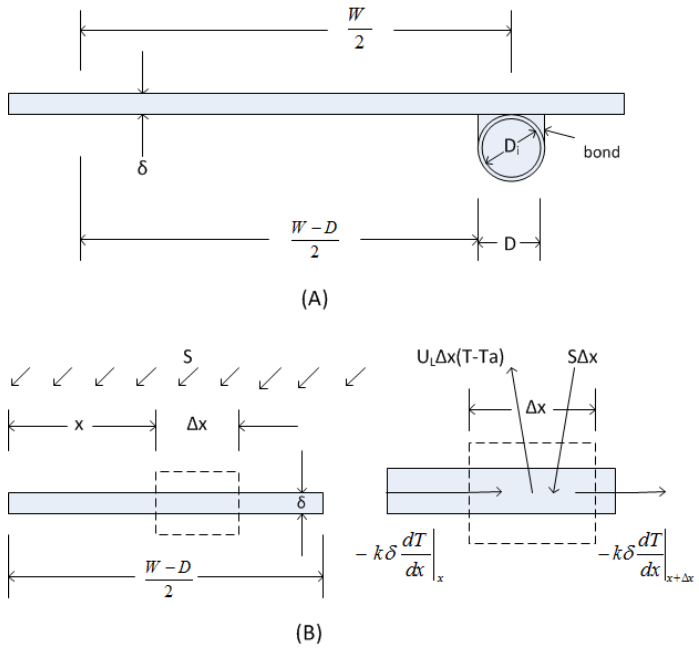

Figure 4-2: Energy balance on fin section (adapted from Duffie and Beckman, 1991)

Through doing this it is possible to determine a value of fin efficiency for the collector. Fin efficiency is dependent on the distance between tubes, *W*, sheet thickness, *δ*, and tube diameter, *D*; the interrelationship between these parameters is illustrated in Figure 4-2. Fin efficiency can be calculated using (4.4) [106].

$$F = \frac{tanh\left[m\left(W-D\right)/2\right]}{m\left(W-D\right)/2} \tag{4.4}$$

$$m = \sqrt{U_L / k\delta} \tag{4.5}$$

The efficiency of a fin will increase as the width of the fin reduces; this is because there is less area for heat loss to occur. The relationship between fin efficiency and (4.5) is shown in Figure 4-3.

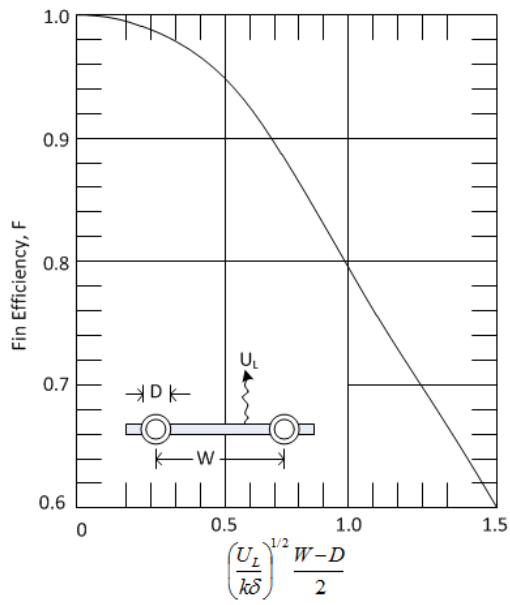

Figure 4-3: Influence of fin width on fin efficiency (adapted from Duffie and Beckman 1991)

Once the fin efficiency has been calculated, it is possible to calculate the collector efficiency factor. This takes into account the resistances to heat flow from the sheet-tube bond and resistance between the tube and the fluid. The collector efficiency factor is shown in (4.6) [106].

$$F' = \frac{1/U_L}{W\left[\frac{1}{U_L\left[D+(W-D)F\right]}+\frac{1}{C_b}+\frac{1}{\pi D_i h_{fi}}\right]} \tag{4.6}$$

Where C_b is the bond conductance, D_i is the internal diameter of the tube and h_{fi} is the heat transfer coefficient between the fluid and the tube wall.

The objective of the HWB model is to express the performance of a solar collector in terms of its inlet temperature. This can be achieved through the use of the heat removal factor, F_R, is the ratio of actual to the maximum possible energy gain (if the entire collector surface is at inlet temperature ,T_i). The heat removal factor is linked to the collector efficiency factor and can be calculated using (4.7) [106].

$$F_R = \frac{\dot{m}C_p}{A_c U_L}\left(1-\exp\left[-\frac{A_C U_L F'}{\dot{m}C_p}\right]\right) \tag{4.7}$$

Once the heat removal factor has been calculated, it is possible to determine the useful energy gain from a solar collector using (4.8).

$$Q_u = A_c F_R\left[\left(S-U_L\left(T_i-T_a\right)\right)\right] \tag{4.8}$$

The HWB model only applies to isothermal collectors. For non-isothermal collectors, such as in parabolic trough collectors a different expression involving entropy is used [88].

4.3.2 Estimating Plate Temperature

The heat removal factor can also be used to estimate the mean surface temperature of the plate using (4.9) [106].

$$T_{pm} = T_i + \frac{Q_u / A_c}{F_R U_L}\left(1 - F_R\right) \tag{4.9}$$

By neglecting the side and bottom losses i.e. U_L consists only of top losses (4.9) can be solved iteratively with (4.3) [106].

4.4 Serpentine Collectors

In a serpentine collector the flow is channelled through a single pipe connected to the back of the absorber see Figure 4-4.

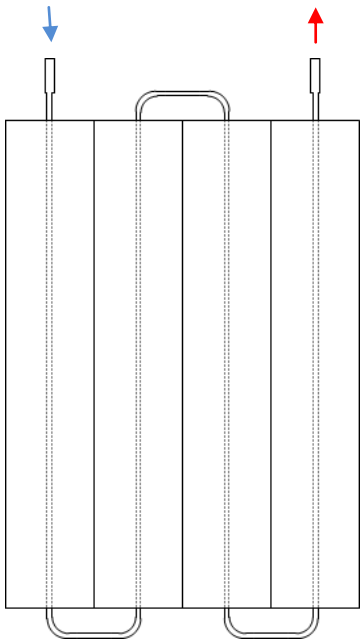

Figure 4-4: Serpentine Collector

The general expression for the performance of a solar collector shown in (4.1) is still applicable to serpentine collectors; however the HWB model cannot be applied to the serpentine collector. Unlike the HR design, where each riser can be treated independently using the fin approach, heat transfer occurs between the pipes of a serpentine collector. This is because there is a gradually increasing temperature profile in the x-direction from inlet to outlet. It has been found that the use of a serpentine collector can increase the overall system efficiency due to increased stratification in the supply tank [109].

The HWB can only be applied to a Serpentine collector if a thermal break is created in the middle of each bend.

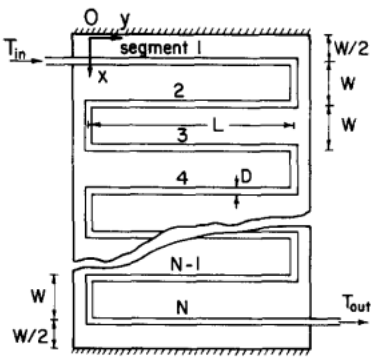

Figure 4-5: Serpentine Collector as analysed by Abdel Khalik. Source Duffie and Beckman 1991.

A single bend of the serpentine collector illustrated in Figure 4-5 was analysed by Abdel- Khalik. They showed that the heat removal factor is dependent on the parameter F_1 and F_2 which are functions of physical characteristics of the collector including plate thickness, conductivity and tube spacing [110].

i. Zang and Lavan Model

Zhang and Lavan proposed a different approach using matrices to find the solution. In their study they solved the heat removal factor for N=2 to N=4. As with Abdel and Khalik, they showed that the solution for F_R in a serpentine collector could be determined using a set of dimensionless parameters, see (4.10) [7]. Abdel Khalik states that differences between the F_R/F_1 for one turn (N=2) and higher values of N are less than 5%. Their findings show that the heat removal factor is at a maximum at 1 and a minimum at N = 2. F_R then begins to increase with N but at a decreasing rate. They showed that as N reaches infinity, the value of F_R begins to reach the value at N=1. This is explained by Dayan as the number of turns increases the tube length increases for a given area [109]. When N=1 the serpentine collector acts as a header riser plate and F_R is greatest as there is no heat transfer between tubes [111].

$$F_R = F_1 F_3 F_5 \left[\frac{2F_4}{F_6 \exp\left[-\sqrt{1-F_2^2} / \mathrm{F}_3 \right] + F_5} - 1 \right]$$

$$F_1 = \frac{\kappa}{U_L W} \frac{\kappa R(1+\gamma)^2 - 1 - \gamma - \kappa R}{\left[\kappa R(1+\gamma) - 1 \right]^2 - (\kappa R)^2}$$

$$F_2 = \frac{1}{\kappa R(1+\gamma)^2 - 1 - \gamma - \kappa R}$$

$$F_3 = \frac{\dot{m} C_p}{F_1 U_L A_c}$$

$$F_4 = \left(\frac{1-F_2^2}{F_2^2} \right)^{\frac{1}{2}}$$

$$F_5 = \frac{1}{F_2} + F_4 - 1$$

$$F_6 = 1 - \frac{1}{F_2} + F_4 \tag{4.10}$$

And

$$\kappa = \frac{(k\delta U_L)^{1/2}}{\sinh\left[(W - D_e)(U_L / \mathrm{k}\,\delta)^{1/2} \right]}$$

$$\gamma = -2\cosh\left[(W - D)\left(\frac{U_L}{k\delta} \right)^{1/2} \right] - \frac{D_e U_L}{\kappa} \tag{4.11}$$

$$R = \frac{1}{C_b} + \frac{1}{\pi D_i h_f}$$

The Zang and Lavan model can be applied to serpentine collectors with any number of bends provided that $\dot{m} C_p / (F_1 U_L A_c)$ is greater than 1.0.

An alternative approach was taken by Lund 1989 who developed an independent method to calculate the heat removal factor using an effective number of transfer units (NTU) relationship and a shape factor linked to the serpentine design. This model was more appropriate for turbulent flows but demonstrated good agreement with the Zhang and Lavan results [112].

To put the empirical models to the test, Dayan used a finite difference technique to calculate the useful energy transferred to the tube from upper and lower parts of the absorber plate[109]. This method is illustrated in Figure 4-6.

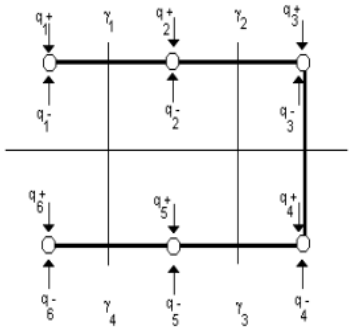

Figure 4-6: Illustration of the Finite Difference Method used by Dayan on a single bend. Source [109]

The finite element approach allows the flow to be analysed without making any assumptions regarding geometry conditions. The collector analysed had a constant area of 1m^2 and varying the number of turns changed the tube spacing. The results show close agreement with the Abdel Kahik model for values of $\dot{m}C_p / \left(F_1 U_L A_c\right)$ greater than unity and for one and two turns, see Figure 4-7. However at N>2, low flow rates and when $\dot{m}C_p / \left(F_1 U_L A_c\right)$ is less than unity the results do not compare favourably with a difference of around 15%. Instead results for these conditions are in closer agreement to the results presented by Zhang and Lavan, see Figure 4-8.

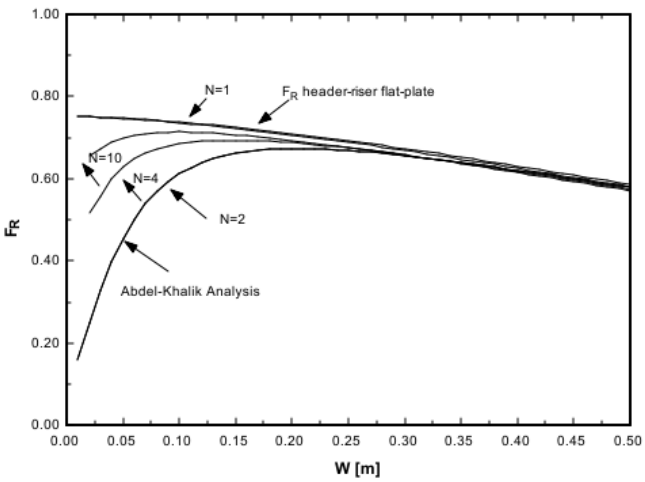

Figure 4-7: Influence of Number of Turns and Tube Spacing on Heat Removal Factor. Source [109]

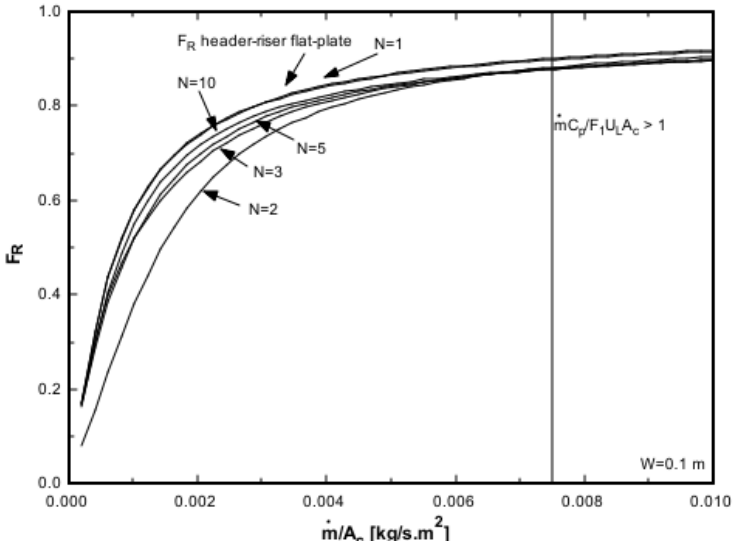

Figure 4-8: Effect of number of turns and mass flow rate on heat removal factor. Source Dayan 1997[109].

The results showed that for a mass flow rate of 0.002kg/(s·m^2), the difference between a flat plate collector and a serpentine 15 turn collector the difference is less than 3%. Therefore the analysis of a serpentine collector with more than 15 turns can be treated as a long straight collector with no turns; however it was noted than the internal heat transfer coefficient will be different due to the difference in flow regime [109].

4.5 Thermal Analysis of a PVT Collector

For the performance analysis of a PVT collector, the models must be modified to take into account the electricity generated from PV cells mounted onto the absorber surface. PV cells on the absorber prevent incident solar radiation from reaching the thermal absorber which reduces the value of *S*; however this energy is not lost because electricity is generated by the PV cell. The value of U_L must also be adjusted to compensate for the temperature dependent losses that occur in the PV cell.

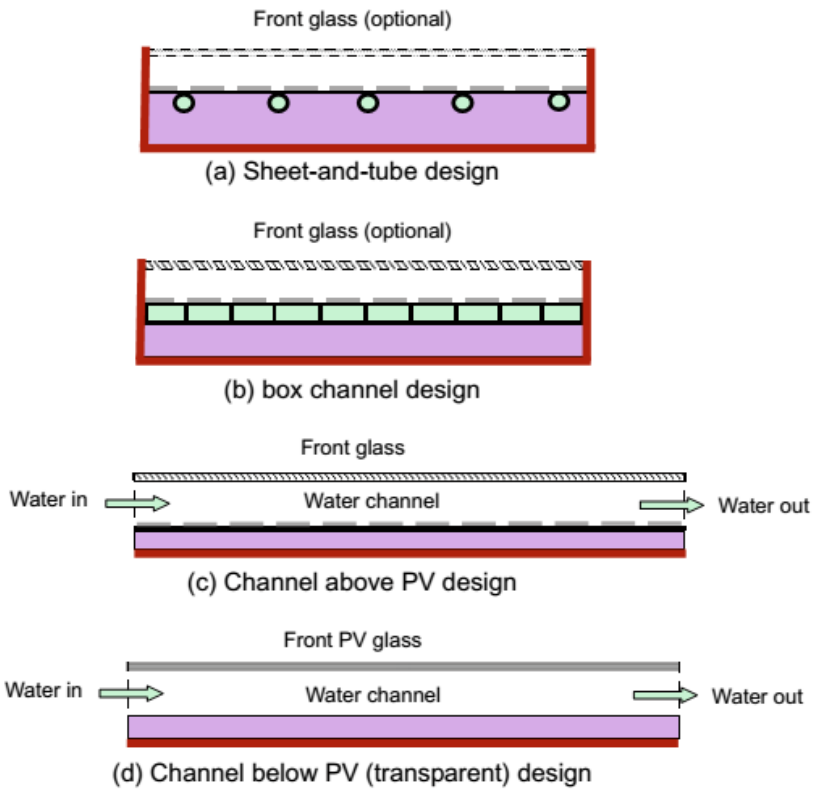

Figure 4-9: Designs of water based PVT systems. Source [50].

4.5.1 Adjusting the Hottel Whillier Bliss Model

Florchuetz modified the HWB model so that it can be extended to PVT collectors [65]. In the modified approach (4.8) is replaced by (4.12).

$$\tilde{Q}_u = A_c \tilde{F}_R \left[\tilde{S} - \tilde{U}_L \left(T_i - T_a \right) \right] \tag{4.12}$$

Where the presence of ~ represents a modification of a HWB parameter making it suitable for the analysis of a PVT collector.

The first step is to determine the instantaneous operating electrical efficiency of the PV cells, η, at their operating temperature, T_{pv}, using (4.13) which takes into account the degradation of cell efficiency as a function of temperature.

$$\eta = \eta_{ref} \left[1 - \beta \left(T_{pv} - T_{ref} \right) \right] \tag{4.13}$$

Where, η_{ref} is the reference efficiency at T_{ref}, and β is the temperature coefficient of efficiency. These values of η_{ref} and β are commonly given on the technical datasheet supplied by the manufacturer of the PV cells.

Once the efficiency of the PV cell has been calculated, it is possible to modify the value of absorbed solar radiation using (4.14). This subtracts the portion of radiation that is converted into electricity.

$$\tilde{S} = S\left(1 - \frac{\eta}{\alpha}\right) \tag{4.14}$$

Where α is the thermal absorbance of the PVT surface.

Unlike in a thermal collector, where the thermal losses go below zero once the average absorber temperature reaches ambient, PV cells always have a finite efficiency. This means that the same amount specified in (4.14) must also be deducted from the value of U_L otherwise (4.12) would become unbalanced. The modification of UL is achieved using (4.15).

$$\tilde{U}_L = U_L - \frac{S}{\alpha}\eta_{ref}\beta = U_L - \tau G \eta_{ref}\beta \tag{4.15}$$

Because the modification only alters the value of U_L and S, the methodologies detailed in the previous section can be used to calculate F_R. Florchuetz showed that F_R differs from $\tilde{F}_R$ by no more than 1% for thermal collectors with a h_f greater than 15W/m^{2}K [65].

Using the methodology proposed by Florchuetz it is possible to determine the electrical output, Q_e, of a PVT collector using conventional thermal design parameters plus the two adjustment parameters, β and η_{ref} for PV cell operation using (4.16).

$$Q_e = \frac{A_c S \eta}{\alpha}\left\{1 - \frac{\eta_{ref}\beta}{\eta}\left[\tilde{F}_R\left(T_i - T_a\right) + \frac{\tilde{S}}{\tilde{U}}\left(1 - \tilde{F}_R\right)\right]\right\} \tag{4.16}$$

4.5.2 Exergy Analysis of a PVT Collector

In addition to determining the energy performance of a solar collector it is also possible to determine the exergy performance. Exergy is based upon the second law of thermodynamics and is a measure of the irreversibility of entropy. It is a measure of the ability energy has to do work on a system and is an indicator of the quality of the energy produced. This is particularly relevant to PVT collectors as electricity and heat are being generated. An exergy analysis on a PVT collector has been presented by Fujisawa [85]. Because electricity can do work on a system of any temperature, its exergetic efficiency is equal to its energetic efficiency, see (4.17).

$$X_e = \eta_e G = \zeta_e G \tag{4.17}$$

Where X_e is the instantaneous electrical exergy, η_e is electrical efficiency of the PV cell, G is the irradiance, ζ_e is the electrical exergetic efficiency.

Thermal energy requires a temperature gradient to perform work. The maximum amount of work that can be performed is limited by the Carnot efficiency, η_c, see (4.18).

$$\eta_c = 1 - \frac{T_0}{T_1} \tag{4.18}$$

Where, T_0 and T_1 are the absolute temperatures of the heat sink and heat source respectively.

Thermal exergy, X_t, can be calculated using (4.19)

$$X_t = \eta_c q = \eta_c \eta_t G = \zeta_t G \tag{4.19}$$

Where q is the instantaneous thermal exergy, η_c is Carnot efficiency, η_t is thermal efficiency, G is the irradiance, ζ_e is the electrical exergetic efficiency.

Using the individual electrical and thermal exergetic efficiencies it is possible to create an overall exergy for the PVT collector, X_{pvt} using (4.20):

$$X_{PVT} = X_e + X_t = \left(\zeta_e + \zeta_t\right) G = \zeta_{PVT} G \tag{4.20}$$

And

$$\eta_{PVT} = \eta_e + \eta_c \eta_t \tag{4.21}$$

Where, ζ_{PVT} is the overall exergetic efficiency of the PVT collector and η_{PVT} is the overall efficiency of the PVT collector.

In the exergy analysis of a domestic scale solar water heater, Xiaowu showed using a case study that the energy efficiency of a solar system was 15.1% and the exergy efficiency was considerably smaller at a mere 0.77% [113]. The reason for this is due to the low grade output of domestic solar collectors. Saidur also showed in a review of exergenic analysis of solar energy systems, that standard solar collectors have the greatest destruction of all reviewed technologies [114]. Xiaowu showed that the main features affecting the exergy of a solar system is the collector width and the top loss coefficient, which is largely dependent on the number of covers; see Figure 4-10.

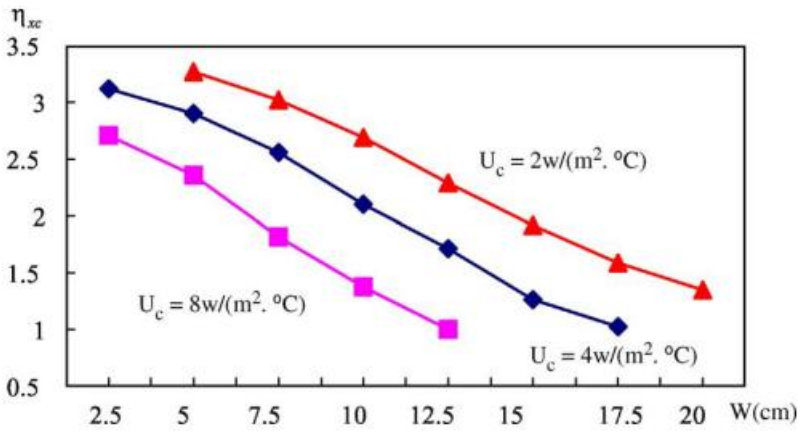

Figure 4-10: Exergy Dependence on UL and Collector Width. Source Xiowu 2005.

As electricity is capable of doing work on a system no matter how hot it is; its value is equivalent to a heat flow from a body of infinite temperature. Using this principle Coventry valued the output of a PVT collector in terms of exergy and compared it with a range of other indicators based on the first law and market energy values. A first law energy analysis gave a ratio of 1 whereas an exergy analysis gave a ratio of 16.8, see Table 4-1. Coventry found that the most suitable measurement of value was to use figures from the renewable energy market, which in 2001 gave a ratio of 4.24 [115]. This means that each unit of electrical energy is 4.24 times more valuable than the same unit of thermal energy produced.

Table 4-1: Exergetic comparison of PVT electrical and thermal output. Source Coventry 2003.

Energy stream	Energy (W)	Exergy equation	Exergy (W)	Energy/exergy ratio
Electrical	1000	$\Delta\dot{A}_{electrical} = \Delta\dot{E}_{electrical} = \dot{m}(h_2 - h_1)$	1000	1
Thermal*	1000	$\Delta\dot{A}_{thermal} = \dot{m}[h_2 - h_1 - T_0(s_2 - s_1)]$	59.5	16.8

* Assuming: $p = 500$ kPa, $T_1 = T_0 = 25$ °C, $T_2 = 65$ °C and $\dot{m} = 5.98$ g/s and $v_1 = v_2$, $z_1 = z_2$ which gives $h_1 = 105$ kJ/kg, $h_2 = 272$ kJ/kg, $s_1 = 0.366$ kJ/kg K and $s_2 = 0.893$ kJ/kg K.

Exergy analysis is only important if the demand is for high grade energy. For domestic systems and some commercial systems the temperature requirement is much lower. A system should be judged on its ability to meet the demand required from it. For example if there is a high demand for low grade thermal energy and all of the energy generated from the collector is going towards this, the system is operating as efficiently as possible. Exergy is important when the collector is producing an excess of thermal energy and cannot store this energy and is wasted. In this scenario it would be more desirable to produce electricity which could be used elsewhere or stored for later use.

4.6 Transient Models

Under real conditions solar collectors do not reach steady state and the numerical model does not take into account the capacitance of the collector components. Each of these components absorbs energy, hindering the flow of heat into the heat removal fluid. Dynamic thermal models are based on an energy balance between the collector components (absorber, heat transfer fluid and the insulation). The energy balance across a collector is shown in (4.22) [116].

$$c_p \frac{\partial T_p}{\partial t} = A_c \eta_0 G - losses \tag{4.22}$$

Where, η_0 is the zero loss efficiency of the solar collector.

The number of nodes in the model depends on the losses that are taken into account. For instance temperature driven losses can occur, between the cover and the ambient, $U_{c\text{-}a,}$ and between the plate and the cover, $U_{p\text{-}c}$. In single node models, it is assumed that these losses are conservative and equal to steady state, see (4.23).

$$U_{c-a}\left(T_c - T_a\right) = U_{p-c}\left(T_p - T_c\right) \tag{4.23}$$

By making this assumption, the collector losses can be grouped and treated as one node. A comparison by Wijeysundera showed that this assumption is suitable for collectors with one cover however with multiple covers a multi-nodal approach should be considered [117].

With knowledge of S, U_L and T_a it is possible to determine the mean plate temperature at the end of each time period using the transient approach. See (4.24) [106].

$$T_p = T_a + \frac{S}{U_L}\left[1 - exp\left(-\frac{A_c U_L t}{\left(mC_p\right)_{effective}}\right)\right] \tag{4.24}$$

During their operation, thermal collectors do not operate under steady state conditions and will be exposed to fluctuations of irradiation and temperature. In order to take this into account, dynamic/transient models have been developed to take into account thermal capacitance. When taking into account thermal capacitance either a value of capacitance for the whole collector can be used (lumped capacitance) or the capacitance of the individual components can be take into account, i.e. glass, absorber, fluid etc. (nodal capacitance). A comparison of steady state (zero capacitance) and transient models was performed by Klein, who found that the steady state model was adequate when hourly meteorological data is used [118]. The main barrier to the use of dynamic models was the increase in complexity however the capability of computers has vastly increased so the use of dynamic models is more feasible. A comprehensive review of dynamic approaches to analysing a flat plate solar thermal collector is given by Tagliafico. [119].Capacitance models are based on an energy balance across the collector – the radiation absorbed will be equal to the temperature increase in the collector. A more recent comparison of steady state and transient models was carried out by Schnieders [120].

The standard flat plate collector in TRNSYS (Type 73) is based on the steady-state HWB model; however this can also be modified to take into account dynamic effects [121]. In their model they treat the optical (zero-loss) efficiency of beam and diffuse radiation independently, with both diffuse and beam having their own Incidence Angle Modifier. The effect of wind on the zero loss efficiency and heat loss is also taken into account. This is done by multiplying both by

wind speed and a wind speed coefficient. The power density output of the collector is calculated using (4.25):

$$P_{out} = \eta_0 K_{\theta b}(\theta) G_b + F'(\alpha\tau)_{en} K_{\theta d} G_d - c_6 u G - c_1 (t_m - t_a) - c_2 (t_m - t_a)^2 \\ -c_3 u (t_m - t_a) + c_4 (E_L - \sigma T_a^4) - c_5 dt_m / dt \quad (4.25)$$

Where;

η_0 = Zero loss efficiency

u = Wind speed [m/s]

E_L = Long wavelength radiation [W/m^2]

$K_{\theta b}(\theta)$ and $K_{\theta d}$ = The incidence angle modifier for beam and diffuse radiation respectively [-]

$F'(\alpha\tau)_{en}$ = The optical (zero-loss) efficiency [-]

t_m = Arithmetic mean temperature between the inlet and outlet of the collector [^{o}C]

G_b and G_d = Incident beam and diffuse radiation onto the collector respectively [W/m^2]

c_1 = Heat loss coefficient at (t_a-t_m) = 0 [W/m2K]

c_2 = Temperature dependence of the heat losses [W/m2K]

c_3 = Wind speed dependence of the heat losses [W/m2K]

c_4 = Long-wave irradiance dependence of the heat losses [-]

c_5 = Effective thermal capacitance [[J/m2K]]

c_6 = Wind dependence of the optical efficiency [s/m]

These constants can be derived from tests specified in ISO 9806-3.

(4.25) is also the collector model used in EN 12975-2 for the outdoor testing of collectors [103].

4.7 Empirical Analysis of Experimental Collectors

In this section the Hottel Whillier Bliss and the Zang and Lavan model are applied to the experimental HR collector and Serpentine collectors that are detailed in the previous experimental chapter. The modelling has been performed using an excel spreadsheet for both cases. The geometrical characteristics of the collectors is shown in Table 4-2.

Table 4-2: The parameters used to determine the internal heat transfer coefficient inside the pipes of the serpentine and header riser collector.

Characteristics for Experimental Collectors		
Pipe Diameter	0.007500	m
Pipe Area	0.000044	m^2
Fluid Density	998.2	kg/m^3
Fluid Dynamic Viscosity	7.98E-04	Pa·s
Mass Flow Rate Serpentine	0.009	kg/s
Mass Flow Rate Parallel*	0.00225	kg/s
Hydraulic Diameter (Circular)	0.007500	m
Kinematic Viscosity	7.99E-07	m^2/s
Internal pipe diameter (m)	0.0075	m
External pipe diameter (m)	0.0080	m
Pipe length (m)	0.79	m
Prandtl number @ 20°C	6.00	
Thermal conductivity water @20°C	0.60	(W/m K)

*This assumes that the inlet flow is split evenly between the 4 risers as per the assumptions of the HWB model

4.7.1 Calculation of Fluid to Tube Heat Transfer Coefficient

The empirical model requires the internal heat transfer coefficient, h_{fi} to be calculated. This is the rate at which heat transfer occurs across the temperature difference between the fluid and the wall of the piping. The mode of heat transfer inside the pipe is forced convection and h_{fi} is dependent on the flow characteristics of the fluid.

4.7.1.1 Reynolds Number

The Reynolds number is the ratio of inertial forces to viscous forces and is used as an indicator of flow regime. Laminar flow occurs at Reynolds numbers of <2300 and turbulent flow occur at >4000. The region in between is defined as transition flow where either turbulent or laminar flow can occur. In laminar flow the viscous forces are dominant and is characterised by stable, constant fluid motion; turbulent flow on the other hand is chaotic and unstable. Turbulent flow is the preferred regime for heat transfer as the constant mixing enables heat to be fully dispersed in the fluid. The Reynolds number for a circular pipe can be calculated using (4.26).

$$\mathrm{Re} = \frac{QD_i}{vA} \tag{4.26}$$

Where Q is the volumetric flow rate, D_i is the hydraulic diameter (for a circular pipe this is equal to the internal diameter), v is the kinematic viscosity (m^2/s) and A is the cross sectional area of the pipe.

4.7.1.2 Nusselt Number

The Nusselt number is the ratio of convective to conductive heat transfer across the boundary and its value is dependent on the flow regime in the pipe.

4.7.1.3 Developing Laminar Flow

When a fluid enters a pipe with uniform velocity profile, the flow does not immediately become laminar. When describing the development of laminar flow, the term entrance region is used to define the transition of uniform velocity profile to that characteristic of laminar flow.

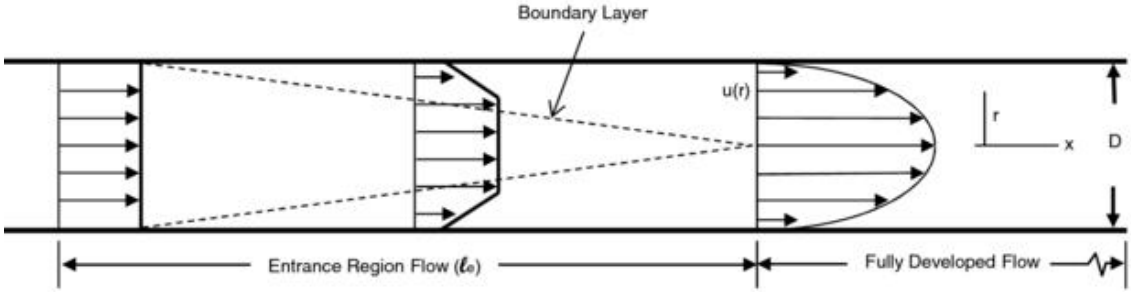

Figure 4-11: Development of internal laminar flow

Figure 4-11 illustrates the development of laminar flow in a pipe. When flow encounters the pipe wall a zero slip condition is experienced; this means that the velocity of the fluid next to the wall becomes zero. As a result a boundary layer is created that separates a viscous region next to the wall and the inviscid flow in the middle of the pipe. The viscous region is basically stationary whereas the inviscid core is turbulent. This region continues through the pipe until the boundary layers meet. At this point the entire flow becomes viscous and is considered fully developed laminar flow. The length of the entrance region, E_L, is dependent on the internal pipe diameter D_i and the Reynolds number, and can be calculated using (4.27).

$$E_L = 0.06 \operatorname{Re} D_i \tag{4.27}$$

To determine the average Nusselt number for a pipe, which takes into consideration the entrance region (4.28) is used [122].

$$\mathrm{Nu}_{\mathrm{lam}} = 1.86 + \left(\frac{\operatorname{Re} \operatorname{Pr} D_i}{L} \right)^{1/3} \left(\frac{\mu_b}{\mu_s} \right)^{0.14} \tag{4.28}$$

Where; Pr, the Prandtl number, is the ratio of kinematic viscosity to thermal diffusivity; L is the length of the pipe; μ_b and μ_s is the dynamic viscosity for the bulk fluid and surface temperature respectively.

Because the inviscid region inside the entrance region contains turbulent flow, there is increased turbulence resulting in greater heat transfer in this region. When applying (4.28), the

longer the pipe, the less influence the entrance region will have on the average Nusselt value. It has been recommended that Nusselt number for a solar collector be calculated for a developing flow because the pipework is not long enough to develop fully developed laminar flow [123].

4.7.1.4 Fully Developed Laminar Flow

In the fully developed region the Nusselt value is dependent on the surface thermal condition. Because the convection coefficient varies across the tube, with a value of zero at the wall, the Nusselt number is a function of duct geometry. For fully developed flow inside a circular pipe the Nusselt values are shown in (4.29).

$$\begin{aligned} \mathrm{Nu} &= 3.66 \text{ for } T_s = \text{constant} \\ \mathrm{Nu} &= 4.36 \text{ for } \dot{q}_s = \text{constant} \end{aligned} \tag{4.29}$$

Where T_s is the surface temperature of the pipe was and $\dot{q}_s$ [W/m2]is heat flux.

4.7.1.5 Turbulent Flow

For turbulent flow the entrance region is neglected because the influence is less than with laminar pipes. For Reynolds values <3000 Re < 5x10^6 the Nusselt number can be calculated using (4.30) [124]

$$\mathrm{Nu} = \frac{(f/8)(\mathrm{Re}-1000)\mathrm{Pr}}{1+12.7(f/8)^{1/2}\left(\mathrm{Pr}^{2/3}-1\right)} \tag{4.30}$$

f is the Darcy friction factor and can be found using Moody Diagram.

4.7.1.6 Heat Transfer Coefficient

The internal heat transfer coefficient can then be calculated using (4.31).

$$h_{fi} = \frac{\mathrm{Nu}k_w}{D_i} \tag{4.31}$$

Where k_w is the thermal conductivity of water.

Using the parameters listed in Table 4-2 the Reynolds number, the Nusselt number and heat transfer coefficient have been calculated for the header riser and serpentine collector, see Table 4-3 and Table 4-4 respectively.

Table 4-3: Calculation of heat transfer coefficient for the header riser collector under different flow regimes

Flow Regime	Developing Laminar	Fully Developed Laminar
Mass Flow Rate [kg/s]	0.00225	0.00225
Reynolds Number	552	NA
Nusselt Number	5.85	4.36
Length to fully developed flow [m]	0.24	NA
Heat Transfer Coefficient [W/m^{2}K]	467.9	348.8

Table 4-4: Calculation of heat transfer coefficient for the serpentine collector under different flow regimes

Flow Regime	Developing Laminar	Fully Developed Laminar
Mass Flow Rate [kg/s]	0.009	0.009
Reynolds Number	1915	NA
Nusselt Number	8.91	4.36
Length to fully developed flow [m]	0.86	NA
Heat Transfer Coefficient [W/m^{2}K]	712.4	348.8

4.8 Empirical Analysis of Serpentine Collector

The overall heat loss coefficient was obtained experimentally for the serpentine collector and used to determine the heat removal factor using the Zang and Lavan approach. The calculation is shown in Table 4-5.

Table 4-5: Example calculation of F_R using the Zang and Lavan approach

Length of Serpentine Segment L	0.785 m
Distance Between W	0.14 m
Number of Segments	4
Plate Thickness	0.5 mm
Tube Outside Diameter D	8.0 mm
Tube Inside Diameter Di	7.5 mm
Plate Thermal Conductivity	237.0 W/m°C
Overall Loss Coefficient	11.8 W/m^2°C
Fluid mass flow rate	0.009 kg/s
Fluid specific heat	4200 J/kg°C
Fluid-to-tube heat transfer coefficient	343.6 W/m^2°C
Bond conductance	10000 W/m°C
κ =	0.66640582
γ =	-4.221013772
R =	0.1236
κR =	0.082390373
F1 =	0.992764580
F2 =	0.25041207
F3 =	7.212334005
F4 =	3.866184835
F5 =	6.859602566
F6 =	0.872767103
FR=	0.71

4.8.1 Experimental Validation

The heat transfer coefficients, calculated for the different flow regimes of the serpentine collector, were used in the calculation of the heat removal factor using the Zang and Lavan model. These were then compared with the experimental value of F_R and the results are shown in Table 4-6.

Table 4-6: Comparison of calculated vs experimental values for the serpentine collector

Flow Regime	Developing Laminar	Fully Developed Laminar
Calculated Heat Transfer Coefficient [W/m^{2}K]	712.4	348.8
Calculated heat removal factor - F_R	0.76	0.71
Experimental heat removal factor - F_R	0.71	

The calculated value of F_R is equal to the measured value when the Nusselt value for fully developed flow is used. This is in agreement with the work of Ghani who assumed that the flow was fully developed [125].

4.9 Empirical Analysis of Header Riser Collector

As with the serpentine collector, the heat removal factor for the header riser has been calculated using the overall heat loss coefficient obtained through experiment. The Hottel Whillier Bliss model is used and the calculation stages are shown in Table 4-7.

Table 4-7: Example calculation of F_R for the header riser collector using the Hottel Whillier Bliss approach

Heat Loss Coefficient	15.88	W/m^2
Tube Spacing	0.14	m
Tube inner diameter	0.0075	m
Tube diameter	0.008	m
Thickness of absorber layer	0.0005	m
Absorber thermal conductivity	237	W/m°C
Heat Transfer Coefficient inside tube	348.8	W/m^2 °C
Collector Area	0.4475	m^2
Specific heat of water	4200	J/kg°C
Mass flow rate	0.009	kg/s
$(U_L/(k_{abs}\delta_{abs}))^{-0.5}$	11.576	
Fin Efficiency	0.842	
Collector Efficiency	0.698	
Collector Flow Factor	0.937	
Heat Removal Factor	0.656	

4.9.1 Experimental Validation

The heat transfer coefficients, calculated for the different flow regimes of the header riser collector, were used in the calculation of the heat removal factor using the Hottel and Whillier Bliss model. These were then compared with the experimental value of F_R and the results are shown in Table 4-8.

Table 4-8: Comparison of calculated vs experimental values for the header riser collector

Flow Regime	Developing Laminar	Fully Developed Laminar	Turbulent
Calculated Heat Transfer Coefficient [W/m^{2}K]	467.9	348.8	2038
Calculated heat removal factor - F_R	0.69	0.66	
Experimental heat removal factor - F_R	0.66		

4.10 Discussion of Results from Empirical Analysis

In both the serpentine and the header riser, the calculated value for the heat removal factor matched that of the experimental results when fully developed laminar flow is assumed. Assuming that the flow inside the pipes is not yet developed, leads to an overestimation of the heat removal factor. This indicates that the inside the pipes of the experimental collector is fully developed laminar flow when the mass flow rate is 0.09kg/s.

4.11 Computational Fluid Dynamics

Computational Fluid Dynamics (CFD) is a numerical simulation that uses algorithms based on the governing equations of fluid flow to solve problems of fluid dynamics.

The first stage in any CFD analysis is definition of the problem. This involves creation of the geometry and its physical boundaries. The next step is to divide the volume of the geometry into discrete elements/volumes. In this step a mesh representation of the geometry is created; each element in the mesh has its own volume and surface area. The properties and behaviour of the fluid at the boundaries of the geometry are then defined. The governing equations of mass, momentum and energy are reformulated algebraically, in conservative form over each control volume in the mesh. This system of equations is then solved iteratively until the residuals converge.

4.11.1 Discretisation Approaches

There are several approaches that are used to discretise the partial differential equations (PDE) in a CFD problem [126]. These include:

- Finite Volume Method
- Finite Element Method
- Finite Difference Method – Taylor expansion is used to approximate the PDEs which are then discretised across a square network of lines. As a result this approach is not suitable for modelling problems in multiple dimensions.

4.11.2 Governing Equations for Finite Volume

The equations obtained from the finite control volume, either in integral or partial differential form are called the conservation form of the governing equations [127].

CFD expands the equations using Taylor series to determine the average time rate of change in the property of a fluid element as it passes through the control volume.

4.11.2.1 Conservation of mass

The continuity principle states that the mass inside the volume is conserved. Mass is related to the element volume using (4.32).

$$\delta m = \rho \delta V \tag{4.32}$$

The continuity principle states that the mass flow out of a volume is equal to the decrease of mass inside the volume, resulting in a net change of zero. This can be represented by:

$$\begin{aligned} &\frac{\partial(\rho \delta V)}{\partial t} = \delta V \frac{\partial \rho}{\partial t} + \rho \frac{\delta(\delta V)}{\delta t} = 0 \\ &\frac{\delta \rho}{\delta t} + \rho \nabla \cdot \vec{V} = 0 \end{aligned} \tag{4.33}$$

Where vector operator, ∇ , is defined as:

$$\nabla \equiv \vec{i}\,\frac{\partial}{\partial x} + \vec{j}\,\frac{\partial}{\partial y} + \vec{k}\,\frac{\partial}{\partial z} \tag{4.34}$$

The continuity principle in conservation form is written as:

$$\frac{\partial \rho}{\partial t} + \nabla \cdot \left(\rho \vec{V}\right) = 0 \tag{4.35}$$

4.11.2.2 Conservation of momentum

This principle is concerned with Newton's second law of motion.

$$\vec{F} = m\vec{a} \tag{4.36}$$

The second law states that the vector sum of the forces F on an object is equal to the mass of that object multiplied by the acceleration vector.

The conservation of momentum states the net momentum that occurs in the volume is zero i.e. the vector forces in opposing directions cancel each other out.

There are two forces that act on a moving fluid element. These can be categorised as;

Body Forces: These act directly on the volumetric mass of the fluid element and include gravitational, electric or magnetic forces.

Surface Forces: These forces act on the surface of the volume and include; pressure from the surrounding fluid, shear stress and normal stresses.

The equations used to determine the momentum of a fluid are known as the Navier-Stokes equations. They are shown in conservation form in (4.37):

$$\begin{aligned}
\frac{\partial(\rho u)}{\partial t} + \nabla \cdot \left(\rho u \vec{V}\right) &= -\frac{\partial p}{\partial x} + \frac{\partial \tau_{xx}}{\partial x} + \frac{\partial \tau_{yx}}{\partial y} + \frac{\partial \tau_{zx}}{\partial z} + \rho f_x \\
\frac{\partial(\rho v)}{\partial t} + \nabla \cdot \left(\rho v \vec{V}\right) &= -\frac{\partial p}{\partial y} + \frac{\partial \tau_{xy}}{\partial x} + \frac{\partial \tau_{yy}}{\partial y} + \frac{\partial \tau_{zy}}{\partial z} + \rho f_y \\
\frac{\partial(\rho w)}{\partial t} + \nabla \cdot \left(\rho w \vec{V}\right) &= -\frac{\partial p}{\partial z} + \frac{\partial \tau_{xz}}{\partial x} + \frac{\partial \tau_{yz}}{\partial y} + \frac{\partial \tau_{zz}}{\partial z} + \rho f_z
\end{aligned} \tag{4.37}$$

f is a specific directional force *(x,y,z)* divided by the mass F/m^2 [m/s^2]

4.11.2.3 Conservation of energy

The energy equation is based on the first law of thermodynamics – conservation of energy. This can be applied to the element as:

$$\text{Energy change} = \text{Net flux in} + \text{Rate of work done on the element} \tag{4.38}$$

The work done on a body is equal to the product of the force and the component of velocity in the direction of the force. The rate of work done by the body force acting on an element moving at a velocity V is equal to:

$$\rho \vec{f} \cdot \vec{V}(\mathrm{dx\ dy\ dz}) \tag{4.39}$$

Work done on a body is a result of shear and pressure forces. Work can be done on the body or the body can do work, the latter results in energy being expended and thus counts as negative work in the calculation of net flux.

The net flux in term shown in (4.38). The net flux can either be a result of volumetric heating such as absorption or emission of radiation or the heat transfer across the surface due to temperature gradients such as thermal conduction. The volumetric heating of the element can be calculated using:

$$Q_v = \rho \dot{q}\ \mathrm{dx\ dy\ dz} \tag{4.40}$$

The total energy of the fluid particle is the sum of its internal energy per unit mass, e, and its kinetic energy per unit mass. From (4.38)

$$\text{Energy Change} = \rho \frac{\delta}{\delta t}\left(e + \frac{V^2}{2}\right)\mathrm{dx\ dy\ dz} \tag{4.41}$$

The conservation form of the energy equation is written as (4.42) for internal energy and when kinetic energy is included; the conservation of total energy is shown in (4.43).

$$\begin{aligned}\frac{\partial(\rho e)}{\partial t} + \nabla \cdot \left(\rho e \vec{V}\right) = \rho \dot{q} &+ \frac{\partial}{\partial x}\left(k\frac{\partial T}{\partial x}\right) + \frac{\partial}{\partial y}\left(k\frac{\partial T}{\partial y}\right) \\ &+ \frac{\partial}{\partial z}\left(k\frac{\partial T}{\partial z}\right) - p\left(\frac{\partial u}{\partial x} + \frac{\partial v}{\partial y} + \frac{\partial w}{\partial z}\right) \\ &+ \lambda\left(\frac{\partial u}{\partial x} + \frac{\partial v}{\partial y} + \frac{\partial w}{\partial z}\right)^2 + \mu\left[2\left(\frac{\partial u}{\partial x}\right)^2\right. \\ &+ 2\left(\frac{\partial v}{\partial y}\right)^2 + 2\left(\frac{\partial w}{\partial z}\right)^2 + \left(\frac{\partial u}{\partial y} + \frac{\partial v}{\partial x}\right)^2 \\ &\left. + \left(\frac{\partial u}{\partial z} + \frac{\partial w}{\partial x}\right)^2 + \left(\frac{\partial v}{\partial z} + \frac{\partial w}{\partial y}\right)^2\right]\end{aligned} \tag{4.42}$$

$$
\begin{aligned}
&\frac{\partial}{\partial t}\left[\rho\left(e+\frac{V^2}{2}\right)\right]+\nabla\cdot\left[\rho\left(e+\frac{V^2}{2}\vec{V}\right)\right] \\
&=\rho\dot{q}+\frac{\partial}{\partial x}\left(k\frac{\partial T}{\partial x}\right)+\frac{\partial}{\partial y}\left(k\frac{\partial T}{\partial y}\right) \\
&+\frac{\partial}{\partial z}\left(k\frac{\partial T}{\partial z}\right)-\frac{\partial(up)}{\partial x}-\frac{\partial(vp)}{\partial y}-\frac{\partial(wp)}{\partial z}-\frac{\partial(u\tau_{xx})}{\partial x} \\
&+\frac{\partial(u\tau_{yx})}{\partial y}+\frac{\partial(u\tau_{zx})}{\partial z}+\frac{\partial(u\tau_{xy})}{\partial x}+\frac{\partial(u\tau_{yy})}{\partial y}+\frac{\partial(u\tau y)}{\partial z} \\
&+\frac{\partial(u\tau_{xz})}{\partial x}+\frac{\partial(u\tau_{yz})}{\partial y}+\frac{\partial(u\tau_{zz})}{\partial z}+\rho\vec{f}\cdot\vec{V}
\end{aligned}
\tag{4.43}
$$

4.12 CFD Modelling of Solar Collectors

CFD is desirable for the modelling of solar thermal systems as it can simultaneously solve fluid flow and heat transfer equations. Post-processing enables visualisation of the performance of the collector and surface temperature distribution can be evaluated. In the past, due to the iterative nature of the solver, number of cells in the model and number of physical models evaluated, CFD simulations have been very time consuming and highly demanding on computing resources. These difficulties have been alleviated with advancements in computing speed.

CFD has been used to model the flow distribution in an absorber with trapezoidal flow cavities [128]. The model was created in FLUENT and excellent agreement was achieved between the flow patterns in the experiment and those predicted by the computational model.

Fan et al. used CFD to investigate the flow distribution in a solar collector consisting of horizontally inclined absorber strips [129]. The model was validated against experimental results and showed good agreement. The temperature on the backside of the absorber tubes was measured using Type T thermocouples. These temperatures were adjusted to convert the wall temperatures into fluid temperatures. A simplified CFD model was used based on Equation 6.1 and heat flux [W/m].

$$heat\ flux = W_{fin}\eta_0 G \tag{6.1}$$

Where W_{fin} is the width of the fin (m) η_0 is the zero loss efficiency and G is the solar irradiance. The only losses that were taken into consideration in the CFD model were convective losses. The heat loss coefficient in the model was adjusted in the CFD program so that the collector efficiency is equal to the experimentally measured efficiency. The simulation was carried out in Fluent. A high density mesh was used which had 1.4 million mesh cell units.

Using the CFD model Fan investigated the influence of:

- Flow distribution under isothermal flow using a non-uniformity parameter
- Inlet flow rate and temperature

- Collector tilt angle
- Properties of the solar fluid

Fan et al. characterised the fluid flow through each tube as a percentage of total flow under isothermal conditions. The purpose of this was to determine the uniformity of flow across the tubes. In an ideal case the flow would be evenly distributed to each of the tubes. There were 16 tubes in the model. Fan found that flow rate decreased from the top to the bottom tubes and worsens when the inlet flow is increased. The lower the flow rate, and steeper the tilt, the stronger the influence of buoyancy effects. There was good agreement between measured and simulated performance. A result, gradual inclinations and faster flow rates had better uniformity.

When compared with experimental results, Fan found that the CFD simulations followed the same trend. He highlighted that there was a risk of boiling in his collector; however his collector was very large, measuring 5.96m x 2.27m.

Another CFD study was carried out by Selmi [130]. The CFD problem was multi-domain and included physical models for radiative and convective heat transfer between the collector components. The simulation was validated and showed close agreement with experimental measurements. The collector geometry modelled by Selmi consisted of a single pipe fixed to an aluminium absorber inside a wooden box with a glazed cover. The collector measured 1.5m x 0.16m wide. Both passive and active flow operating conditions were modelled and measured. Selmi measured; water inlet temperature, water outlet temperature, absorber plate temperature, pipe temperature, ambient temperature, solar irradiation and water flow rate. The CFD package used was a package from the Computational Fluid Dynamics Research Corporation (CFDRC). A transient simulation was carried out over the course of a day with changing values of solar irradiation. When the experimental results were compared with the results from the simulation, there was good agreement. However in the case of Selmi, it is interesting to note that the difference between inlet and outlet did not reduce when the inlet temperature was higher. This could be a result of the model not taking into account the heat loss coefficient of the collector appropriately.

CFD has also been used to determine the average heat transfer coefficients for forced convection over a flat plate collector [131]. A finite volume approach using Fluent 6.3 software was taken. For ease of experimental validation, mass transfer was used and later converted to heat transfer. The study investigated the influence angle of attack on Nusselt number. It was that the Nusselt number was not greatly affected by the range of angles investigated. The work concluded that

"…the two dimensional boundary layer theory does not take into account the flow of motions directed towards the lateral edge of the collector plate."

This causes an overestimation of wind-related heat losses using the standard equation, which in the opinion of the authors is not appropriate for the calculation of heat losses.

Manjunath and Karanth carried out studies using CFD models based on conjugate heat transfer and discrete transfer radiation model (DTRM) [132] [133]. These models, like that of Selmi, only takes into account a single pipe and absorber configuration. In their study they investigate the impact of unique serrated tubes on thermal performance. They conclude that serrations enhance the heat transfer between plate and the absorber due to increased surface area.

Martinopoulos used CFD to simulate the performance of a polymer solar collector [134]. The model was validated experimentally and good agreement was achieved.

Dovic developed a CFD model to simulate the performance of corrugated plate solar collectors [135]. In his study Dovic carried out a parametric investigation of common characteristics of solar thermal collectors, such as bond conductance, tube diameter, distance between cover and absorber, optical properties of the absorber and flow rate. Dovics' simulations were confined to a single fin segment of the absorber.

Unlike many of the other studies, which only simulated of a segment of the collector, Marroquin carried out a CFD simulation of a full size collector and compared the performance of absorbers with rectangular and circular cross sectional tubes [136].

Iordanou developed a simplified CFD model to simulate the performance of a solar collector exposed to the Mediterranean Climate [137]. The study investigated the use of a porous mesh in the solar collector to enhance performance. The experimental and simulation work were in close agreement with a 10% enhancement in convective heat transfer in the collector which contained the aluminium mesh insert. In addition to the CFD simulation Iordanou also developed a lumped parameter model that can be used to rapidly determine the thermal performance of a solar collector. The conclusion of the research was that the metallic insert improves the performance of a solar collector. Even though the author makes this claim, there is no comparison provided, of the pumping required with and without the porous metallic insert. If more pumping power is required then enhanced performance may be overshadowed by the extra input energy that is required.

4.12.1 Creating the CFD Model

This section details the methodology used in the CFD approach.

4.12.2 Problem Definition

The objective of this study was to create a numerical model in CFD that simulates the thermal performance of a solar thermal flat plate collector. The key output from the simulation will be the temperature distribution across the collector surface. The model will be validated against both the empirical models and experimental results to determine the accuracy of the solution. The model inputs will be:

1. Incident irradiation
2. Inlet temperature
3. Overall heat loss coefficient

4.12.3 Creation of Geometry

Three dimensional models were created in Rhino 3D. The length and width of the model matched that of the experimental collector; however the thickness of the absorber plate was increased from 0.5mm to 8mm to ensure enough space for the volume meshing; as the simulation is performed under steady state conditions, the capacitive effects of the thicker plate will not be taken into account.

The diameter of the pipes connected to the back of the absorber is 8mm. The simulation assumes $D_e = D_i$. In the simulations, thermal contact was achieved through a recession of the tubes into the plate. A contact length of 8mm was assumed as it was not possible to measure the contact length on the experimental collector. In a solar collector, heat transfer mainly occurs through width of the fin (x-dimension), not through the thickness (z-dimension). For this reason it was appropriate to use the reference conductivity of aluminum from the CFX material library (237W/m°C at 25°C).

4.12.4 Meshing

4.12.4.1 Rebuild Curves

The meshing application used in this study was Ansys ICEM, Version 13.0. The 3D geometries were imported as IGES files. The curves were then deleted and rebuilt using the imported surfaces. The reason for this was to prevent the mesh snapping to any unnecessary curves that were not essential or were accidentally included in the import step. A diagnostic topology was created to check the surfaces were imported correctly. Curves were filtered so that no topology was created if the tangency of two adjacent surfaces was less than 30°. Topologies were highlighted by colour and if successful, should resemble those shown in Figure 4-12.

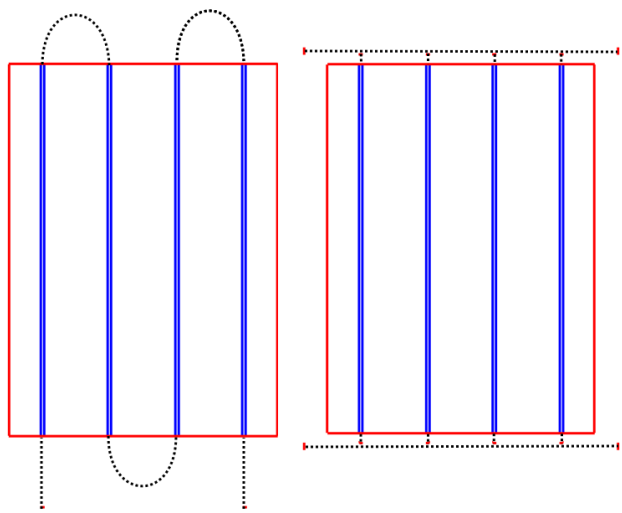

Figure 4-12: Successful diagnostic topology showing the curves for the serpentine (left) and header riser (right). The red lines indicate the geometry boundaries and the blue lines indicate the interface between the absorber and the pipes.

4.12.4.2 Part Assignment

The surfaces of the model were then assigned to the following parts:

a. Collector-Boundary
b. Collector-Air-Interface
c. Collector-Water-Interface
d. Collector-outer
e. Tubeinlet
f. Tubeoutlet
g. Tubeboundary

The next step was to specify the domains in the model. The models in this study consisted of two material domains:

h. SolidDomain
i. WaterDomain

4.12.4.3 Global Meshing Parameters

Under the global meshing tab, the maximum element size was specified as 5mm. The global parameters for volume meshing were then set. The mesh type was unstructured Tetra/Mixed because this could accommodate for the bends in the pipework and provided a good interface between the absorber and pipe work. An Octree meshing method was used as this allowed for refinement of the mesh in pertinent areas. The Octree method is a top-down approach that uses subdivision to ensure that the element size requirements are met throughout each of the domains.

A prism mesh was applied to surfaces where heat exchange takes place. Prism meshing allows for better modelling of boundary layer physics. In this case they were applied to the interface layers to ensure accurate capture of the heat transfer processes. Layers of prisms are extruded from the specified surfaces of the tetra mesh. The global prism parameters are shown in Figure 4-13.

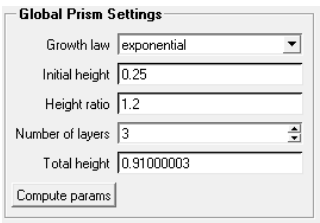

Figure 4-13: Global prism settings

4.12.4.4 Surface Meshing Parameters

To add refinement to the areas of interest, surface controls were applied to the mesh. The most import areas were those where heat transfer was occurring. It was also important to capture the boundary layer effects in the pipework as this influences the internal heat transfer inside the pipe. The surface controls were specified by the maximum size of element. Other important parameters include the height ratio of the prism and tetra layers. In both of these cases the growth rate was set to 1.3. This means that from the layers from the surface will grow at a size

rate of 1.3 which ensures smooth transitions in the mesh. A summary of the surface meshing controls is shown in Figure 4-14.

part	prism	hexa-core	max size	height	height ratio	num layers	tetra size ratio	tetra width	min size limit	max deviation	int wall
COLLECTOR-AIR-INTERFACE	☑		5	0	1.3	0	1.3	0	0	0	☐
COLLECTOR-BOUNDARY	☐		5	0	0	0	1.3	0	0	0	☐
COLLECTOR-WATER-INTERFACE	☑		1.5	0	1.3	0	1.3	0	0	0	☐
SOLIDDOMAIN	☐	☐									
TRIMSRF	☐		0						0	0	
TUBE-BOUNDARY	☑		2	0	1.3	3	1.3	0	0	0	☐
TUBEINLET	☑		2	0	1.3	3	1.3	0	0	0	☐
TUBEOUTLET	☑		2	0	1.3	3	1.3	0	0	0	☐
WATERDOMAIN	☐	☐	3								

☑ Show size params using scale factor
☐ Apply inflation parameters to curves
☐ Remove inflation parameters from curves
Highlighted parts have at least one blank field because not all entities in that part have identical parameters.
Apply Dismiss

Figure 4-14: Surface meshing controls applied to the geometry

4.12.4.5 Mesh Creation

The mesh was generated using the volume meshing algorithm and the option to extrude the prism layers immediately after the tetra meshing had finished was selected. The total number of elements in the serpentine model was just under 4 million elements, after the prism layers had been extruded. The header-riser model had a greater number of cells, at just over 4 million, due to the inclusion of the header pipes at the top and bottom of the absorber.

4.12.4.6 Mesh Quality

To assess the quality of the generated mesh, the aspect ratio of the tetra elements were calculated and a histogram produced. The quality indicator in ICEM calculates the aspect ratio for all tetra elements. The aspect ratio for a tetra element is defined as the ratio of the radii of an inscribed sphere to a circumscribed sphere for each element. A ratio of 1 is perfectly regular and a ratio of 0 indicates an element with zero volume. It was found that when all elements have a quality >0.2 the solution shows good convergence. To ensure that this was achieved the mesh was smoothed globally. A comparison of the histograms before and after the smoothing process is shown in Figure 4-15.

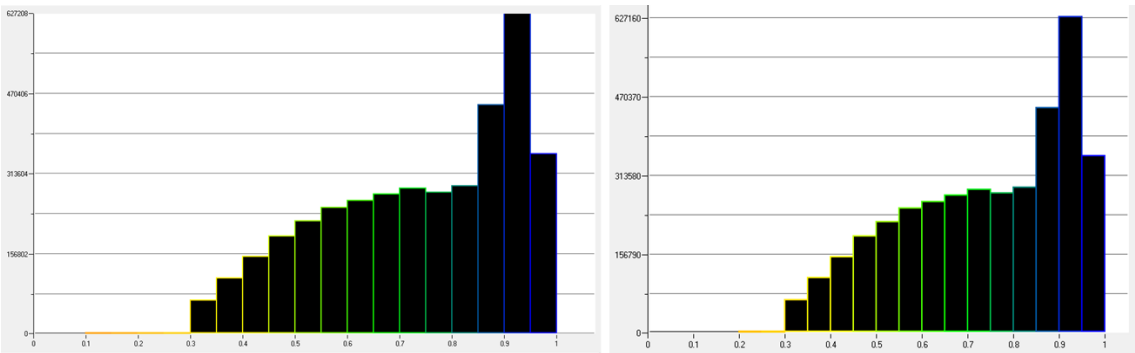

Figure 4-15: Comparison of Histogram before (left) and after (right) smoothing operations had been carried out for the mesh of the serpentine collector.

From the before and after histogram it can be seen that the vast majority of elements have high aspect ratio before smoothing iterations are applied. The smoothing operation helped improve

the quality of 100 elements that were below the 0.2 threshold. Even though they are few in number, these cells could have led to problems in solution convergence.

To ensure the mesh was consistent throughout each domain, a cut plane was generated through the y-axis. Figure 4-16 shows a section of the cut plane through the mesh at the absorber-pipe interface. It is clear to see the layers of prisms at the tube interface and the top surface of the absorber. It can also be seen that the tetra elements are smaller in size around the absorber-tube interface to accurately model the physics in this area.

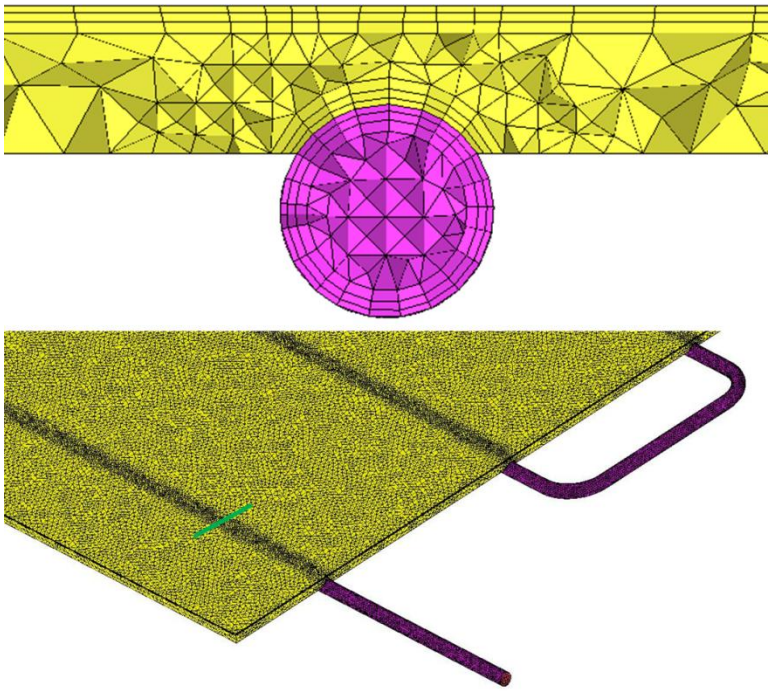

Figure 4-16: Segment of cut plane through the mesh

4.12.4.7 Mesh Export

The generated mesh was exported in CFX5 format. A 0.001 scaling factor was applied to convert units from millimetres into meters.

4.12.4.8 General Boundary Conditions

The mesh was then imported into was Ansys CFX Pre Version 13.0 and the following steps were then taken to specify the boundary conditions of the problem:

1. **Creation of absorber domain**: This is a solid domain and was assigned the properties of Aluminium from the material library. The thermal energy option for heat transfer is selected and the initialisation temperature was set at the inlet temperature plus 15°C.

2. **Creation of pipe domain**: This is specified as a fluid domain and was assigned the properties of water from the material library. As the collector is horizontal in this study the effects of buoyancy are neglected. The thermal energy equation is activated in this domain and the turbulence model is set to laminar. The initialisation temperature is set at the inlet temperature.

3. **Inlet and outlet specification**: To achieve the desired mass flow rate through the inlet, the appropriate velocity normal to the surface was created. The reason this option was selected and not mass flow rate is because velocity is a universal parameter in the CFD simulation and mass flow is only a calculated value. The velocities used at each inlet temperature are shown in Table 4-9. The outlet condition was set with an average static pressure of 0 pa.

4. **Absorber surface specification**: The top surface of the absorber is specified as a wall. The value of incident radiation, as measured in the experimental testing, is entered as a boundary energy source. The overall heat loss coefficient, as determined from the experimental thermal efficiency curve is also assigned to this boundary. The experimental ambient temperature is also assigned and this is used to drive the losses from the absorber surface. The relationship between temperature of the top surface as calculated by the CFX solver is shown in (4.44).

$$q_{loss} = U_L \left(T_b - T_a \right) \tag{4.44}$$

Where UL is the heat loss coefficient, T_b is the temperature at the boundary and T_a is the specified ambient temperature.

Table 4-9: Velocity parameters for each inlet temperature

	Inlet Temperature [C]	Collector Area [m2]	Required Mass Flow Rate [kg/s]	Density of Water [kg/m3]	Inlet Area [m^2]	Velocity for Inlet [ms^{-1}]
Serpentine	21	0.45	0.009	998	5.03E-05	0.17941
	35	0.45	0.009	994	5.03E-05	0.18013
	50	0.45	0.009	988	5.03E-05	0.18122
	65	0.45	0.009	980	5.03E-05	0.18270
	80	0.45	0.009	971	5.03E-05	0.18440
Header-Riser	21	0.45	0.009	998	1.77E-04	0.05103
	35	0.45	0.009	994	1.77E-04	0.05124
	50	0.45	0.009	988	1.77E-04	0.05155
	65	0.45	0.009	980	1.77E-04	0.05197
	80	0.45	0.009	971	1.77E-04	0.05245

4.12.4.9 Developed flow at inlet

An expression was applied to the inlet boundary to generate a velocity profile representative of fully developed flow. The equation used is shown in (4.45) [122].

$$u_r = 2u_{ave}\left(1-\frac{r^2}{R_{\max}^2}\right)$$
$$r = \sqrt{(i-i_o)^2+(j-j_o)^2} \tag{4.45}$$

Where R_{max} is the radius of the pipe, u_{max} is the velocity at the centre of the pipe, r is the distance from the centre, and i and j are coordinates (x,y,z) when the inlet is positioned on the plane ij. The subscript o denotes the central coordinate of the inlet. A velocity cross section through the inlet pipe, using the simulation results is shown in Figure 4-17.

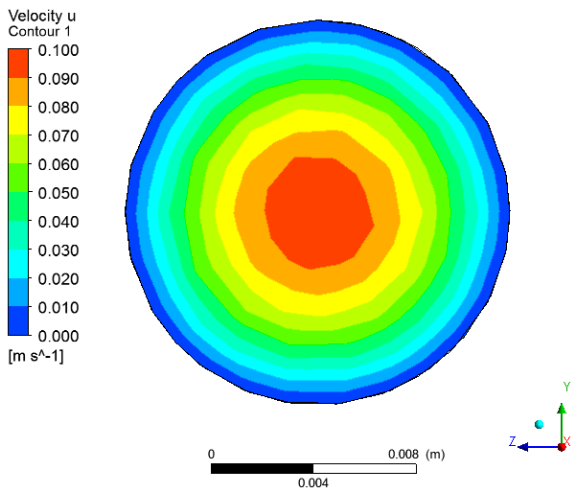

Figure 4-17: Velocity contour across inlet assigned with develop flow profile

4.12.4.10 CFD Solver

The definition file was solved using the Ansys CFX Solver Version 13.0. Convergences of the following residuals were monitored; momentum, mass, heat transfer and energy balance. All of the runs were carried out for a minimum of 600 iterations. The convergence plots for the serpentine and header riser collector are shown in Figure 4-18 and Figure 4-19 respectively. In all cases the residuals reached less than 1.0^{-5} and an energy imbalance of zero. The time taken for the simulation ranged from 1.5 hour to 3 hour per simulation, depending on partitioning, on a quad core processor. The convergence was consistent across the inlet temperature range investigated.

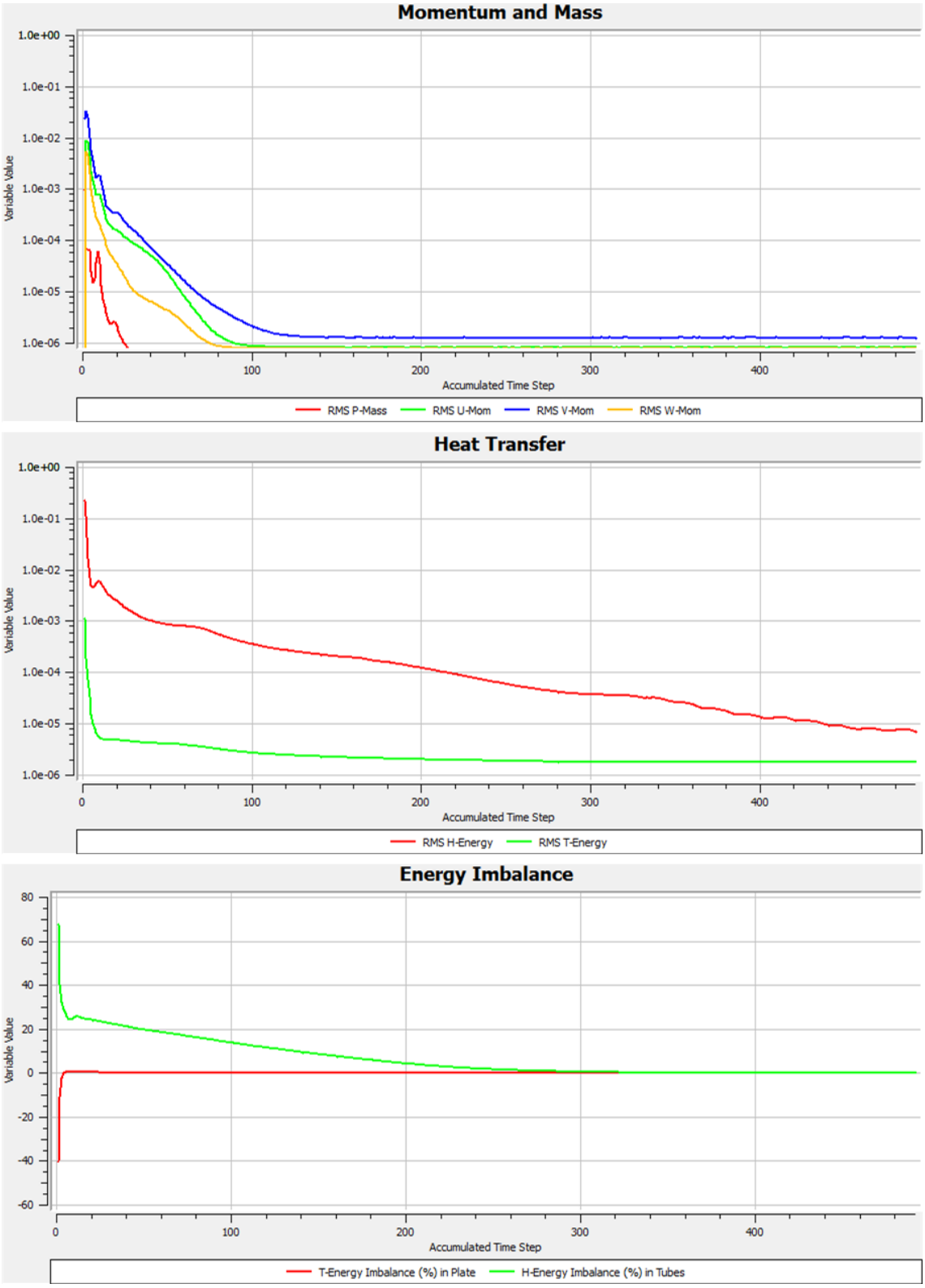

Figure 4-18: Solution residuals for serpentine collector with 50°C inlet temperature

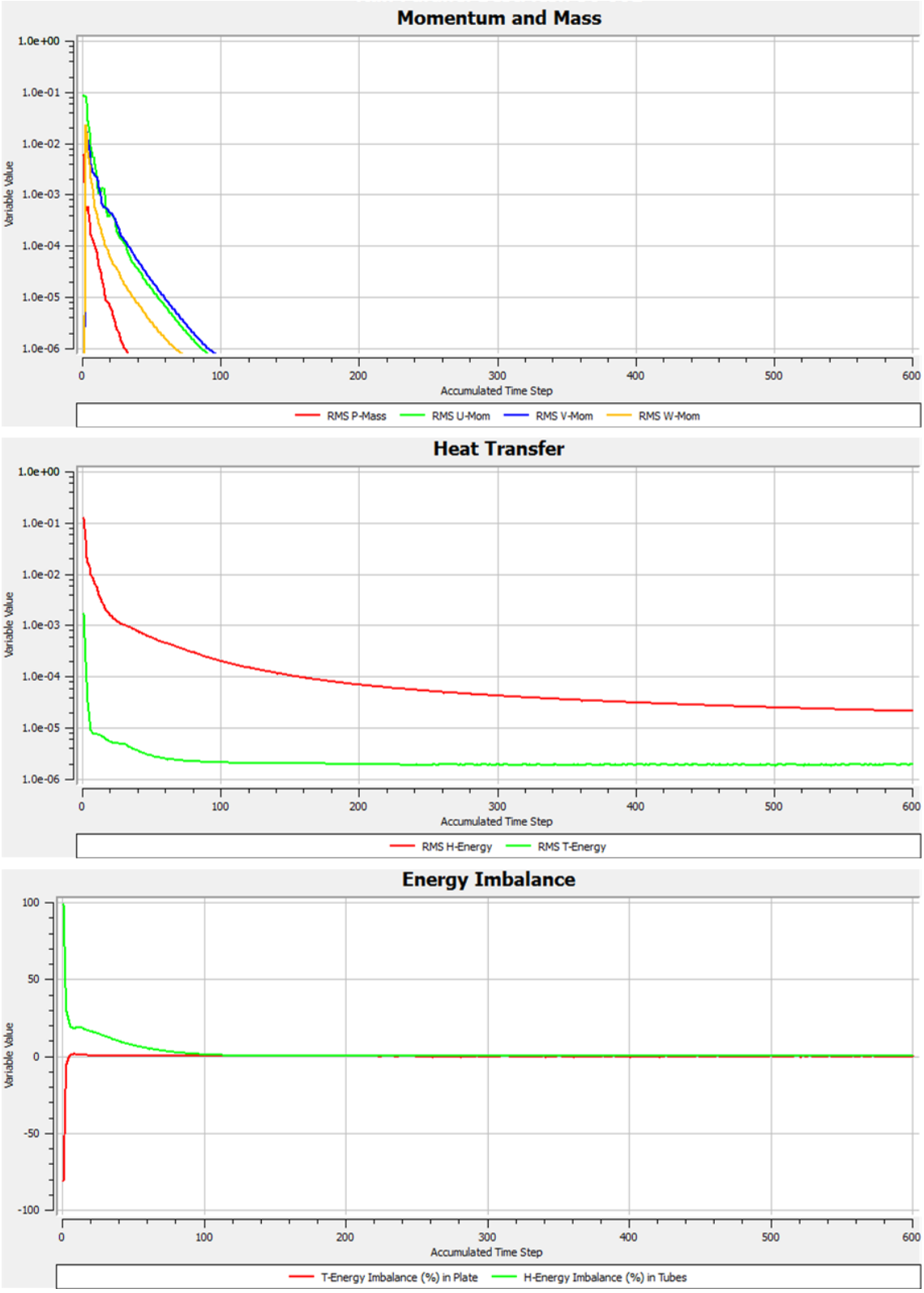

Figure 4-19: Solution residuals for parallel collector with 50°C inlet temperature

4.12.4.11 Mesh Sensitivity

To investigate the sensitivity of the solution three different resolutions of mesh were created and the results compared. Mesh refinement was carried out by adding a sizing control on the absorber-water interface as this was the area where heat transfer between the domains takes place. The highest density mesh had a surface control of 1.0mm and the lowest density mesh

had a surface control of 2.0mm, the influence of mesh sensitivity is shown in Table 4-10. It was decided that the best trade-off between accuracy and computation time was the 1.5mm size control.

Table 4-10: Results of mesh sensitivity study for the serpentine collector

Size of Surface Control on Interface	Total Elements in Mesh	Collector Efficiency
2mm	2035986	0.736
1.5mm	3800363	0.705
1.0mm	4884033	0.699

4.12.4.12 Simulation of thermal efficiency curve

The experimental thermal efficiency curves were simulated by creating a separate definition file for each inlet temperature. Each simulation was used to plot an individual point on the curve. The inlet temperatures investigated were; 21°C, 35°C, 50°C, 65°C and 80°C. The ambient temperature for all simulations was set at 21°C; therefore the result at T_i = 21°C is equal to the zero loss efficiency.

4.13 Simulation Results

The results were post processed in CFX CFD-Post, Version 13.0. In this section the simulation data is first compared with the experimental data.

4.13.1 Experimental Validation

4.13.1.1 Comparison of Thermal Efficiency Curves

The experimental and simulated efficiency curves for the serpentine and header riser collector are compared in Figure 4-20 and Figure 4-21 respectively.

In the calculation of efficiency for the CFD model the irradiance, specified as a heat flux at the boundary layer, was divided by 0.95 to compensate for the surface absorbtance. For each inlet temperature the efficiency has been calculated during outputs from the post processing using the CFX function calculator. The calculation of efficiency at each steady state inlet temperature was calculated using Eq. (4.46).

$$\eta_t = \frac{c_p \dot{m}\left(T_o - T_i\right)}{G_{\exp} / \alpha} \tag{4.46}$$

Where G_{exp} is the value of irradiance measured during the experimental testing.

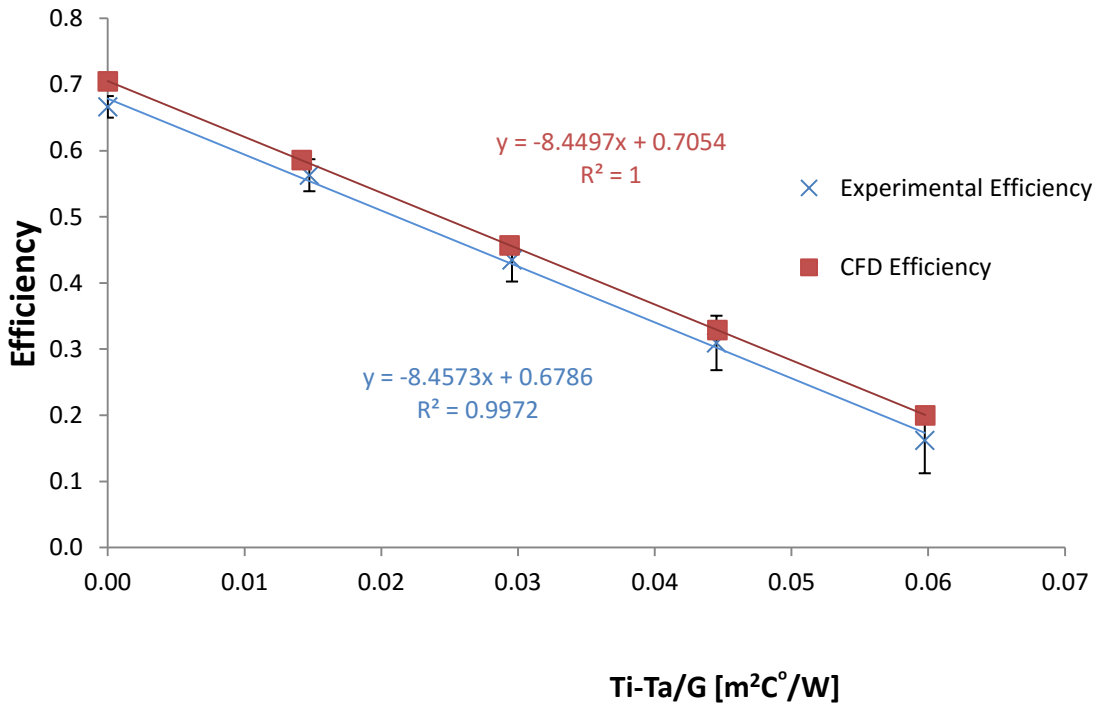

Figure 4-20: Comparison of experimental and CFD thermal efficiency curves for serpentine collector

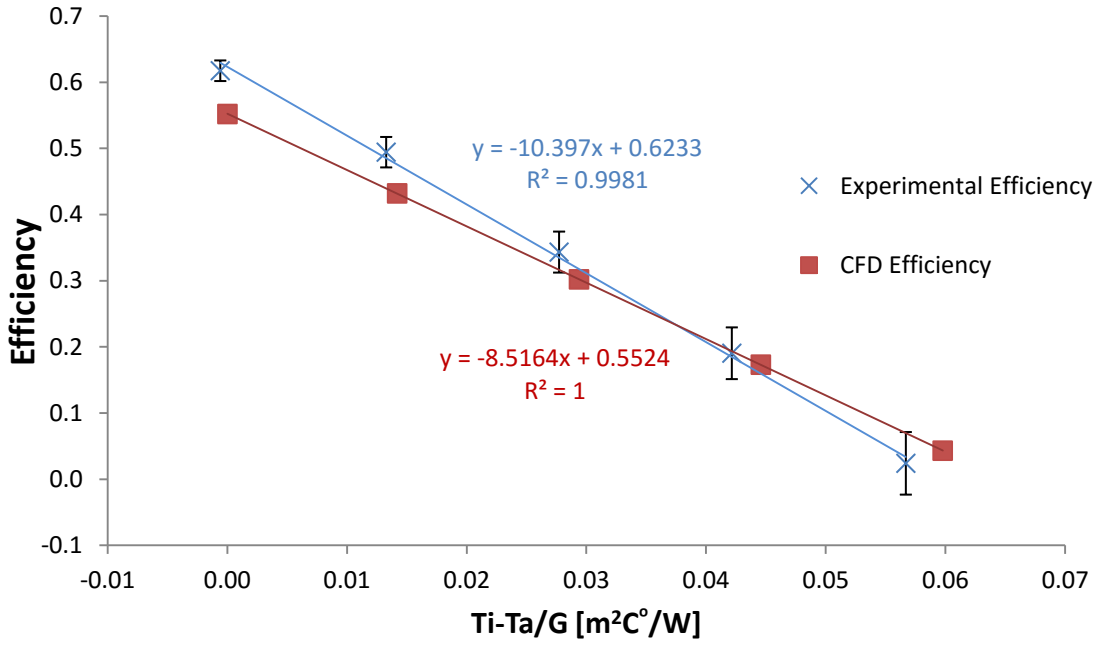

Figure 4-21: Comparison of experimental and CFD thermal efficiency curves for header riser collector

The values of $F_R(\alpha\tau)$ and U_LF_R were extracted from the equation of the line using the same approach detailed in the experimental methodology section. A comparison between the experimental and simulated values of F_R and U_L are shown in Table 4-11.

Table 4-11: Comparison of values of F_R and U_L measured experimentally and calculated using CFD

Parameter	Experimental		Simulation	
	Serpentine (abs)	**Header Riser (abs)**	**Serpentine (abs)**	**Header Riser (abs)**
Zero Loss Efficiency $F_R(\alpha\tau)$	67.86 (± 2.19)%	62.71 (± 2.08)%	70.54	0.5524
U_LF_R [W/m^2°C]	8.4573 ± 0.071	10.486 ± 0.08	8.4497	8.5164
F_R	0.71 ± 0.037	0.66 ± 0.035	0.74	0.58
U_L [W/m^2°C]	11.84 ± 0.60	15.89 ± 0.84	11.39	14.64

The simulated value of F_R for the serpentine collector was calculated at 0.74; this is 4.2% higher than the experimental value. There is less agreement seen in the header riser collector where the simulated value of F_R is 12.1% less than the experimental value. To explain the discrepancies between the simulated and measured values of F_R, the factors that influence it must be identified. It can be seen from (4.7) that F_R is influenced by the collector efficiency factor (4.6) which in turn is influenced by parameters such as fin width, conductance of the plate, contact resistance between the pipe and the absorber, pipe diameter and internal heat transfer coefficient in the pipe. It can also be seen that F_R is dependent on U_L ; with its value decreasing as U_L increases. All of these factors will influence the ability of the CFD simulation to match the experimental value. An attempt must also be made to identify the reason why the agreement varies so much between the two models. Over the next few sections results are reported on varying the influencing factors of F_R.

The simulated value of U_L is 3.8% less than the experimental value for the serpentine collector and 7.87% less than the experimental value for the header riser collector. There is a problem with this approach though as the value of U_L is calculated using F_R so the errors could be introduced into the calculation.

Another check on the value of U_L can be carried out by plotting the graph of Eq. (4.1). By doing this the value of U_L is independent of F_R. The values of U_L calculated using this approach is 12.18 and 15.78 respectively; see Figure 4-22 and Figure 4-23. This results in a difference of +2.9% and -0.70% between the experimental and simulated results for the serpentine and header riser collector respectively. This check is performed to establish if the simulation is matching the heat loss coefficient that was specified on the boundary of the top surface. Using this approach there is a good agreement between the specified value and the simulated value. Despite this there is still some deviation in the value and this could be indicative of simulation error. Such simulation errors can arise from round off error, iteration error, solution error or model errors.

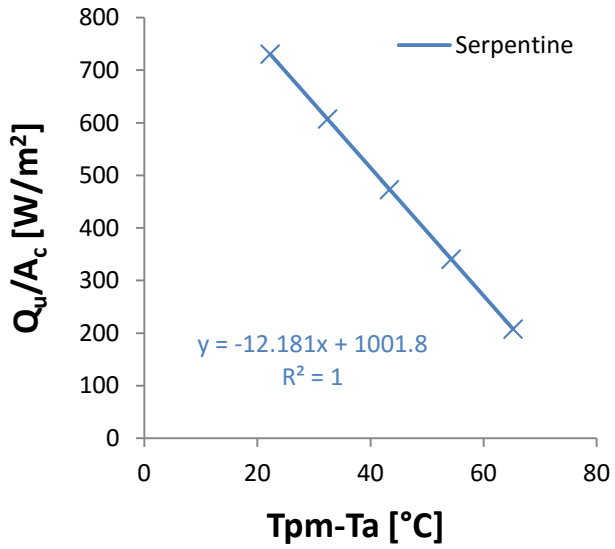

Figure 4-22: Plot of energy useful energy per m^2 of collector surface for simulated serpentine collector

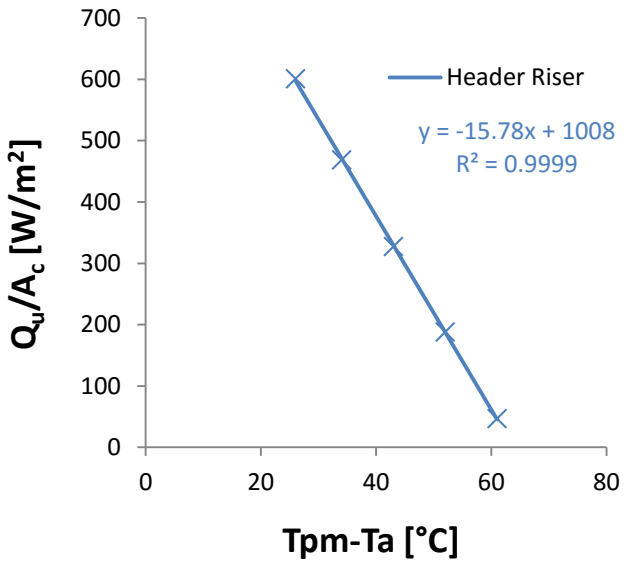

Figure 4-23: Plot of energy useful energy per m^2 of collector surface for the simulated header riser collector

The y-intercept of the graphs shown in Figure 4-22 and Figure 4-23 is the optical efficiency when the surface temperature of the collector is equal to the ambient. This value should be equal to the irradiance specified on the boundary in the simulation. In the header riser simulation the specified irradiance was 1034W/m^2 and in the serpentine simulation 987W/m^2; these values are equal to those measured during the experimental test. This means that the difference between the specified boundary condition and final result is -2.5% for the header riser and +1.5% for the serpentine collector.

4.13.1.2 Comparison of Average Absorber Temperature

A comparison has been made between the simulated values of average absorber temperature and those measured using the thermocouples attached to the back of the absorber. The results for the serpentine collector are shown in Figure 4-24.

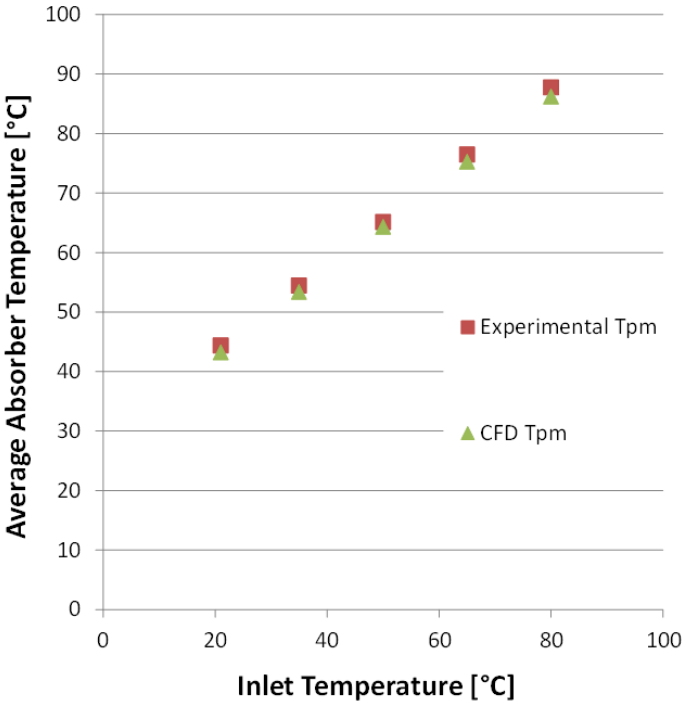

Experimental [°C]	Simulated [°C]	Difference
44.37	43.2	2.54%
54.45	53.4	1.91%
65.10	64.3	1.17%
76.45	75.3	1.56%
87.72	86.2	1.73%

Figure 4-24: Comparison of experimental and CFD results for average absorber temperature for serpentine collector. The difference is shown as a percentage from the experimental value.

For the serpentine collector the simulated absorber temperature was less than the experimental value at all data points. The difference varied from 1.17% at 50°C inlet temperature to 2.54% at the 21°C inlet temperature.

The results for the header riser are presented in Figure 4-25. In this case the simulated value is over estimated by 4.87% at the first data point at inlet temperature of 21°C and then becomes increasingly underestimated until the last data point where the simulated value is 7.16% less than the experimental value.

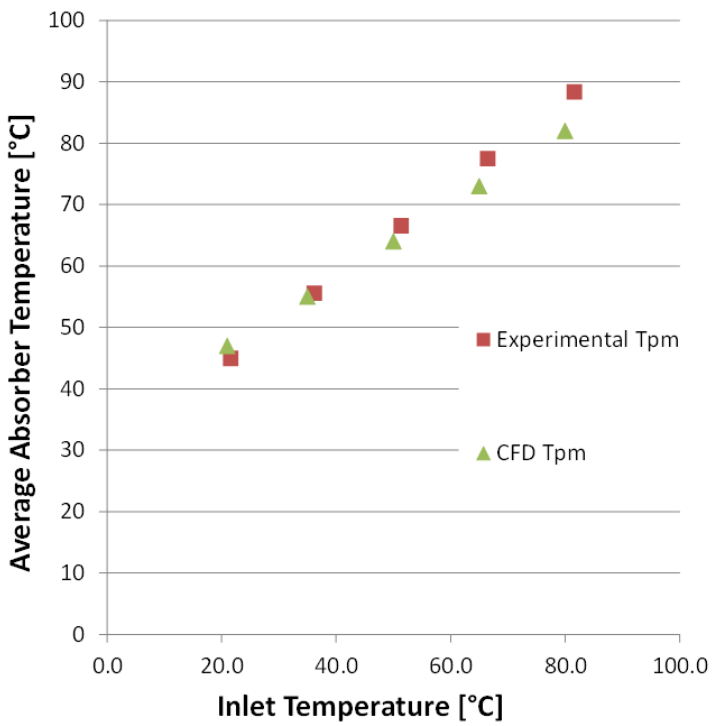

Experimental [°C]	Simulated [°C]	Difference
44.94	47.1	-4.87%
55.59	55.4	0.36%
66.54	64.3	3.44%
77.48	73.1	5.63%
88.33	82.0	7.16%

Figure 4-25: Comparison of experimental and CFD results for average absorber temperature of header riser collector. The difference is shown as a percentage from the experimental value.

To further compare the results from the CFD, the minimum and maximum temperatures have been plotted for the experimental and simulated data. The results are presented in Table 4-12 for the serpentine collector.

Table 4-12: Distribution of absorber temperature for serpentine collector

	Experimental				CFD			
	Mean	**Max**	**Min**	**Range**	**Mean**	**Max**	**Min**	**Range**
21	44.2	47.0	40.0	7.0	43.2	46.3	36.4	9.8
35	54.3	56.4	48.9	7.5	53.4	55.9	47.8	8.1
50	64.9	67.1	58.7	8.4	64.3	66.3	60.0	6.3
65	76.2	78.4	69.9	8.5	75.3	76.7	72.1	4.6
80	87.5	89.6	81.0	8.6	86.2	87.1	84.3	2.8

4 rows of thermocouples were placed in the centre of each fin making a total of 32 thermocouples. The readings therefore represent an average temperature of the fin. The surface temperatures for the CFD simulation are taken from the entire surface area and therefore include temperature extremes at the end of the fin and directly above the pipe. The results in Table 4-12 show a discrepancy in the temperature range on the absorber for the experimental and CFD simulation. In the experimental results the range of temperature on the absorber increases with temperature and in the CFD simulation the temperature range decreases with temperature.

Table 4-13: Distribution of absorber temperature for header riser collector

	Experimental				CFD			
	Mean	**Max**	**Min**	**Range**	**Mean**	**Max**	**Min**	**Range**
21	44.8	47.2	42.3	4.9	47.1	50.9	39.9	11.0
35	55.4	57.8	52.7	5.1	55.4	58.3	49.8	8.6
50	66.3	68.5	63.4	5.1	64.3	66.3	60.3	6.0
65	77.2	79.4	72.6	6.8	73.1	74.3	70.9	3.4
80	88.1	90.2	83.3	6.9	82.0	82.3	81.5	0.8

The same trend is seen in the results for the header riser collector presented in Table 4-13; however in this case the experimental temperature range is even greater than that measured in the serpentine collector. The range from the CFD simulation again reduces with inlet temperature whereas the range in the experimental increases slightly.

Figure 4-26 shows the thermal processes that occur in the fins of the collector to explain the discrepancies in the results. In Figure 4-26A the collector is operating under optimal conditions; the temperature at the inlet is low and close to ambient. This means that there is a large temperature gradient across the width of the fin. The result of this temperature gradient means that the heat from fin is readily transferred into the collector fluid. Because the temperature of the collector is close to ambient, the temperature driven losses from the surface are minimised. In Figure 4-26B the inlet temperature has been increased but the incident irradiance remains the same. As the inlet temperature increases, the temperature of the collector increases and thermal losses increase; this results in a reduction of the maximum possible energy gain by the collector. The collector will eventually reach equilibrium when the temperature driven losses equal the irradiance gain. At this point the temperature across the collector will be uniform. Figure 4-26C shows the condition when the inlet temperature continues to increase after reaching equilibrium; after this point the collector experiences a net loss. The temperature profile of the collector has been reversed and the coldest part of the collector is now midway between the fins.

The calculation of irradiance assumed a value of absorbtance for the absorber. This was supplied by the manufacturer and its value was 0.95. In this calculation the useful energy gain was used to determine the irradiance. In the experimental chapter it is discussed that absorbtance is a factor of incident angle. If the absorbtance was less, due to a non-ideal angle of incidence from the simulator, then the irradiance would have been under estimated. The calculation of irradiance also assumes perfect contact between the absorber and the tube. Figure 4-27 shows that the laser welding of the copper pipe to the aluminium pipe does not always create good contact at the interface.

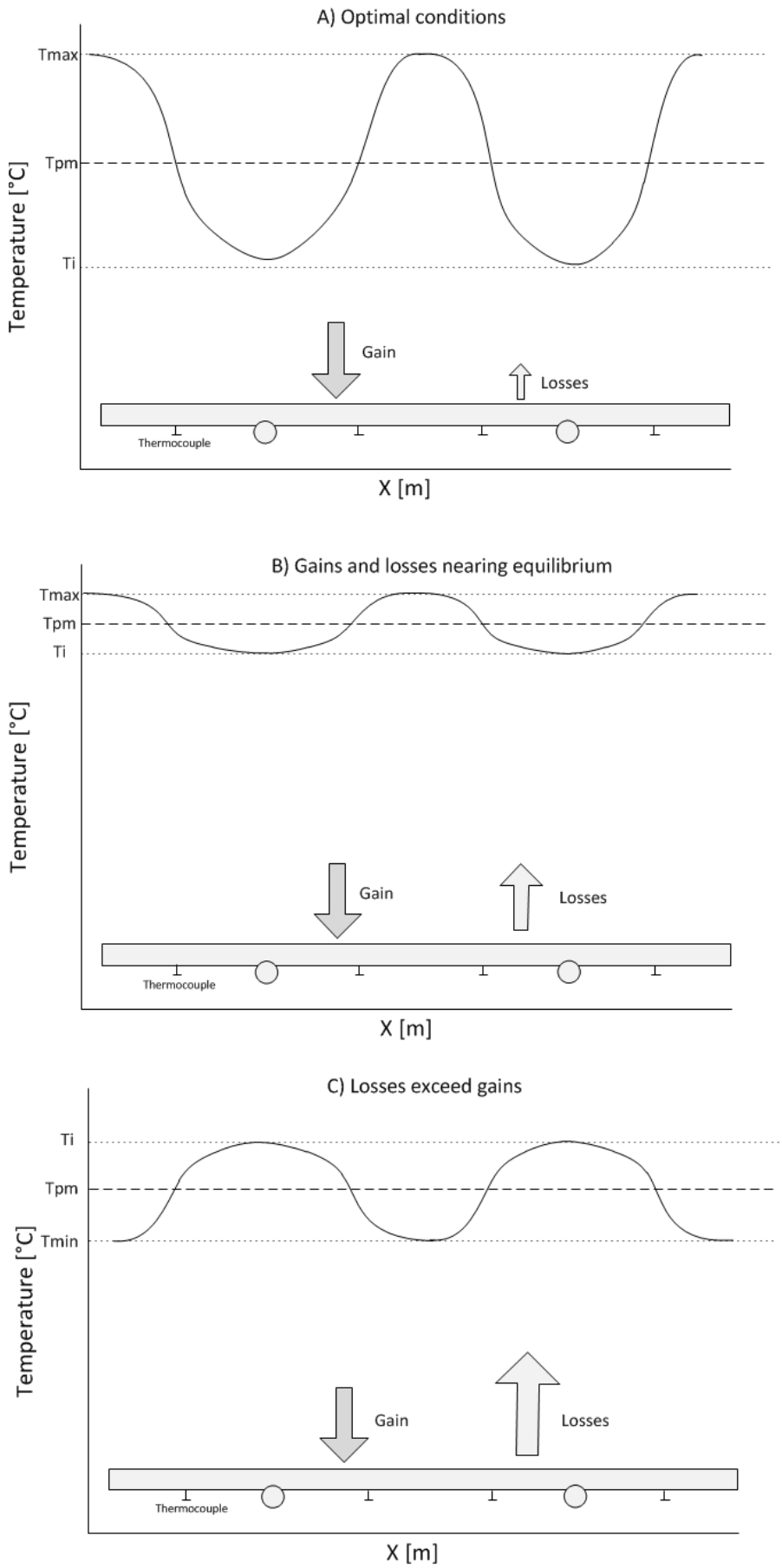

Figure 4-26: Heat transfer process and surface temperature across an absorber

Figure 4-27: Separation of laser welded pipes on similar absorber. Source [104]

This non-ideal contact creates thermal resistance between the tube and the pipe. The result is that the temperature of the plate would increase more rapidly and heat losses from the surface will be higher at lower inlet temperatures. If this is occurring in the experimental study, it could explain why the temperature of the plate is higher. The problem is that the efficiency of experimental system is higher than that of the CFD simulation. The reason for this is that efficiency is being calculated using the measured value of irradiance, if this has been underestimated then it will lead to higher calculations of efficiency. The discrepancy in thermocouple readings could be a result of poor conductance between the plate and the pipe, if this is less than optimal, it will lead to higher surface temperatures in the plate.It is contradictory however that the performance of the experimental collector is better than the simulation. The reason for this could be due to the heat transfer coefficient in the tubes. The CFD model has assumed that the pipes are completely smooth but on inspection there were joins that could have disturbed the flow and created turbulent regions in the pipe with higher heat transfer coefficient. It is also possible that trapped air bubbles are in the pipe work of the experimental absorber reducing the heat transfer coefficient. To overcome this problem the collector should be tilted and purged prior to the experiment.

4.13.1.3 Comparison of Surface Temperature Distribution

The low emissivity coating (5% at 100°C as specified by manufacturer) meant that is was not possible to carry out thermal imaging of the absorber surface during thermal efficiency testing. When the light source was on, an image of the light was reflected in the thermal image and gave misleading results. The only way to prevent this reflection was to reverse the operation by testing under zero irradiance. The results of this test are shown Figure 4-28. In the image on the left an inlet fluid temperature of 10°C is supplied to the collector and on the right hand side is an image of the collector cover at a temperature of 80°C. It is possible to see from these images that there is a temperature gradient between the centre of the pipe and the middle of the fin.

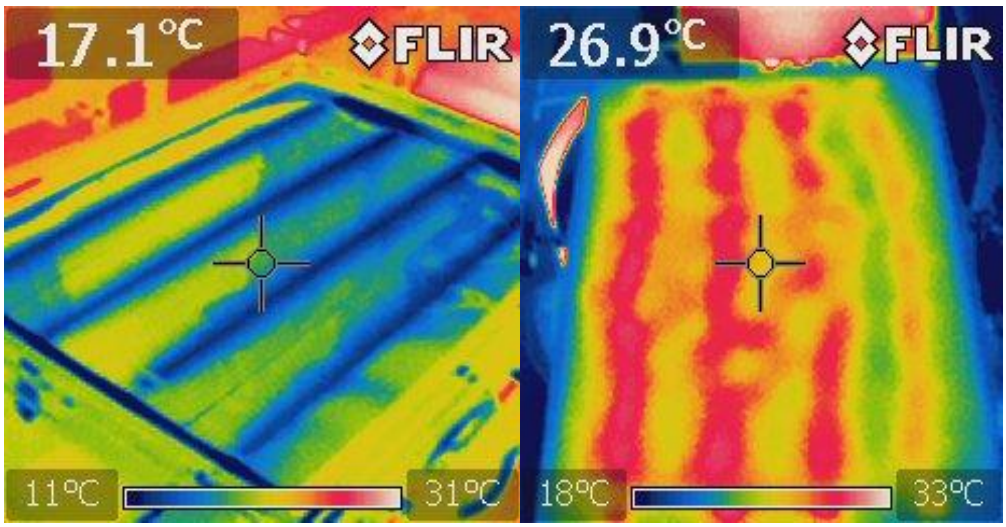

Figure 4-28: Thermal image of serpentine collector during dark testing – 10°C inlet temperature on the left and 80°C inlet temperature on the right. In both cases there was no irradiance.

Despite differences in the measured and simulated of average temperature, the distribution of the temperature is compared in Figure 4-29 and Figure 4-30 for the serpentine and header riser collector respectively.

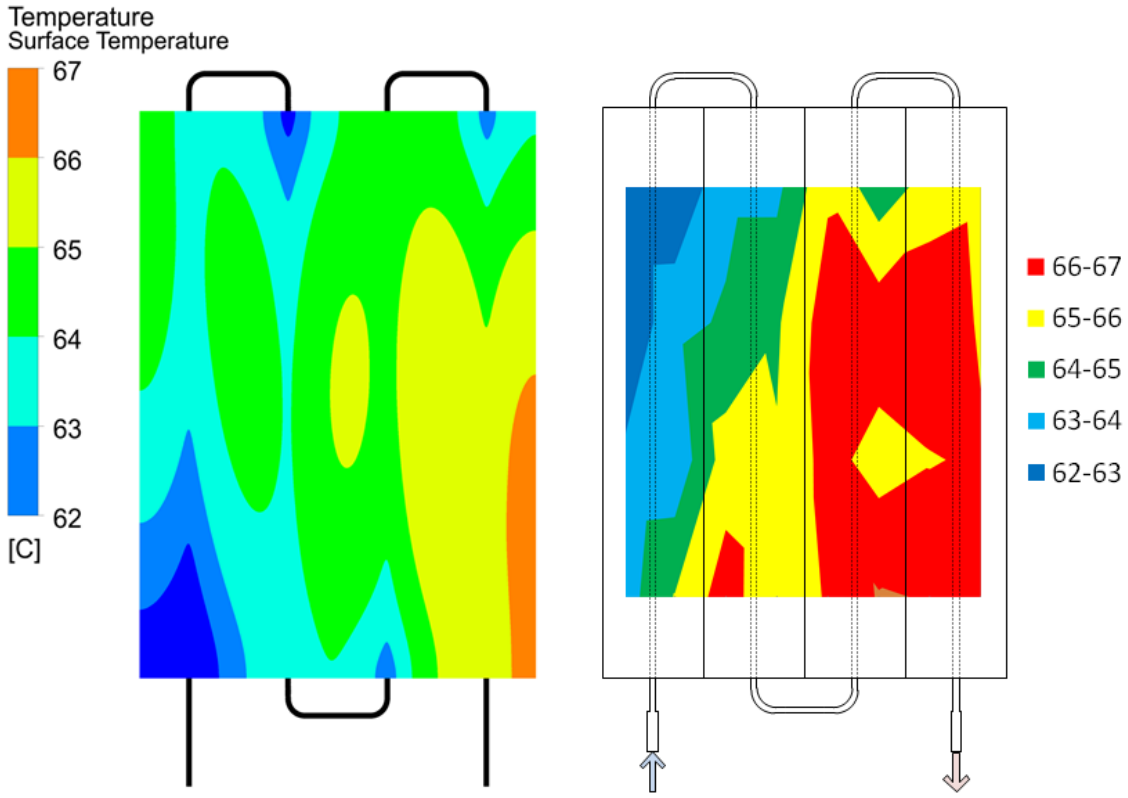

Figure 4-29: Comparison of temperature distribution for serpentine collector with 50°C inlet temperature. Simulated results are on the left and measured on the right.

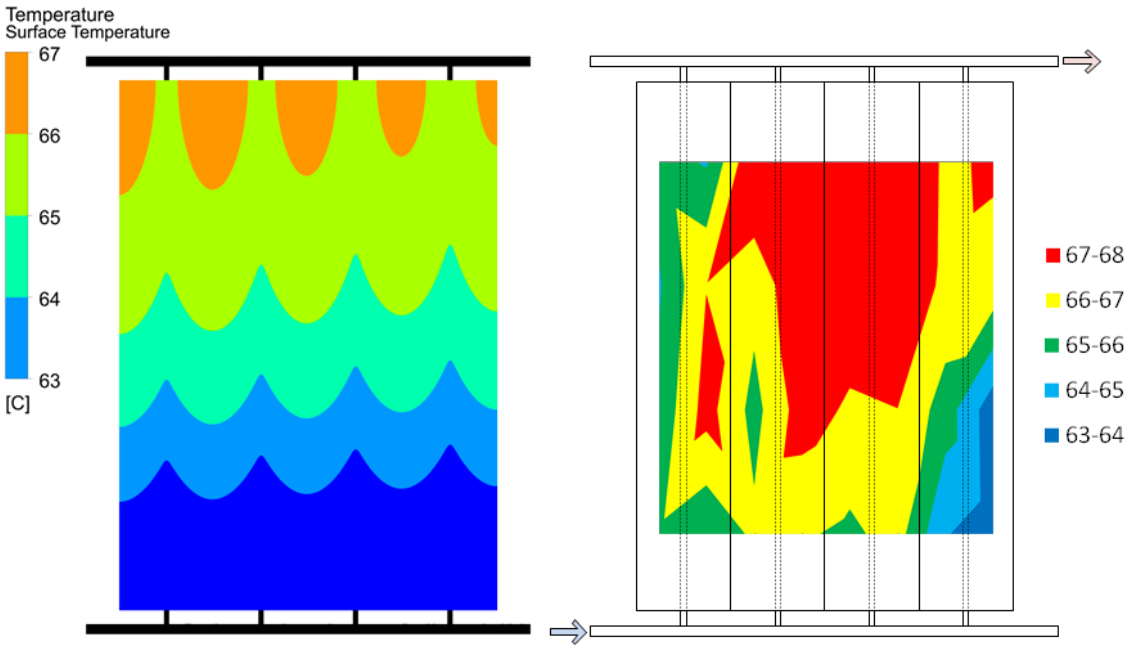

Figure 4-30: Comparison of temperature distribution for header riser collector with 50°C inlet temperature. Simulated results are on the left and measured on the right

A visual comparison of the simulated and the experimental results show there is a different trend seen in the serpentine and header riser collector. In the serpentine collector there is temperature variation across the width of the collector in both the simulated and the experimental results. In the serpentine simulation, cold areas occur on the collector surface after each bend. This is a result of increased heat transfer due to fluid mixing as it moves around the bend. In contrast to the serpentine collector where a temperature gradient was seen across the x-axis, in the header riser collector, the temperature gradient occurs in the y-axis.

4.14 Analysis of Results

4.14.1 Increased resistance at the interface

The impact of increasing the contact resistance between the tube and the plate thermal efficiency is shown in Table 4-14. These were carried out by assigning the resistance value to the pipe-absorber interface in the CFD simulation.

Table 4-14: Influence of increasing the thermal contact resistance between the absorber and the pipe on efficiency of serpentine collector

Resistance [m^2°C/W]	Thermal Efficiency
0	0.729
0.00025	0.693
0.0005	0.667
0.001	0.629

The contact boundary length is defined as the segment of the inner tube that is in contact with both the heat removal fluid and the metal of the absorber plate. This concept is explained in Figure 4-31. The integrity of the bond between the pipe and the absorber is uncertain and

without an accurate measurement of the conductivity across this boundary, this could be the cause of discrepancy between experimental and simulated values.

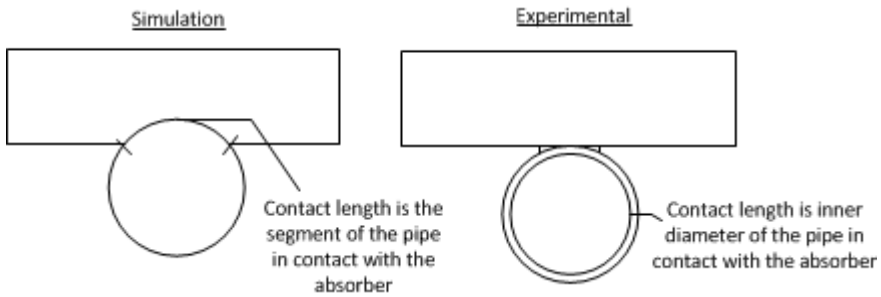

Figure 4-31: Difference in thermal contact design between the simulation and the actual collector

The impact of efficiency of changing the contact length is quantified in Table 4-15. It can be seen from these results that by increasing the contact length by embedding the pipe deeper into the plate, the efficiency is increased.

Table 4-15: Influence of increasing the contact length between the fluid and the absorber for the serpentine absorber

Contact Length	Thermal Efficiency
4 mm	0.681
8 mm	0.729
12 mm	0.82

4.14.2 Modelling heat transfer at the interface

In the simulation detailed in this study heat transfer only occurs through the top section of the pipe in contact with the absorber. In reality there will be heat transfer around the entire internal circumference of the tube. Capturing the heat transfer in the bottom section of the tube poses a problem for meshing as the element count increases considerably due to additional elements in the pipe wall. To investigate the effect of heat transfer through the lower sections of the pipe wall, a section of absorber (37 x 470 x 5.5mm) and pipe were modelled. It was found that the volume averaged temperature of the absorber for the top-contact model was 1.09°C (3.3%) higher than the full-contact model, see Figure 4-32. Further work should be carried out to investigate more efficient meshing practice or it may be possible to develop a coefficient that links the amount of heat transferred to the length of contact between the pipe and the absorber.

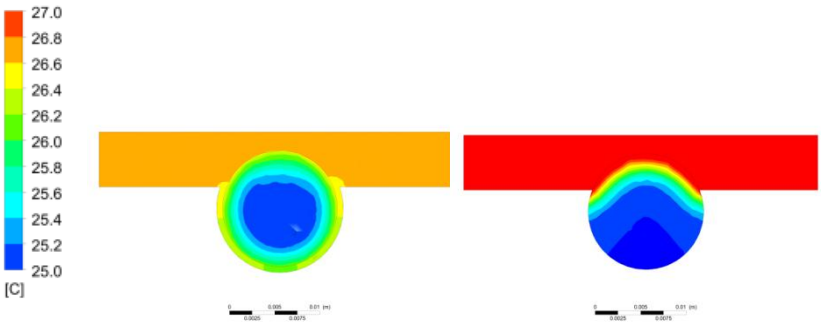

Figure 4-32: Temperature distribution across the cross section of different contact situations. The full contact model is shown on the left and top contact model is shown on the right.

4.14.3 Calculation of heat transfer coefficient in simulation

The heat transfer coefficient in the pipe was estimated using Eq. (4.47).

$$h_{fi} = \frac{Q_u / A_i}{T_{pb} - T_{wb}} \tag{4.47}$$

Where T_{pd} is the average bulk temperature of the plate domain, T_{wb} is the average bulk temperature of the water domain, Q_u is the useful steady energy output of the collector and A_i is the area of the pipe-collector interface.

The heat transfer coefficient for each inlet temperature is shown in Table 4-16.

Table 4-16: Calculation of internal heat transfer coefficient from CFD resultsusing mass flow rate at inlet

Inlet Temperature [°C]	Header-Riser	Serpentine
	h_{fi} [W/m^2°C]	
21	485.23	776.42
35	485.83	778.80
50	486.69	779.99
65	487.70	782.25
80	489.25	785.87

4.14.4 Velocity profiles in the pipes

By plotting the velocity profiles inside the pipes attached to the absorber it is possible to visualise areas of fluid mixing. These areas are indicated by regions of high velocity. These can create localised regions of turbulence that increases the heat transfer coefficient.

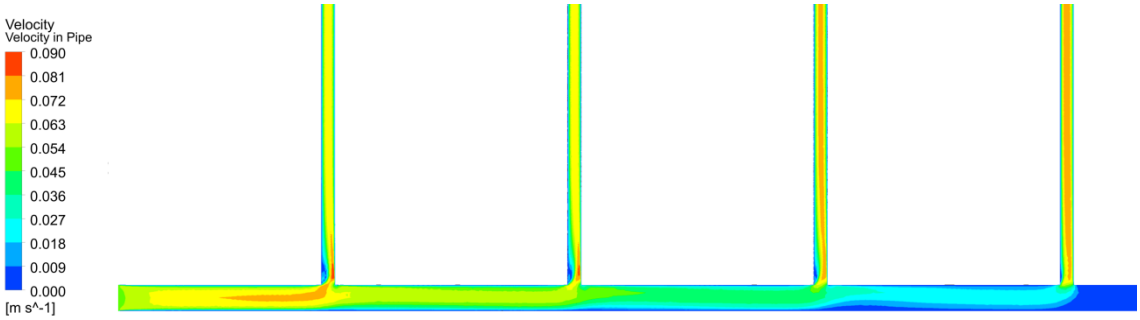

Figure 4-33: Velocity profile along the header and risers

Figure 4-33 shows the velocity profile in the centre of the pipe where each of the risers branch from the header pipe. The velocity builds up just before the first riser but the development of a wake at the riser entrance reduces the flow in this pipe. The majority of the flow is channelled through the final tube which is in agreement with other published work. The velocity to each of the tube increases across the width of the tube. The effect of the variation in flow rate can be seen in Figure 4-30, where the absorber over the pipes is colder in regions above the highest velocity risers. The influence the flow has on the absorber surface can be seen in Figure 4-30.

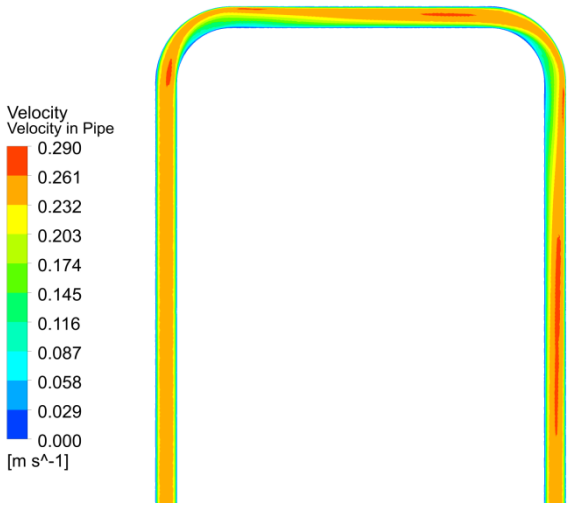

Figure 4-34: Velocity profile in one of the U bends of the serpentine collector

Figure 4-34 shows the velocity profile in the U bend of the serpentine collector. There are regions of high velocity before, during and after the fluid moves through the U-bend. The result of this is increased mixing. Because the Reynolds number is greater in the serpentine collector, these regions of high velocity extend further than the regions of high velocity in the header riser collector. The effect of increased fluid mixing on absorber temperature is shown in Figure 4-29, where the absorber temperature is coldest when the pipe regions the collector after the fluid has been mixed as it moves through the bend. Streamlines have been plotted inside the tubes and these are shown in Figure 4-35.

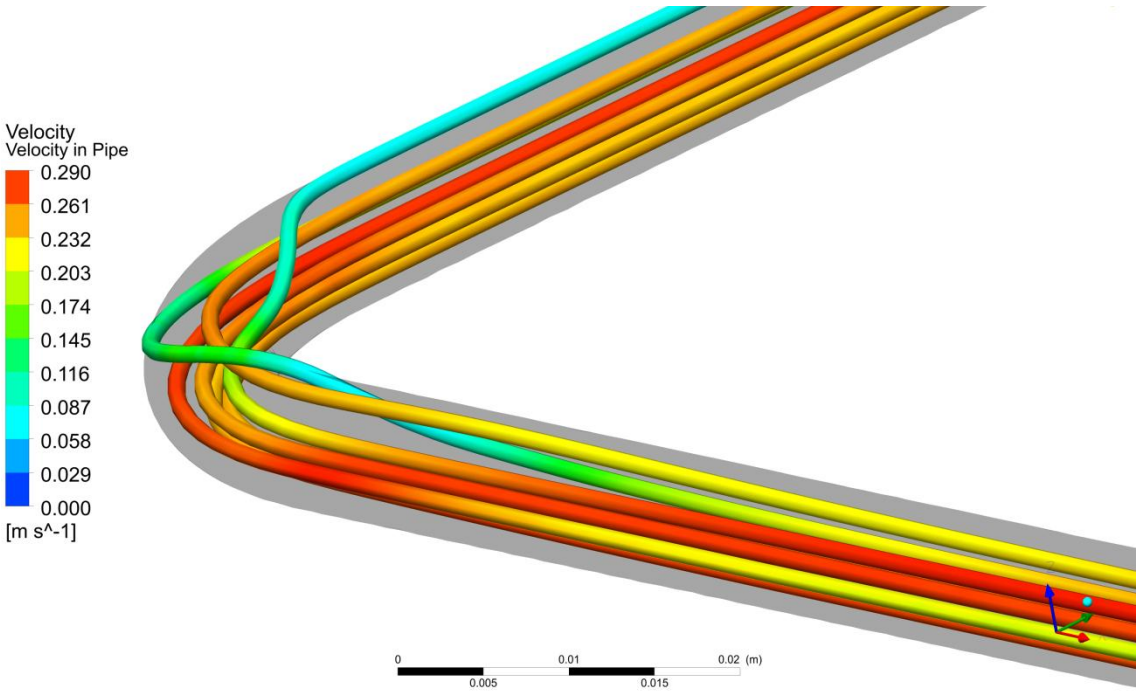

Figure 4-35: Streamlines in the U bend of the serpentine collector to show fluid mixing

i. Pumping power to energy gain

The electrical power consumed to pump water through the collector can be calculated using:

$$P_{pump} = \dot{m}p \tag{4.48}$$

Where, $\dot{m}$ is the mass flow rate and p is the pressure drop across the collector in Pascal's. In this case we assume that the pump is 100% efficient which is suitable for a comparison to be made. Table 4-17 and Table 4-18 show the calculation of thermal output per unit of power required to pump fluid through the collector for the serpentine and header riser collector respectively. It can be seen that as the inlet temperature increases, the pressure drop increases. As the viscosity decreases with temperature, kinetic energy is increasing and the increased friction results in the greater pressure drop.

Table 4-17: Calculation of thermal output to pumping power for serpentine collector

Inlet Temperature [°C]	Serpentine			
	Pressure Drop [Pa]	Required Pumping Power [W]	Q_u [W]	Q_u/P_{pump}
21	506	4.55	326	71.59
35	509	4.58	271	59.16
50	513	4.62	211	45.7
65	518	4.66	152	32.6
80	524	4.71	92.7	19.70

Table 4-18: Calculation of thermal output to pumping power for header riser collector

Inlet Temperature [°C]	Header Riser			
	Pressure Drop [Pa]	Required Pumping Power [W]	Qu [W]	Qu/P_{pump}
21	29.12	0.262	268	1022
35	29.26	0.298	209	793.2
50	29.47	0.265	147	553.9
65	29.76	0.268	84	312.9
80	30.09	0.271	20.1	76.83

The pressure drop in the serpentine collector is much greater than the header riser collector due to the 180 degree bends. This requires much more power from the pump to circulate water. Even though the header riser produces less thermal output, less power is required to pump the water through the collector. The result is that the header riser collector produces much more thermal energy per unit of electrical energy used to circulate the fluid. The pressure drop across each of the collectors is illustrated in Figure 4-36.

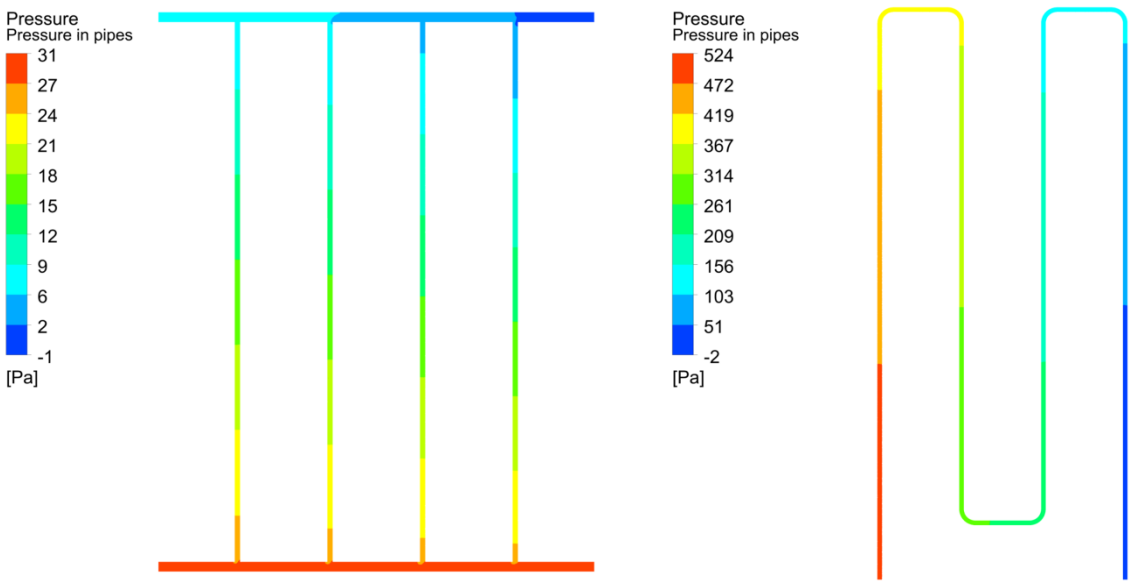

Figure 4-36: Pressure drop comparison in the header-riser and serpentine collector

4.14.5 Influence of non-uniform irradiation

When measuring the irradiance it was discovered that there was a degree of non-uniformity across the surface of the collector. These readings are detailed in the experimental chapter. It was thought that if this variability in irradiance occurred in regions that were particularly efficient at absorbing heat, for example on an area where the fluid is mixed, then the overall efficiency could be influenced. This study involved re-meshing the geometry, but this time the top surface was split into individual segments that would be assigned a different irradiation quantity based on the deviation from the mean at that point. The average irradiance would remain the same across the entire collector. Table 4-19 shows the adjustment coefficient for each segment of the collector. The work was carried out on the header riser collector as this displayed the largest discrepancy between simulated and experimental results. The individual segments across the surface of the absorber are shown in Figure 4-37.

Table 4-19: Coefficients used to adjust the average value of irradiance across the surface of the absorber

		Column			
		A	B	C	D
Row	1	0.89	0.97	0.96	0.87
	2	1.00	1.13	1.14	1.03
	3	0.93	1.03	1.04	0.96
	4	1.02	1.09	1.07	0.95
	5	0.95	1.02	1.01	0.93

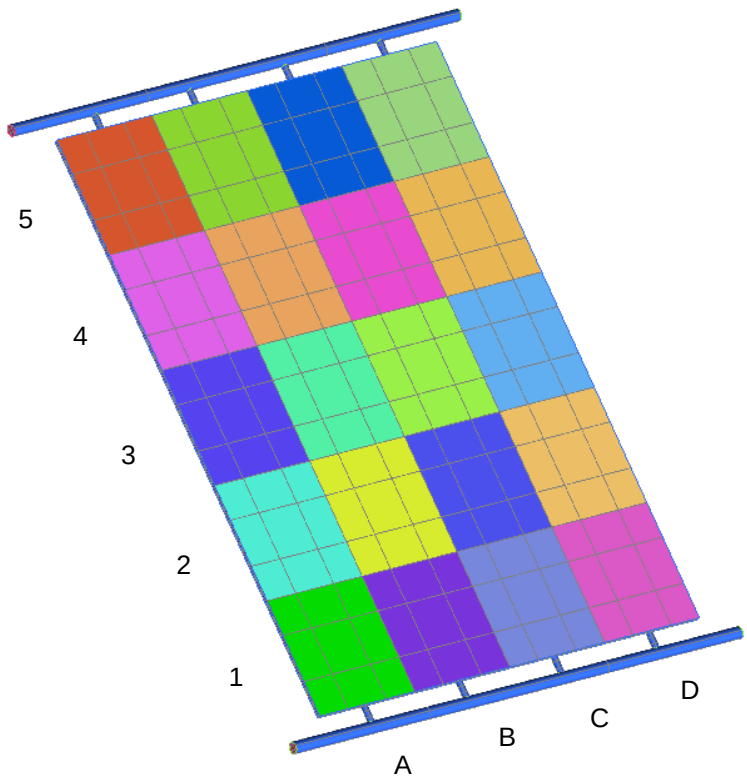

Figure 4-37: The control surfaces of the parallel collector in ICEM which were assigned varying quantities of irradiance

The coefficients of the average irradiance were assigned to each surface. It was found that by varying the irradiation across the surface of the collector, the efficiency was slightly increased from 0.55 to 0.57. This therefore did not explain the entire discrepancy between the experimental and the simulated result however it is a contributing factor. The influence on surface temperature distribution from changing the distribution of irradiance is shown in Figure 4-38.

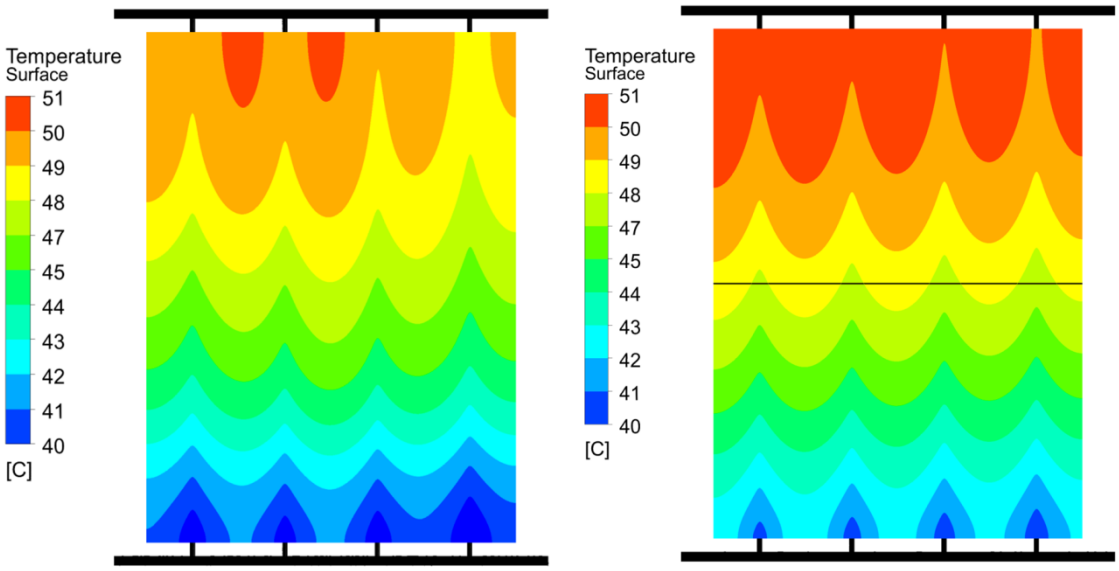

Figure 4-38: Comparison of temperature distribution for non-uniform (left) and uniform (right) irradiance

ii. Comparison of different flow patterns in header riser collector

The flow in a manifold is split between the pipes that serve it. To investigate the effect this has on surface temperature of the absorber different flow patterns in a header riser collector were simulated using CFD. The flow patterns investigated in this study are shown in Figure 4-39 and the results are summarised in Figure 4-40 and Figure 4-41.

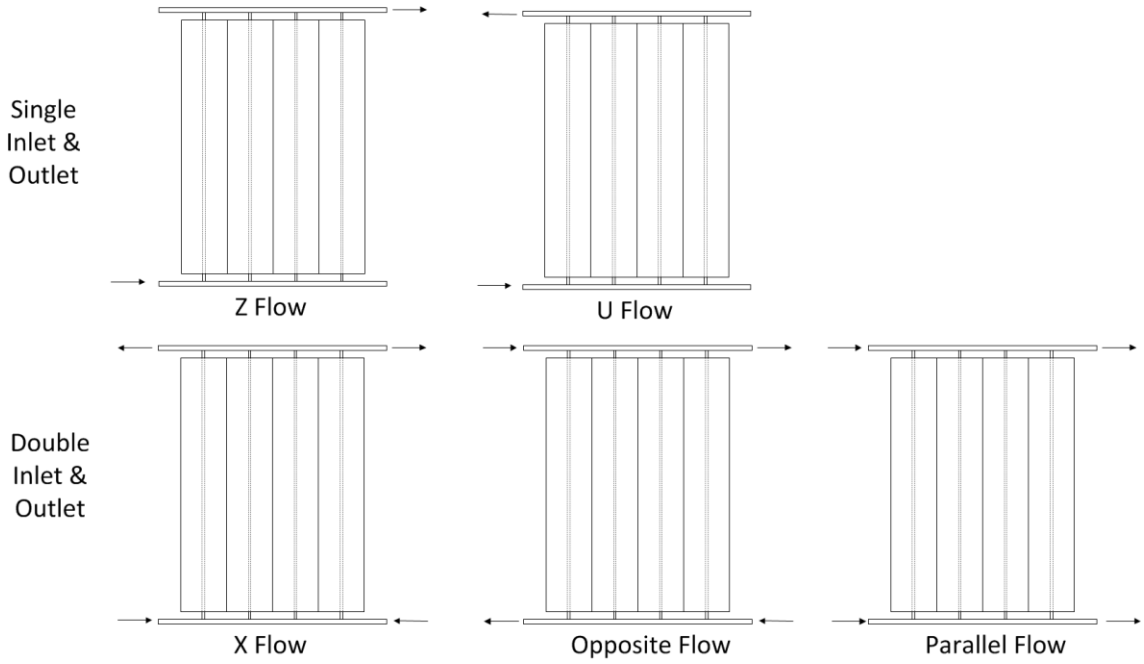

Figure 4-39: Flow patterns for header riser collector

There is variation in the distribution of temperature for each design and this influences the efficiency of the system. Even if the temperature distribution is relatively small across a single collector, care must be taken when connecting collectors in an array as the effect will be multiplied. The flow distribution simulated in these individual collectors is in agreement with the results of previous studies [138] [139]. In this study the collector only consisted of four risers, this is a relatively small number for a thermal collector. It has been shown that as the number of risers increases, the flow becomes less uniform [139]. The most uniform distribution through the pipe was achieved using the X flow configuration. In this case two inlets and outlets were used. The reason this designed performed so well in terms of uniformity is because the parallel component only consists of 2 risers. The reason this configuration is not as efficient as the single flow conditions is due to a slightly higher average surface temperature. This could be a result of a loss in fluid momentum as the two flows collide in the centre of the bottom header. The catastrophic loss in efficiency is shown in the opposite and parallel dual flow systems. These cases represent an infinitely long parallel connection. This effect was also seen in the study by Wang where the flow distribution was measured in a parallel connected array consisting of 16 collectors, each with 10 risers. The study showed that the vast majority of the flow travelled through the pipes of the first and last collector [140].

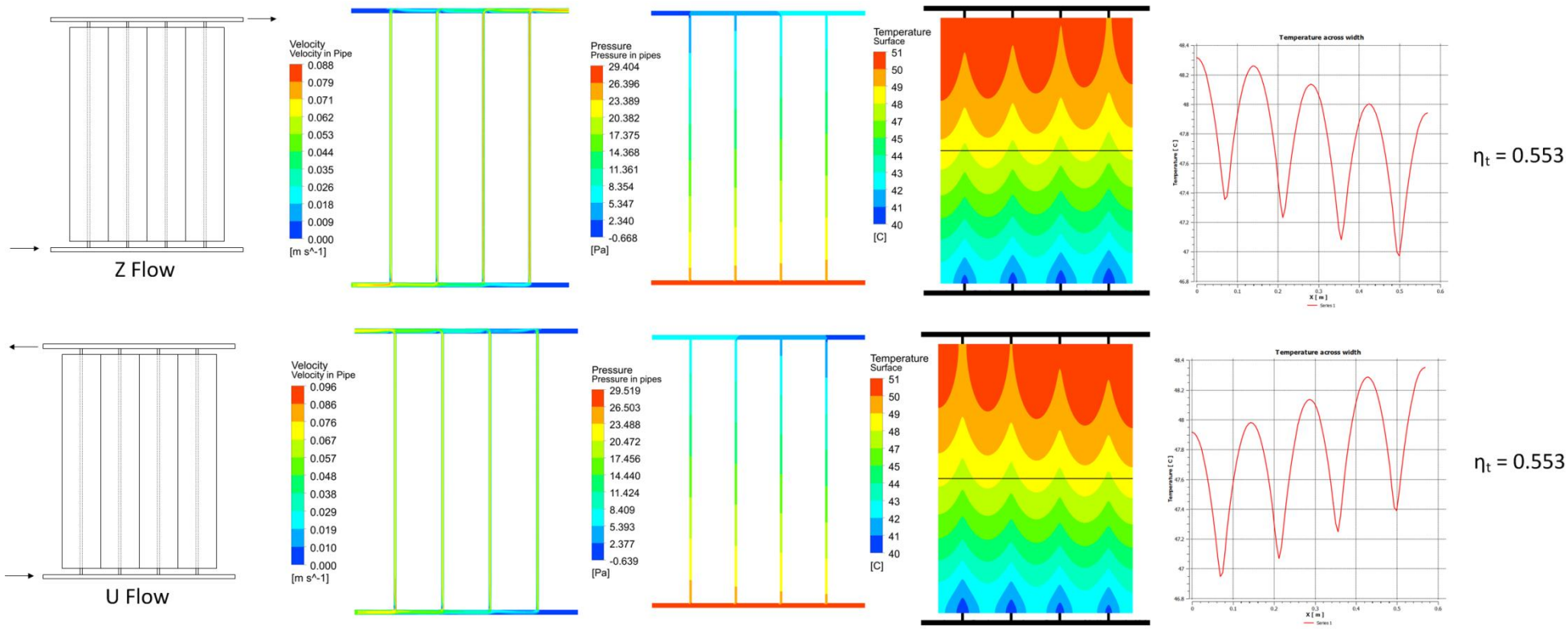

Figure 4-40: Comparison of single flow conditions for a parallel collector

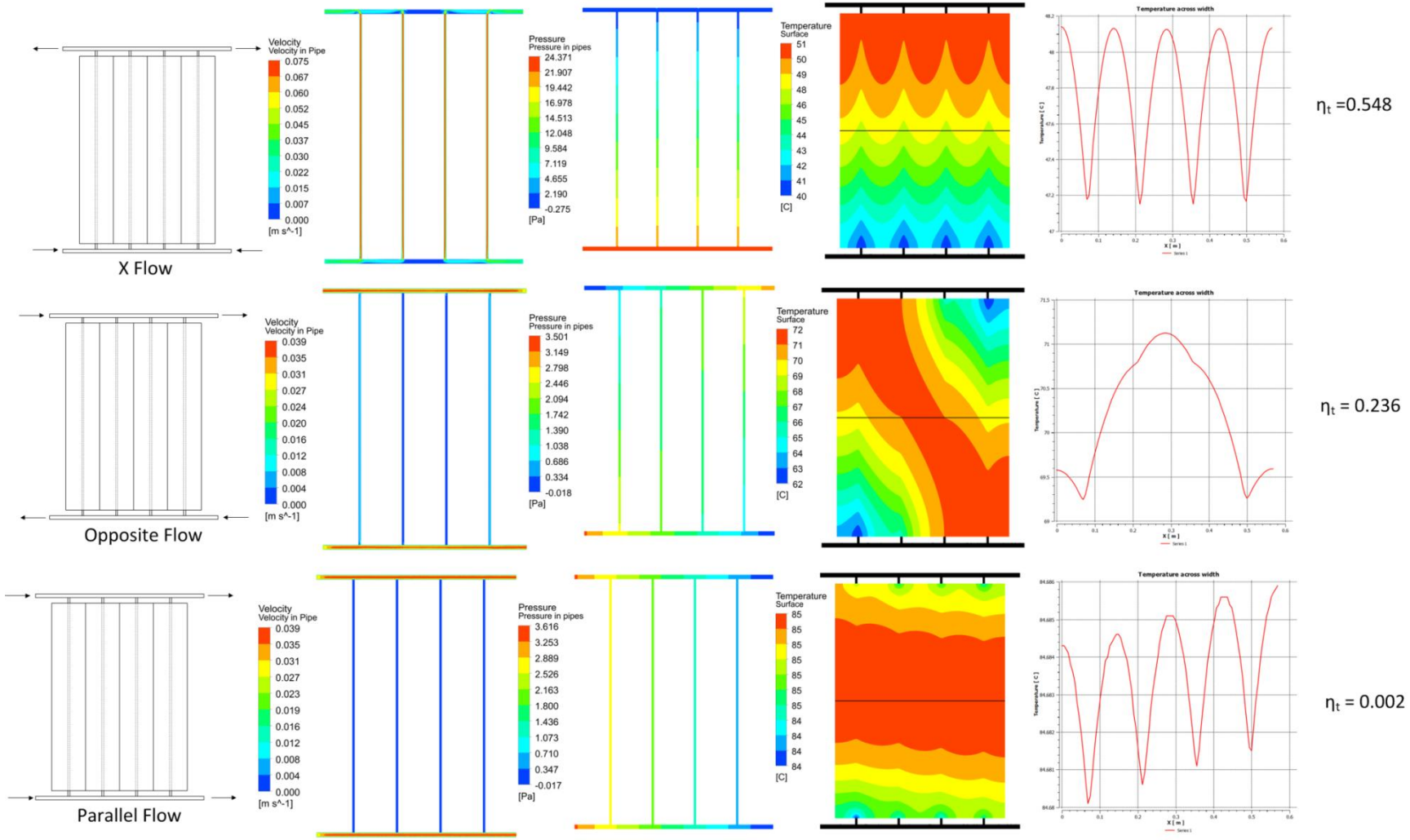

Figure 4-41: Comparison of dual flow systems

4.15 Discussion of discrepancies

As mentioned in the methodology, the thickness of the plate was increased in the simulation to create a high quality volume mesh. The increase in thermal resistance is offset by the reduction in distance between the absorber and the fluid in the pipe. Therefore increasing the thickness has a positive impact on performance. Analysis with the Hottel Whillier Bliss model reveals that an increase from 0.5mm to 8mm results in a 12% increase in heat removal factor [7]. Fin efficiency is an expression that is based on the relationship of the width of the fin to the width of the pipe. As the thickness of the plate increases, the distance between the absorber and the pipe is reduced and fin efficiency is increased. Figure 4-42 shows that heat no longer has to travel the entire width of the fin to reach the fluid because more heat is available in the absorber above the pipe join. In order to compensate for this in future simulations, the conductivity of the plate material should be reduced in proportion to the increase in thickness.

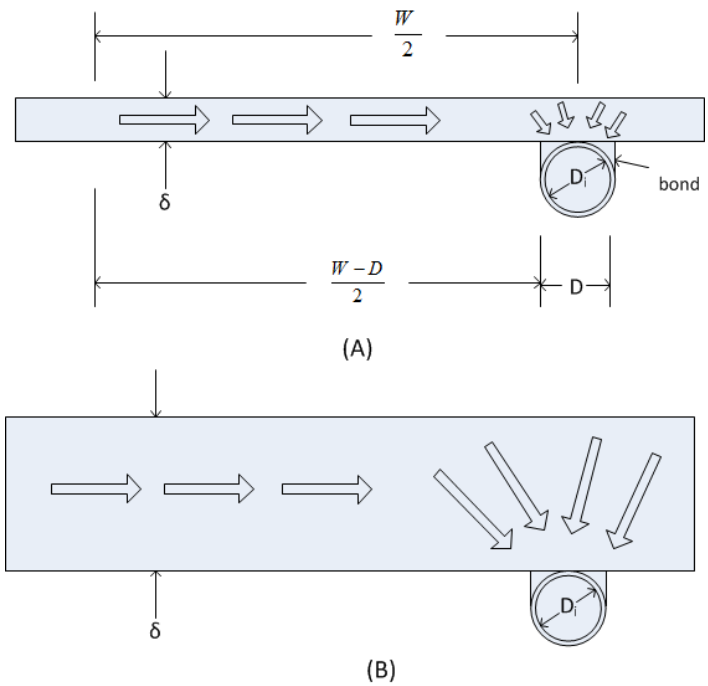

Figure 4-42: Effect of absorber thickness on heat transfer in the simulation

This could explain the case for the serpentine collector but for the header riser collector, a decrease in efficiency is seen in the CFD model. As overall heat loss U_L is dependent on heat removal factor F_R, see (4.49), a thicker collector should have a lower heat loss coefficient under the same conditions.

$$F_R = \frac{Q_u}{A_c\left[\left(S - U_L\left(T_i - T_a\right)\right)\right]} \tag{4.49}$$

In the CFD model an increase in thickness should increase the energy output; however in order to satisfy the specified heat removal factor from the experimental measurement the value of F_R is reduced to maintain energy balance.

This however contradicts the results from the serpentine collector, where the simulation outperforms the experimental measurement. The difference in experimental and simulated results from the serpentine collector could be explained by the influence of poor resistance on efficiency, resistance values were assigned to the pipe absorber boundary during boundary definition. The impact of increasing the contact resistance between the tube and the plate thermal efficiency is shown in Table 4-14.

The thermal contact has proven to be unreliable in laser welded thermal collectors, see Figure 4-27. The integrity of the bond between the pipe and the absorber is uncertain and without an accurate measurement of the conductivity across this boundary, it is feasible that this could be the cause of discrepancy between the experimental and simulated values. The poor contact between the plate and the collector could cause the experimental model to perform worse than the simulated model.

It can be seen from Table 4-14, that it is possible to adjust the simulation to account for poor thermal contact between the pipe and the absorber. In order to better understand this phenomena, it is suggested that an experimental model be created with quantifiable thermal contact between the pipe and the absorber. Once the simulation has been validated against this known case, it can be again applied to the experimental model using the known value of conductivity. The discrepancy between the simulation and experimental performance would be an indication of the thermal contact and could be useful in the development of methods to bond pipes to the absorber.

The heat transfer surface area can also influence efficiency of the collector, to investigate, 3 models were created with varying contact length between the pipe and the absorber. It was found that if the contact length was increased to 12mm the thermal efficiency increased to 0.82 and if the contact length was reduced to 4mm the thermal efficiency reduced to 0.68.

4.16 Summary of CFD Approach

This section has demonstrated a methodology to simulate the performance of a solar collector in CFD by using experimental values of incident solar radiation and overall heat loss coefficient as boundary conditions. The irradiance is specified as a heat flux and the resulting calculation of thermal efficiency takes into account the absorbtance of the collector. When comparing the results with experimental findings, the simulated value of F_R for the serpentine collector was 4.2% higher and the header riser 12.1% less. To explain these results, the fundamental parameters that effect F_R were investigated. Further work is needed to address the discrepancies between the simulated and experimental values. Further investigation showed that poor thermal conduct was a contributing factor to incorrect heat removal factor calculations. The focus should be on quantification of thermal properties of the experimental model before validating the simulation.

The results from the thermocouples placed on the back of the collector indicate that there is less than ideal contact with the piping as the temperature reading is higher than the simulated value. There is confidence in the thermocouples as they were calibrated and tested under the same conditions; however it is possible that there was variation in the contact with the absorber and this could explain the discrepancy in the results. It is recommended that further in further testing the thermocouples should be metallically bonded to the absorber surface. Provided that both wires are in contact with the base metal, the voltage response of the thermocouple will not be affected.

The average temperature of the absorber varied between the two designs. There was better agreement for the serpentine collector where the average plate temperature was underestimated by between 1.17-2.54% compared to the experimental value. The simulation of the header riser collector began by overestimating the mean plate temperature by 4.86%, at an inlet temperature of 21°C, and at all other inlet temperatures the mean temperature was over estimated by an increasing amount until the simulated reading at 80°C was 7.16% greater than the experimental value.

The comparison of simulated and measured absorber surface temperature is in agreement for each absorber design. The calculation of heat transfer coefficient inside the pipe is in agreement with the suggestion by [123] that the regime inside a solar collector must be considered developing laminar for heat transfer calculations. In the CFD model it was shown that areas of high velocity and mixing occurred at the bends of the collector.

It has been shown that, by taking into account heat transfer across the entire pipe wall, the efficiency of the collector is improved; however the majority of heat transfer occurs in the upper section of the pipe. It was not possible to efficiently mesh the pipe walls due to the large increase in elements. A hexa-meshing technique was trialled but it was difficult to take into account the bends and transition between each of the domains. If this technique can be refined, it would allow for a smaller number of elements to be used in the mesh.

It was also shown that the irradiance distribution across the surface did not influence the overall efficiency of the collector; however there was a slight change in the temperature distribution across the surface.

The pressure drop was much greater in the serpentine collector due to the 180 degree bends in the piping. This results in a lower net energy production compared with the header riser collector. This finding is perhaps one of the reasons why header riser collectors dominate the market. The calculation of net energy is a useful indicator for anyone developing solar thermal collectors.

4.17 PV Cell Mismatch

Mismatch occurs when two PV cells with different electrical characteristics are connected together. By applying Kirchoffs law it can be seen that the following rules apply for two identical PV cells connected in parallel and in series:

Parallel Connection

$$V_1 = V_2 \qquad (4.50)$$
$$I_T = I_1 + I_2$$

Series Connection

$$I_1 = I_2 \qquad (4.51)$$
$$V_T = V_1 + V_2$$

The current generated by a PV cell is proportional to the amount of incident light and can be severely reduced due to shading. In such situations, the current for a string of series connected PV cells is limited by worst performing cell/module. The difference in power between the worst performing and the best performing PV cell is dissipated as heat in the shaded PV cell/module. This results in localised heating and can cause damage to the PV cell/module [141]. This effect can be avoided through the use of bypass diodes [142].

In a standard PV module the temperature distribution across the surface is assumed to be constant. There are no published studies on the open circuit voltage mismatch in collectors because cells are usually connected in series and voltage is additive as shown in (4.51).

The distribution in temperature on the surface of a PVT collector could cause a variation in voltage between PV cells mounted on the surface. Voltage mismatch becomes an issue when PV cells are connected in parallel. In this situation the output voltage of the connected cells is the average of the two cells [143].

4.17.1 Experimental validation of voltage mismatch

The only reference to voltage mismatch in PV cells found in literature was [144]. Voltage mismatch occurs when the combined voltage is greater than that of the open circuit voltage of the poor performing cell. This concept is illustrated in Figure 4-43.

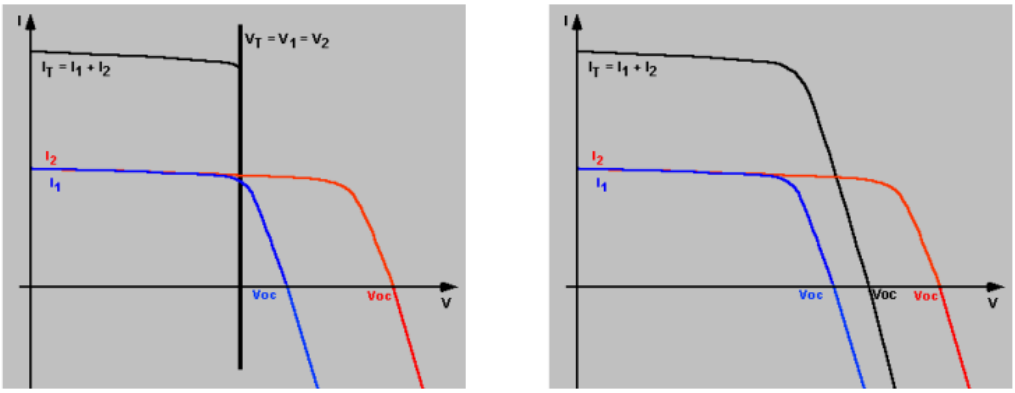

Figure 4-43: Effect of voltage mismatch on a bad and good cell connected in parallel. The blue and red lines are the IV curves for the bad and good cell respectively and black line indicates combined V_{oc}. When the combined voltage is below the V_{oc} of the poor performing cell then the rules $V_1=V_2=V_T$ apply, as shown in the left image. However if the combined voltage exceeds the V_{oc} of the bad cell then the overall voltage falls in between the V_{oc} of the good and the bad cell as shown in the right image. Source: [144].

The degree in which the overall current is limited is dependent on the IV curves of the good and bad cell. In order to determine combined operating voltage the IV curves for each individual cell needs to be obtained and then the good cell is reflected across the voltage axis. This is shown in Figure 4-44.

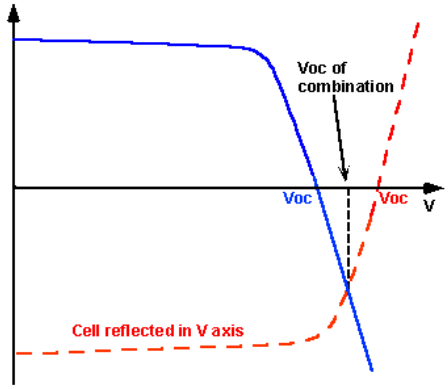

Figure 4-44: Calculation of operating voltage of two mismatched cells connected in parallel. Source: [144].

Due to the limited literature, experiments were carried out to investigate the impact of temperature mismatch on the overall voltage of connected PV cells. To achieve this, the voltage of a PV cell (the bad cell) was reduced with by heating the cell using a (12V 2A) ceramic heating mat. The surface temperature of the heated PV cell was measured using an infrared thermometer and the overall voltage readings were measured using a multimeter. The voltage temperature coefficient was determined for a single bad PV cell and compared to figures on the manufacturer's datasheet. The bad cell was also connected to unheated, good cells and the overall open circuit voltage was measured using a source meter.

4.17.2 Open circuit voltage temperature coefficient

The open circuit voltage of a PV cell degrades with temperature as shown in equation (4.52).

$$V_{oc} = V_{ref}\left[1-\beta_v\left(T-T_{ref}\right)\right] \tag{4.52}$$

Where, β is the open circuit voltage temperature coefficient [%/°C]. This can be determined experimentally by plotting $\left(V_{oc}/V_{ref}\right)-1$ against $\left(T-T_{ref}\right)$. Where T_{ref} is 25°C as specified by the manufacturer.

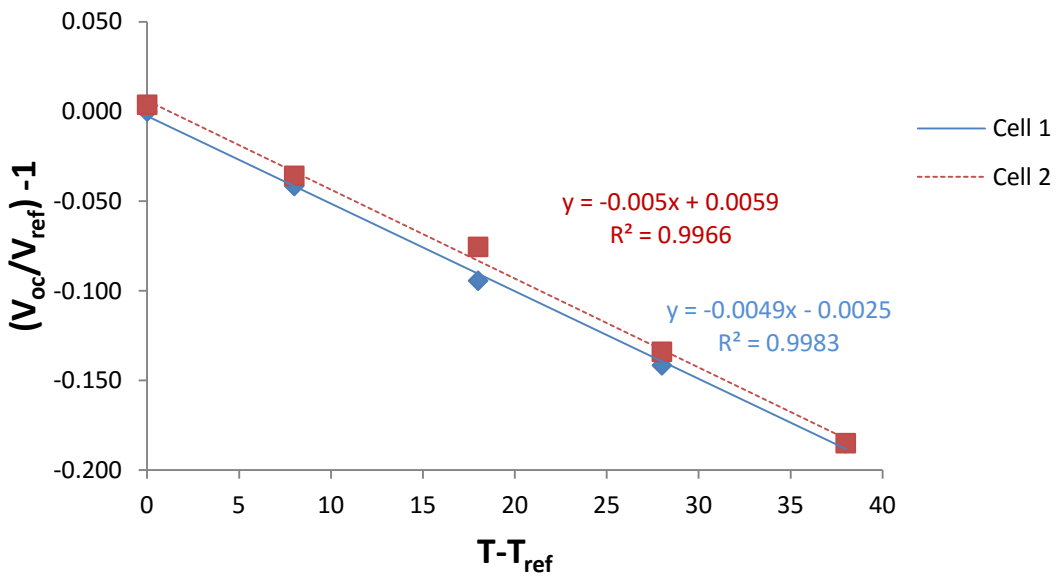

Figure 4-45: Graph used to calculate temperature coefficient

The value of β is equal to the gradient of the line shown in Figure 4-45. In this case the voltage coefficient has been calculated at 0.49%/°C and 0.5%/°C. This is more than the manufacturer's claim of 0.329%/K but is in agreement with another published study [35].

iii. Open circuit voltage mismatch

To determine voltage mismatch the PV cells were connected in series and parallel, a single cell in the connection was heated while the rest were unheated. The combined voltage of both cells was measured using a multimeter and the temperature of the heated cell was continually monitored. The experimental process is shown in Figure 4-46.

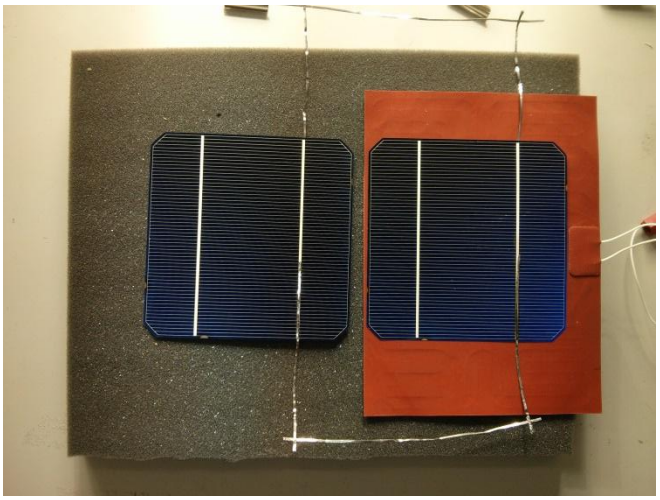

Figure 4-46: Experimental testing of output voltage for two cells connected in parallel.

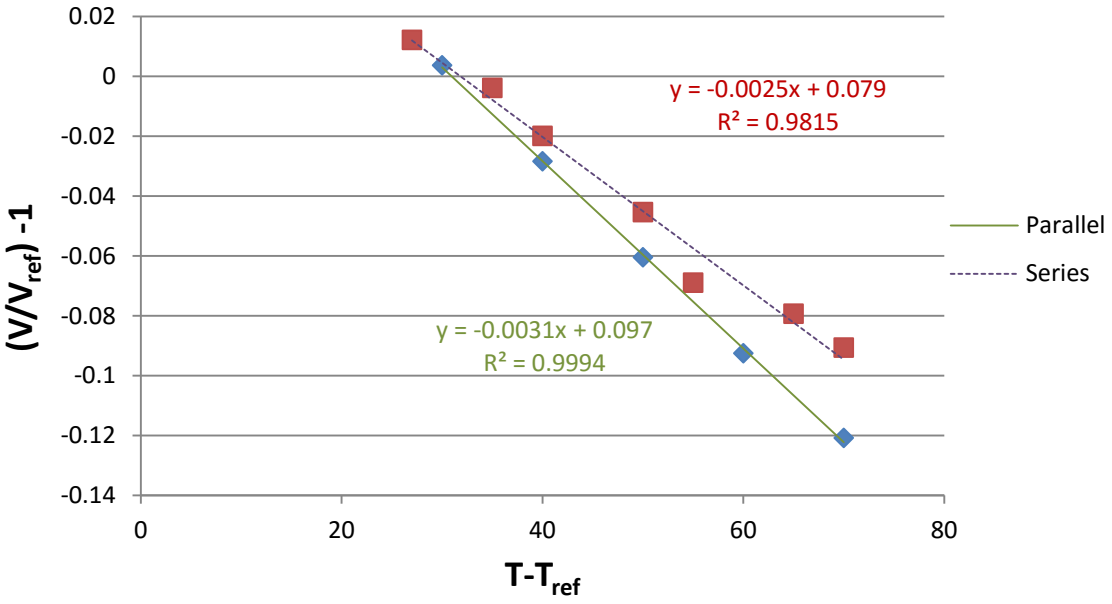

Figure 4-47: Effect of temperature difference on total voltage for two cells connected in series and parallel

From Figure 4-47 the influence of temperature difference on the total voltage of the parallel and series connection. In series, the influence of temperature for an is divided by the number of connected cells, which in this case is (4.53)

$$\beta_{series} = \frac{\beta}{n} \tag{4.53}$$

$$\beta_{parallel} = 1.24\left(\frac{\beta}{n}\right) \tag{4.54}$$

Where *n* is the number of connected cells.

The individual voltages will be calculated for all cells and then the connected voltage will be calculated using (4.54).

4.17.3 Applying to cells connected in series

The heated PV cell was connected to four other unheated cells and the impact on the overall open circuit voltage was measured. The experimental test is shown in Figure 4-48.

Figure 4-48: Experimental testing of output voltage for four cells connected in parallel.

Figure 4-49 shows the effect of temperature difference on the total voltage of 5 cells connected in parallel with one bad cell. This result can be compared with (4.54) which was derived from the two cells connected in parallel. Using (4.54) we can see that the adjusted heat coefficient should be $1.24(0.005/5)=0.0012$ for 5 cells connected in series; but the measured value shown in Figure 4-49 is 0.0009. This shows that the performance degradation for 5 cells is less that that seen in the two cells case. An explanation for this could be a result of heat passing through the bus wire contacts and increasing the temperature of the cells that are assumed to be unheated in the calculation. The result would be a reduction in overall voltage. For the two cells connected in parallel the effect would be more severe as the heat would be distributed only to one cell whereas in the case of 5 cells the heat is dissipated between four cells. This methodology could be improved using better temperature control over the unheated cells, such as placing them in contact with a heat sink.

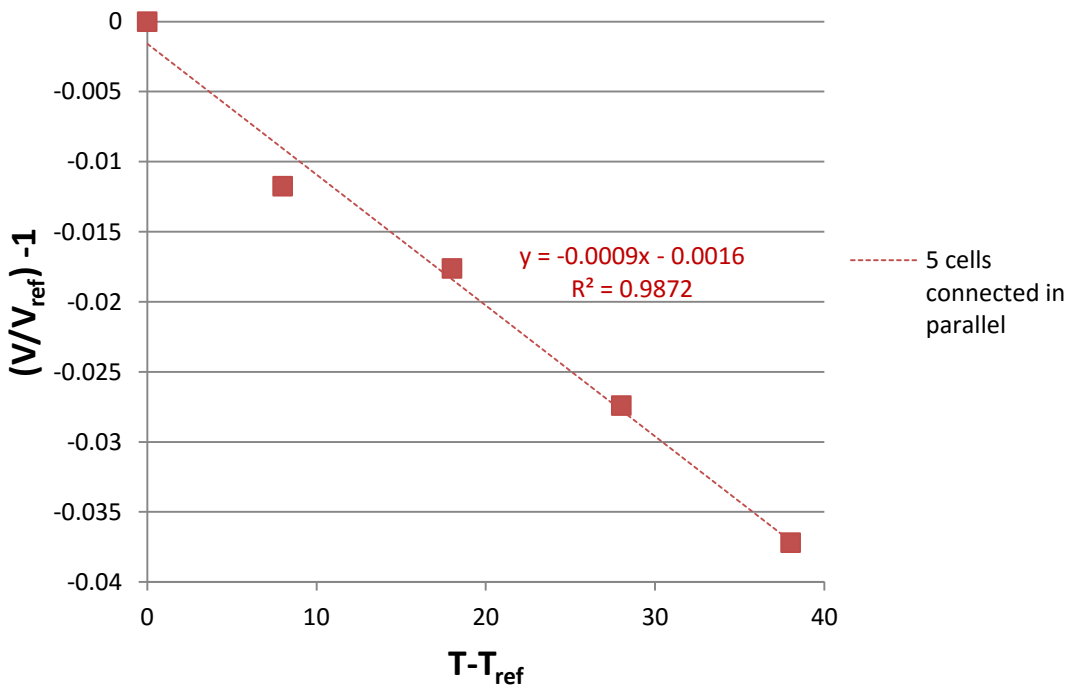

Figure 4-49: Effect of temperature difference on total voltage for five cells connected in parallel

From Figure 4-44 it can be seen that the combined voltage will lie somewhere between the open circuit of the bad and good performing cell depending on the IV curve of the two cells.

The absolute impact of temperature increase on the voltage of the cell is shown in Figure 4-50 and Figure 4-51 respectively. From this graph it can be seen that the measured open circuit voltage is less than that of the average V_{oc}, which is calculated using (4.55):

$$V_{oc_av} = \left(\frac{\left(n_g \cdot V_{oc_g}\right) + \left(n_b \cdot V_{oc_b}\right)}{n_g + n_b} \right) \tag{4.55}$$

Where, n is the number of cells and the subscripts *g* and *b* denote good and bad performing cells respectively. The reason the measured V_{oc} is less than the average V_{oc} indicates unheated cells are performing at a higher temperature than assumed. Ideally the temperature of the unheated cells should be controlled and their temperature monitored. Despite this disagreement, the measured value lies between the V_{oc} of the bad and good cell as predicted by Figure 4-44.

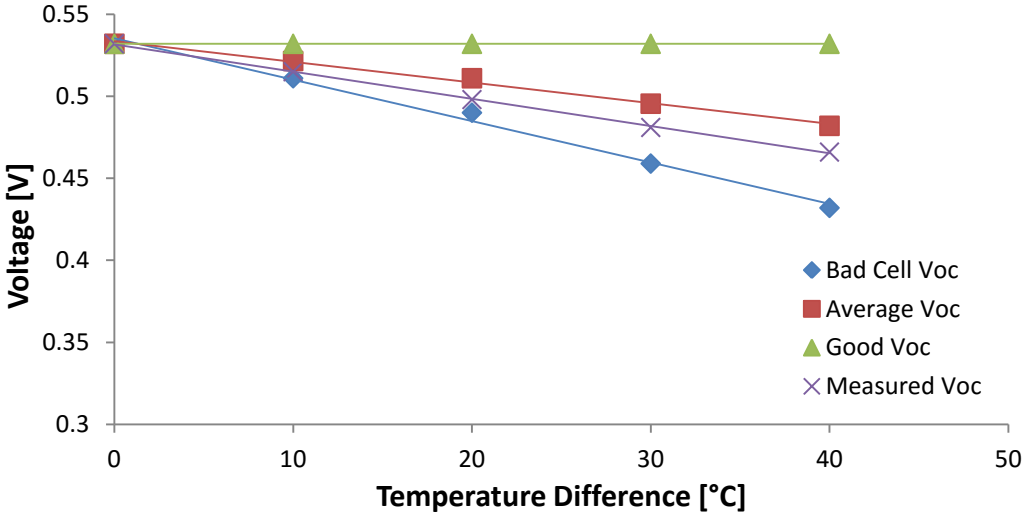

Figure 4-50: Comparison of the impact of a low voltage cell on the overall voltage of 2 PV cells connected in parallel.

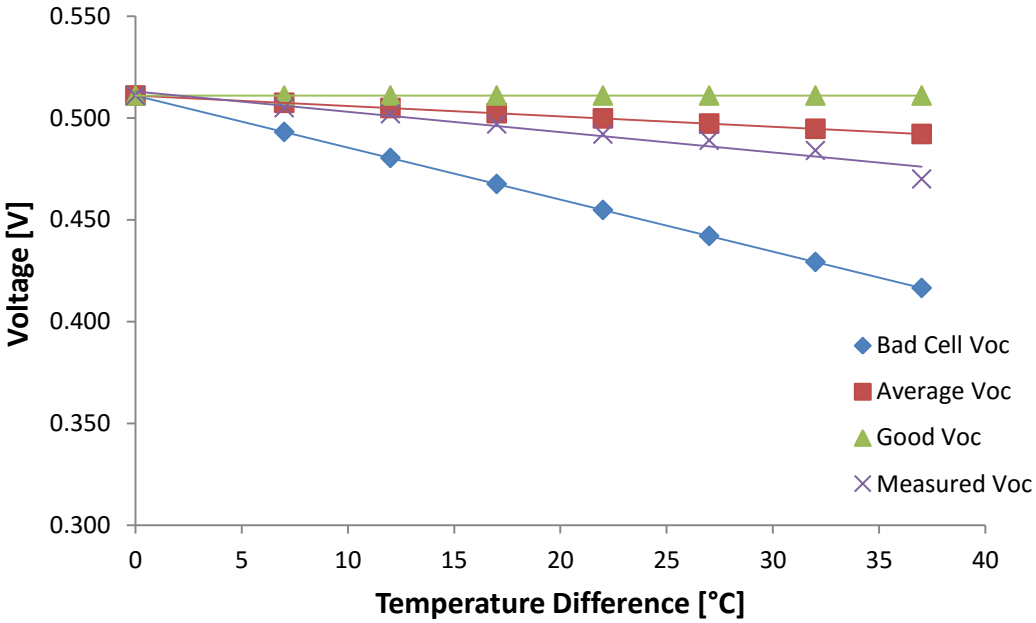

Figure 4-51: Comparison of the impact of a low voltage cell on the overall voltage of 5 PV cells connected in parallel.

To determine the influence of temperature mismatch across the surface temperature distribution, as simulated in CFD models, average V_{oc} will be calculated using (4.55). Due to the disagreement between the experimental and the calculated average, the difference between the measured and the average V_{oc} will be used as the uncertainty for future results.

Comparison with IV results

IV curves were generated for the PV cells fixed to an absorber and the inlet temperature was varied. From these results it is possible to determine the temperature coefficients for maximum power point voltage V_{mp} open circuit voltage V_{oc} and maximum power $P_{mp,}$ see Figure 4-52, Figure 4-53 and Figure 4-54 respectively.

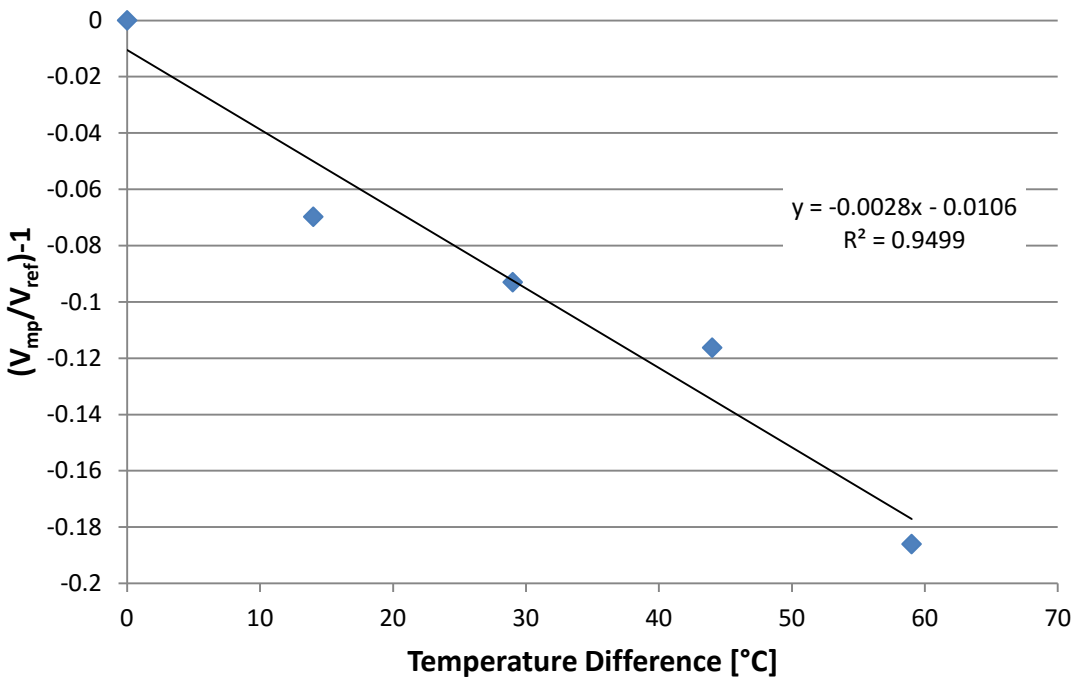

Figure 4-52: Calculation of V_{mp} coefficient using data from the IV curve. The voltage reading at the lowest inlet temperature was used as the reference value.

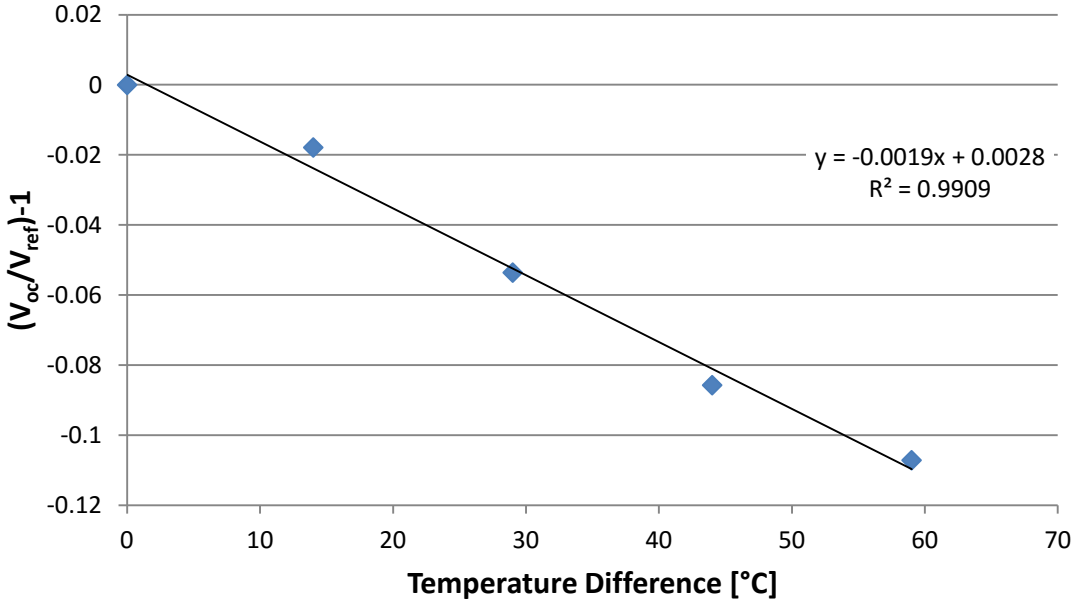

Figure 4-53: Calculation of V_{oc} temperature coefficient using data from the IV curve. The voltage reading at the lowest inlet temperature was used as the reference value.

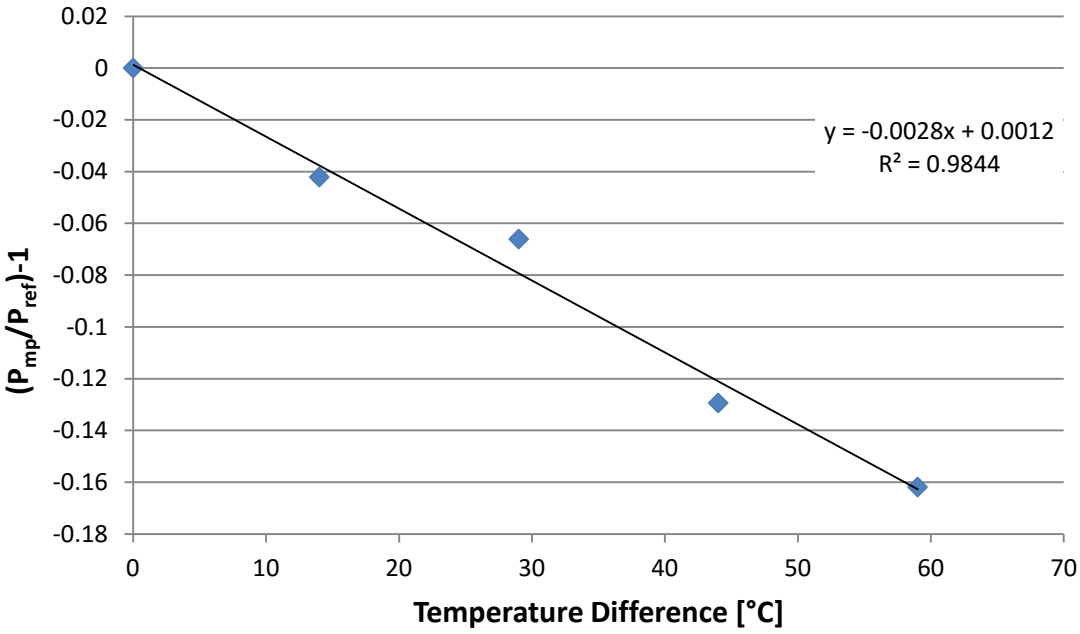

Figure 4-54: Calculation of maximum power point (P_{mp}) temperature coefficient using data from IV curve. The power reading at the lowest inlet temperature was used as the reference value.

The differences in the measurement each temperature coefficient for each method is shown in Table 4-20.

Table 4-20: Comparison of temperature coefficient values obtained from different methods. The presence of NA means that there is no data available on this coefficient using this method.

Temperature Coefficient	Data Sheet [%/K]	Heating Plate [%/K]	IV Curve [%/K]
V_{oc}	-0.329	-0.5	-0.19
P_{mp}	-0.42	NA	-0.28
V_{mp}	NA	NA	-0.28

The differences in the calculated coefficient values could be due to inaccurate assumptions of the temperature of the unheated cells in the heating plate method and capacitance effects in the IV curve method (the presence of the lamination materials could absorb heat differently at different temperatures therefore the temperature difference used in the calculation would not be correct).

For this reason, the values on the manufacturer's datasheet have been used in the calculations of power output from the PV. To determine the voltage at maximum power point, the power at different inlet temperatures has been calculated using the maximum power point coefficient given on the datasheet, this value is then divided by the maximum power point current, I_{mp}, which is assumed to be constant, to give the maximum power point voltage, see Figure 4-55. The change in this value is then compared with the open circuit voltage temperature coefficient.

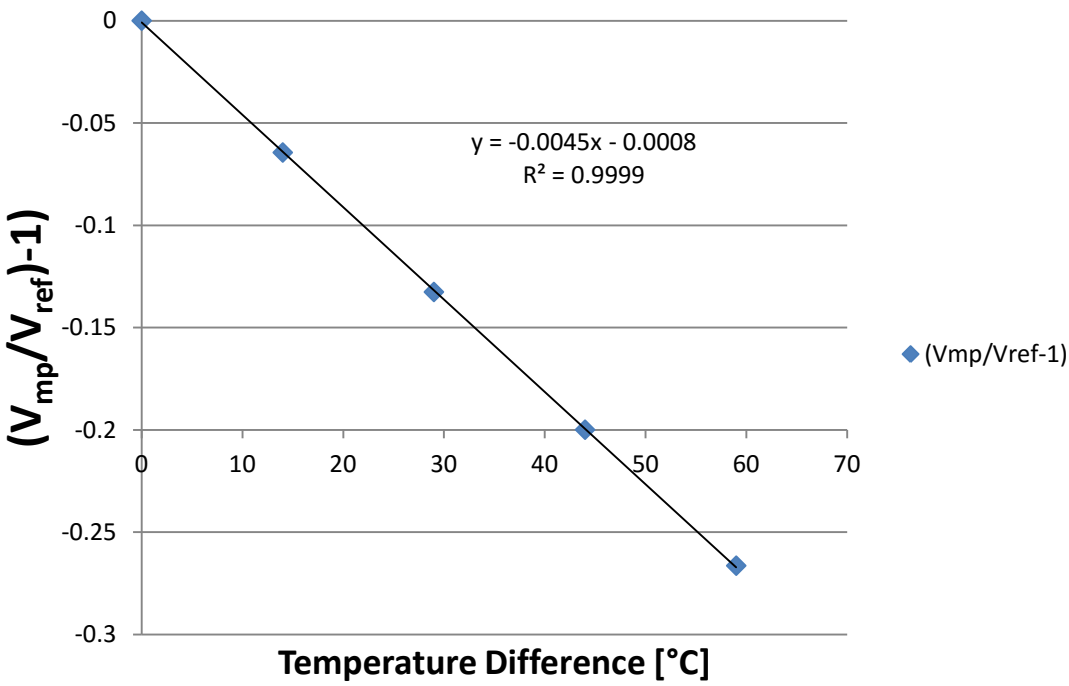

Figure 4-55: Calculation of V_{mp} temperature coefficient using datasheet values and assuming Imp to be constant.

The experimental work carried out in this study has largely under estimated the open circuit voltage compared to the technical datasheet and other studies [145] [146].

The difficulty of measuring the temperature coefficient of solar cells is discussed in [145]. The measurement of temperature coefficient is a complex procedure in which the cell temperature needs to be accurately recorded under standard AM 1.5 conditions. In the experiments this was not the case so the comparison between datasheet values and those obtained experimentally is not useful.

Manufacturer datasheets generally do not publish the temperature coefficient of the maximum power point voltage, V_{pm}, and current, I_{pm}. A study carried out by King [146] showed that non-uniformity of temperature across the cell led to an underestimate of the temperature coefficient. King presents a normalised effective temperature coefficient of V_{mp} to take into account outdoor performance. The results showed that the coefficient of V_{mp} is higher that the coefficient of V_{oc} for crystalline modules with a value of approximately -0.005V/°C for crystalline modules.

4.18 Analysing Mismatch using CFD Models

To determine the best cell configuration for PVT performance, the impact of voltage mismatch has been investigated for the surface temperature distribution of a parallel PVT collector under the different flow conditions shown in Figure 4-40 and Figure 4-41.

Three wiring configurations have been investigated to determine whether a particular wiring configuration is suited to a temperature distribution. The three wiring conditions investigated in this study are vertical strings, horizontal strings and all in series, these are illustrated in Figure 4-56.

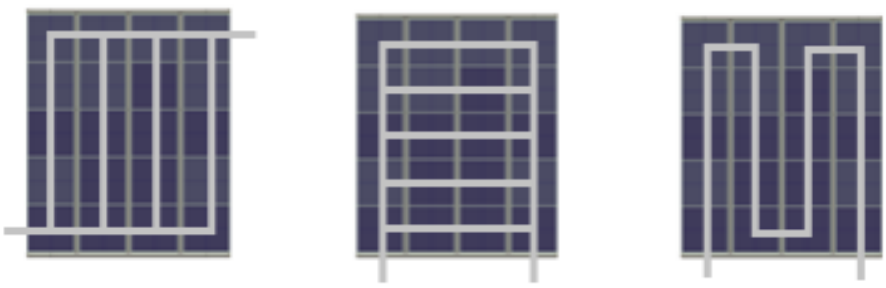

Figure 4-56: The wiring configurations of PV cells applied to each flow configuration. Left, the PV cells are connected in 4 vertical strings of 6 cells connected in parallel. Centre, the PV cells are connected in 6 horizontal strings of 4 cells. Right, all of the PV cells are connected in series.

The operating point for each cell was calculated using (4.56).

$$\begin{aligned} V_{mp} &= V_{mp(STC)} + \beta_{Vmp} \cdot (T_{cell} - T_{STC}) \\ I_{mp} &= I_{mp(STC)} + \beta_{Imp} \cdot \left(T_{cell} - T_{STC}\right) \end{aligned} \tag{4.56}$$

Where β_{Vmp} and β_{Imp} are the normalised temperature coefficient [1/°C] for current and voltage at maximum power point. The average values of β_{Vmp} and β_{Imp} for a crystalline module, as published by King [146], are -0.005 V/°C and -0.00046 A/°C respectively.

Sample planes were created in CFX Post to obtain the average cell temperature, T_{cell}. Each PV cell on the absorber of the PVT collector was assigned its own sample plane. The collector surface was evenly divided into 24 sample planes and the average temperature was calculated in CFX post. The process is illustrated in Figure 4-57.

The overall voltage of the module is determined using two rules; for cells connected in strings the voltage is additive and for cells connected in parallel, the average is taken. The reasoning behind this approach is explained in the previous section.

The electrical current of two connected cells is limited by the short circuit current of the poorest producing cell [141]. The current temperature coefficient is an order of magnitude less than the voltage temperature coefficient, so any variation in current as a result of temperature difference will be negligible. Also current at maximum power point is less that the short circuit current and to create a current mismatch due to temperature would require a temperature difference of over 1000°C. This is beyond the possibility of a standard PVT collector and therefore current mismatch will not be addressed in this study. The total maximum power point current will be determined using the rules shown in (4.50) and (4.51).

The total electrical power output from the connected PV cells is then calculated using (4.57).

$$P_{mp} = I_{mp} V_{mp} \tag{4.57}$$

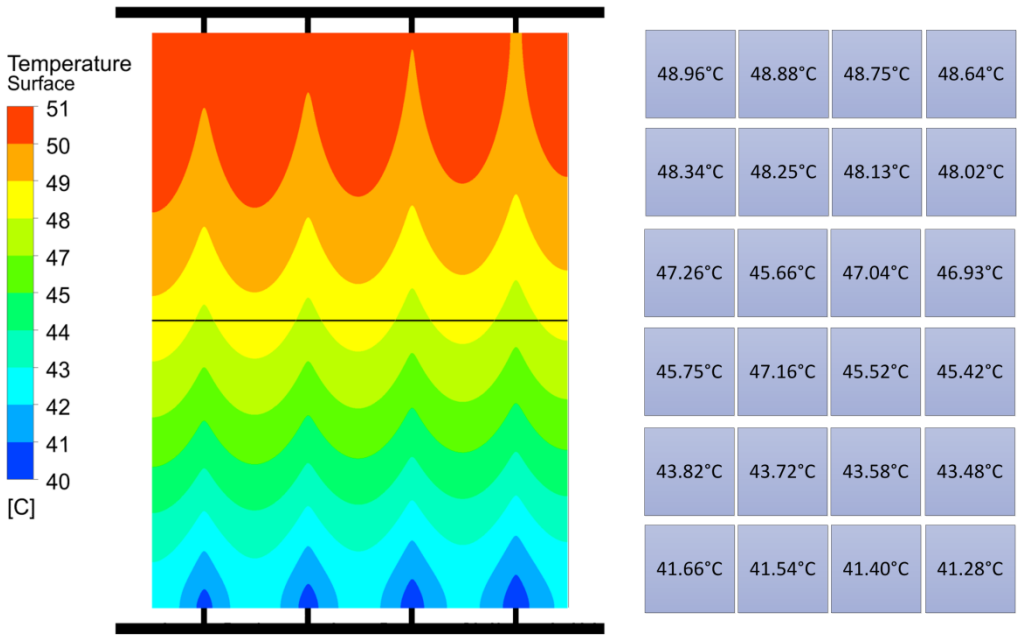

Figure 4-57: Extracting average cell temperature using sample planes in CFX Post.

4.19 Results from Temperature Mismatch Study

The electrical power output for each flow configuration is shown in Table 4-21. Because voltage mismatch is averaged and the temperature variation not large enough to cause current mismatch above the short circuit threshold of the poor performing cell, the electrical power output is the same regardless of how the PV cells are connected on the absorber surface. The

electrical performances for the Z, U and X are similar due to having a similar average absorber temperature. The electrical performance is worst for the opposite and parallel flow conditions due to the high surface temperature that is a result of poor flow through the risers as shown in Figure 4-41.

Table 4-21: The electrical power output of each flow configuration for a header riser PVT collector

	Average Temperature [°C]	Electrical Power [W]		
		Vertical Strings	Horizontal Strings	All in Series
Z Flow	45.8	52.36	52.36	52.36
U Flow	47.1	51.52	51.52	51.52
X Flow	47.1	51.52	51.52	51.52
Opposite Flow	69.4	37.59	37.59	37.59
Parallel Flow	84.6	28.05	28.05	28.05

4.20 Conclusions

A CFD model has been developed and has been compared with experimental results. The value of U_L was in good agreement between the experiments and the simulation, a difference of +2.9% and -0.70% for the serpentine and header riser collector respectively. There was less agreement for the value of F_R; for the serpentine collector it was 4.2% higher and for the header riser it was 12.1% less than the experimental value.

The discrepancy between the value of F_R was the thermal contact and surface area between the fluid and the absorber. It was not possible to quantify the thermal contact in the experimental collector and future work should be focused on this.

Despite not matching the experimental results the CFD simulation served as a useful tool to carry out relative comparisons of different collector designs and flow conditions. In this study it was found that the reduced pressure drop in the header riser collector gave a higher thermal yield to pumping power of 1022 W_{th} compared to 71 W_{th} per $W_{electricity}$ using an optimal inlet temperature.

The effect of different flow configurations for a parallel collector was also investigated. It was found that the most efficient designs of collector had the most uniform flow through the risers. The opposite and parallel flow systems had low flow rate in the risers that led to high surface temperatures and poor thermal efficiency. This finding was in agreement with other studies that have investigated the flow in large arrays of parallel collectors.

The surface temperature distribution across the collector surface was used to estimate the temperature of PV cells in perfect thermal contact with the surface of the absorber. Voltage mismatch occurs when two connected cells are operating at different temperatures. In this study the voltage was assumed to be the average of the two cells, which is a reasonable assumption if the cells are identical. This meant that the temperature variation was not limiting and the way in which PV cells are wired together on the surface of a PVT collector did not influence the combined electrical power output.

4.21 Recommendations for Future Work

Improvements to methodology:

- **Control experimental parameters that influence F_R:** The discrepancy between the experimental and simulated value of F_R needs further investigation. The simulation made assumptions regarding thermal contact between the absorber and the fluid and an accurate experimental model or section of absorber must be created in order to carry out further validation.
- **STC testing of temperature mismatch under accurate temperatures:** In this study it was not possible to get a close agreement between the datasheet value of temperature coefficient and the experimental value. The reason for this is because the experimental testing was not performed under STC conditions. The amount of irradiance used in this study was only enough to invoke a voltage response in the PV cell and much less than the 1000W/m^2 used in the manufacturers testing. To carry out this technique accurately also requires equipment that can accurately control the temperature of the PV cells being tested.
- **Increased mesh density in the pipe walls connected to the absorber:** The mesh density would need to be reduced thus increasing the element count significantly. This would require greater computational resource in order to solve the problem. If this is not possible, the relationship between contact area and heat transfer coefficient must be determined so that an adjustment factor can be used. This may be a non-linear relationship which would help in understanding the discrepancy between the experimental and simulated value of F_R.

Future research studies:

- **Parametric CFD studies of different designs of collector:** This study has shown that it is possible to carry out a parametric study of different flow configurations of a parallel collector. The study could be further extended to completely different designs of collector, and parametric studies where the impact of varying number of risers, aspect ratio, absorber thickness etc. could be investigated.
- **CFD study of connected collectors in an array:** If every collector in an array is to be meshed individually this would result in a large mesh and would require more computational power to solve the simulation. An alternative would be to simulate the thermal performance of a single collector in an array by applying different pressure drops at the inlet and outlet of the collector that occur given its position in the array. The opposite and parallel flow examples in this study are indicative of collectors that would be installed in the centre of a large parallel array. In such instances the system would be highly inefficient due to such poor flow rate through the central collectors.

5. Enhancing the Thermal Conductivity of EVA

5.1 Introduction

The performance of a photovoltaic cell is limited by its temperature. In a crystalline PV cell, for every degree rise in temperature, the power output is reduced by around -0.5 %. This occurs due a reduction in the open-circuit voltage across the p-n junction of the semiconductor.

EVA is a commonly used material to encapsulate PV cells. In this study the thermal conductivity of the encapsulate is increased by mixing EVA with Boron Nitride. After encapsulation the enhanced composite is in contact with rear surface of the PV cell to aid temperature dissipation.

This chapter investigates the use of EVA/BN composite for the encapsulation of PV cells and the implications it has on performance.

The studies covered in this section include:

- The manufacture of thermally enhanced EVA by doping with boron nitride
- The development of a method to test the thermal conductivity of the doped material using differential scanning calorimetry
- The manufacture of a PV laminate using the enhanced material
- An experimental comparison of the performance of the PV laminate with the doped material
- The use of numerical models to simulate the temperature distribution through the cross section

5.2 Influence of Temperature on Photovoltaic Efficiency

As the temperature of a PV cell increases, its electrical efficiency decreases. Estimates of the annual losses in performance due to temperature vary from 2.2-17.5% [28]. Much of this variation is a result of the type of PV system and its installation method; it has been shown that free-standing and ground mounted systems have less temperature losses than their building integrated counterparts [147].

5.3 Layers of a Photovoltaic Laminate

Encapsulation materials are used in photovoltaic modules to protect the PV cells from environmental degradation; however these materials have low thermal conductivity which acts as a barrier to heat escaping. The multiple layers found in a typical PV laminate are shown in Figure 5-1.

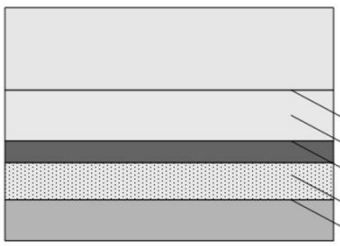

Layer	Layer Thickness (m)	Thermal Conductivity (W/m•K)
Glass	0.003	0.98
EVA	0.0004	0.23
Solar Cell	0.00018	148
EVA	0.0004	0.23
Tedlar	0.0005	0.36

Figure 5-1: The layers of a PV laminate and their respective thicknesses and thermal conductivities

The conductivity through the collector can be calculated using (5.1).

$$k_{total} = \frac{\delta_{total}}{\frac{\delta_{eva}}{k_{eva}} + \frac{\delta_{si}}{k_{si}} + \frac{\delta_{ted}}{k_{ted}} + \frac{\delta_{alu}}{k_{alu}}} \tag{5.1}$$

By inputting the values from Figure 5-1 the calculated conductivity of the composite collector is 0.82W/(m·K). If the conductivity of the EVA layer on the backside of the PV cell is increased from 0.23W/(m·K) to 2.85W/(m·K) [102], the overall composite conductivity increases by nearly 25% to 1.02W/(m·K).

5.4 Enhancing the Thermal Conductivity of EVA

Like other polymers, one of the characteristics of EVA is that it can be mixed with other materials to form composites with intrinsically different properties to the parent material. The use of such thermally conductive fillers in polymers has become an area of interest in microelectronics, where heat needs to be efficiently dissipated away from sensitive chips and processors [101].

The use of thermally conductive EVA materials can be used in photovoltaic devices to dissipate heat more effectively; thus maintaining PV cell efficiency. A previous study by Lee et al. has shown that filler materials can increase the thermal conductivity of EVA from 0.23 to 2.85W/(m·K) [102]. After preparing and characterising the material, Lee et al. went on to investigate the performance of the composite, as a PV laminate material, by comparing the PV cell power output against a reference laminate. The study showed that when using a range of different composite materials at a concentration of 20% v/v there was a -0.97% – 5.05% change in power output against the parent material reference.

The variation in power output seen by Lee et al. could have been due to a variation in PV cell quality rather than being a true indication of the performance achieved through the use of the enhanced encapsulants. This study investigates further the enhancement that can be achieved through the use of composite encapsulant in a PV laminate by monitoring the temperatures at each interface of the layers that make up the PV laminate.

The aspect ratio of the filler is an important consideration to take into account as this can aid the formation of a conductive network. Lee attempted to maximise the abundance of thermally conductive paths by using the hybrid filler at its maximum loading. Hybrid fillers consisting of spherical and fibrous filler were found to have enhanced thermal conductivity at low – intermediate filler content [101].

Analysis based on the packing principle is a useful tool to determine the optimal composition of hybrid filler. Beyond the maximum packing fraction thermal paths are already established and the use of more fibrous filler is weak.

Kemaloglu used Boron Nitride filler with a particle size of approximately 10µm. He commented that the thermal conductivity is associated with particle size and future work will be carried out using nanoparticles (1-100nm) [148]

Lee has also investigated the use of thermally conductive and electrically insulating EVA composites for solar photovoltaic cells. A number of different filler materials were used in volume fractions up to 0.6. The conductivity of the composite relies on the particles touching each other in the matrix; this only begins to happen at high loading so the trend is a very low increase in conductivity at low loading fractions.

5.5 Measuring Thermal Conductivity

5.5.1 Conventional Thermal Conductivity Measurement

Thermal conductivity is the ability of a material to permit the flow of heat between two mediums at different temperatures. The methods for characterizing the thermal conductivity of polymers are categorized in BS ISO 22007 [149] as:

- Hot-wire method
- Line source method
- Transient plane source
- Temperature wave analysis
- Laser flash
- Guarded hot-plate
- Guarded heat flow

The methods listed above are either steady-state (measurements taken at equilibrium) or transient (measuring the change with time). Some of the techniques are also based on measuring other thermo-physical properties and then deriving the thermal conductivity. Thermal conductivity is linked to specific heat, which is the amount of energy required to change the temperature of the material, and thermal diffusivity, a type of thermal inertia, using (5.2).

$$k = \alpha \rho c_p \tag{5.2}$$

Where c_p is specific heat, ρ is density, and α is thermal diffusivity.

A summary of the testing methods reported in the literature is presented in Table 5-1.

Table 5-1: Summary of methods used to test the thermal conductivity of polymers and the quantity of material required. Source [150]

Lab. ref.	Method	Thermal conductivity/ diffusivity	Nominal specimen thickness (mm)	Specimen size (mm; φ, diameter)	Pre-treatment	Uncertainty estimate (95% confidence level)
L1	Hot Disk®	λ, α, (Cp)	2, 3	φ 5; φ 10		λ, 2–5%; α, 5–10% (repeatability 1–2%) [5]
L2	Temperature wave analysis	α	0.01	3 × 5		5%[a] (repeatability < 1%) [9]
L3	Laser flash (cast PMMA only)	α	2	Disk	Silver paint (30 μm)	3–5% (repeatability < 1%) [11]
L4	Laser flash	α	1.14, cast; 1.49, extruded	Disk	Sputtered graphite	3–5% (repeatability < 1%) [11]
L4	Transient line-source probe	λ	Moulded in-situ	Formed in barrel	Moulded in-situ	(Repeatability 3–6%) [14]
L4	Heat flow meter	λ	2, 3			5% [18]
L5	Heat flow meter	λ	2, 3	φ 80		(Repeatability 3%) [19]

5.5.2 DSC Methods for Measuring Thermal Conductivity

Another method that can be used to measure the thermal conductivity of a material is detailed in ASTM E1952 [151]. This method uses modulated differential scanning calorimetery (mDSC) to determine the specific heat capacity of a material, which is then used to determine the thermal conductivity. This method requires two samples of the material, a thick sample (3.5mm) and a thin sample (0.4mm). The diameter of each sample is 6.3mm and the quantity of material required is in the range of 10-100mg.

Another technique using DSC has been developed which involves placing a 'melting standard' on top of the specimen [152]. When heat is supplied from the DSC's furnace, the specimen's conductivity is proportional to the melting rate of the standard and can be quantified by comparison with the known thermal conductance of a reference material. The method was developed using metals such as gallium and indium as the melting reference material and has since been applied to a number of other applications [153] [154] [155] [156].

The benefit of the melting standard method is that only one sample is required and a small quantity is required relative to the methods summarized in Table 1.

5.5.3 Melting Standard Method

In this study an organic ester wax which has a melting point of 25°C is used in place of the liquid metals that were used in the previously published studies. The concept behind the method remains the same and is explained below.

The effective thermal conductivity is calculated from (5.3).

$$\lambda = -\frac{\dot{Q}}{A}\frac{D}{\Delta T} \tag{5.3}$$

Where A is the cross sectional area, Q is the energy supplied to the material per unit time, D is the material thickness and ΔT is the temperature difference across the thickness.

The technique involves the use of a 'melting standard' which is applied to both the reference and sample. The reference and sample are run separately. In each case the sample and reference is heated at a constant rate to above the melting point of the standard (in this experiment the melting standard is PCM, the melting temperature is 25°C). The heat from the DSC furnace flows through the sample or reference material and causes the melting standard to melt. The rate of melting will depend on the conductivity of the sample, the higher the thermal conductivity, the faster the sample will melt. This means that the slope of the melting curve is proportional to the thermal conductivity of the sample. If we consider the following thermal conductivities of the reference λ_r and unknown sample λ_s we can calculate the effective thermal conductivity using the following set of equations:

$$\lambda_x = -\frac{\dot{Q}_s}{A_s}\frac{D_s}{\Delta T_s} \tag{5.4}$$

$$\lambda_r = -\frac{\dot{Q}_r}{A_r}\frac{D_r}{\Delta T_r} \tag{5.5}$$

Dividing (5.4) by (5.5) gives:

$$\lambda_s = \lambda_s \frac{\dot{Q}_s D_s A_r \Delta T_r}{\dot{Q}_r D_r A_s \Delta T_s} \tag{5.6}$$

The heat flow per unit time is the heat of fusion of the melting standard ΔH_F divided by the time taken for the standard to completely melt.

$$\dot{Q} = \frac{\Delta H_F}{\Delta t} \tag{5.7}$$

Where Δt is the time between onset of melting and the melting peak. In [157] the onset of melting is defined by the intersection between the maximum melting slope and the extrapolated base line. If the same mass of standard is used then equation 1.6 becomes:

$$\lambda_s = \lambda_r \frac{D_s A_r \Delta T_r \Delta T_r}{D_r A_s \Delta T_s \Delta T_s} \tag{5.8}$$

Using the readings from the DSC, this can be further simplified to:

$$\lambda_s = \lambda_r \frac{D_s A_r}{D_r A_s}\left(\frac{M_{si}}{M_{ri}}\right)^2 \tag{5.9}$$

M_{si} is the melting rate gradient of the slope using the sample material. And M_{ri} is the melting rate when using the reference material.

5.6 Project Summary

Enhancing the conductivity of encapsulant materials in PVT collectors is a novel concept. This project will investigate the use of thermally enhanced laminate materials in PVT collectors with the aim of increasing electrical efficiency and heat recovery.

This research project:

- Reviews the use of filler materials to increase the thermal conductivity of polymers
- Models the improvement of enhanced encapsulant materials using a numerical transient model
- Reviews the methods of testing thermal conductivity and electrical resistivity of polymers
- Measures the thermal conductivity of doped EVA samples using a novel differential scanning calorimetry (DSC) technique
- Validates the numerical model transient numerical model

The advantage of using enhanced materials is proven though measuring the maximum power output when a cell is encapsulated using the enhanced material. Despite showing an improvement, it is believed that the small increases in power output measured are too small to be statistically significant. Measurement of performance over a longer period of time, such as in the techniques used in the characterisation of solar thermal systems, may provide a greater understanding of the benefits of using thermally enhanced encapsulate material. .

The challenges encountered in this project will mainly be concerned with maintaining workability of the material, while at the same time increasing the thermal conductivity. The inclusion of a hard filler material into a polymer will typically produce a compound that has a greater mechanical modulus and brittleness than the unfilled resin. Samples will therefore need to be mechanically tested for their suitability as a PV cell laminate.

5.7 Methodology

5.7.1 Sample Preparation

BN powder (Carbotherm, Saint-Gobain, France) was mixed with EVA granules, in concentrations ranging from 10-60% w/w, using twin screw extrusion (HAAKE MiniLab II, Thermo Scientific, US), see Figure 5-2. The resulting extrusions were compression molded, to form sheets with a thickness of 1mm.

Figure 5-2: Twin screw extrusion of the composite material

5.7.2 Thermal Conductivity Testing

6mm discs were punched from the compressed sheets and placed into a DSC sample pan. Thermal interface resistances between the pan and the sample were reduced using a thin film of silicone oil applied directly to the underside of the sample disc. Crodatherm-25 phase change material (PCM) (Croda, UK) was chosen as the melting standard because its melting point (25°C) is well below that of EVA (89°C). Approximately 2mg of the PCM melting standard was deposited on the surface of the sample disc. This was achieved by gently heating the PCM material above its melting point in a glass pipette, before releasing it and allowing it to recrystallise on the surface of the sample. The method assumes unidirectional heat flow from the DSC furnace, through the sample and into the melting standard. Care had to be taken to ensure that there was no contact between the aluminum pan and the melting standard. The sample pan was then placed, un-crimped, into the sample chamber of the DSC (Perkin Elmer, US), the DSC process is illustrated in Figure 5-3. The sample was cooled to -10°C before being heated to 40°C at 5°C/min. The graph of heat flux vs. temperature, produced by the DSC was analyzed to determine melting rate of the sample. Low Density Polyethylene (LDPE) with a certified conductivity of 0.33W/m·K (Goodfellow Cambridge Ltd., UK) was used as the reference material and was prepared using the same method detailed above. Raw heat flux data from the DSC was imported into a thermal analysis programme, scripted in Python, which detects the onset of melting and the melting point, see Figure 5-4.

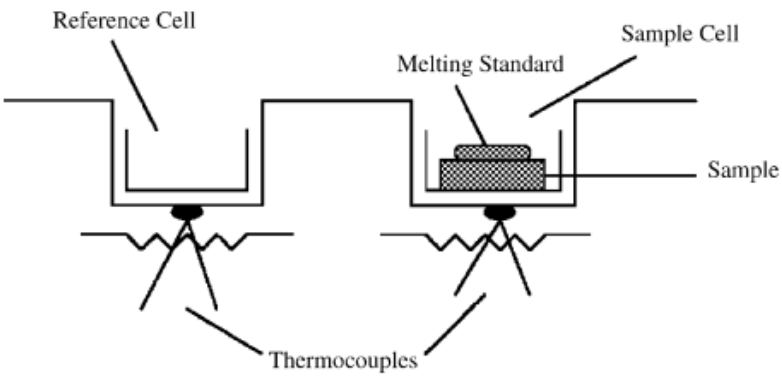

Figure 5-3: Illustration of the DSC melting standard method. Source [154].

The melting rate is then calculated as the gradient of a line connecting the melting onset and melting point. The program then uses (5.10) to determine the thermal conductivity of the sample [154].

$$\lambda_s = \lambda_r \frac{D_s A_r}{D_r A_s} \left(\frac{M_s}{M_r} \right)^2 \tag{5.10}$$

Where the subscripts *r* and *s* denote reference and sample respectively, *D* is disc thickness, *A* is the disc area, *M* is the melting rate and *λ* is the thermal conductivity.

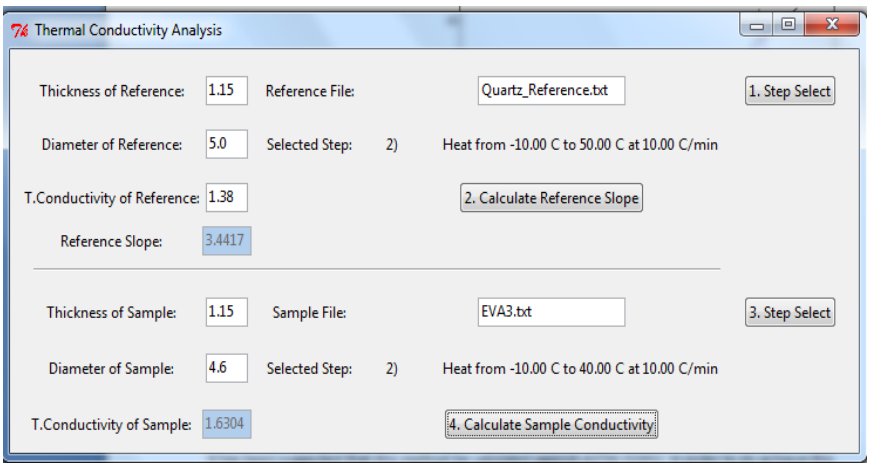

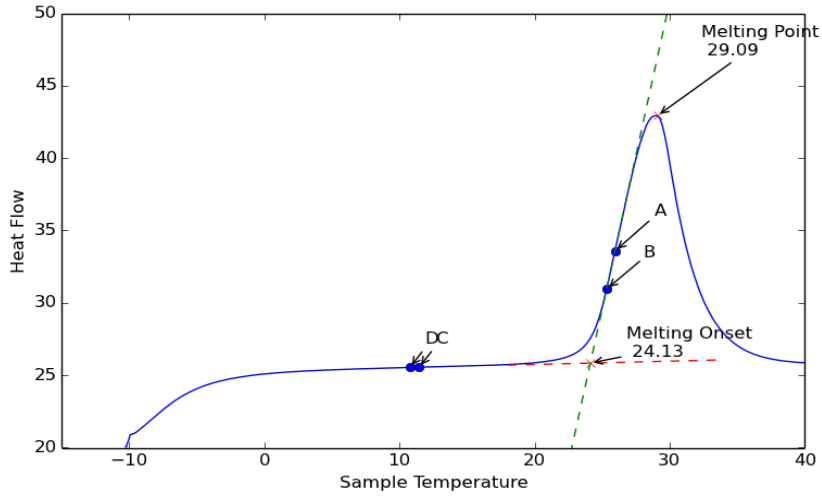

Figure 5-4: Interface of the results analysis program and the resulting graph

Table 5-2: The general properties of CrodaTherm 25 as detailed in manufacturer datasheet

Test	Typical Value	Units
Melting Temperature	25	°C
Latent Heat, Melting	186	kJ/kg
Crystallisation temperature	22	°C
Latent Heat, Crystallisation	-184	kJ/kg
Volumetric Heat Capacity	170	C(mJ/m³)
Specific Heat Capacity, Solid	1.9	kJ/(kg·°C)
Specific Heat Capacity, Liquid	2.3	kJ/(kg·°C)
Thermal conductivity, solid	0.21	W/(m·°C)
Thermal conductivity, liquid	0.15	W/(m·°C)

5.7.3 Manufacture of PV laminate

The parent EVA material and doped extrusions were compression molded into 0.5mm thick sheets measuring 155mm x 155mm. Two cells were laminated independently; one using the parent EVA, the other using the 50% BN/EVA w/w composite. The laminated PV cells are shown in Figure 5-5.

Figure 5-5: Laminated photovoltaic cells. Enhanced on the left and standard EVA on the right.

5.7.4 Temperature measurements at each interface

Thermocouples were positioned between the layers shown in Figure 5-1. The laminate was then placed between a constant heat source (25W ceramic heating mat) and heat sink (chilled absorber plate with inlet set to 21°C) to generate a one directional heat flux through the laminate, see Figure 5-6. The thermocouples recorded the temperature at each layer as the heat flux passed through the laminate.

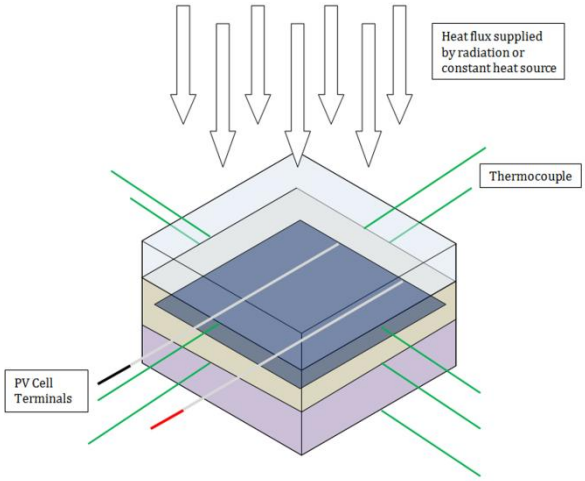

Figure 5-6: Experimental measurement of the temperature at the interface of each layer

5.8 Heat Transfer Numerical Models

5.8.1 Steady State Analysis

A numerical model based on the finite difference approach was developed to simulate the temperature distribution across the cross section of the PV laminate. The finite difference approach is shown in Figure 5-7.

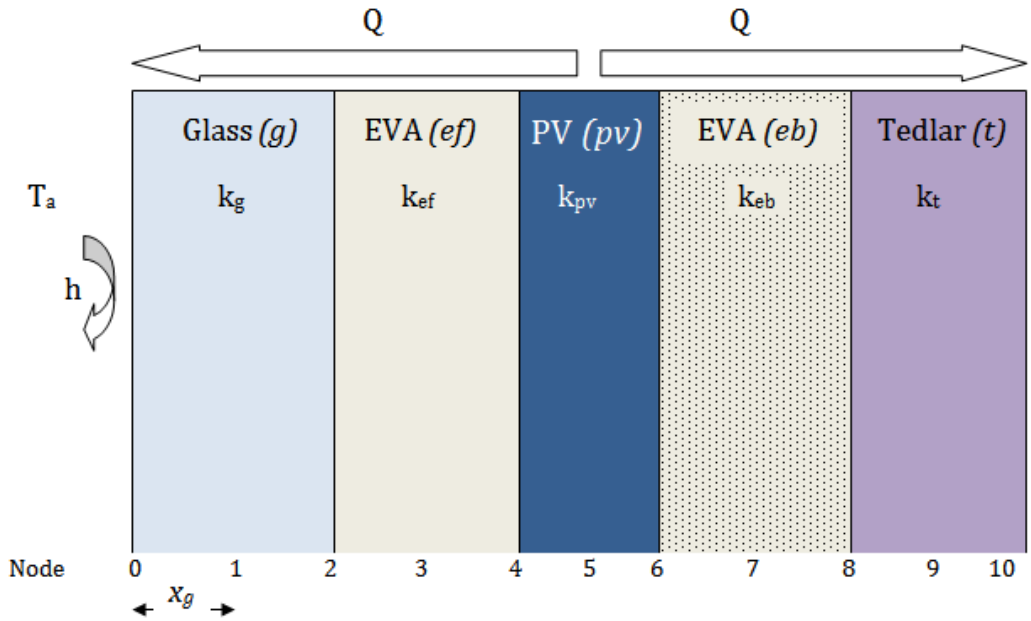

Figure 5-7: Illustration of the finite difference model used to determine the temperature at the interface of each material and at the internal nodes

At exterior interfaces, (5.11) shows the calculation of temperature at Node 0.

$$T_0 = \frac{hT_a + \left(\frac{1}{x_g} k_g T_1\right)}{h + \left(\frac{1}{x_g} k_g\right)} \tag{5.11}$$

At internal interfaces, (5.12) shows the calculation of temperature at Node 4

$$T_4 = \frac{k_{ef}\frac{1}{x_{ef}}(T_3) + k_{pv}\frac{1}{x_{pv}}(T_5) + \dot{g}_{pv}\left(\frac{x_{pv}}{2}\right)}{k_{ef}\frac{1}{x_{ef}} + k_{pv}\frac{1}{x_{pv}}} \tag{5.12}$$

At internal nodes, (5.13) shows the calculation of temperature at Node 1.

$$T_1 = (T_0 + T_2)/2 \tag{5.13}$$

The PV layer was modelled as a volumetric heat generator. The temperature at the centre of the PV cell, at Node 5 was calculated using (5.14).

$$T_5 = \frac{\frac{1}{x_{pv}^2}(T_4) + \frac{1}{x_{pv}^2}(T_6) + \frac{\dot{g}_{pv}}{k_{pv}}}{2\left(\frac{1}{x_{pv}^2}\right)} \tag{5.14}$$

A system of equations is created across the layers of the PV laminate. This was solved iteratively using a program coded in Fortran. The coding used is shown below:

```
PROGRAM STEADY
   DATA T0,T1,T2,T3,T4,T5,T6,T7,T8,T10/10*50./
   DATA T9/50./

!Boundary Temperatures and heat loss coefficient
   real,parameter::Tp= 25., Ta = 20., h = 11.,Tb = 20., hb = 11.

!Material Conductivity
   real,parameter:: kg = 0.98, kef = 0.23, kpv = 148., keb = 2.85, kt = 0.36

!Nodal Spacing
   real,parameter:: xg = 0.0015, xef = 0.0002, xpv = 0.00009, xeb = 0.0002, xt = 0.00025

!Volumetric Energy Generation
   real,parameter:: gpv = 3.46E6


!Results file

   integer, parameter :: out_unit=20

  OPEN (unit=out_unit,file="results.txt",action="write",status="replace")

   DO 20 K = 1,500000

      T10 =((h*tb)+((1/xt)*(kt)*(T9)))/(h+((1/xt)*(kt)))

      T9 = (T8+T10)/2.

      T8 = (((1./xeb)*keb*t7)+((1./xt)*kt*t9))/((keb*(1./xeb))+(kt*(1./xt)))

      T7 = (T6+T8)/2.

      T6 =
(((1./xpv)*kpv*t5)+((1./xeb)*keb*t7)+(gpv*(xpv/2.)))/((kpv*(1./xpv))+(keb*(1./xeb)))

      T5 = (((1./(xpv**2))*t4)+((1./(xpv**2))*t6)+(gpv/kpv))/(2.*(1./(xpv**2)))

      T4 = (((1./xef)*kef*t3)+((1./xpv)*kpv*t5)+(gpv*(xpv/2.)))/((kef*(1./xef))+(kpv*(1./xpv)))

      T3 = (T2+T4)/2.

      T2 = (((1./xg)*kg*t1)+((1./xef)*kef*t3))/((kg*(1./xg))+(kef*(1./xef)))

      T1 = (T0+T2)/2.

      T0 = ((h*ta)+((1/xg)*(kg)*(T1)))/(h+((1/xg)*(kg)))

      WRITE (*,10)K,T0,T1,T2,T3,T4,T5,T6,T7,T8,T9

      if (mod(k,1000)==0) WRITE
(out_unit,*)K,",",T0,",",T1,",",T2,",",T3,",",T4,",",T5,",",T6,",",T7,",",T8,",",T9,",",T10

      10 FORMAT (' ',I3,10(F8.1))

      20 CONTINUE
```

END PROGRAM STEADY

5.8.2 Transient Analysis of Solar Collector

Under real conditions a collector will not reach steady state conditions. The models described in the previous section do not take into account the capacitance effects caused by the components of the collector. Transient models are discussed in Section 4.6. A transient analysis would provide more insight into how the collector would perform when exposed to varying temperatures over a given time period. To carry out a transient analysis the equations in the previous section have to be modified to take into account the capacitance effects. In doing so:

(5.11), at exterior interfaces, becomes:

$$\frac{d\left(\frac{dT_0}{dt}\right)}{dT_1} = \frac{2k_g}{\rho_g \Delta x_g c_g} \tag{5.15}$$

(5.12), at internal interfaces, becomes:

$$\begin{aligned}\frac{dT_4}{dt} = &\left(\frac{1}{\left(\rho_{ef}\frac{x_{ef}}{2}c_{ef} + \rho_{pv}\frac{x_{pv}}{2}c_{pv}\right)}\right)k_{ef}\frac{1}{x_{ef}}T_3 - T_4 + \\ &\left(\frac{1}{\left(\rho_{ef}\frac{x_{ef}}{2}c_{ef} + \rho_{pv}\frac{x_{pv}}{2}c_{pv}\right)}\right)k_{pv}\frac{1}{x_{pv}}T_5 - T_4 + \\ &\left(\frac{1}{\left(\rho_{ef}\frac{x_{ef}}{2}c_{ef} + \rho_{pv}\frac{x_{pv}}{2}c_{pv}\right)}\right)\dot{g}_{pv}\left(\frac{x_{pv}}{2}\right)\end{aligned} \tag{5.16}$$

(5.13), at internal nodes, becomes:

$$\frac{dT_1}{dt} = \frac{\alpha_g}{x_g^2}T_0 - \frac{2\alpha_g}{x_g^2}T_1 + \frac{\alpha_g}{x_g^2}T_2 \tag{5.17}$$

(5.14), at the PV cell, becomes:

$$\frac{dT_5}{dt} = \frac{\alpha_{pv}}{x_{pv}^2}T_4 - \frac{2\alpha_{pv}}{x_{pv}^2}T_5 + \frac{\alpha_{pv}}{x_{pv}^2}T_6 + \frac{\alpha_{pv}\dot{g}_m}{k_{pv}} \tag{5.18}$$

Each equation must be solved by differentiating each of the variables with respect to each parameter. For example the derivative of the first parameter of the function shown in (5.18) is shown in (5.19).

$$\frac{d\left(\frac{dT_5}{dt}\right)}{dT_4} = \frac{\alpha_{pv}}{x_{pv}^2} \tag{5.19}$$

This process needs to be done for all of the equations, at each node and interface, in the layers shown in Figure 5-7. This leads to a system of 38 equations that are solved iteratively. Such a system can be solved using a program such as LSODE.

5.9 Results

5.9.1 Thermal Conductivity

Composite material was prepared with varying concentration of BN filler (10,20,30 and 60%). The thermal conductivity was measured for each sample and the results are shown in Figure 5-8.

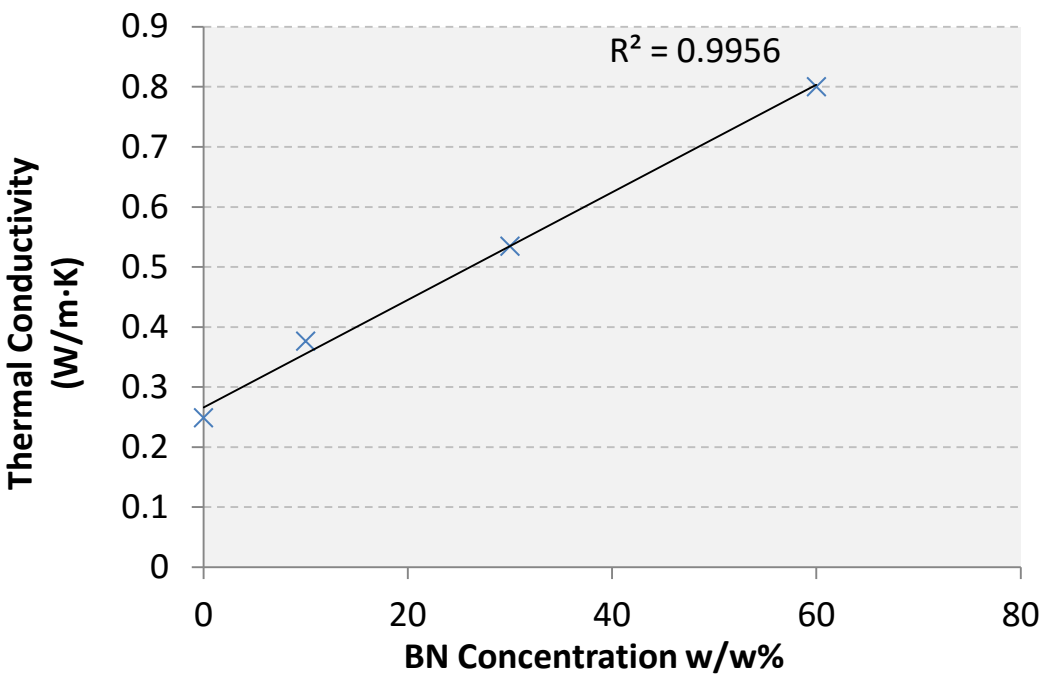

Figure 5-8: Thermal conductivity vs. BN concentration of the composite

The study found that by increasing the BN concentration from 0% to 60% w/w, thermal conductivity increases from 0.23 W/m·K to 0.83 W/m·K. The confidence in the method was measured using linear regression. A R^2 value of 0.9956 indicates a good level of confidence in the experimental procedure. To compare the results with the findings of the study by Lee [102] the mass fraction must be converted to volume fraction, φ, using (5.20).

$$V = \frac{W_E}{\rho_E} + \frac{W_B}{\rho_B} = V_E + V_B$$
$$\varphi_B = \frac{V_B}{V} \tag{5.20}$$

Where *W*, *V* and *ρ* are the weight, volume and density respectively; and subscripts, *E* and *B* denote EVA and BN respectively.

Table 5-3: Calculation of volume fraction

	Weight [%]	Density (g/cm^3)	Volume [cm^3]	Volume Fraction
EVA	40	0.935 [158]	42.78	62.1%
Boron Nitride	60	2.3 [159]	26.09	37.9%

For 60% w/w Boron Nitride to EVA, the corresponding volume fraction is approximately 40% v/v as shown in Table 5-3. For 40% v/v BN concentration Lee reported a thermal conductivity of approximately 0.75 W/m·K [102] which is in close agreement with the 0.83W/m·K measured in this study. The study by Lee continued to increase the BN concentration up to 60% v/v; however it was found that as the BN concentration increased there was a noticeable change in texture and stiffness of the material. More work is required to determine how these changes in property will influence the workability of the material during PV encapsulation and throughout the laminate's lifetime.

5.9.2 Interface Temperatures

The temperature at each of the interfaces, shown in Figure 5-7 (T2, T4, T6 and T8), were measured using thermocouples inserted between each of the layers before lamination. The temperature was recorded for a period of 3000 seconds. The results for the standard and doped EVA are shown in Figure 5-9 and Figure 5-10 respectively.

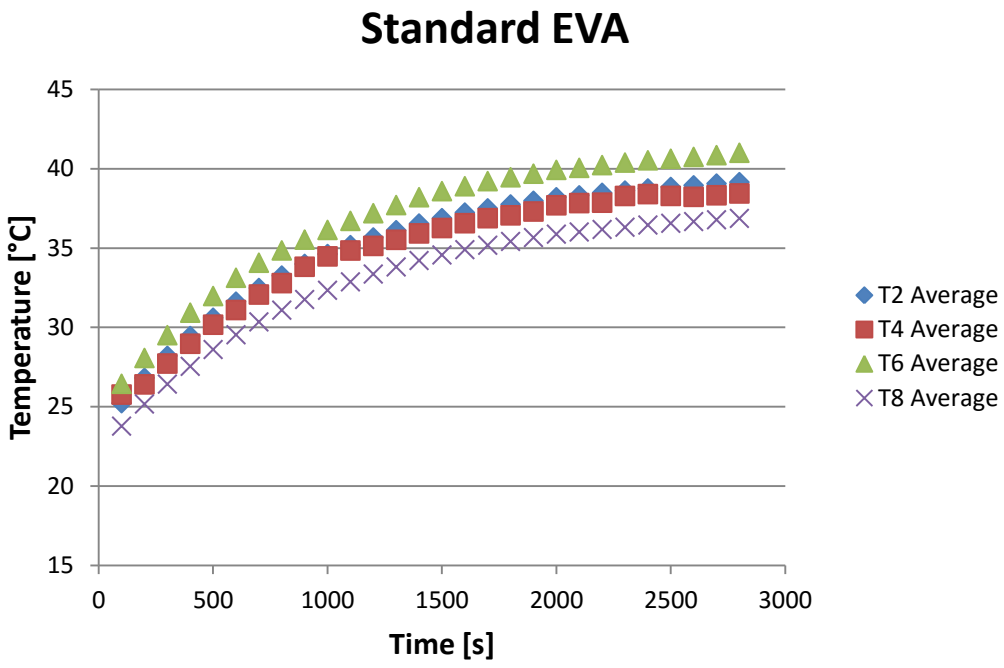

Figure 5-9: Average temperature at each interface vs time for standard EVA backed PV cell

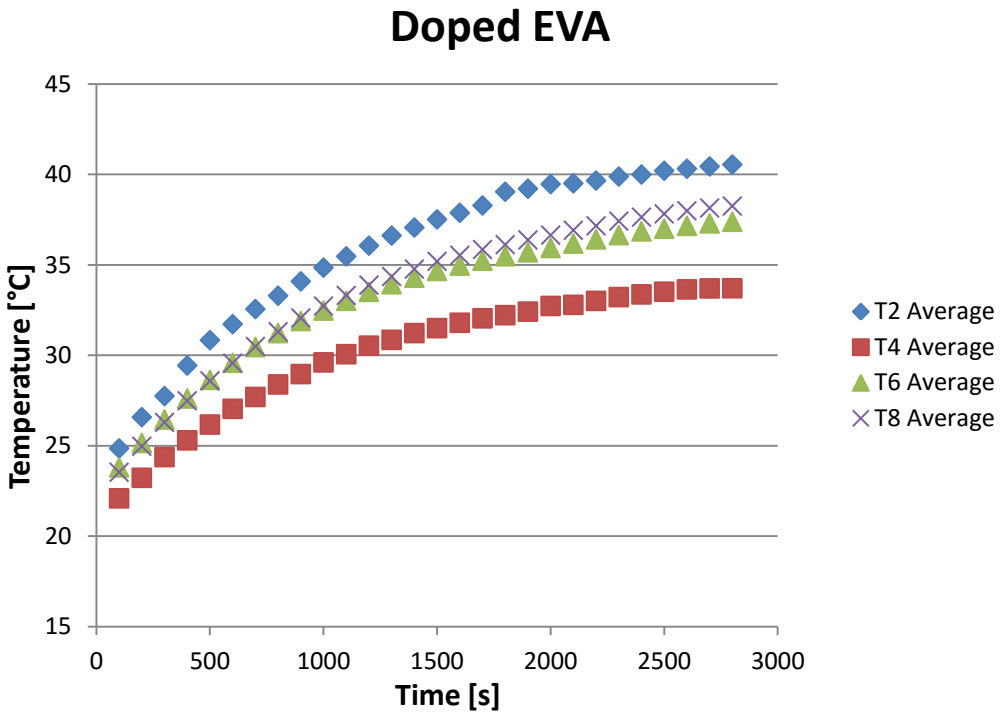

Figure 5-10: Average temperature at each interface vs. time for composite EVA backed PV cell

When the results from these two experiments are compared, there is no agreement between the relative temperature at each interface. For instance in the standard EVA experiment, T6 has the highest temperature and in the doped experiment T2 is the highest temperature.

This variation suggests there were irregularities in the way the laminates were constructed. It was noted that the thermocouples did not embed seamlessly into the layers, instead air bubbles of varying sizes would form around each thermocouple. This may suggest the discrepancies in temperature readings between each layer and even thermocouples on each layer. An attempt was made to reduce the thickness of the thermocouple wire to 0.12mm and even though there was some reduction in the size of the air bubble, there was still variation in the resulting temperature. The results presented above were obtained using 0.12mm thermocouples.

Despite this variation an average laminate temperature was calculated using all of the thermocouples in each laminate. A comparison of the doped vs standard EVA case is shown in Figure 5-11.

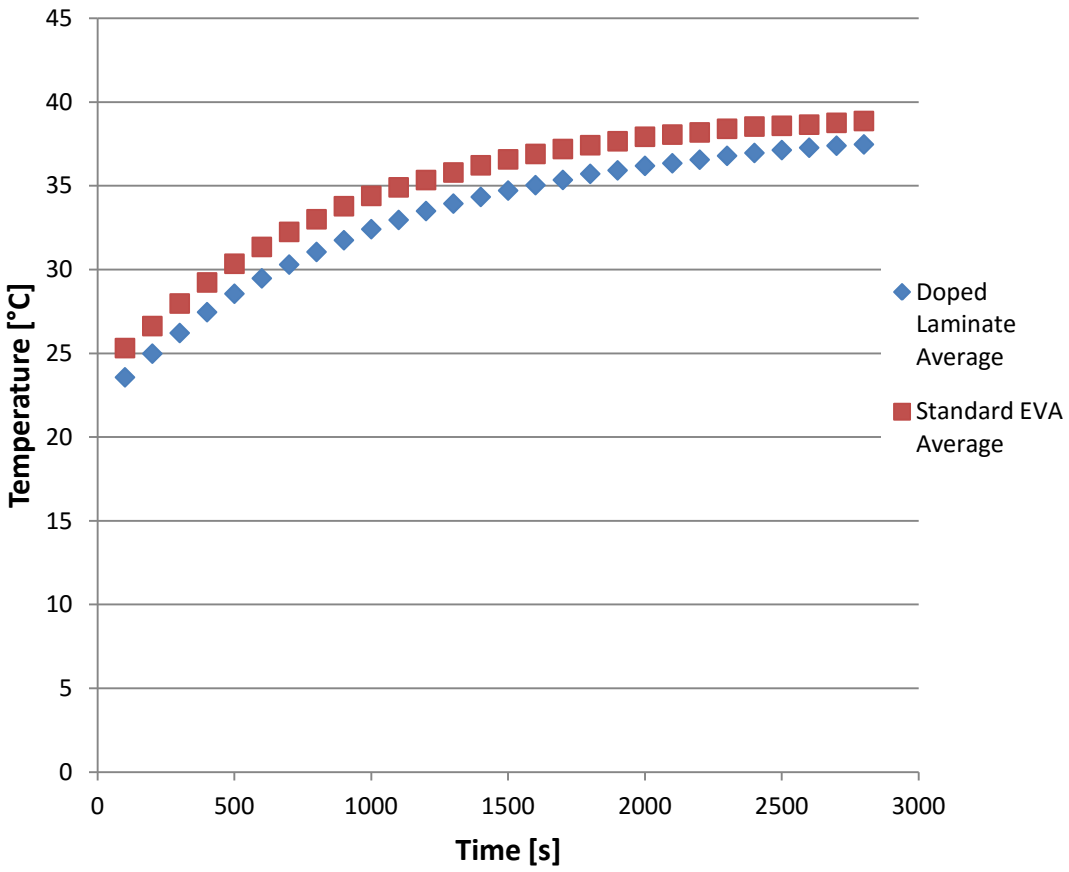

Figure 5-11: A comparison of the average laminate temperature, as measured by thermocouples, for the laminates containing BN doped and standard EVA.

Figure 5-11 shows that the average temperature of the doped laminate is consistently below that of the laminate containing standard EVA when tested under the same conditions. This indicates that the enhanced laminate is having a cooling effect across the entire laminate.

5.9.3 Steady State Temperature Modelling

The temperature profile across the external, interior and interface nodes were plotted for two cases and three conductivities of backing-EVA. In Case 1 the rear surface temperature of the laminate, T10 on Figure 5-7, was fixed at a 25°C. This case resembles a temperature controlled absorber plate of a PVT collector. The top surface was assigned an overall loss coefficient of 11W/m^2·°C . The temperature profile for Case 1 is shown in Figure 5-12.

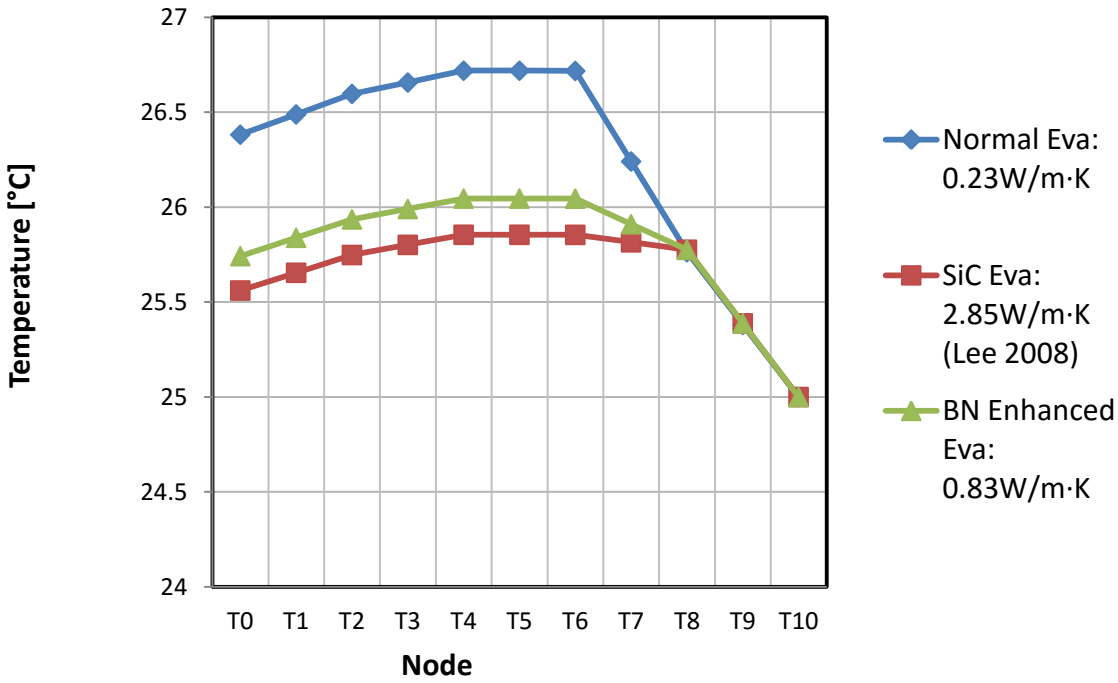

Figure 5-12: Temperature profile for Case 1

In Case 1, the temperature of the PV cell, T5, is highest for the un-doped EVA. As the thermal conductivity of the backing-EVA increases, the PV cell temperature reduces. A temperature reduction of 0.7°C in PV cell temperature is seen when thermal conductivity of the backing-EVA is increased from 0.23W/m·K to 0.83W/m·K. Using the power temperature coefficient for a crystalline cell, as supplied by the manufacturer (-0.42%/K), this would enhance the performance by 0.3%. By further increasing the thermal conductivity to 2.85 W/m·K, the PV cell temperature is further reduced by 0.2°C. This shows that the relationship between the conductivity of the backing-EVA and PV cell temperature is non-linear.

These results show that the increased thermal conductivity of the backing-EVA improves the heat flow between the PV cell and the rear surface, T10. This effect also reduces the overall

temperature of the laminate. The front surface of the panel is hottest for the 0.23W/m·K and coldest for the 2.85W/m·K backing-EVA.

In Case 2, a heat loss coefficient was applied to both the top surface and the rear surface of the laminate; thus resembling a PV module that is evenly ventilated on either surface. The ambient temperature was kept at 20°C. The temperature profile for Case 2 is shown in Figure 5-13.

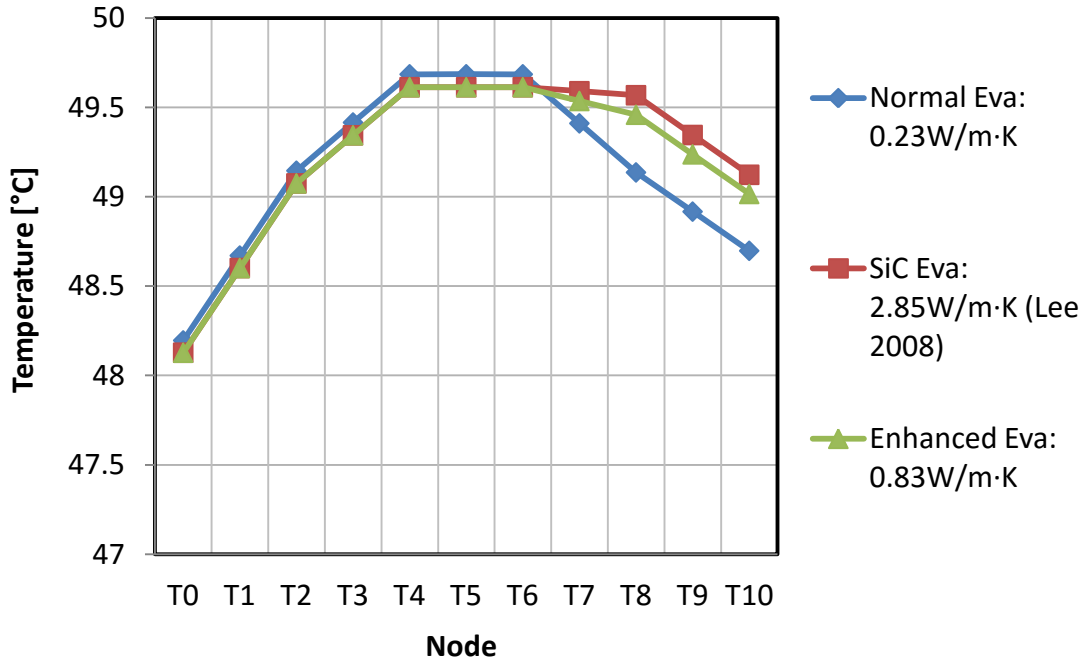

Figure 5-13: Temperature profile for Case 2

In Case 2 the temperature of the PV cell is again highest for the standard EVA; however, when the thermal conductivity is increased from 0.23 W/m·K to 0.83 W/m·K, the temperature difference is much smaller than Case 1 at 0.1°C, equating to a power improvement of 0.04%. The temperature difference between 0.83 W/m·K and 2.85 W/m·K is negligible. The rear surface temperature, T10, is lowest for the 0.23 W/m·K backing-EVA and highest for the 2.85 W/m·K . This is due to the low thermal conductivity of the backing material reducing heat flow and insulating the PV cell. This results in a higher PV cell temperature and lower surface temperature. Considering the cost of the filler material was 240€/kg; it is believed that these mediocre improvements in thermal performance would not justify the additional material and manufacturing costs incurred to produce the enhanced material.

The PV cell temperature for Case 2 is higher (49.6°C) than that of Case 1 (26.7°C); which is a 10% improvement in power output from the PV cell thus showing the ability of active cooling to maintain the operating efficiency of the PV cell. Although this is only true when the

fluid temperature is less than the cell operating temperature. In some instances the water in the heating system may be higher than that reached by the PV cell under normal conditions.

5.10 Conclusions

This study successfully developed a methodology to produce EVA doped with Boron Nitride for use in photovoltaic lamination. A methodology using differential scanning calorimtery was developed to test the thermal conductivity of the low melting point polymers using an ester wax melting standard. A range of filler percentages were investigating from 0% to 60% w/w (0-40% v/v). The conductivity of the EVA increased from 0.23W/m·K for the parent material to 0.83 W/m·K for the 60% w/w composite. This was in close agreement with a previously reported study that used a different thermal conductivity method. The physical properties of the composite became rigid with increasing percentage of boron nitride. More work will be required to investigate the influence this has on the workability of the material during the lamination of PV and during the lifetime of the PV device.

A one dimensional numerical model was developed to model the heat flow through the layers of the laminate. Two cases were simulated; one that resembled an actively cooled PVT collector, and the other, a PV module ventilated on both the front and rear surfaces. For each case different conductivities of the EVA-backing were investigated. The study found that the use of 60% BN composite was most useful in the actively PVT collector where a 0.7°C temperature difference in PV cell temperature between the composite and standard material was achieved. This achieved an improvement in PV performance of 0.3%. For the ventilated PV laminate, an improvement of 0.04% was achieved. It is believed that this mediocre improvement would not justify the additional material and manufacturing costs incurred to produce the enhanced material.

The biggest difference in PV cell temperature of 23°C was between the PVT and ventilated module resulting in an electrical performance improvement of 10% at a fluid temperature of 21°C. At higher fluid temperatures this benefit would be reduced.

To investigate the impact on performance, the composite material was used in the lamination of a PV cell. Thermocouples places at the interface of each layer within the laminate recorded the temperature as the laminate was exposed to a unidirectional heat flow. The integration of thermocouples was not seamless, and the presence of air gaps and areas of de-lamination were identified as root causes for the inconsistent readings. It was hoped that this would provide experimental validation to the numerical models but more work is required to ensure the integrity of the laminate.

5.11 Recommendations for future work

- **Electrical resistivity testing**: Electrical resistivity testing was carried out however the resistance for the highest concentrations remained too high for the available apparatus

>1000Ω. It would be useful to see how the increase in filler influence the electrical resistivity and if this would pose a problem for the voltages experienced in large arrays.

- **Testing of a range of different ceramics**: Lee [102] carried out testing on difference ceramic fillers and found that silicon carbide achieved the highest conductivity per composite fraction. It would be useful to extend testing to the same materials to determine if there is conformity across all samples. This would also increase confidence in the thermal conductivity method used.
- **Development of transient thermal model:** As steady state conditions rarely occur under normal conditions, it would be useful to model the laminate transiently. Using this method it would be possible to model the interactions between the laminate and changing irradiance and ambient conditions that occur daily, monthly or yearly. The performance could be evaluated over a given time period. This would better help understand the real benefits of using enhanced composites.
- **Validation of steady state and transient models:** The inconsistencies in the readings from the thermocouples inserted into the interfaces meant that it was not possible to validate the steady state model.
- **Extensive development of the melting standard method:** The melting standard method was promising in the thermal conductivity testing of small quantities of low melting point polymers. Due to limited availability of the equipment, a rigorous assessment of the confidence in the methodology could not be completed. The high value of linear regression gave some degree of confidence but further work should be carried out to increase the confidence in this method. This would involve comparison with other established methods such as the ASTM E1952 and certified reference materials.
- **Implication BN percentage has on PV lamination and durability:** Although the increase in thermal conductivity is desirable for increased heat removal, the addition of BN could impact other material properties that are critical to functioning of a PV device. Electrical resistivity has been mentioned but there is also durability, water permeability, adhesion to glass substrate, mechanical properties to name a few. Further research should investigate how these properties will be influenced by increased filler proportions and if so whether they would be suitable for use in a PV device.

6. General Conclusions

The aim of this project was to develop and characterise the performance of PVT collectors that produce both heat and electricity from a single device. To achieve this an experimental system has been created to evaluate the performance of PV-T collectors and act as a blue print for others working in the field.

The experimental system was used to; characterize the performance of a header riser and serpentine design of solar thermal collector; quantify the impact of using a cover to reduce heat loss and quantify the combined efficiency of a PV-T collector. The results show that when using the same mass flow rate, the serpentine design has superior performance due to a reduced heat loss coefficient. It was also shown that the use of a cover reduces the overall heat loss coefficient of the serpentine collector by 50%. In a PV-T collector, the thermal energy is the biggest contributor to overall output, because of this, the serpentine collector has the highest combined efficiency. When electricity is generated by laminates the thermal efficiency is reduced by a further 3.5%; however this drop in thermal efficiency is a result of the incident radiation producing electricity before reaching the absorber. The combined efficiency of the PV-T collectors were compared at controlled inlet temperatures. The serpentine design had the highest combined efficiency of 61% with 8% electricity at the lowest inlet temperature (21°C). The dominant form of loss in the PV-T system is temperature driven; as the thermal efficiency decreases, electricity generation makes up a larger percentage of the combined output. This study highlights the potential for manufacturers of bespoke thermal absorbers and PV devices to combine their products into a single PV-T device that could achieve improved efficiency over a given roof area.

The experimental facility was then used to validate empirical models and develop a CFD approach to assess and visualise performance of a PVT collector- a tool that will be useful to those working on the design and development of PVT and solar thermal collectors. In the CFD model, irradiance is specified as a heat flux and the resulting calculation of thermal efficiency takes into account the absorptance of the collector. When comparing the results the simulated heat removal factor of the serpentine collector was 4.2% higher and the header riser 12.1% less than the measured experimental values. The reason for this discrepancy could be a result of increased thickness of the absorber in the CFD model, variation in the contact length and contact integrity between the pipe and the absorber in the simulated and experimental cases. It has been shown that a laser welded pipe does not always have perfect contact with the absorber and separation can occur. Any of these reasons could result in an over or underestimation of collector performance, as the simulation tries to fit the specified boundary conditions. Despite the discrepancies between the experimental and simulated cases, the use of CFD is useful for the relative comparison of different designs of collector. In this study the methodology was used to investigate the impact of different flow patterns in a header riser collector. The most efficient design was the cross flow design and there was close agreement to other published studies.

The third project involved the enhancement of low conductivity EVA encapsulant to aid heat removal from the PV cells in a PVT collector. This study successfully developed a methodology to produce EVA doped with Boron Nitride for use in photovoltaic lamination. A methodology using differential scanning calorimtery was developed to test the thermal conductivity of the low melting point polymers using an ester wax melting standard. It was

found that by doping the parent material with a 60% w/w concentration of thermal filler, the conductivity could be increased fourfold.. This was in close agreement with a previously reported study that used a different thermal conductivity method. The physical properties of the composite became rigid with increasing percentage of boron nitride. More work will be required to investigate the influence this has on the workability of the material during the lamination of PV and during the lifetime of the PV device. A one dimensional numerical model was developed to model the heat flow through the layers of the laminate. Two cases were simulated; one that resembled an actively cooled PVT collector, and the other, a PV module ventilated on both the front and rear surfaces. For each case different conductivities of the EVA-backing were investigated. The study found that the use of 60% BN composite was most useful in the actively PVT collector where a 0.7°C temperature difference in PV cell temperature between the composite and standard material was achieved. This achieved an improvement in PV performance of 0.3%. For the ventilated PV laminate, an improvement of 0.04% was achieved. It is believed that this improvement would not justify the additional material and manufacturing costs incurred to produce the enhanced material. The biggest difference in PV cell temperature of 23°C was between the PVT and ventilated module resulting in an electrical performance improvement of 10% at a fluid temperature of 21°C. At higher fluid temperatures this benefit would be reduced. To investigate the impact on performance, the composite material was used in the lamination of a PV cell. Thermocouples places at the interface of each layer within the laminate recorded the temperature as the laminate was exposed to a unidirectional heat flow. The integration of thermocouples was not seamless, and the presence of air gaps and areas of de-lamination were identified as root causes for the inconsistent readings. It was hoped that this would provide experimental validation to the numerical models but more work is required to ensure the integrity of the laminate.

Recommendations for future work have been proposed and are included at the end of the each respective project chapter. The experimental recommendations are given in Chapter 3, simulation recommendations in Chapter 4 and thermal enhancement of EVA, in Chapter 5.

7. References

[1] BP. Statistical review of world energy 2011. 2011.

[2] WHO. The world health report 2002: reducing risks and promoting healthy life. 2002.

[3] A. Salam. Impact of weather change: The challenges for public health. *2nd International Conference: Climate, Sustainability and Development*, 2010.

[4] M. Wicks. Energy security: A national challenge in a changing world. *DECC*, 2009.

[5] EERE. Weather data. *http://apps1.eere.energy.gov/buildings/energyplus/weatherdata_about.cfm*, 2015.

[6] Z. Kadziulis. Integration of hydrogen energy storage in a low carbon renewable electricity generation system. *Brunel University, Mechanical Engineering Major Individual Project Dissertation*, 2014.

[7] John A Duffie and William A Beckman. *Solar engineering of thermal processes*. John Wiley & Sons, 4th edition, 2013.

[8] Ali Mohammad Noorian, Isaac Moradi, and Gholam Ali Kamali. Evaluation of 12 models to estimate hourly diffuse irradiation on inclined surfaces. *Renewable energy*, 33(6):1406–1412, 2008.

[9] Janet L. Sawin. Renewables 2012 global status report. Technical report, REN21, 2011.

[10] Paris Secretariat REN21. *Renewables 2014: Global Status Report*. REN21 Secretariat Paris, France, 2014.

[11] Alexandre-Edmond Becquerel. Mémoire sur les effets électriques produits sous l'influence des rayons solaires. *Comptes Rendus*, 9(567):1839, 1839.

[12] A. Chodos. This month in physics history april 25, 1954: Bell labs demonstrates the first practical silicon solar cell. *http://www.aps.org/publications/apsnews/200904/physicshistory.cfm accessed 08/08/2014*, 2014.

[13] Adolf Goetzberger, Christopher Hebling, and Hans-Werner Schock. Photovoltaic materials, history, status and outlook. *Materials Science and Engineering: R: Reports*, 40(1):1–46, 2003.

[14] Martin A Green, Keith Emery, Yoshihiro Hishikawa, Wilhelm Warta, and Ewan D Dunlop. Solar cell efficiency tables (version 45). *Progress in photovoltaics: research and applications*, 23(1):1–9, 2015.

[15] Fraunhofer ISE. Photovoltaic report october 2014. *http://www.ise.fraunhofer.de/de/downloads/pdf-files/aktuelles/photovoltaics-report-in-englischer-sprache.pdf*, 2014.

[16] MA Green. Recent developments in photovoltaics. *Solar energy*, 76(1):3–8, 2004.

[17] David E Carlson and Cristopher R Wronski. Amorphous silicon solar cell. *Applied Physics Letters*, 28(11):671–673, 1976.

[18] DL Staebler and CR Wronski. Reversible conductivity changes in discharge-produced amorphous si. *Applied Physics Letters*, 31(4):292–294, 1977.

[19] Masatsugu Izu, Vincent D Cannella, and Stanford R Ovshinsky. Continuous amorphous solar cell production system, October 18 1983. US Patent 4,410,558.

[20] Antonio Luque and Steven Hegedus. *Handbook of photovoltaic science and engineering*. John Wiley & Sons, 2011.

[21] E. Wesoff. Solar grim reaper alert: Cigs aspirant heliovolt gives up the ghost. *http://www.greentechmedia.com/articles/read/Solar-Grim-Reaper-Alert-CIGS-Aspirant-HelioVolt-Gives-Up-the-Ghost accessed 08/08/2014*, 2014.

[22] William Shockley and Hans J Queisser. Detailed balance limit of efficiency of p-n junction solar cells. *Journal of applied physics*, 32(3):510–519, 1961.

[23] Tom Tiedje, Eli Yablonovitch, George D Cody, and Bonnie G Brooks. Limiting efficiency of silicon solar cells. *Electron Devices, IEEE Transactions on*, 31(5):711–716, 1984.

[24] Navid S Fatemi. Satellite market trends and the enabling role of multi-junction space solar cells. In *Photovoltaic Specialists Conference, 2008. PVSC'08. 33rd IEEE*, pages 1–4. IEEE, 2008.

[25] J. Allan. The use of nanostructured silicon in photovoltaic cells. Master's thesis, Brunel University, 2009.

[26] Gavin Conibeer. Third-generation photovoltaics. *Materials today*, 10(11):42–50, 2007.

[27] Martin A Green. Third generation photovoltaics: Ultra-high conversion efficiency at low cost. *Progress in Photovoltaics: Research and Applications*, 9(2):123–135, 2001.

[28] Brian Norton, Philip C Eames, Tapas K Mallick, Ming Jun Huang, Sarah J McCormack, Jayanta D Mondol, and Yigzaw G Yohanis. Enhancing the performance of building integrated photovoltaics. *Solar Energy*, 85(8):1629–1664, 2011.

[29] E. Hughes. Infinite energy introduce the uk's first modular solar car park canopy. *http://www.solarpowerportal.co.uk/news/infinite_energy_introduce_the_uks_first_modular_solar_car_park_canopy5478 accessed 05/04/2014*, 2011.

[30] World Highways. Photovoltaic finish to road noise pollution. *http://www.worldhighways.com/sections/irf/features/photovoltaic-noise-barriers/ accessed 15/07/2014*, 2014.

[31] HKV Lotsch, Adolf Goetzberger, and Volker U. Hoffmann. Solar cells and solar modules. *Photovoltaic Solar Energy Generation*, pages 85–94, 2005.

[32] T. Markvart and L. Castner. *Practical Handbook of Photovoltaics: Fundamentals and Applications*, chapter Principles of Solar Cell Operation, page 79. Elsevier, 2003.

[33] Z. Dehouche. *Renewable Energy Technologies Textbook*. Brunel University, 2014.

[34] DL Evans and LW Florschuetz. Cost studies on terrestrial photovoltaic power systems with sunlight concentration. *Solar Energy*, 19(3):255–262, 1977.

[35] A Virtuani, D Pavanello, and G Friesen. Overview of temperature coefficients of different thin film photovoltaic technologies. In *25th European Photovoltaic Solar Energy Conference and Exhibition/5th World Conference on Photovoltaic Energy Conversion*, pages 6–10, 2010.

[36] EPIA. Global market outlook for photovoltaics 2014–2018. *EPIA Report*, 2014.

[37] M. Schachinger. pvxchange module price index. *http://www.pv-magazine.com/investors/module-price-index*, 2015.

[38] EPIA. Global market outlook for photovoltaics until 2016. *EPIA Report*, 2012.

[39] DECC. Monthly feed-in tariff commissioned installations by month. *https://www.gov.uk/government/statistics/monthly-small-scale-renewable-deployment*, 2015.

[40] DECC. Solar pv cost data. *https://www.gov.uk/government/statistics/solar-pv-cost-data*, 2014.

[41] Michael Hermann. Development of a bionic solar collector with aluminium roll-bond absorber. Technical report, Fraunhofer Institute for Solar Energy Systems ISE, 2011.

[42] Baerbel Epp. Laser welding captures the market, 04 2009. http://www.solarthermalworld.org/node/40401.

[43] SAP BRE. The governments standard assessment procedure for energy rating of dwellings, 2012.

[44] Franz Mauthner and Werner Weiss. Solar heat worldwide: markets and contribution to the energy supply 2012. *IEA Solar Heating & Cooling Programme. Germany*, 2014.

[45] IEA. Technology roadmap solar heating and cooling. Technical report, 2012.

[46] BJ Huang, TH Lin, WC Hung, and FS Sun. Performance evaluation of solar photovoltaic/thermal systems. *Solar energy*, 70(5):443–448, 2001.

[47] J Bystrom. Iea shc task 35 subtask ada 1-2 outcome of pv/t market survey interviews. *http://archive.iea-shc.org/publications/task.aspx?Task=35*, 2008.

[48] HA Zondag, DW De Vries, WGJ Van Helden, RJC Van Zolingen, and AA Van Steenhoven. The yield of different combined pv-thermal collector designs. *Solar Energy*, 74(3):253–269, 2003.

[49] Xingxing Zhang, Xudong Zhao, Stefan Smith, Jihuan Xu, and Xiaotong Yu. Review of r&d progress and practical application of the solar photovoltaic/thermal (pv/t) technologies. *Renewable and Sustainable Energy Reviews*, 16(1):599–617, 2012.

[50] TT Chow. A review on photovoltaic/thermal hybrid solar technology. *Applied Energy*, 87(2):365–379, 2010.

[51] R Daghigh, MH Ruslan, and K Sopian. Advances in liquid based photovoltaic/thermal (pv/t) collectors. *Renewable and Sustainable Energy Reviews*, 15(8):4156–4170, 2011.

[52] Jai Prakash. Transient analysis of a photovoltaic-thermal solar collector for co-generation of electricity and hot air/water. *Energy Conversion and Management*, 35(11):967–972, 1994.

[53] Y Tripanagnostopoulos. Aspects and improvements of hybrid photovoltaic/thermal solar energy systems. *Solar Energy*, 81(9):1117–1131, 2007.

[54] H Zondag. Commercially available pvt products, 2006.

[55] Lus Ricardo Bernardo, Bengt Perers, Håkan Håkansson, and Björn Karlsson. Performance evaluation of low concentrating photovoltaic/thermal systems: A case study from sweden. *Solar Energy*, 85(7):1499–1510, 2011.

[56] Ricardo Bernardo, Bengt Perers, Håkan Håkansson, and Björn Karlsson. Evaluation of a parabolic concentrating pvt system. In *Eurosun 2008*. Curran Associates, Inc.(Apr 2011), 2008.

[57] P. Affolter, W. Eisenmann, H. Fechner, M. Rommel, H. Tripanagnostopoulos Y. Schaap, A. Sorensen, and H. Zondag. A european guide for the development and market introduction of pv-thermal technology. *The 6th Framework Programme*, 2006.

[58] WIP. Pv catapult european collaboration for identification of pv research and markets opportunities, socio-economics, studies, performance assessment and dissemination of pv and pv-thermal technology, 03 2015.

[59] Ofgem. An introduction to the domestic renewable heat incentive scheme. 2015.

[60] JA Clarke, JW Hand, CM Johnstone, N Kelly, and PA Strachan. Photovoltaic-integrated building facades. *Renewable energy*, 8(1):475–479, 1996.

[61] Timothy N Anderson, Mike Duke, GL Morrison, and James K Carson. Performance of a building integrated photovoltaic/thermal (bipvt) solar collector. *Solar Energy*, 83(4):445–455, 2009.

[62] HA Zondag, DW De De Vries, WGJ Van Helden, RJC Van Zolingen, and AA Van Steenhoven. The thermal and electrical yield of a pv-thermal collector. *Solar energy*, 72(2):113–128, 2002.

[63] Englert. Connecticut architect uses “solar sandwich”. *http://www.englertinc.com/project-of-the-month/connecticut-architect-uses-%E2%80%9Csolar-sandwich%E2%80%9D.html*, 2011.

[64] H Zondag, N Van der Borg, and W Eisenmann. D8-6: Pvt performance measurement guidelines: Guidelines for performance measurements of liquid-cooled non-concentrating pvt collectors using c-si cells. *Petten: ECN & ISFH: Emmerthal*, 2005.

[65] LW Florschuetz. Extension of the hottel-whillier model to the analysis of combined photovoltaic/thermal flat plate collectors. *Solar Energy*, 22(4):361–366, 1979.

[66] T. Jiblle. Jiblem. *The Jibble Jobble of Jibby Jobby*, 1930.

[67] Trond Bergene and Ole Martin Løvvik. Model calculations on a flat-plate solar heat collector with integrated solar cells. *Solar energy*, 55(6):453–462, 1995.

[68] B.Ø. Sandnes and J. Rekstad. A photovoltaic/thermal (pv/t) collector with a polymer absorber plate. experimental study and analytical model. *Solar Energy*, 72(1):63–73, 2002.

[69] Gunter Rockendorf, Roland Sillmann, Lars Podlowski, and Bernd Litzenburger. Pv-hybrid and thermoelectric collectors. *Solar Energy*, 67(4):227–237, 1999.

[70] D.W. De Vries. Design of a photovoltaic/thermal combi-panel. 1998.

[71] Adel A Hegazy. Comparative study of the performances of four photovoltaic/thermal solar air collectors. *Energy Conversion and Management*, 41(8):861–881, 2000.

[72] JK Tonui and Y Tripanagnostopoulos. Air-cooled pv/t solar collectors with low cost performance improvements. *Solar Energy*, 81(4):498–511, 2007.

[73] Anand S Joshi and Arvind Tiwari. Energy and exergy efficiencies of a hybrid photovoltaic–thermal (pv/t) air collector. *Renewable Energy*, 32(13):2223–2241, 2007.

[74] TT Chow. Performance analysis of photovoltaic-thermal collector by explicit dynamic model. *Solar Energy*, 75(2):143–152, 2003.

[75] Swapnil Dubey and GN Tiwari. Thermal modeling of a combined system of photovoltaic thermal (pv/t) solar water heater. *Solar Energy*, 82(7):602–612, 2008.

[76] A. Ibrahim, MY Othman, MH Ruslan, MA Alghoul, M. Yahya, A. Zaharim, and K. Sopian. Performance of photovoltaic thermal collector (pvt) with different absorbers design. *WSEAS Transactions on Environment and Development*, 5(3):321–330, 2009.

[77] R. Zakharchenko, L. Licea-Jimenez, SA Perez-Garcia, P. Vorobiev, U. Dehesa-Carrasco, JF Perez-Robles, J. Gonzalez-Hernandez, and Y. Vorobiev. Photovoltaic solar panel for a hybrid pv/thermal system. *Solar energy materials and solar cells*, 82(1-2):253–261, 2004.

[78] SMA. Publicly available pv system.

[79] Fin O'Flaherty, James Pinder, and Craig Jackson. Evaluating the performance of domestic solar thermal systems, 2012.

[80] Ashish Shukla, Dan Nchelatebe Nkwetta, YJ Cho, Vicki Stevenson, and Phil Jones. A state of art review on the performance of transpired solar collector. *Renewable and Sustainable Energy Reviews*, 16(6):3975–3985, 2012.

[81] I Katic. Measurement report: Test of pv/t module "solar wall pvt". *http://archive.iea-shc.org/publications/task.aspx?Task=35*, 2007.

[82] BP Cartmell, Neil J Shankland, Dusan Fiala, and V Hanby. A multi-operational ventilated photovoltaic and solar air collector: application, simulation and initial monitoring feedback. *Solar Energy*, 76(1):45–53, 2004.

[83] Encraft. Innovative solar pvt for a private home. *http://www.encraft.co.uk/case-studies/innovative-solar-pvt-solution-for-a-private-home/ accessed 24/01/14*, 2014.

[84] Solimpeks. Company presentation. *http://www.solimpeks.com/wp-content/uploads/2012/06/pvt_presentation_en.pdf accessed 08/08/2014*, 2014.

[85] Toru Fujisawa and Tatsuo Tani. Annual exergy evaluation on photovoltaic-thermal hybrid collector. *Solar energy materials and solar cells*, 47(1):135–148, 1997.

[86] Soteris A Kalogirou. Use of trnsys for modelling and simulation of a hybrid pv–thermal solar system for cyprus. *Renewable energy*, 23(2):247–260, 2001.

[87] SA Kalogirou and Y Tripanagnostopoulos. Hybrid pv/t solar systems for domestic hot water and electricity production. *Energy Conversion and Management*, 47(18):3368–3382, 2006.

[88] Soteris A Kalogirou. Solar thermal collectors and applications. *Progress in energy and combustion science*, 30(3):231–295, 2004.

[89] LA Chidambaram, AS Ramana, G Kamaraj, and R Velraj. Review of solar cooling methods and thermal storage options. *Renewable and sustainable energy reviews*, 15(6):3220–3228, 2011.

[90] Francesco Calise, Massimo Dentice d'Accadia, and Laura Vanoli. Design and dynamic simulation of a novel solar trigeneration system based on hybrid photovoltaic/thermal collectors (pvt). *Energy Conversion and Management*, 60:214–225, 2012.

[91] S Ito, N Miura, and K Wang. Performance of a heat pump using direct expansion solar collectors. *Solar Energy*, 65(3):189–196, 1999.

[92] Sadasuke Ito, Nakatsu Miura, Jin Qi Wang, and Miwako Nishikawa. Heat pump using a solar collector with photovoltaic modules on the surface. *Journal of Solar Energy Engineering*, 119(2):147–151, 1997.

[93] M Bakker, HA Zondag, MJ Elswijk, KJ Strootman, and MJM Jong. Performance and costs of a roof-sized pv/thermal array combined with a ground coupled heat pump. *Solar energy*, 78(2):331–339, 2005.

[94] Anant Shukla, D Buddhi, and RL Sawhney. Solar water heaters with phase change material thermal energy storage medium: a review. *Renewable and Sustainable Energy Reviews*, 13(8):2119–2125, 2009.

[95] Emilio Rebollo, Francisco R Blanquez, Israel Lopez, Carlos Platero, C Carrero, et al. Overall feasibility of low cost conversion from pv to pvtw. In *Renewable Energy Research and Applications (ICRERA), 2013 International Conference on*, pages 638–643. IEEE, 2013.

[96] Wei He, Tin-Tai Chow, Jie Ji, Jianping Lu, Gang Pei, and Lok-shun Chan. Hybrid photovoltaic and thermal solar-collector designed for natural circulation of water. *Applied energy*, 83(3):199–210, 2006.

[97] AS Joshi, A Tiwari, GN Tiwari, I Dincer, and BV Reddy. Performance evaluation of a hybrid photovoltaic thermal (pv/t)(glass-to-glass) system. *International Journal of Thermal Sciences*, 48(1):154–164, 2009.

[98] Arvind Tiwari and MS Sodha. Parametric study of various configurations of hybrid pv/thermal air collector: experimental validation of theoretical model. *Solar Energy Materials and Solar Cells*, 91(1):17–28, 2007.

[99] Laetitia Brottier, Jean-Michel Hugo, and Rachid Bennacer. An innovative pv-t collector: Cfd and experimental results. *Research Gate*, 2014.

[100] Li Zhu, Robert F Boehm, Yiping Wang, Christopher Halford, and Yong Sun. Water immersion cooling of pv cells in a high concentration system. *Solar Energy Materials and Solar Cells*, 95(2):538–545, 2011.

[101] Geon-Woong Lee, Min Park, Junkyung Kim, Jae Ik Lee, and Ho Gyu Yoon. Enhanced thermal conductivity of polymer composites filled with hybrid filler. *Composites Part A: Applied Science and Manufacturing*, 37(5):727–734, 2006.

[102] B Lee, JZ Liu, Bin Sun, CY Shen, and GC Dai. Thermally conductive and electrically insulating eva composite encapsulants for solar photovoltaic (pv) cell. *eXPRESS Polymer Letters*, 2(5):357–363, 2008.

[103] BSI. Bs en 12975-2:2006 thermal solar systems and components - solar collectors - part 2 test methods. 2006.

[104] Alanod Solar. Microtherm absorber fact book. 2012.

[105] Douglas C Giancoli. Physics for scientists and engineers with modern physics. *International Edition*, 4, 2000.

[106] J. Duffie and W. Beckman. Solar engineering of thermal processes, 1991.

[107] SA Klein. Calculation of flat-plate collector loss coefficients. *Solar Energy*, 17:79, 1975.

[108] Hoyte Hottel and Austin Whillier. Evaluation of flat-plate solar collector performance. In *Trans. Conf. Use of Solar Energy;()*, volume 3, 1955.

[109] Myrna Dayan. High performance in low-flow solar domestic hot water systems. Master's thesis, University of Winconsin-Madison, 1997.

[110] SI Abdel-Khalik. Heat removal factor for a flat-plate solar collector with a serpentine tube. *Solar Energy*, 18(1):59–64, 1976.

[111] MF Zhang and Z. Lavan. Thermal performance of a serpentine absorber plate. *Proc. Annu. Meet.-Am. Sect. Int. Sol. Energy Soc.;(United States)*, 6(CONF-830622-), 1983.

[112] K.O.F. Lund. General thermal analysis of serpentine-flow flat-plate solar collector absorbers. *Solar energy*, 42(2):133–142, 1989.

[113] W. Xiaowu and H. Ben. Exergy analysis of domestic-scale solar water heaters. *Renewable and sustainable energy reviews*, 9(6):638–645, 2005.

[114] R. Saidur, G. Boroumand, S. Mekhlif, and M. Jameel. Exergy analysis of solar energy applications. *Renewable and Sustainable Energy Reviews*, 2011.

[115] JS Coventry and K. Lovegrove. Development of an approach to compare the 'value'of electrical and thermal output from a domestic pv/thermal system. *Solar Energy*, 75(1):63–72, 2003.

[116] DJ Close. A design approach for solar processes. *Solar Energy*, 11(2):112–122, 1967.

[117] NE Wijeysundera. Comparison of transient heat transfer models for flat plate collectors. *Solar Energy*, 21(6):517–521, 1978.

[118] SA Klein, JA Duffie, and WA Beckman. Transient considerations of flat-plate solar collectors. *Journal for Engineering for Power*, 96(2):109–113, 1974.

[119] Luca A Tagliafico, Federico Scarpa, and Mattia De Rosa. Dynamic thermal models and cfd analysis for flat-plate thermal solar collectors - a review. *Renewable and Sustainable Energy Reviews*, 30:526–537, 2014.

[120] Jürgen Schnieders. Comparison of the energy yield predictions of stationary and dynamic solar collector models and the models' accuracy in the description of a vacuum tube collector. *Solar Energy*, 61(3):179–190, 1997.

[121] B. Perers and C. Bales. A solar collector model for trnsys simulation and system testing. Technical report, International Energy Agency, 2002.

[122] YA Cengel. *Heat Transfer a Practical Approach*. McGraw-Hill, 1998.

[123] R.C. Jordan and B.Y.H. Liu. Applications of solar energy for heating and cooling of buildings. Technical report, American Society of Heating, Refrigerating and Air Conditioning Engineers, Inc., New York, 1977.

[124] V1 Gnielinski. New equations for heat and mass-transfer in turbulent pipe and channel flow. *International Chemical Engineering*, 16(2):359–368, 1976.

[125] F Ghani, Mike Duke, and James K Carson. Effect of flow distribution on the photovoltaic performance of a building integrated photovoltaic/thermal (bipv/t) collector. *Solar Energy*, 86(5):1518–1530, 2012.

[126] Joaquim Peiró and Spencer Sherwin. Finite difference, finite element and finite volume methods for partial differential equations. In *Handbook of materials modeling*, pages 2415–2446. Springer, 2005.

[127] JD Anderson Jr. Governing equations of fluid dynamics. In *Computational fluid dynamics*, pages 15–51. Springer, 2009.

[128] DJ Reynolds, MJ Jance, M Behnia, and GL Morrison. An experimental and computational study of the heat loss characteristics of a trapezoidal cavity absorber. *Solar Energy*, 76(1):229–234, 2004.

[129] Jianhua Fan, Louise Jivan Shah, and Simon Furbo. Flow distribution in a solar collector panel with horizontally inclined absorber strips. *solar energy*, 81(12):1501–1511, 2007.

[130] Mohamed Selmi, Mohammed J Al-Khawaja, and Abdulhamid Marafia. Validation of cfd simulation for flat plate solar energy collector. *Renewable energy*, 33(3):383–387, 2008.

[131] Oguz Turgut and Nevzat Onur. Three dimensional numerical and experimental study of forced convection heat transfer on solar collector surface. *International Communications in Heat and Mass Transfer*, 36(3):274–279, 2009.

[132] M.S. Manjunath, K. Karanth Vasudeva, and Yagnesh N. Sharma. Three dimensional numerical analysis of conjugate heat transfer for enhancement of thermal performance using finned tubes in an economical unglazed solar flat plate collector. In *Proceedings of the World Congress on Engineering 2011*, 2011.

[133] K Vasudeva Karanth, MS Manjunath, and N Yagnesh Sharma. Numerical simulation of a solar flat plate collector using discrete transfer radiation model (dtrm)–a cfd approach. In *Proceedings of the World Congress on Engineering*, volume 3, pages 6–8, 2011.

[134] G Martinopoulos, D Missirlis, G Tsilingiridis, K Yakinthos, and N Kyriakis. Cfd modeling of a polymer solar collector. *Renewable Energy*, 35(7):1499–1508, 2010.

[135] Damir Dovic and Mladen Andrassy. Numerically assisted analysis of flat and corrugated plate solar collectors thermal performances. *Solar energy*, 86(9):2416–2431, 2012.

[136] JA Marroquin, J.M. Manuel, Olivares-Ramrez, J.S. Omar, M. Antonio, Zamora-Antuñano, and A. Encinas-Oropesa. Analysis of flow and heat transfer in a flat solar collector with rectangular and cylindrical geometry using cfd. *Ingenierá Investigación y Tecnologá*, 14(4):553–561, 2013.

[137] G. Iordanou. *Flat-Plate Solar Collectors for Water Heating with Improved Heat Transfer for Application in Climatic Conditions of the Mediterranean Region*. PhD thesis, Durham University, 2009.

[138] Volker Weitbrecht, David Lehmann, and Andreas Richter. Flow distribution in solar collectors with laminar flow conditions. *Solar Energy*, 73(6):433–441, 2002.

[139] GF Jones and Noam Lior. Flow distribution in manifolded solar collectors with negligible buoyancy effects. *Solar energy*, 52(3):289–300, 1994.

[140] XA Wang and LG Wu. Analysis and performance of flat-plate solar collector arrays. *Solar Energy*, 45(2):71–78, 1990.

[141] David Roche, Hugh Outhred, and R John Kaye. Analysis and control of mismatch power loss in photovoltaic arrays. *Progress in Photovoltaics: Research and Applications*, 3(2):115–127, 1995.

[142] S Silvestre, A Boronat, and A Chouder. Study of bypass diodes configuration on pv modules. *Applied Energy*, 86(9):1632–1640, 2009.

[143] PVEducation. Mismatch for cells connected in parallel, 06 2014.

[144] S.Bremner. Solar electric systems, 04 2009.

[145] K Emery, J Burdick, Y Caiyem, D Dunlavy, H Field, B Kroposki, T Moriarty, L Ottoson, S Rummel, T Strand, et al. Temperature dependence of photovoltaic cells, modules and systems. In *Photovoltaic Specialists Conference, 1996., Conference Record of the Twenty Fifth IEEE*, pages 1275–1278. IEEE, 1996.

[146] David L King, Jay A Kratochvil, and William E Boyson. Temperature coefficients for pv modules and arrays: measurement methods, difficulties, and results. In *Photovoltaic Specialists Conference, 1997., Conference Record of the Twenty-Sixth IEEE*, pages 1183–1186. IEEE, 1997.

[147] T. Nordmann and L. Clavadetscher. Understanding temperature effects on pv system performance. In *Photovoltaic Energy Conversion, 2003. Proceedings of 3rd World Conference on*, volume 3, pages 2243–2246. IEEE, 2003.

[148] Sebnem Kemaloglu, Guralp Ozkoc, and Ayse Aytac. Thermally conductive boron nitride/sebs/eva ternary composites:â€œprocessing and characterizationâ€? *Polymer Composites*, 31(8):1398–1408, 2010.

[149] BSI. Bs en iso 22007:2012 plastics - determination of thermal conductivity and thermal diffusivity. 2012.

[150] Martin Rides, Junko Morikawa, Lars Halldahl, Bruno Hay, Hubert Lobo, Angela Dawson, and Crispin Allen. Intercomparison of thermal conductivity and thermal diffusivity methods for plastics. *Polymer Testing*, 28(5):480–489, 2009.

[151] ASTM. Standard test method for thermal conductivity and thermal diffusivity by modulated temperature differential scanning calorimetry. Technical report, ASTM Internation, 2006.

[152] G Hakvoort, LL Van Reijen, and AJ Aartsen. Measurement of the thermal conductivity of solid substances by dsc. *Thermochimica acta*, 93:317–320, 1985.

[153] Joseph H Flynn and David M Levin. A method for the determination of thermal conductivity of sheet materials by differential scanning calorimetry (dsc). *Thermochimica acta*, 126:93–100, 1988.

[154] Z Dehouche, N Grimard, F Laurencelle, J Goyette, and TK Bose. Hydride alloys properties investigations for hydrogen sorption compressor. *Journal of Alloys and compounds*, 399(1):224–236, 2005.

[155] H Fukushima, LT Drzal, BP Rook, and MJ Rich. Thermal conductivity of exfoliated graphite nanocomposites. *Journal of thermal analysis and calorimetry*, 85(1):235–238, 2006.

[156] Duncan M Price and Mark Jarratt. Thermal conductivity of ptfe and ptfe composites. *Thermochimica acta*, 392:231–236, 2002.

[157] Adriano Antunes Souza Araújo, Marlia dos Santos Bezerra, Slvia Storpirtis, and Jivaldo do Rosário Matos. Determination of the melting temperature, heat of fusion, and purity analysis of different samples of zidovudine (azt) using dsc. *Brazilian Journal of Pharmaceutical Sciences*, 46(1):37–43, 2010.

[158] Total. Ethylene vinyl acetate copolymers (eva), 2014.

[159] Azom. Boron nitride (bn) - properties and information on boron nitride.